Novel inhibitors for the protease Taspase1

Inaugural-Dissertation zur Erlangung des Doktorgrades
Dr. rer. nat.

Fakultät für Biologie der Universität Duisburg-Essen
Campus Essen

vorgelegt von
Johannes van den Boom
aus Essen

Juni 2014

Die der vorliegenden Arbeit zu Grunde liegenden Experimente wurden in der Abteilung Strukturelle und Medizinische Biochemie am Zentrum für Medizinische Biotechnologie der Universität Duisburg-Essen durchgeführt.

1. Gutachter: Prof. Dr. Peter Bayer
2. Gutachter: Prof. Dr. Shirley Knauer
3. Gutachter: Prof. Dr. Michael Ehrmann

Vorsitzender des Prüfungsausschusses: Prof. Dr. Markus Kaiser

Tag der mündlichen Prüfung: 09.09.2014

WIRKLICHES NEULAND IN EINER WISSENSCHAFT
KANN WOHL NUR GEWONNEN WERDEN,
WENN MAN AN EINER ENTSCHEIDENDEN STELLE
BEREIT IST, DEN GRUND ZU VERLASSEN,
AUF DEM DIE BISHERIGE WISSENSCHAFT RUHT,
UND GEWISSERMASSEN INS LEERE ZU SPRINGEN.

WERNER HEISENBERG (1901-1976)

Für meine Eltern,
die mir all dies ermöglicht haben

List of abbreviations

Å	Ångström
ALL	acute lymphatic leukemia
AML	acute myeloic leukemia
Amsil	amorphous silica nanoparticle
APS	ammonium peroxydisulfate
AU	arbitrary units
BioTasp	artificial Taspase activity sensor for cellular assays
CD	circular dichroism
CLL	chronic lymphatic leukemia
CML	chronic myeloic leukemia
CS1, CS2	Taspase cleavage sites 1 and 2 in the MLL protein, respectively
C-terminus	carboxy-terminus / COOH-terminus
Da	Dalton
DMSO	dimethyl sulfoxide
DOL	degree of labeling
DTT	dithiothreitol, reducing agent
E. coli	*Escherichia coli*, bacterium
EC_{50}	effective concentration, necessary for 50 % effect
ESI	electron spray ionization
Fmoc	fluorenylmethyloxycarbonyl, a protection group
FPLC	fast protein liquid chromatography
FRET	Förster resonance energy transfer
G, A, T, C	DNA bases: guanine, adenine, thymine, cytosine
GFP	green fluorescent protein
GST	glutathione S-transferase
Hela	cervical cancer cell line
Hox	homeobox
HSQC	heteronuclear single quantum coherence
IC_{50}	inhibitory concentration, necessary for 50 % inhibition
IPTG	isopropyl-thiogalactopyranoside
K_d	dissociation constant
K_i	inhibitory constant
K_m	Michaelis constant
KP_i	potassium phosphate
LC	liquid chromatography
LDH	lactate dehydrogenase
M	molar, mol/l
MALDI	matrix-assisted laser desorption/ionization
MD	molecular dynamics
MLL	mixed lineage leukemia
MS	mass spectrometry
MST	microscale thermophoresis
NADH	nicotineamide adenine dinucleotide
NES	nuclear export signal
NiNTA	nickel nitrilotriacetic acid, binds hexahistidine-tagged proteins
NLS	nuclear localization signal
NMR	nuclear magnetic resonance
N-terminus	amino-terminus / NH_2-terminus
Ntn	N-terminal nucleophile
OD_{600}	optical density at 600 nm wavelength

PCR	polymerase chain reaction
PDB	Protein Data Bank
PMT	photomultiplier tube, a light detector
RBS	ribosomal binding site
RMSD	root mean square distance
rpm	rounds per minute
SDS-PAGE	sodium dodecyl sulfate polyacrylamide gel electrophoresis
Taspase	threonine aspartase1 / Taspase1 / TASP1
T_m	melting temperature
UV	ultraviolet
wt	wild type

Amino acids

A	Ala	alanine
C	Cys	cysteine
D	Asp	aspartate
E	Glu	glutamate
F	Phe	phenylalanine
G	Gly	glycine
H	His	histidine
I	Ile	isoleucine
K	Lys	lysine
L	Leu	leucine
M	Met	methionine
N	Asn	asparagine
P	Pro	proline
Q	Gln	glutamine
R	Arg	arginine
S	Ser	serine
T	Thr	threonine
V	Val	valine
W	Trp	tryptophan
Y	Tyr	tyrosine

List of figures

List of tables

Table of contents

1 Introduction

1.1 Mixed lineage leukemia

1.1.1 Cancer and leukemia

Cancer constitutes a group of diseases characterized by uncontrolled cell division. This results in unregulated cell growth and the formation of malignant tumors that can spread to other organs. Cancer typically originates from a single cell which has undergone progressive genetic aberrations to escape cell death and promote proliferation.

In 2011, roughly 450 in 100 000 individuals were newly diagnosed with cancer [1]. The most common forms of cancer in Europe are lung cancer (13.3 %), colorectal cancer (13.2 %), and breast cancer (13 %) [2]. In principle, tumors can occur in every tissue, and currently more than 200 cancer types are described [3].

However, all tumor cells share some features by which they can be distinguished from healthy cells. Essentially, they found ways to successfully unbalance the delicate and strictly regulated balance of proliferation and apoptosis. Hanahan and Weinberg proposed six essential alterations common for the majority of tumors: (i) apoptosis evasion, (ii) self-sufficiency in growth signals, (iii) insensitivity to anti-growth signals, (iv) metastasis, (v) limitless replicative potential, and (vi) sustained angiogenesis (figure 1.1; [4]).

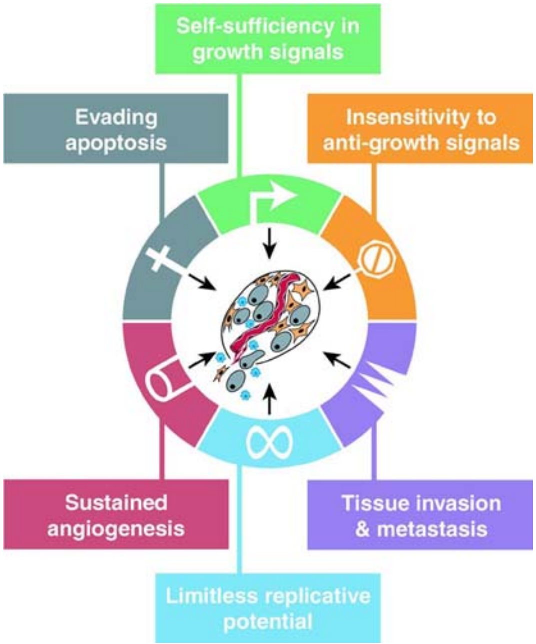

Figure 1.1 Hallmarks of cancer.

Most cancers have acquired the same set of functional alterations in a series of steps. These new capabilities are termed hallmarks of cancer. According to [4].

This model was later on extended by evasion of immune surveillance and mechanisms to compensate for stress generated by the tumor transformation, including metabolic, proteotoxic, mitotic, oxidative, as well as DNA damage stress. Each aberration depicted in figure 1.1 represents the breaching of an anticancer mechanism and is acquired by point mutation, gene amplification, deletion, or chromosomal translocation. Tumor-associated genes can be classified as oncogenes or tumor suppressor genes. While oncogenes, such as growth factors, can promote tumor proliferation, tumor suppressors are responsible for cell cycle control as well as apoptosis, and are therefore often repressed in tumors.

Malignant transformations occur not only in solid tissues, but also in blood cells. Such types of cancer are referred to as leukemia and describe cancers of the hematopoietic system characterized by a rapid proliferation of white blood cells. These cells replace the normal bone marrow cells, which results in an increased release of immature progenitor cells, called blasts, to the peripheral blood system. Eventually, these malignant cells suppress the production of normal blood cells, which causes a deficiency of functional red and white blood cells. As a consequence, most patients suffer from immunodeficiency, impaired blood clotting, or anemia. In Germany, 26 in 100 000 individuals are newly diagnosed with leukemia every year (number from 2012; [5]). Moreover, concerning children under the age of 15, leukemia is the most frequent malignancy accounting for 31 % of all cancer cases [6].

Clinically, leukemias can be subdivided into acute and chronic forms. Patients with acute leukemia usually show a sudden appearance of symptoms in combination with a rapid progression of the disease. Acute leukemias end lethal within weeks, if not treated immediately [7]. In contrast, chronic leukemias typically develop over a longer period of time and progress slowly [8]. Additionally, both acute and chronic leukemia can be subdivided into lymphocytic and myelogenous forms, according to the type of affected blood cells. While lymphocytic forms arise in progenitor cells of lymphocytes, myelogenous forms affect myeloid cells which normally differentiate into erythrocytes, as well as thrombocytes and other types of white blood cells. Altogether, the four major types of leukemia are acute lymphatic leukemia (ALL), acute myeloic leukemia (AML), chronic lymphatic leukemia (CLL) and chronic myeloic leukemia (CML).

One exception from this classification is the myeloic-lymphoid or mixed lineage leukemia (MLL). This aggressive leukemia affects both the lymphoid and myeloid lineage [9] and its molecular pathogenesis is explained in detail below.

1.1.2 Translocations are associated with leukemia

Although the causative factors for leukemia are still unclear in most cases, some risk factors were determined. Especially ionizing radiation contributes significantly to acute leukemias [10], but also chemicals, such as pesticides [11] or benzenes [12] increase the risk for leukemia. Nevertheless, even if other factors, such as age, smoking, obesity and familial background, are considered, only 15-20 % of all leukemia cases can be explained with these risk factors [13].

Moreover, also at the molecular level the causes for most cases of leukemia are yet to be identified. However, several studies pinpointed that translocations play an important role in leukemogenesis and are commonly observed in all four major types of leukemia, with more than 400 different translocations described for acute leukemias [14]. Translocations require a double strand break, occurring either spontaneously or induced by irradiation or cytotoxic agents, with subsequent reciprocal fusion to a nonhomologous chromosome [15]. Importantly, two separate genes can be joined to a fusion gene in this process. If a proto-oncogene is fused to an abundantly expressed gene with a strong promoter or the fusion protein has different functions, the cell can be transformed to a tumor cell.

Interestingly, particular translocations are associated with certain leukemias [16]. The most prominent example is the CML-related Philadelphia chromosome, which is the result of a reciprocal translocation of chromosomes 9 and 22 (t(9;22)(q34;q11)). This translocation fuses the *ABL* gene (*Abelson murine leukemia viral oncogene homolog 1*) to the *BCR* gene (*breakpoint cluster region*; [17]) and generates a fusion protein with permanently active tyrosine kinase activity.

1.1.3 11q23 translocations cause mixed lineage leukemia

11q23 translocations involving the *MLL* gene, also referred to as *ALL-1* or *HRX*, are among the most common non-random translocations [16]. Such rearrangements join the N-terminal part of the *MLL* gene to a fusion partner gene by non-homologous end joining [18–20] and are related to mixed lineage leukemia (MLL). In contrast to other translocations, *MLL* is a promiscuous oncogene with more than 60 different fusion partner genes [21]. However, the fusion partners can be categorized into two groups. The first group comprising the six most frequent fusion partners *AF4*, *AF9*, *ENL*, *AF10*, *ELL*, and *AF6* accounts for more than 85 % of all clinical cases [19].

Further studies showed that all frequent partners except for AF6 are nuclear proteins, while the remaining fusion partners of the second group are predominantly localized in the cytoplasm (table 1.1). Due to the nuclear localization signal in the MLL protein, all resulting fusion proteins are found in the nucleus [9].

Table 1.1 Selection of MLL fusion partners.
According to [9].

Name	Features	Localization
ENL	Binds histone H3, assembles ENL associated proteins elongation/chromatin remodeling complex	Nucleus
AF4	ENL homolog	Nucleus
AF6	Dimerization domain	Cytoplasma
AF9	Founder of AF4 family, member of ENL associated proteins	Nucleus
AF10	Interacts with DOT1L histone methyltransferase	Nucleus
ELL	Elongation factor, interacts with a AF4 related protein	Nucleus
AF1p	Dimerization domain	Cytoplasma
ABI1	Interacts with ENL when imported to nucleus	Cytoplasma
GAS7	Dimerization domain	Cytoplasma

In spite of the promiscuity of MLL with respect to its fusion partners, not every protein causes leukemia in mice when fused to MLL [22,23]. Moreover, a mere truncation of the MLL protein is not sufficient to cause leukemia [19]. For most *MLL* translocations, the double strand break occurs in an 8 kb spanning region of the *MLL* gene called breakpoint cluster region [24]. Such *MLL*-involving translocations are of high clinical relevance, as they are found in roughly 70 % of infant ALL and occur in 10 % of all other ALL cases [9,25].

The cellular mechanisms leading to the exhibition of tumor features are multifaceted [19]. Current data indicate that *MLL* translocations cause increased expression of Hox genes by MLL itself and recruitment of transcription control complexes by the fusion partner genes, which also enhances transcription of MLL target genes. Altogether, this t(4;11)-triggered mixed lineage leukemia is a very aggressive type of acute leukemia with dismal prognosis: Only 40 % of all infants survive five years after MLL diagnosis [26], whereas the five-year survival rate of infants with non-mixed lineage leukemia is near 90 % [27].

In 1996, the first mouse model for MLL studies was successfully generated. These mice expressed the MLL-AF9 fusion protein under the control of the endogenous *MLL* promoter and were found to develop AML and rarely ALL [28]. Moreover, *MLL* translocations differ from other translocations in that both of the two fusion genes generated by the reciprocal translocation were recently reported to function as oncogenes. In the respective study, the two oncoproteins resulting from the fusion of *AF4* and *MLL*, namely AF4-MLL and MLL-AF4, contributed concertedly to the pathologic mechanism [29,30].

1.2 The MLL protein

1.2.1 MLL is a multidomain protein

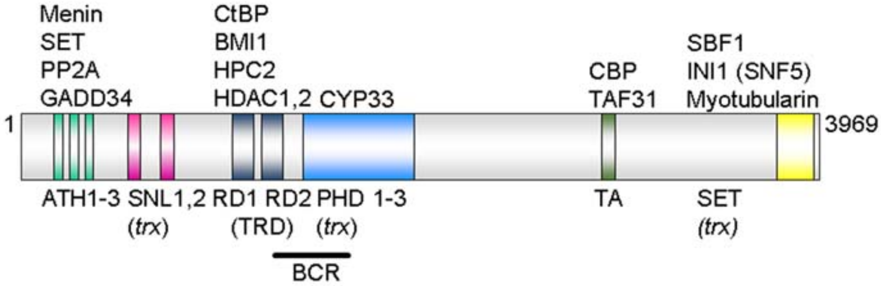

Figure 1.2 Domains of the MLL protein.

Schematic representation of the mixed lineage leukemia (MLL) gene. Protein binding sites are indicated above the respective domains. ATH: AT-hook motif mediating binding to the minor groove of AT-rich DNA sequences; SNL: speckled nuclear localization site; TRD: transcriptional repression domain comprising the two functional subunits RD1 and RD2; PHD: plant homology domain; TA: transcriptional activation domain; SET: Su(var)3-9, enhancer-of-zeste, trithorax domain; BCR: breakpoint cluster region. According to [19].

Owing to the high clinical importance of the ubiquitously expressed MLL protein for leukemia, several studies were conducted to unravel its functions. Consisting of 3969 amino acids, the MLL protein comprises multiple conserved domains (figure 1.2): Binding to AT rich DNA regions is mediated by three N-terminal AT-hook motifs [31], which are followed by a repression domain with DNA methyltransferase homology [32], and zinc fingers that mediate binding to the cyclophilin CYP33 [33]. In the C-terminal region of the MLL protein, a transactivation domain interacting with CREB-binding protein (CBP) is found, as well as a SET (Su(var)3-9, enhancer-of-zeste, trithorax) domain with histone H3K4 methyltransferase activity.

With the help of these domains, MLL functions as transcriptional regulator. In particular, it regulates Hox gene expression and is therefore found widely expressed during embryonic development, while most adult tissues display only low expression levels [16]. Of note, *MLL* seems indispensable for vertebrate development and thus *MLL* knockout mice show embryonic lethality in addition to homeotic transformations [16,34,35].

Closer mechanistic analysis of the underlying processes revealed that especially the H3K4 methyltransferase activity of the SET domain is reported to be important for Hox gene regulation [36]. Consequently, mice with MLL protein lacking the SET domain showed skeletal defects and altered Hox gene expression similar to *MLL* knockout mice [37].

1.2.2 MLL fusion proteins

MLL fusion proteins result from genetic translocations involving the MLL gene (section 1.1.2).

Both the wild type and MLL fusion proteins exert their central role in gene expression regulation by interactions with a plethora of other proteins. For this, MLL and also the MLL fusion proteins serve as a platform for the formation of a supercomplex composed of more than 30 proteins (figure 1.3; [38,39]).

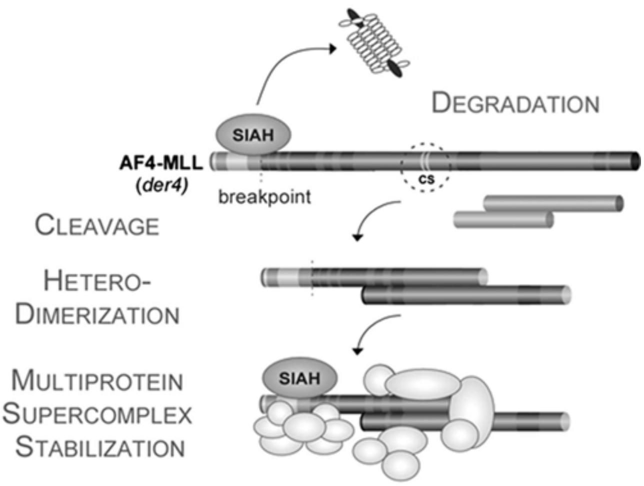

Figure 1.3 MLL fusions proteins.

The AF4-MLL fusion protein is bound by SIAHs and subjected to proteasomal degradation. Activation by proteolytic cleavage at defined cleavage sites (CS) allows heterodimerization and formation of a stable multiprotein supercomplex resistant to SIAH-mediated degradation. According to [38].

In 2003, Hsieh and colleagues reported another critical step necessary for MLL activity: The MLL protein requires proteolytic cleavage and the two subunits form a heterodimer mediated by the interaction of a FYRN domain in the 320 kDa N-terminal fragment and the FYRK and SET domains in the 180 kDa C-terminal fragment (figure 1.4; [40]).

The uncleaved AF4-MLL fusion protein interacts with seven in absentia homologs (SIAHs) via the SIAH-dependent degron located in the N-terminal half of the AF4 protein, which subjects the precursor fusion protein to proteasomal degradation. In contrast, the activated MLL heterodimer is protected against degradation and the MLL complex including SIAHs is stabilized (figure 1.3; [38]). This mechanism is thought to trap SIAH and prevent SIAH-mediated degradation of other tumor-relevant proteins.

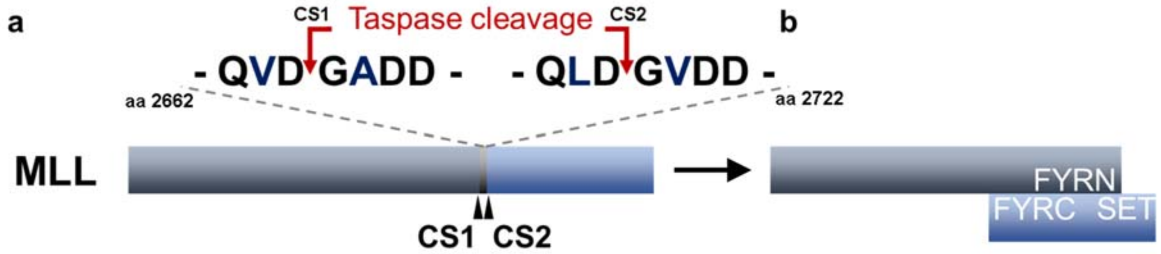

Figure 1.4 Processing of Taspase and MLL.

a The MLL protein comprises two similar Taspase cleavage sites, termed CS1 (left sequence) and CS2 (right sequence). **b** Upon Taspase cleavage, the 52 amino acids fragment between the two cleavage sites is degraded and the two large MLL fragments assemble to a dimer via a FYRN interaction domain in the N-terminal fragment and FYRC and SET domains in the C-terminal fragment.

Further analyses revealed that MLL is cleaved at two similar proteolytic cleavage sites 53 amino acids apart from each other, referred to as CS1 and CS2 (figure 1.4). While CS2 is highly conserved among all MLL homologs, including the human MLL2 protein and the trithorax protein in *Drosophila melanogaster*, CS1 is present only in vertebrates. Subsequently, the protease for MLL cleavage was discovered. Due to the threonine as its active site residue and the specific cleavage after aspartate, this protease was named threonine aspartase 1 (Taspase). Taspase is able to cleave both cleavage sites (CS1 and CS2) in the MLL protein and has gained in importance as protease-mediated cleavage is indispensable for MLL activation.

1.3 The role of Taspase in cancer

1.3.1 Proteases and cancer

Proteases are enzymes that catalyze the hydrolysis of peptide bonds and are therefore able to cleave proteins and peptides. They play key roles in food digestion, degradation of misfolded and unneeded proteins, but also in the regulation of other cellular processes, such as apoptosis, blood coagulation, immune response, and cell cycle progression [41].

Due to the irreversibility nature of proteolytic cleavage, proteases are strictly regulated in the body. Besides posttranslational modification [42,43], activation of an inactive precursor protein (zymogen) by limited proteolysis is a common mechanism, which represents an essential step in many important cellular pathways: The activation of caspases during apoptosis [44], the activation of blood clotting factors [45], the activation of trypsin and other proteases as well as signaling via protease-activated receptors (PARs) [46] are only a few examples for proteolytic activation. In contrast to protein degradation, proteolytic activation events occur in a site-specific manner and the respective proteases are highly specific [41].

Cleavage of target proteins by proteases occurs either at the N- or C-termini (exopeptidases) or within the polypeptide chain (endopeptidases) at protease specific cleavage sites, termed consensus sequences. The amino acids N-terminal of the cleavage site are referred to as P1, P2, etc., while the amino acids C-terminal of the scissile bond are numbered P1’, P2’, etc. (figure 1.5a). The sites at the surface of the protease that can bind a single substrate residue are called subsites, and numbered S_n or S_n’ according to its respective substrate position. Consequently, the scissile bond is located between the P1 and P1’ site.

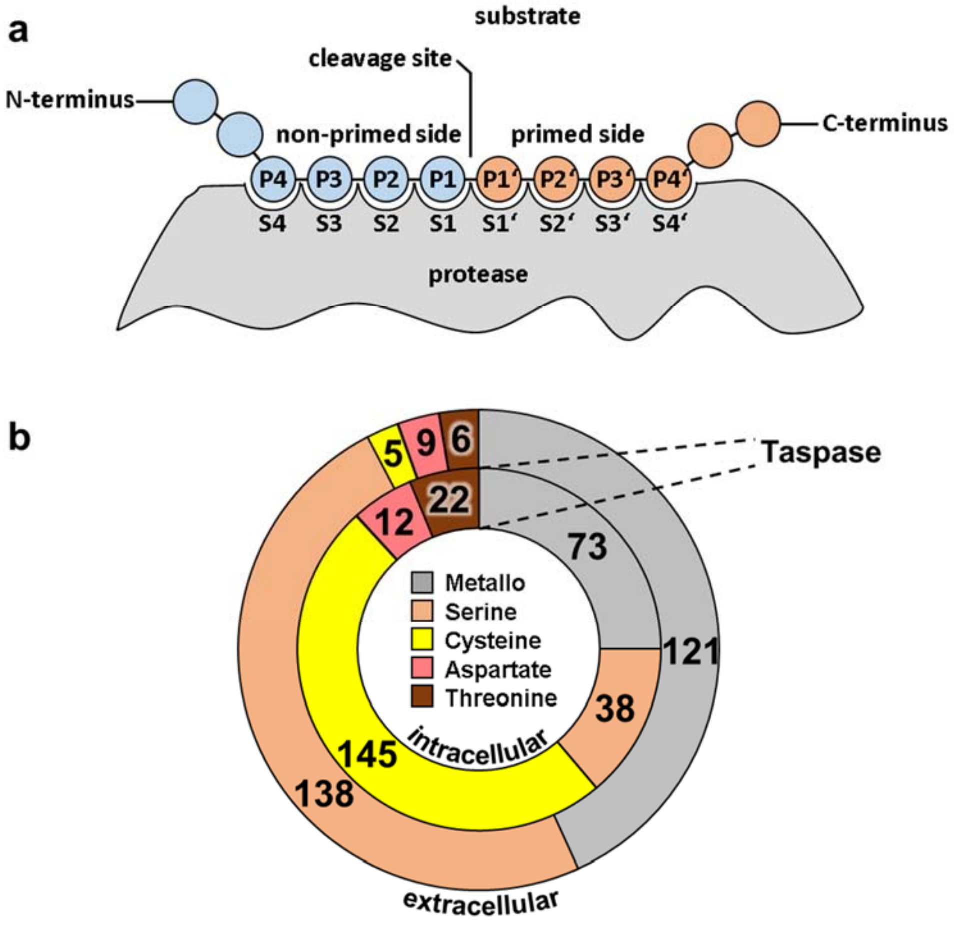

Figure 1.5 Substrate binding and protease families.

a Substrate binding to a protease. Substrate residues participating in binding to the protease (gray) are numbered P1-P_n (non-primed sites; blue) N-terminal of the cleavage site and P1’-P_n’ (primed sites; red) C-terminal of the cleavage site. The respective binding sites at the surface of the protease that accommodate the amino acid side chains are numbered S1-S_n and S1’-S_n’, respectively. Cleavage occurs between the P1 and P1’ position.

b Human proteases can be classified according to their active site into five classes that can be either intra- (inner ring) or extracellular (outer ring). Numbers inside the rings indicate the number of members of the color coded classes. According to [47].

The more than 500 human proteases can be classified into five classes according to their active site, that is, serine, cysteine, cysteine, aspartate, and metalloproteases (figure 1.5b; [47,48]). All five classes of proteases are involved in tumor initiation, growth, metastasis as well as invasion into other sites [49]. For this, the tumor associated proteases target and regulate diverse cellular processes. Up regulation of cell proliferation, down regulation of cell death, angiogenesis, as well as induction of multi-drug resistance are only a few examples of cellular processes governed by proteases [50]. In this regard, trypsin is involved in colorectal carcinogenesis, as it positively regulates proliferation and metastasis [51], cathepsins B and D are closely related with invasion and progression of oral squamous cell carcinoma [52], and caspase deregulation is known to cause neuroblastomas [53]. As some proteases are specific for certain cancer types, proteases can also serve as useful prognostic and diagnostic markers to improve cancer treatment [54].

Some proteases possess tumor suppressive effects and loss-of-function mutations in the respective genes promote malignant transformation [55]. Investigating the role of tumor-related proteases and their mechanism can therefore yield new targets for cancer therapies.

1.3.2 Taspase is a type II asparaginase

Taspase was discovered in 2003 as the protease responsible for the proteolytic activation of the MLL protein. As a member of the type II asparaginase family, Taspase displays the typical asparaginase fold with a central β-sheet sandwich surrounded on both faces by α-helices [56]. However, Taspase shares only low sequence similarity with other type II asparaginases and the proteasome as related threonine protease (table 4.1). Nevertheless, the structure of this family is highly conserved with RMSD values below 2 Å (figure 1.6a).

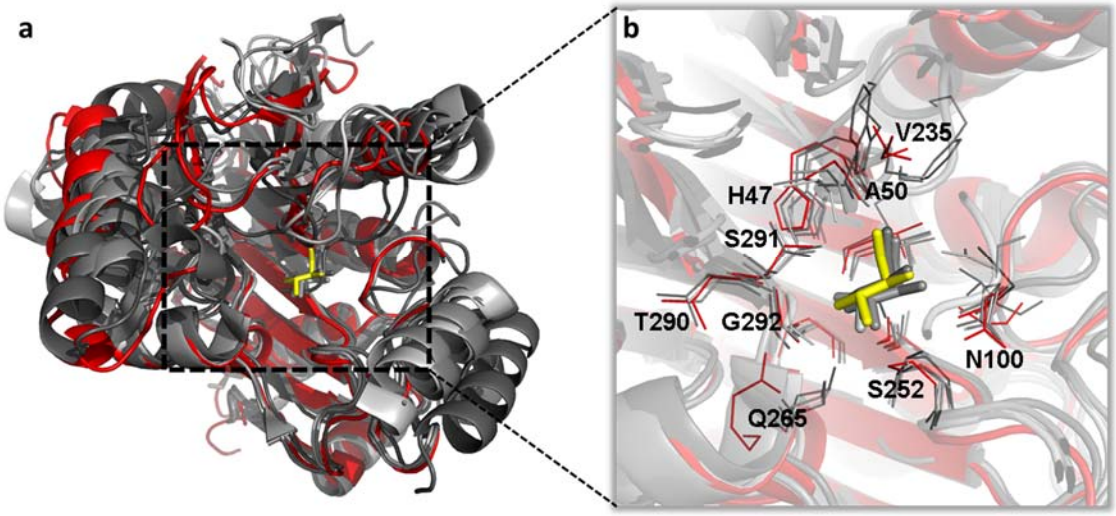

Figure 1.6 Taspase displays a conserved asparaginase fold.

a Overlay of the crystal structure of Taspase (red; PDB 2a8j) with human asparaginase (4gdw), plant asparaginase (2gez), *E. coli* asparaginase (2zal) and *F. meningosepticum* glycosylasparaginase (1ayy) reveals a conserved asparaginase fold. The structures were aligned using PyMOL. **b** Close-up view of the active site residues of Taspase (red) and its homologs (gray) shows a conserved side chain orientation. Side chains are displayed as sticks and the catalytic threonine is highlighted in yellow.

Although all other asparaginases do not act as proteases but hydrolyze the free amino acid asparagine to aspartate [57], the active site is similar to Taspase, including the orientation of the catalytic threonine (figure 1.6b). Despite the small differences found between the active sites of Taspase and other type II asparaginases, the reason for the diverse reactions which are catalyzed is yet to be elucidated. To become catalytically competent, the 45 kDa Taspase proenzyme undergoes proteolytic cleavage into two subunits (figure 1.7).

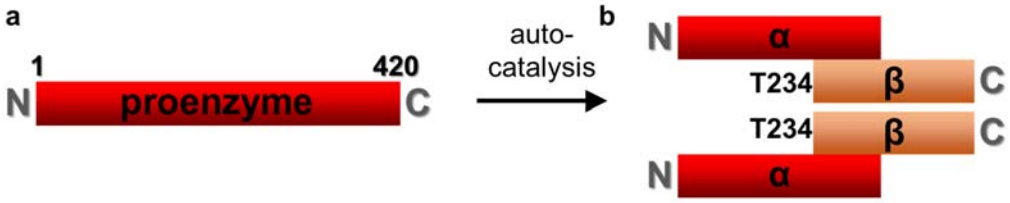

Figure 1.7 Autocatalytic processing of Taspase.

a The Taspase proenzyme comprises 420 amino acids and undergoes spontaneous autoproteolytic cleavage between Asp233 and Thr234. **b** This process yields a 25 kDa α-subunit (amino acids 1-233; red) and a 20 kDa β-subunit (amino acids 234-420; orange). In this process, Thr234 becomes the N-terminal amino acid of the β-subunit and its free hydroxyl group renders Taspase proteolytically active. Two αβ-heterodimers assemble to a hetero-tetramer with αββα structure. N: Amino-terminus; C: carboxy-terminus

Such a removal of a propeptide is typical for type II asparaginases and other proteases, with renin [58] and chymotrypsin [59] as well-studied examples, and serves to inhibit enzyme activity and as folding helper [60]. The autocatalytic proteolytic processing of the type II asparaginase proenzymes has been elucidated in detail [61,62]. In short, the catalytic threonine side chain attacks the peptide bond to the preceding aspartate, before the protein backbone and side chain bonds between threonine and aspartate are broken (figure 1.8). For Taspase, the whole maturation process was found to be a spontaneous reaction and not catalyzed by other Taspase proteins *in trans* [63].

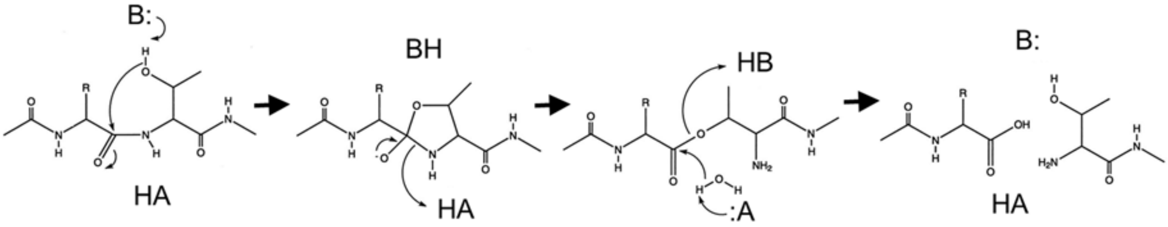

Figure 1.8 Autocatalytic activation of Taspase and other type II asparaginases.

The side chain OH-group of the catalytic threonine forms a covalent bond to the CO of the preceding aspartate, yielding a tetrahedral intermediate and a general base (B) captures the proton of the threonine OH-group (first reaction). Subsequently, the backbone C-N bond is broken and a general acid (HA) donates a proton to the newly created N-terminus (second reaction). Eventually, a water attack to the CO breaks the bond between the aspartate backbone and the threonine side chain (third reaction). Modified according to [61].

Eventually, this process renders a free hydroxyl group at the N-terminal threonine 234 of the β-subunit. Hence, Taspase and other asparaginases belong to the N-terminal nucleophile (Ntn) family of proteases. Detailed analysis of the crystal structure of Taspase revealed a rotation of the Thr234 side chain in addition to a backbone shift upon activation [56]. Mutation of the active site threonine to valine does not only prevent the autocatalytic activation event, but also renders Taspase unable to cleave its substrates *in trans* [56,57].

After autoprocessing, the α- and β-subunits form a heterodimer, and two of these dimers are supposed to assemble to a hetero-tetramer (figure 1.7b; [64]). The resulting αββα fold after autoprocessing is a common feature of all Ntn hydrolases despite very low sequence similarity and was described for glycosylasparaginase [65], plant asparaginase [66], and the only other threonine protease in the Ntn family, the proteasome [67]. However, the formation of a αββα shaped hetero-tetramer in solution is controversially discussed for Taspase, as analytical gel filtrations indicate the presence of Taspase as heterodimer and enforced dimerization could effectively inhibit Taspase in cells [68].

In 2005, Lee and colleagues presented a hypothetical cleavage mechanism based on the close homology to asparaginases (figure 1.9). In this model, Taspase does not directly hydrolyze the peptide bond of the protein backbone, but the substrate first undergoes a rearrangement. After an attack of the P1' glycine by the P1 aspartate side chain, a succinimide-hydrate intermediate is formed. In a second step, the former peptide bond is hydrolyzed, yielding an isoaspartate with the protein backbone transferred to the aspartate side chain. Finally, Taspase cleaves the newly formed isoaspartate and releases the two fragments.

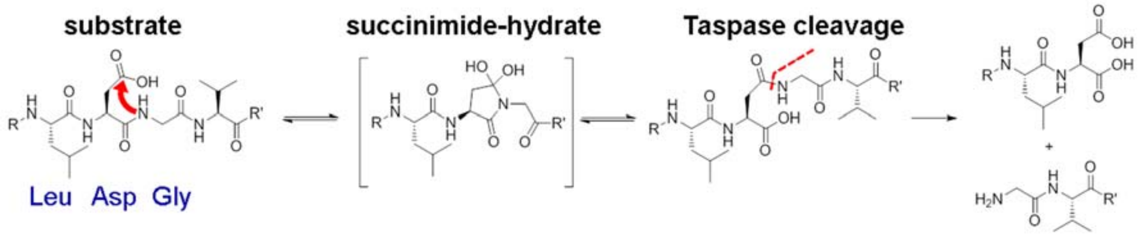

Figure 1.9 Proposed Taspase cleavage mechanism.

The aspartate side chain of the substrate attacks the following glycine (red arrow), yielding a succinimide-hydrate intermediate. Subsequently, hydrolysis of the former peptide bond results in a transfer of the protein backbone chain to the aspartate side chain. This isoaspartate is then cleaved by Taspase (red dashed line) and the two fragments are released. According to [69].

Furthermore, the chloride ion found in the crystal structure revealed another surprising feature of Taspase. It is bound to the active site and inhibits Taspase activity already at intracellular chloride concentrations [56]. Hence, Taspase is assumed to be present as inhibited enzyme in the cell and its substrate proteins are expected to temporarily displace the chloride ion for proteolytic processing. The first substrate described for Taspase was the MLL protein [57], which is activated after Taspase cleavage at two cleavage sites (figure 1.4). Subsequent alanine scans determined the Taspase consensus sequence as either Q-[F,I,L,V]-D | G-X-D-X or Q-[F,I,L,V]-D | G-X-X-D [63,70]. With this sequence at hand, 27 putative Taspase target proteins were identified [71]. By now, the experimentally verified targets comprise MLL, MLL2 [72], the transcription factors TFIIA [73] and ALF [73], upstream stimulatory factor 2 (USF2), myosin 1F (MYO1F), and MLL4 [70]. Strikingly, many Taspase substrates are nuclear factors involved in gene expression control, indicating a role of Taspase-mediated cleavage in the regulation of these factors. However, for other targets than MLL, the role of Taspase cleavage is still elusive. For example, Taspase-mediated cleavage of transcription factor IIa (TFIIA) seems to be a fine tuning mechanism of TFIIA activity and was speculated to be important for the expression of a certain subset of genes [73].

Localization studies with fluorescent tags pinpointed a nuclear localization of Taspase due to its bipartite nuclear localization signal [74]. However, closer investigation revealed a dynamic shuttling process between nucleus and cytoplasm. The nuclear import via a nuclear localization signal (NLS) is mediated by importin-α and could also be confirmed for the proenzyme. In contrast, interaction with the nucleolar shuttle protein nucleophosmin was only observed for autocatalytically processed Taspase. Although Taspase does not possess a nuclear export signal, it has access to the cytoplasm and is able to process its cytoplasmic target proteins. This export process is nucleophosmin-dependent and can be inhibited by leptomycin B [74].

Taspase knockdown in Hela cells resulted in impaired MLL cleavage and verified that no other protease is able to activate MLL. The close correlation of Taspase and MLL is also reflected in the fact that both genes coevolved in vertebrates [57]. Consequently, Taspase plays a key role for MLL, as the histone methyltransferase activity of MLL is crucially dependent on activation by Taspase cleavage [72]. Accordingly, also the MLL fusion proteins are inactive, unless they are processed by Taspase [29].

1.3.3 Taspase is a non-oncogene addiction protease

Despite the importance of Taspase for leukemia, Taspase alone is not sufficient for the transformation of fibroblasts. Hence, Taspase is not classified as oncogene, but as non-oncogene addiction protease [75,76]. This means that although Taspase is no oncogene, certain leukemias heavily rely on Taspase and are therefore susceptible for Taspase inhibition (figure 1.10).

This permissive role of Taspase in leukogenesis was corroborated by the finding that mouse embryonic fibroblasts (MEFs) lacking Taspase are resistant to oncogenic transformation induced by Myc, E1A, RAS, and p53 [76]. Moreover, Taspase-deficient mice exhibited decreased cyclin levels as well as increased expression of cyclin dependent kinase (CDK) inhibitors and thus showed a disrupted cell cycle [72]. Additionally, Taspase expression is upregulated in many human cancers as well as cancer cell lines and required for tumor maintenance. Generally, increased Taspase levels correlate with a dependency on Taspase expression [72,76]. Of note, recent studies imply a crucial role of Taspase not only in leukemia, but also in solid tumors [57,70,76]. Consequently, Taspase knockdowns in these tumors cause a disruption of proliferation and promote apoptosis [76]. Interestingly, although Taspase is critical for mouse embryonic development, the few surviving Taspase-deficient adult mice exhibited a normal life span [63]. Hence, inhibition of Taspase is regarded as new approach to treat leukemia.

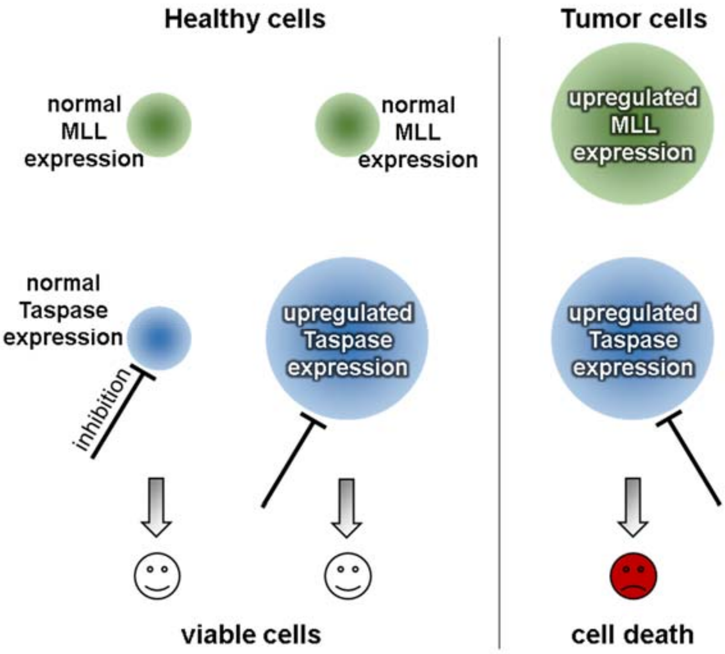

Figure 1.10 Taspase addiction in tumor cells.

Taspase inhibition is only lethal for MLL tumor cells, while healthy cells are not affected. Healthy cells express normal Taspase and MLL levels, and Taspase inhibition (black line) does not impair viability (left column). Aberrant Taspase expression is not sufficient for a malignant transformation, as long as MLL levels are normal. Under these conditions, Taspase inhibition is not fatal (middle column). Aberrant levels of the oncogene MLL cause malignant transformation and are often accompanied by aberrant Taspase levels. As these cells heavily rely on Taspase for the activation of MLL, Taspase inhibition results in cell death.

Targeting non-oncogene addiction proteins opens new ways in combating cancer and differs from the classical approaches that either aim at suppressing oncogene activity or restoring tumor suppressor function [75]. In recent years, several non-oncogene addiction proteins were detected and detailed analyses of these proteins achieved novel concepts for cancer therapy. In fact, some inhibitors for non-oncogene addiction proteins are already approved as anticancer drugs.

One example in this respect is the heat shock protein 90 (HSP90) inhibitor geldanamycin™. Since HSP90 client proteins are crucial for the regulation of cell survival, cell growth, cell cycle, and apoptosis, tumor cells relying on these client proteins are effectively hit by the HSP90 inhibitor geldanamycin™ [77]. Furthermore, Luo and colleagues reported that inhibition of the non-oncogene polo-like kinase 1 (PLK1) is toxic for cells with mutated Ras oncogene [78]. Moreover, also the proteasome inhibitor bortezomib can be regarded as a non-oncogene addiction drug. It is active against a variety of tumors, including myeloma, CLL, prostate and colon cancer, and is approved for treating multiple myeloma and mantle cell lymphoma [79]. Tumor cells acquire a variety of genetic aberrations and thus suffer from the stress generated by mutated and aggregated proteins. Consequently, inhibition of the proteasome exacerbates the stress in tumor cells more than in healthy cells.

1.3.4 Endeavors towards Taspase inhibition

As non-oncogene addiction protease, Taspase is of high interest for cancer therapy, since inhibition of Taspase is considered a promising way to prevent leukemogenesis. However, inhibition of Taspase activity is not trivial, as Taspase is insensitive against inhibition by general serine, cysteine, or metalloprotease inhibitors [57]. Hence, different approaches were hypothesized to obtain Taspase inhibitors, including compound screening, virtual docking, rational design, and enforced dimerization (figure 1.11).

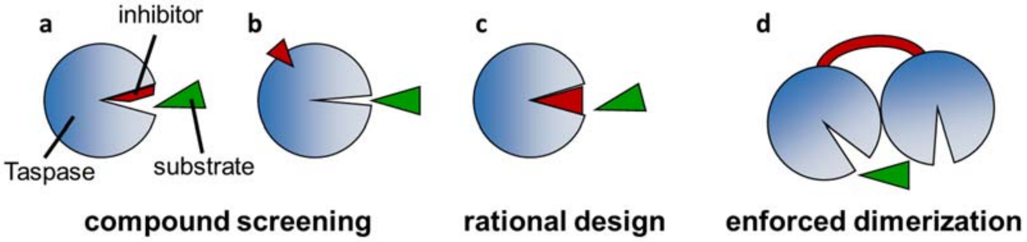

Figure 1.11 Strategies for new Taspase inhibitors.

a+b Inhibitors (red) for Taspase (blue) can be found by databank screening. The compounds can bind to the active site (**a**) or allosteric (**b**). **c** Rational design can yield substrate analog compounds **d** Genetically enforced dimerization was found to inhibit Taspase activity.

1.3.4.1 Compound screening

High-throughput screening of small molecules (figure 1.11a+b) is a common method to find new inhibitors and has been applied successfully for many other enzymes [80,81]. Consequently, small molecule screenings aiming at Taspase inhibitors have been published previously [63,71,82]. The most promising candidate was the anti-angiogenic arsenic inhibitor NSC48300. This compound was found in a high-throughput screening assay of a small molecule library and was reported to inhibit Taspase allosterically with a K_i of 4.2 µM [63]. However, the arsenic moiety of the compound poses a high toxic risk, is known for unspecific effects [83] and its application *in vivo* is limited.

1.3.4.2 Virtual docking

The available crystal structure reveals the conformation of the active site and thus allows targeting Taspase by virtual docking (figure 1.11a). Knauer and colleagues performed an *in silico* screening with a database comprising roughly 180 000 compounds [71]. However, the resulting top candidates (CHC-A4 and DHC-C1) displayed only weak inhibition of Taspase activity.

1.3.4.3 Substrate analogs

Besides compound library screening, inhibitors can be derived from the substrate by rational design (figure 1.11c). Regarding this, the Bogyo group developed a series of substrate-derived vinyl sulfone and vinyl ketone derivatives [69]. However, these compounds displayed only moderate inhibition of Taspase activity with an IC_{50} of 30 µM determined for the best compound yzm18.

1.3.4.4 Enforced dimerization

Another way for Taspase inhibition exploits the quaternary structure by enforced protein interaction (figure 1.11d), as suggested by Thiel *et al*. [84]. Notably, co-expression of active and inactive Taspase does not reduce Taspase activity, indicating that catalysis in the two protomers of the hetero-tetramer is independent [85]. However, Bier and colleagues enforced the Taspase dimer by the fusion of Jun- and Fos-tags to the C-terminus of Taspase and found that the enforced dimer was catalytically inactive [68]. So far, Taspase dimerization was only artificially achieved by genetic manipulation and no chemical dimerizers for Taspase have been developed.

In summary, all these studies failed to find a potent inhibitor for *in vivo* applications. Consequently, novel Taspase inhibitors are still urgently needed.

1.4 Nanoparticles

Nanoparticles are solid particles with a size of roughly 10-100 nm [86] and have gained in importance during the last decades. These particles can either be released incidentally (car and industrial exhausts, volcanic eruptions) or engineered purposefully [87]. The latter are frequently prepared either by dispersion of preformed polymers or built up by polymerization of monomers [88]. Important parameters of nanoparticles besides size include the material, particle shape, zeta potential (i. e. charge), curvature, hydrophilicity, biodegradability, and surface modifications [89]. The surface-to-volume ratio of spherical particles increases with decreasing particle diameter. For example, particles of 50 nm diameter possess a surface area of 44 m^2 per gram. As a consequence of this, materials possess different properties at nanoscale compared to the bulk material and are therefore industrially used for example for cosmetics (e. g. sunscreen), textiles (e. g. self-cleaning textiles) as well as computers (e. g. nanotransistors).

Nevertheless, the progressive usage of nanoparticles is controversially discussed, as nanoparticles taken up via the skin, lung, and gut are distributed by the bloodstream [90] and possible hazards and long-term influences are insufficiently researched [90]. Especially the long retention half-times of inhaled nanoparticles in the alveolar region of 70 days in rats and two years in humans [91] pose a threat to cells, since nanoparticles are internalized by endocytosis [92]. Once the particles are inside the cell, they can generate reactive oxygen species (ROS) [93], disrupt membranes [94], cause protein aggregation [95], interfere with cellular pathways [96], unfold proteins [97], or intercalate into DNA [98].

On the other hand, the interaction with biomolecules and the nano-bio-interface is of high interest for medical applications. In particular, the high free surface energy and therefore strong adsorption of biomolecules is exploited. Hence, nanoparticles do not exist as bare particles in a biological environment, but are covered by a surface layer of biomolecules, which is named the corona [99]. The effect of this corona is essential for biomedical research and medicine to improve the properties of pharmaceutical drugs. In most cases, medicinal applications of nanoparticles aim at cancer treatment and improved drug delivery. Examples are (i) alginate coated chitosan nanoparticles, which enhance the oral absorption of enoxaparin, a low molecular weight heparin [100], (ii) specifically designed silica particles to deliver peptide mimetics to transplanted cells [101], and (iii) recently described gold nanorods of 5-15 nm diameter with promising results in the thermal therapy of cancer in mice [102].

As the vasculature of tumors is usually leaky, nanoparticles can accumulate in tumors due to a phenomenon termed enhanced permeability and retention (EPR) effect [103]. Especially the accumulation of nanoparticles in solid tumors with a reduced lymphatic drainage and deficient vasculature can help to reverse multidrug resistance due to an improved drug delivery to cancer cells [104]. Recently, also L-asparaginase was entrapped in hydrogel-magnetic nanoparticles of 30 nm diameter for improved bioavailability and cell penetration [105]. Moreover, another group showed that 200 nm silica shells can be used to overcome allergic reactions against asparaginase while retaining the enzyme activity [106].

Another medical application for nanoparticles is the diagnosis of diseases in biochemical assays. Recently, a gold nanoparticle-based immunoassay was described to detect the Alzheimer's disease related β-amyloid peptide in cerebrospinal fluids [107]. Even lung cancer diagnosis in exhaled breath was reported. For this, chemiresistors (microsensors) based on 5 nm gold nanoparticles covered with different organic substances were used to quantify volatile organic compounds in the exhaled breath [108].

The versatile applicability of nanoparticles furthermore allows the inhibition of enzymes, as shown for soybean peroxidase and chymotrypsin with carbon nanotubes [109]. However, interactions of nanoparticles with Taspase are not described so far.

1.5 Aims of this thesis

Although the survival rates for leukemia have significantly improved in the last decades [110], leukemias still account for more than one third of all cancer deaths in children and 9 % of all cancer deaths [1]. Therefore, new anticancer targets are of high interest, as they allow the design of novel anticancer drugs. Recently, the non-oncogene addiction protease Taspase has moved into focus as new target for cancer drugs, since Taspase is required for the initiation and progression of certain types of mixed lineage leukemia (MLL) and is upregulated in various solid tumors [71,76]. In this respect, these tumors are highly dependent on Taspase and thus hypersensitive to a loss of Taspase activity [76]. Despite first achievements in the direction of Taspase inhibitors, the compounds originating from these studies exhibit either weak inhibition [69,71] or broad bioactivities [63]. Hence, potent Taspase inhibitors are still of paramount importance.

To develop novel Taspase inhibitors, a comprehensive analysis of the biochemical properties, such as activity, substrate specificity, and stability, is helpful and can give deeper insights into Taspase-mediated catalysis. To this end, Taspase as well as active and inactive mutants will be characterized. Moreover, the structure of the long loop regions lacking in the Taspase crystal structure will be assessed by nuclear magnetic resonance (NMR) and circular dichroism (CD) spectroscopy, as the structure of the loop could reveal new structural targets for inhibitors. The resulting data will be used to evaluate Taspase inhibitors and understand their mechanisms.

To obtain novel inhibitors, three approaches will be employed:

- Compounds will be derived from virtual docking of a databank comprising 12 million small molecules.
- Silica based nanoparticles, which were recently found to bind proteins, will be tested for size dependence and inhibition mechanism.
- Substrate analog succinimide peptides will be tested and optimized in cooperation with the Kaiser group for chemical biology.

First, the inhibitors will be tested in a fluorogenic *in vitro* assay and subsequently *in vivo* using cell lysates and a cell-based activity assay. The resulting data can yield both novel classes of Taspase inhibitors and assist the design of future Taspase inhibitors. Additionally, these studies could shed light on the catalytic mechanism and might contribute to understand the interaction of enzymes with nanoparticles in general.

2 Material and Methods

2.1 Material

2.1.1 Chemicals

All chemicals used for this project are listed in table 2.1. Names can differ from the conventional names. Some names are trademarks and underlie copyright restrictions.

Table 2.1 Chemicals used.

Name (abbreviation)	Supplier
Acetic acid	Caldic, Düsseldorf
Acetonitrile	Caldic, Düsseldorf
Adenosine-5-triphosphate disodium salt (ATP)	Roth, Karlsruhe
Agar	Roth, Karlsruhe
Agarose	Roth, Karlsruhe
^{15}N Ammonium chloride ($^{15}NH_4Cl$)	Cambridge Isotopes, Andover
Ammonium hydrogen citrate (DAC)	Fluka, Buchs
Ammonium peroxydisulfate (APS)	Roth, Karlsruhe
Ampicillin sodium salt (Amp)	Roth, Karlsruhe
Amsil8, Amsil20, Amsil125	Nyacol, Ashland
Antifade gold™	Life technologies, Darmstadt
Antifoam™	Sigma-Aldrich, Steinheim
Atto488 maleimide	Attotec, Siegen
Atto594 NHS ester	Attotec, Siegen
Biotin	AppliChem, Darmstadt
Boric acid (H_3BO_3)	Roth, Karlsruhe
Bovine serum albumin (BSA)	NEB, Ipswich
Bromophenole blue	Roth, Karlsruhe
Buffer green DNA polymerase (10x)	Thermo Scientific, Darmstadt
Buffer green restriction enzymes (10x)	Fermentas, St. Leon-Rot
Calcium chloride dihydrate ($CaCl_2$)	Roth, Karlsruhe
CasyTon solution™	OMNI Life Science, Bremen
Chloramphenicol (Cam)	Roth, Karlsruhe
Cobalt(II) chloride hexahydrate ($CoCl_2$)	Fluka, Buchs
cOmplete protease inhibitor™	Roche, Basel
Coomassie Brilliant Blue G250	Fluka, Buchs
Copper(II) chloride ($CuCl_2$)	Sigma, Steinheim
Desoxyribonucleotide triphosphates (dNTPs)	Metabion, Martinsried
Deuterium oxide (D_2O) 99,9 %	Sigma-Aldrich, Steinheim
Dihydroxyacetone phosphate lithium salt (DHAP)	Sigma-Aldrich, Steinheim
2,2-Dimethyl-2-silaptane-5-sulfonate (DSS)	Sigma-Aldrich, Steinheim
Dimethyl sulfoxide (DMSO)	Roth, Karlsruhe
1,4-Dithiothreitol (DTT)	Biomol, Hamburg
Dulbecco's Modified Eagle's Medium (DMEM)	PAN-Biotech, Aidenbach
Ethanol	Caldic, Düsseldorf
Ethylendiamine tetraacetic acid (EDTA) disodium salt	Roth, Karlsruhe
Fetal calf serum (FCS)	PAN-Biotech, Aidenbach

Name (abbreviation)	Supplier
Fmoc-valine	Novabiochem, Darmstadt
Gel Filtration HMW Calibration Kit	GE Healthcare, Solingen
Gel Filtration LMW Calibration Kit	GE Healthcare, Solingen
D-Glucose	Roth, Karlsruhe
$^{13}C_6$ D-Glucose	Cambridge Isotopes, Andover
L-Glutathione reduced (GSH)	Roth, Karlsruhe
Glycerol	Roth, Karlsruhe
Glycine	AppliChem, Darmstadt
Hellmanex II™	Hellma Analytics, Müllheim
Hoechst 33258	Life technologies, Darmstadt
Hydrochloric acid (HCl)	AppliChem, Darmstadt
4-(2-Hydroxyethyl)piperazine-1-ethanesulfonic acid (HEPES)	Roth, Karlsruhe
Imidazole	Fluka, Buchs
Immersion oil	Roth, Karlsruhe
Iron(III) citrate	Sigma-Aldrich, Steinheim
Isopropanol	Caldic, Düsseldorf
Isopropyl-β-D-thiogalactopyranoside (IPTG)	Applichem, Darmstadt
Kanamycin sulfate (Kan)	Roth, Karlsruhe
Magnesium chloride ($MgCl_2$)	Roth, Karlsruhe
Magnesium sulfate ($MgSO_4$)	Fluka, Buchs
Manganese(II) chloride ($MnCl_2$)	Fluka, Buchs
Meat extract	Fluka, Buchs
2-Mercaptoethanol	Roth, Karlsruhe
Midori Green™	Nippon Genetics, Düren
Minimum Essential Medium (MEM; 1000x)	PAN-Biotech, Aidenbach
Nickel(II) chloride ($NiCl_2$)	Roth, Karlsruhe
Nicotineamide adenine dinucleotide (NADH)	Roth, Karlsruhe
Optimem	Life technologies, Darmstadt
Orange G	Sigma-Aldrich, Steinheim
Paraformaldehyde (PFA)	Sigma-Aldrich, Steinheim
PCR water	Life technologies, Darmstadt
Penicillin-streptomycin	Life technologies, Darmstadt
Peptone	Fluka, Buchs
Phenylmethylsulfonyl fluoride (PMSF)	Serva, Heidelberg
Phosphoenolpyruvic acid (PEP)	Sigma-Aldrich, Steinheim
Potassium chloride (KCl)	Roth, Karlsruhe
Potassium dihydrogen phosphate (KH_2PO_4)	Roth, Karlsruhe
Reaction buffer T4 ligase	Metabion, Martinsried
Rotiphorese Gel 30	Roth, Karlsruhe
Rubidium chloride ($RbCl_2$)	Sigma-Aldrich, Steinheim
Sodium chloride (NaCl)	Roth, Karlsruhe
Sodium dihydrogen phosphate (NaH_2PO_4)	Roth, Karlsruhe
Sodium dodecyl sulfate (SDS)	Roth, Karlsruhe
Sodium hydroxide (NaOH)	Roth, Karlsruhe
Sodium molybdate (Na_2MoO_4)	Roth, Karlsruhe
Sodium selenite (Na_2SeO_3)	Fluka, Buchs
D-Sucrose	Roth, Karlsruhe
N,N,N',N'-Tetramethylethylenediamine (TEMED)	Roth, Karlsruhe

Name (abbreviation)	Supplier
Thiamine hydrochloride (vitamin B_1)	Merck, Darmstadt
Tricine	Roth, Karlsruhe
Trifluoroacetic acid (TFA)	Caldic, Düsseldorf
Tris(hydroxymethyl)aminomethane (Tris)	AppliChem, Darmstadt
Triton X-100	AppliChem, Darmstadt
Trypsin-EDTA	PAN-Biotech, Aidenbach
Tryptone	Roth, Karlsruhe
Tween 20	Roth, Karlsruhe
XtremeGene™	Roche, Basel
Yeast extract	Roth, Karlsruhe
ZINC database compounds	ChemDiv, San Diego
Zinc sulfate ($ZnSO_4$)	Roth, Karlsruhe

2.1.2 Purchased peptides

Purchased peptides used for this thesis are listed in table 2.3. All peptides were synthesized by the manufacturers using solid phase peptide synthesis and purified to > 95 % purity using high-pressure liquid chromatography (HPLC).

Table 2.2 Peptides used.

Sequence*	Description	Supplier
[Mca]-GKGQVDGADDK-[DNP]	CS1 Taspase substrate	China Peptides, Shanghai
[Abz]-KISQLDGVDDK-[DNP]	CS2 Taspase substrate	CASLO ApS, Lyngby
[Abz]-KISQLAAVDDK-[DNP]	Mutated Taspase substrate	CASLO ApS, Lyngby
[Succ]-AAPF-[pNA]	Chymotrypsin substrate	Bachem, Bubendorf
APPNIMTTRFSLAAFKRNKRKLELAERV DTDFMQLKKRRQSS	Short Taspase loop	CASLO ApS, Lyngby

* [Mca]: 7-amino-4-methylcoumarin; [Dnp]: dinitrophenol; [Abz]: anthranilic acid; [Succ]: succinate; [pNA]: p-nitroaniline

2.1.3 Buffers and media

Buffers and media used for this thesis are listed in table 2.3. pH values were adjusted at room temperature. Media were autoclaved for sterilization.

Table 2.3 Buffers and media used.

Solution	Composition
Bradford reagent	5 % ethanol, 10 % H_3PO_4, 0.01 % Coomassie brilliant blue G250, ddH_2O
4x Laemmli stacking gel buffer	500 mM Tris/HCl pH 6.8, ddH_2O
4x Laemmli separating gel buffer	3 M Tris/HCl pH 8.8, ddH_2O
2x Laemmli sample buffer	125 mM Tris/HCl pH 6.7, 50 % glycerin, 10 % SDS, 10 mM 2-mercaptoethanol, 0.01 % bromophenole blue, ddH_2O

Solution	Composition
Laemmli buffer	0.1 % SDS, 0.303 % Tris, 1.441 % glycine, ddH$_2$O
Coomassie staining solution	1.25 g Coomassie brilliant blue G250, 227 ml ethanol, 46 ml acetic acid, 227 ml ddH$_2$O
Coomassie destaining solution	50 ml acetic acid, 75 ml ethanol, 875 ml ddH$_2$O
PBS	137 mM NaCl, 2.7 mM KCl, 10 mM NaH$_2$PO$_4$, 2 mM KH$_2$PO$_4$, ddH$_2$O
TBST buffer	50 mM Tris-HCl, 150 mM NaCl, 1 % Tween-20, ddH$_2$O, pH 7.5
TAE buffer	40 mM Tris pH 8.5, 1 mM EDTA, 20 mM acetic acid, ddH$_2$O
Lysis buffer	25 mM Tris pH 7.4, 150 mM KCl, 5 mM MgCl$_2$, 5 % glycerol, 1 % Triton X-100, 2 mM 2-mercaptoethanol, 1 mM PMSF, 1 tablet cOmplete, ddH$_2$O
GST wash buffer	50 mM NaH$_2$PO$_4$, 450 mM NaCl, 1 mM DTT, 1 % Triton X-100, pH 7.3
GST elution buffer	50 mM NaH$_2$PO$_4$, 450 mM NaCl, 1 mM DTT, 20 mM glutathione, pH 8.0
GST equilibration buffer	50 mM NaH$_2$PO$_4$, 450 mM NaCl, 1 mM DTT, 1 % Triton X-100, pH 7.3
NiNTA equilibration buffer	50 mM NaH$_2$PO$_4$, 450 mM NaCl, 10 mM imidazole, pH 8.0
NiNTA wash buffer	50 mM NaH$_2$PO$_4$, 450 mM NaCl, 20 mM imidazole, pH 8.0
NiNTA elution buffer	50 mM NaH$_2$PO$_4$, 450 mM NaCl, 250 mM imidazole, pH 8.0
Gel filtration buffer	50 mM NaH$_2$PO$_4$, 450 mM NaCl, 1 mM DTT, pH 7.9
Activity assay buffer	50 mM NaH$_2$PO$_4$, 10 % sucrose, 1 mM DTT, pH 7.9
50x TS2	2.4 mM ZnSO$_4$, 0.15 mM MnCl$_2$, 4.9 mM H$_3$BO$_3$, 0.84 mM CoCl$_2$, 0.84 mM NiCl$_2$, 58 µM CuCl$_2$, 4.3 mM Na$_2$MoO$_4$, 0.12 mM Na$_2$SeO$_4$, ddH$_2$O
LB medium	1 % tryptone, 0.5 % yeast extract, 1 % NaCl, ddH$_2$O, pH 7.0
LB agar plates	500 ml LB medium, 7.5 g agar
M9 medium	0.68 % Na$_2$HPO$_4$, 0.3 % KH$_2$PO$_4$, 0.05 % NaCl, 0.1 % NH$_4$Cl, 0.2 % 1 M MgSO$_4$, 0.2 % 50x TS2, 0.1 % 10 mM iron(III) citrate, 0.4 % glucose, 0.01 % CaCl$_2$, 0.01 % 0.5 % vitamin B$_1$, ddH$_2$O
Nutrient medium	0.5 % peptone, 0.3 % meat extract, ddH$_2$O
SOC medium	2 % tryptone, 0.5 % yeast extract, 10 mM NaCl, 2.5 mM KCl, 10 mM MgCl$_2$, 10 mM MgSO$_4$, 20 mM glucose, ddH$_2$O
Hela medium	10 % FCS, 1 % MEM, 1 % penicillin-streptomycin, DMEM
HCT116/HEK293T medium	10 % FCS, 1 % penicillin-streptomycin, DMEM

2.1.4 Kits

All kits used are listed in table 2.4.

Table 2.4 Kits used.

Kit	Supplier
Lightning QC site-directed mutagenesis kit	Agilent, Santa Clara
Nucleo Spin Plasmid	Macherey Nagel, Düren
Nucleo Spin Extract II kit	Macherey Nagel, Düren
Pierce ECLplus kit	Thermo Scientific, Waltham

2.1.5 Instruments

Instruments and devices used are listed in table 2.5. Standard laboratory equipment is not listed.

Table 2.5 Instruments and devices used.

Description	Instrument	Manufacturer
Agarose gel analyzer	BioDoc Analyze	Biometra, Göttingen
Casy TT	Cell counter	OMNI Life Science, Bremen
CD spectrometer	J-710 CD spectrometer	Jasco, Gross-Umstadt
Centrifuge	Centrifuge 5415R	Eppendorf, Hamburg
Cleanbench	HERA safe	Thermo Scientific, Langenselbold
Cuvettes	Quartz cuvettes (104-QS, 108F-QS, 105.251-QS, 110-QS)	Hellma Analytics, Müllheim
Developer for films	Cawomat 2000	Cawo, Schrobenhausen
DNA gel system	Mini Subcell GT	BioRad, Berkeley
Electroporation cuvette	Electroporation cuvette, 0.2 cm	BioRad, Berkeley
Electroporation device	MicroPulser	BioRad, Berkeley
Fluorescence microscope	BX61 fluorescence microscope	Olympus, Hamburg
Fluorescence spectrometer	Cary Eclipse	Agilent Technologies, Waldbronn
FPLC system	BioRad DuoFlow	BioRad, Berkeley
FPLC system	Äkta FPLC P920	GE Healthcare, Solingen
Incubator	BD53	Binder, USA
Incubator	Thermomixer HT	Infors, Bottmingen
LC-MS ESI-TOF system	LCQ Fleet ESI spectrometer	Thermo Scientific, Darmstadt
MALDI-MS system	Autoflex speed	Bruker Daltonics, Bremen
Microwave		Sharp
MST device	Monolith NT.115	NanoTemper, Munich
MST device (label free)	Monolith NT.LabelFree	NanoTemper, Munich
Nanodrop	NanoDrop ND 1000	Peqlab, Erlangen
NMR spectrometer	Ultrashield 700 NMR	Bruker BioSpin, Fällanden
PCR cycler	T 3000 thermocycler	Biometra, Göttingen
pH meter	SevenEasy	Mettler-Toledo, Gießen
Photometer	Bio Photometer	Eppendorf, Hamburg
Power supply	PowerPac basic	BioRad, Berkeley
Scanner	Scanjet 8200	Hewlett Packard, China
SDS gel shaker	Duomax 1030	Heidolph, Schwalbach
SDS gel system	XCell Mini Protean 3	BioRad, Berkeley
Thermomixer	Thermomixer comfort	Eppendorf, Hamburg
Triggered Fview II FW camera	Fluorescence microscopy camera	Olympus, Hamburg
Ultracentrifuge	Optima L-90 K	Beckmann, Palo Alto
Ultrasound device	Sonopuls	Bandelin, Hamburg
UV/Vis spectrophotometer	Cary 100	Agilent Technologies, Waldbronn
Water filter unit	Milli-Q Biocel	Millipore, Schwalbach

2.1.6 Consumables

Consumables used are listed in table 2.6. Standard laboratory equipment is not listed.

Table 2.6 Consumables used.

Description	Name	Supplier
Cell culture dishes	100x20 mm	Greiner Bio One, Solingen
Centricon	Amicon Ultra concentrator	Millipore, Schwalbach
Centricon	Concentrator 5301	Eppendorf, Hamburg
Cover slips	15x15 mm	Menzel, Brunswick
Desalting tips	Supel Tips C18	Sigma-Aldrich, Seelze
Gel filtration column	HiLoad 16/600 Superdex 200 pg	GE Healthcare, Solingen
Gel filtration column	HiLoad 26/600 Superdex 200 pg	GE Healthcare, Solingen
Gel filtration column	10/300 GL Superdex 200 pg	GE Healthcare, Solingen
GST column	GSTrap FF 16/10, 20 ml	GE Healthcare, Solingen
NiNTA column	Protino NiNTA Agarose	Macherey Nagel, Düren
MALDI target frame	MTP 384 ground steel	Bruker Daltonics, Bremen
NAP column	PD-10 gravity flow column	GE Healthcare, Solingen
Nitrocellulose membrane	Protran	Whatman, Dassl
NMR tubes	AP5-800-7 NMR tubes	Schott Economics, Mainz
Object slides	Superfrost Plus	Thermo Scientific, Darmstadt
Sterile filter	0.22 µm	Millipore, Tullagreen
X-Ray films	CL-Xposure films	Thermo Scientific, Darmstadt

2.1.7 Software

Software used is listed in table 2.7

Table 2.7 Software used.

Software	Application	Reference
CcpNmr Analysis 2.3	Visualization, editing and evaluation of NMR spectra	[111]
ACD/ChemSketch 12.00	Visualization of chemical structures, calculation of logP	Advanced Chemistry Development, Toronto
Chimera	Visualization of protein structures, preparation of structures for docking	[112]
ClustalO	Sequence alignments	[113]
DOCK 6	Virtual docking	[114]
Flex Control	MALDI mass spectra	Bruker Daltonics, Bremen
GraphPad Prism 5.04	Statistical data evaluation	[115]
Image J 1.47v	Evaluation of microscopy images	[116]
NanoTemper analysis software	NanoTemper analysis software	NanoTemper, Munich
OligoCalc	Calculation of primer properties	[117]
CellP	Florescence microscopy imaging	Olympus, Hamburg
OPTIMIZER	*E. coli* optimization of DNA sequences	[118]

Software	Application	Reference
Protparam	Calculation of protein properties	[119]
PyMOL 1.4	Visualization of protein structures	[120]
SIAS	Calculation of sequence homology	[121]
SnapGene Viewer 2.2.2	Visualization of plasmid maps	GSL Biotech, Chicago
Spectra Manager 2.0	Evaluation of CD spectra	Jasco, Gross-Umstadt
Swiss-Model	Homology modeling	[122]
Topspin 3.0	Recording and processing of NMR spectra	Bruker Biospin, Rheinstetten
YASARA Twinset 11.12.31 / WHAT IF	Visualization of protein structures, MD simulations, homology modeling	YASARA Biosciences, Vienna

2.1.8 Enzymes and antibodies

Enzymes and antibodies used are listed in table 2.8 and were stored at -20 °C.

Table 2.8 Enzymes and antibodies used.

Enzyme	Supplier
ApaI	Fermentas, St. Leon-Rot
Chymotrypsin	Sigma-Aldrich, Steinheim
DreamTaq Green DNA polymerase	Thermo Scientific, Darmstadt
Lactic dehydrogenase	Sigma-Aldrich, Steinheim
Lysozyme	Fluka, Buchs
Parvalbumin	made in-house
PreScission protease	made in-house
Proteinase K	New England Biolabs
T4 ligase	Metabion, Martinsried
Trypsin	Sigma-Aldrich, Steinheim
XhoI	Fermentas, St. Leon-Rot
Actin (ACTB/ACTC) polyclonal antibody (N-term)	Abgent, Heidelberg
TASP1 monoclonal antibody	Origene, Rockville

2.1.9 Bacterial strains

Bacterial strains used for plasmid amplification and protein expression are given in table 2.9.

Table 2.9 Bacterial strains used.

Strain	Genotype	Supplier
***E. coli* ElectroSHOX competent cells**	F- mcrA Δ(mrr-hsdRMS-mcrBC) ϕ80lacZ ΔM15 ΔlacX74 recA1 endA1 ara Δ139 Δ(ara, leu)7697 galU galK - rpsL (Str^R) nupG λ$^-$	Bioline, Luckenwalde
***E. coli* BL21(DE3)-T1^R**	F- *ompT hsdS*$_B$(r$_B^-$ m$_B^-$) *gal dcm* λ(DE3) *ton*A	Sigma-Aldrich, Steinheim
***E. coli* C43 pLys DE3**	F – ompT hsdSB (rB- mB-) gal dcm (DE3) pLysS (CmR)	Lucigen, Heidelberg
***E. coli* Rosetta2(DE3)**	F$^-$ *ompT hsdS*$_B$(r$_B^-$ m$_B^-$) *gal dcm* (DE3) pRARE2 (Cam^R)	Merck, Darmstadt

2.1.10 Plasmids

Vector maps of the plasmids used in this work can be found in the supplement (supplemental figure 7.1 and figure 7.2). The plasmid with human Taspase cDNA and Taspase plasmids for eukaryotic transfection were courtesy of the Knauer group and the pRARE2 plasmid was courtesy of the Ehrmann group. For cloning with GST tag, a modified pET-41b(+) vector (Merck, Darmstadt) was used. In this vector, a PreScission cleavage site and an ApaI cleavage site were inserted in the multiple cloning site after the GST tag between the BamHI and SacII cleavage sites. The original ApaI cleavage site in the *lacI* gene was mutated (figure 2.1). With this vector, the target protein has only an N-terminal Gly-Pro addition after PreScission cleavage.

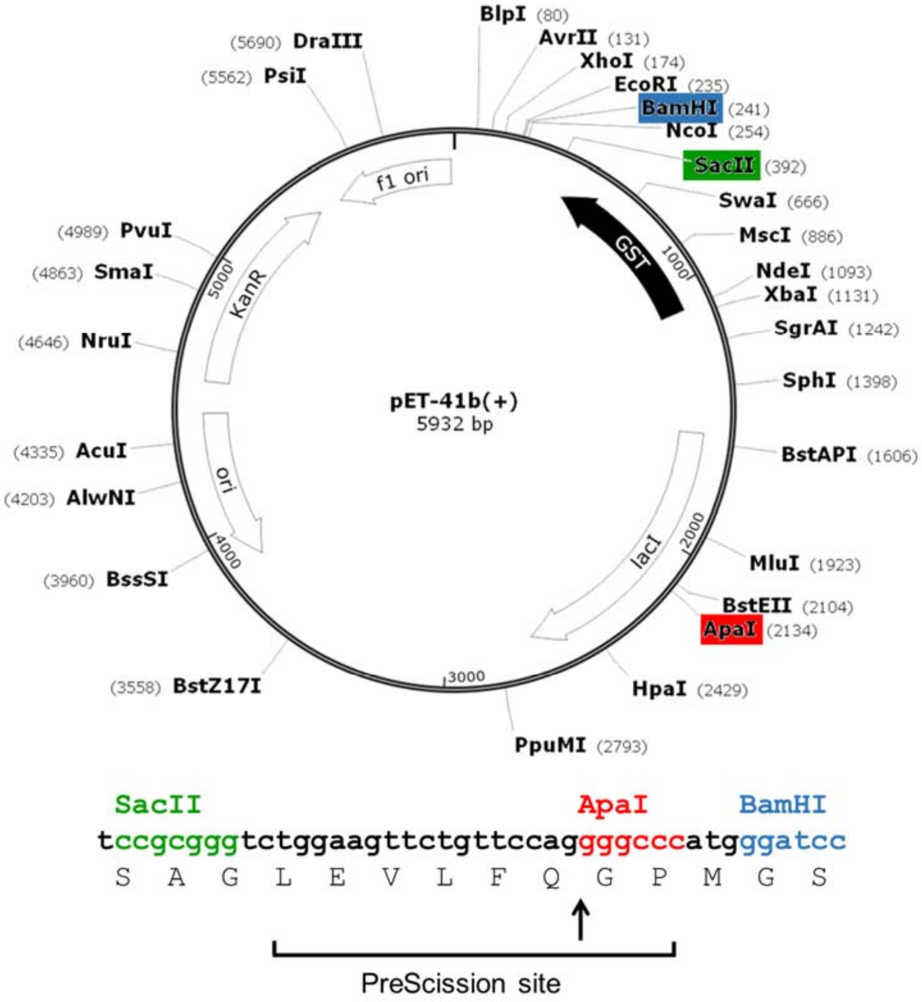

Figure 2.1 Vector map of the modified pET-41b vector.

The ApaI restriction site (red) was mutated and a PreScission cleavage site was inserted between the SacII (green) and BamHI (blue) restriction site. The inserted sequence is shown at the bottom.

2.1.11 Protein and DNA marker

PageRuler Unstained Broad Range Protein Ladder (Thermo Scientific; figure 2.2a) and PageRuler Plus Prestained Protein Ladder (Metabion; figure 2.2b) were used as protein markers. mi-100 bp+ DNA marker Go (Metabion; figure 2.2c) and mi-1 kb(-) DNA Marker Go (Metabion; figure 2.2) were used as DNA marker.

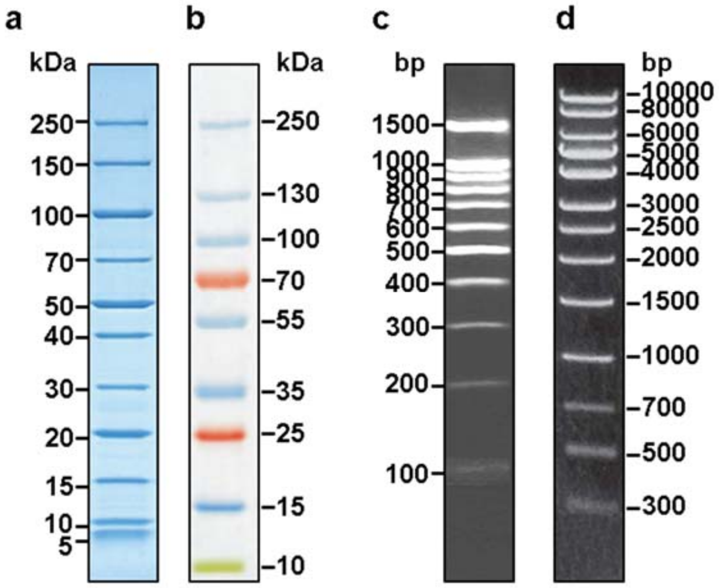

Figure 2.2 Protein and DNA marker.

a PageRuler Unstained Broad Range Protein Ladder for SDS-PAGE. **b** PageRuler Plus Prestained Protein Ladder for SDS-PAGE. **c** mi-100 bp+ DNA marker Go for agarose gel electrophoresis. **d** mi-1 kb(-) DNA Marker Go for agarose gel electrophoresis.

2.2 Molecular biological methods

2.2.1 Cloning of active Taspase and the inactive mutant

The nucleotide sequence of the bicistronic construct referred to as active Taspase was designed *in silico* based on the construct described by Khan *et al.* [56]. The expression construct comprises the α-subunit with an N-terminal hexahistidine tag, followed by a stop codon and a second ribosomal binding site for the β-subunit following downstream (figure 2.3). The unstructured loop at the C-terminus of the α-subunit was shortened by 27 amino acids, ending at Ala 206. The codon usage of the whole sequence was optimized for expression in *E. coli* using OPTIMIZER [118]. The gene was synthesized and cloned into a modified pET-41b vector described in figure 2.1 (GeneArt, Regensburg).

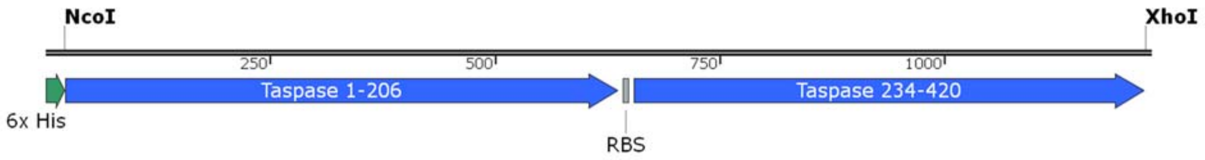

Figure 2.3 Construct for active Taspase.

The construct comprises an N-terminal His-tag, followed by the shortened α-subunit (amino acids 1-206) and a stop codon. After a short linker sequence, the ribosomal binding site (RBS) enables the transcription of the β-subunit (amino acids 234-420). This construct was cloned in a modified pET-41b vector.

The inactive mutant is based on the wild type construct of human Taspase cDNA in a pET-22b vector with N-terminal hexahistidine tag generated by Jens Rabenstein [82]. Two mutations in the active site (D233A and T234A) prevent autocatalytic activation of the proenzyme and hence reduce catalytic activity. These mutations were inserted with the help of a QuikChange kit (Agilent, Santa Clara) using wild type Taspase as template. Primers were designed with NEBaseChanger (NEB, Ipswich; table 2.10), synthesized (Metabion, Martinsried) and used for QuikChange according to the manufacturer's protocol (table 2.11) with a PCR program described in table 2.12.

Table 2.10 Primers used to generate the inactive Taspase mutant.

Substituted bases are highlighted in yellow.

Primer	Sequence
Forward	`5′-CTCAGGCACTTTGGCGGCGGTAGGCGCTGTGG-3′`
Reverse	`5′-CCACAGCGCCTACCGCCGCCAAAGTGCCTGAG-3′`

Table 2.11 PCR components to generate the inactive Taspase mutant.

Component	Amount [µl]
10x buffer	2.5
Wild type Taspase (template)	1 (=100 pg)
Forward primer	0.6 (=125 ng)
Reverse primer	0.6 (=125 ng)
dNTP mix	0.5 (=0.5 mM)
QuikChange reagent	0.75
DNA polymerase	0.5
PCR water	19.2

Table 2.12 PCR program to generate the inactive Taspase mutant.

Temperature [° C]	Time [min]	Number of cycles
95	2:00	1
95	0:20	25
68	0:10	
68	4:00	
68	5:00	1
37	∞	

The PCR product was treated with 1 µl DpnI for 20 minutes at 37 °C to digest template DNA and then transformed into competent *E. coli* shox cells (section 2.3.2). Three clones were selected for DNA isolation using the MiniPrep kit (Macherey Nagel, Düren) according to the manufacturer's instructions and the construct was sequenced (GATC Biotech, Cologne) to verify the correct DNA sequence (supplemental figure 7.1b). Permanent plasmid stocks in shox cells were obtained by mixing 600 µl of an overnight culture with 400 µl of sterile 86 % glycerol. The stock solution was shock frozen and stored at -80 °C.

2.2.2 Cloning of the Taspase loop

The construct for the GST-tagged Taspase loop comprising 56 amino acids (G178-D233) was generated by amplification of the loop sequence using wild type Taspase as template and subsequently cloned into a modified pET-41 vector with N-terminal GST tag (supplemental figure 7.3 and figure 2.1).

PCR amplification of the insert:
For PCR, the primer pair listed in table 2.13 was used with the plasmid for wild type Taspase (supplemental figure 7.1a and figure 2.1) as template. The pipetting scheme and PCR program are listed in table 2.16 and table 2.17, respectively. After amplification, a 1.3 % agarose gel was used to verify the correct size of the fragment and the DNA was extracted using a gel extraction kit (Macherey Nagel, Düren) according to the manufacturer's instructions.

Table 2.13 PCR primers used to generate the Taspase loop.

Primer	Sequence	T_m [°C]
Forward	5′-CACACAGGGCCCGGAATACCGTCTTGCCCTCC-3′	59.5
Reverse	5′-GGTTGGCTCGAGCTTAGTCCAAAGTGCCTGAGTCGTTC-3′	61.2

Restriction and ligation:
Both the amplified Taspase loop and the target vector pET-41-PreSc were digested with ApaI and XhoI for 30 minutes at room temperature (table 2.14).

Table 2.14 ApaI/XhoI restriction assay.

Component	Vector [µl]	Insert [µl]
pET-41-PreSc DNA	2 (=300 ng)	-
Loop DNA	-	8 (=2 µg)
ApaI	1 (=1 FDU)	1 (=1 FDU)
XhoI	1 (=1 FDU)	1 (=1 FDU)
10x buffer	3	5
PCR water	23	35

After DNA cleanup (Macherey Nagel, Düren), vector and insert were mixed in a molar ratio of 1:3 and ligated for 1 h at 16 °C (table 2.15).

Table 2.15 Ligation of the Taspase loop and pET-41-PreSc.

Component	Vector [µl]
pET-41b DNA	1.26 (=50 ng)
Loop DNA	0.95 (=4.33 ng)
T4 ligase	0.5 (=125 U)
10x buffer	2
PCR water	15.3

Subsequently, 1 µl of the ligated DNA was used for transformation into electrocompetent *E. coli* shox cells and the cells were plated on LB medium with kanamycin.

Table 2.16 PCR components to amplify the Taspase loop.

Component	Amount [µl]
Wild type Taspase (template)	0.5 (=10 ng)
10x buffer	5
Forward primer	5 (=50 pg)
Reverse primer	5 (=50 pg)
dNTP mix	2.5 (=0.5 mM)
DMSO	0.5 (=1 %)
DNA polymerase	1 (=5 U)
PCR water	30.5

Colony PCR:

Ten colonies were tested for loop DNA employing a colony PCR (table 2.18) with the same PCR program used for the amplification of the loop (table 2.17).

Table 2.17 PCR program used to amplify the Taspase loop.

Temperature [° C]	Time [min]	Number of cycles
95	0:30	1
95	0:30	3
56	0:30	
72	0:30	
95	0:30	32
58	0:30	
72	0:30	
72	10:00	1
4	∞	

Table 2.18 Colony PCR components to amplify the Taspase loop.

Component	Amount [µl]
Cell suspension (template)	10
10x buffer	4
Forward primer	2 (=20 pg)
Reverse primer	2 (=20 pg)
dNTP mix	1 (10 mM)
DNA polymerase	0.5 (2.5 U)
PCR water	20

The plasmids of clones with correct size were isolated using a MiniPrep kit (Macherey Nagel, Düren) and verified by sequencing.

2.3 Microbiological methods

2.3.1 Preparation of competent cells

Competent cells were courtesy of other group members. For the preparation of electrocompetent cells, 500 ml nutrient medium were inoculated with 1 % of an overnight culture of shox cells (Bioline, Luckenwalde) and cultivated to an OD_{600} of 0.8 at 37 °C and 160 rpm. The cells were cooled down on ice for 15 minutes and pelleted at 4000 g for 15 minutes at 4 °C. The pellet was resuspended in 500 ml cold ddH_2O and centrifuged again. The pellet was washed once more by resuspension in 250 ml cold ddH_2O and centrifugation, afterwards resuspended in 20 ml 10 % glycerol, centrifuged and finally resuspended in 0.5 ml 10 % glycerol. 50 µl aliquots were shock frozen in liquid nitrogen and stored at -80 °C.

Chemically competent BL21(DE3)T1r cells were generated starting from 200 ml LB medium inoculated with 2 ml of an antibiotic-free overnight culture (160 rpm, 37 °C). At an OD_{600} of 0.6, cells were pelleted for 5 minutes at 3000 rpm, 4 °C (slow start and stop) and resuspended in 45 ml cold 0.5 M $CaCl_2$ solution. After incubation on ice for 30 minutes, cells were pelleted again and resuspended in 2 ml 0.5 M $CaCl_2$ solution. 50 µl aliquots were shock frozen and stored at -80 °C.

2.3.2 Transformation of competent cells

Electrocompetent cells were incubated on ice with 1 µl of the PCR product and electroporated subsequently with the respective bacterial program in a MicroPulser (BioRad, Berkeley). After incubation for 60 minutes in 300 µl SOC medium at 37 °C and 400 rpm, cells were plated on LB agar dishes containing respective antibiotics and incubated over night at 37 °C.

Chemically competent cells were incubated with 1 µl of plasmid DNA for 20 minutes on ice, followed by a heat shock at 42 °C for 45 seconds and another incubation step on ice for 2 minutes. After that, the cells were transferred to 300 µl of SOC medium and incubated for 60 minutes at 37 °C and 400 rpm. Subsequently, the cells were plated on LB agar dishes with respective antibiotics and incubated at 37 °C over night.

2.3.3 Expression test

To find optimal conditions for the expression and solubility of the different Taspase constructs, their expression was assayed after various times and at various temperatures. The expression plasmid was transformed into chemically competent *E. coli* BL21(DE3)T1r cells and grown over night. For wild type Taspase, the *E. coli* strain Rosetta2, which is designed to express eukaryotic proteins with codons rarely used in *E. coli*, was tested in addition to the BL21(DE3)T1r strain. 1.5 % of an LB overnight culture of transformed bacteria was used to inoculate 100 ml of TB medium. At an OD_{600} of 0.8, 200 µM IPTG was added and the cell suspension was split up to allow expression at different temperatures. Before induction and at defined times after induction, 10 ml samples were taken from the cell suspensions, pelleted (4000 g, 4 °C, 20 min) and frozen. The pellets were resuspended in 50 mM NaH_2PO_4, 450 mM NaCl, 10 mM imidazole, pH 8.0 (supplemented with 1 % Triton X-100 for the Taspase loop), lysed by sonification (3 cycles à 30 seconds at 30 % intensity) and insoluble cell fragments were removed at 14000 rpm, 4 °C, 90 min. The supernatant was collected and the pellets were resuspended in 500 µl buffer (50 mM NaH_2PO_4, 450 mM NaCl, 10 mM imidazole, pH 8.0). For SDS-PAGE, 20 µl of supernatant or pellet solution were added to 20 µl of 2x SDS sample buffer.

2.3.4 Expression of Taspase constructs

The plasmids containing the sequence for Taspase (sections 2.2.1 and 2.2.2) were transformed into competent expression strains of *E. coli*. For active Taspase, the pET-41b plasmid encoding the active Taspase was transformed into the C43(DE3)pLysS strain as described above (section 2.3.2). Cells were plated on LB medium with 60 µg/ml kanamycin and 50 µg/ml chloramphenicol. After incubation over night at 37 °C, a single clone was used to inoculate an overnight culture (see below).

The sequences coding for wild type Taspase, inactive Taspase and the Taspase loop were based on human cDNA and therefore not optimized for expression in *E. coli*. To overcome this, 1 µl of a pRARE2 plasmid (Merck, Darmstadt) containing the tRNA for codons rarely used by *E. coli* was co-transformed additionally to the Taspase construct (in pET-22b vector) into BL21(DE3)T1r chemically competent cells (section 2.3.2). Plating on LB medium with 140 µg/ml ampicillin and 50 µg/ml chloramphenicol allowed for selection of cells that had taken up both the Taspase plasmid (with ampicillin resistance gene) and the pRARE2 plasmid (with chloramphenicol resistance gene).

Overnight cultures were grown in LB medium with respective antibiotics. 4 l TB medium with antibiotics were inoculated with 15 ml overnight culture per liter of medium and bacteria were grown at 37 °C and 160 rpm. Growth of bacteria was monitored by measuring the optical density at 600 nm wavelength.

For NMR spectroscopy, ^{15}N or $^{15}N/^{13}C$ labeled protein was used. To achieve expression of isotopic labeled protein, first, 1 l of LB medium was inoculated with 15 ml of an overnight culture and

grown at 37 °C, 160 rpm until the OD_{600} reached 0.7. Cells were pelleted gently (20 °C, 3000 rpm, 15 min) and resuspended in 4 l of M9 minimal medium supplemented with ^{15}N ammonium chloride and/or ^{13}C glucose. Bacterial growth was allowed to continue at 37 °C, 160 rpm.
For both labeled and unlabeled Taspase protein expression, at OD_{600} of 0.8, expression was induced by addition of 200 µM IPTG and the temperature was reduced to 30 °C. 6 h after induction, cells were pelleted at 4 °C, 6300 g for 20 minutes and resuspended in 50 mM NaH_2PO_4, 450 mM NaCl, 10 mM imidazole, pH 8.0. The Taspase loop was expressed over night at 25 °C and the bacteria pellet was resuspended in 50 mM NaH_2PO_4, 450 mM NaCl, 1 mM DTT, 1 % Triton X-100, pH 7.0. Cell pellets were shock frozen in liquid nitrogen and stored at -20 °C until used for purification.

2.3.5 Cultivation of eukaryotic cell lines

Cervical cancer cells (Hela) were cultivated, cryopreserved and passaged as suggested by the American Type Culture Collection (ATCC): Cells were cultivated in 10 cm dishes with 10 ml cell culture medium and split at 70 to 90 % confluency. For this, cells were washed with PBS, before 1 ml of trypsin-EDTA was added and the cells were incubated for 5 minutes to detach. 9 ml prewarmed medium was added and cells were dispersed, prior to seeding in a split ratio of 1:5 to 1:25 in fresh medium. Medium was changed as needed. For cryopreservation, $2x10^6$ cells/ml were centrifuged gently (3 min, 300 g, 25 °C) and resuspended in freeze medium containing 10 % DMSO. Aliquots of 1 ml were placed in a controlled-rate freezer precooled to 4 °C and cooled down to -70 °C with a rate of -1 °C per minute. For long-term storage, cells were transferred to a -130 °C freezer. Recovery of cryopreserved cells was performed by rapid thawing to 37 °C, followed by addition of 1 ml fresh medium and gentle centrifugation (3 min, 300 g, 25 °C). The supernatant was discarded, cells were resuspended in 10 ml of their respective medium and transferred into 10 cm dishes. Medium was changed the next day.

2.3.6 Transfection of eukaryotic cells and preparation for microscopy

Transfection was performed in 12 well plates with cover slips one day after seeding $2x10^5$ cells per well. Cells were counted in a Casy TT (OMNI Life Science, Bremen) calibrated individually for Hela and HEK293T cells. Trypsin-EDTA was used to detach the cells, before they were dispersed in 9 ml culture medium. 50 µl of cells were diluted in 10 ml of CasyTon solution (OMNI Life Science) and only counts with more than 3000 events were regarded as valid. 1 µg DNA was mixed with 3 µl XtremeGene Transfection reagent in 100 µl Optimem (Life technologies) medium and incubated for 15 minutes at room temperature. This solution was added to the cells with 900 µl of their medium. If needed, nanoparticles were added 3 hours after transfection.
One day after transfection, cells were washed with PBS and 500 µl of 3.7 % PFA with 0.1 % Tween was added for fixation. After incubation for 20 minutes at 4 °C, cells were washed twice with PBS and 1 µg/ml Hoechst 33258 in PBS was added for 5 minutes to stain the nuclei. Subsequently, the

cells were washed first with PBS and then with water. 10 µl Antifade gold (Life technologies, Darmstadt) was spotted on a microscope slide, on which the cover slip was placed.

2.3.7 Fluorescence microscopy and image evaluation

After the Antifade gold solution had dried over night, fluorescence microscopy images were taken with an Olympus BX61 fluorescence microscope equipped with a triggered Fview II FW camera. The microscope was operated by the Olympus CellP software. Exposure times for Hoechst, Taspase-mCherry, Taspase-GFP, Substrate-mCherry and Substrate-GFP are listed in table 2.19.

Table 2.19 Channel settings used for fluorescence microscopy.

Channel	Excitation wavelength	Emission wavelength	Exposure time
Hoechst	345 nm	455 nm	25 ms
GFP	480 nm	510 nm	500 ms
mCherry	545 nm	610 nm	500 ms

Images were processed with ImageJ [116] and comprised the following steps. First, cell borders were identified with the help of bright-field and autofluorescence. Second, nuclei were defined using the DAPI channel. The area of the cell borders minus the nucleic area was defined as cytoplasm. The average intensities of the nucleic and cytoplasmic areas were calculated, and the ratio of nucleus to cytoplasm (N/C) was computed. Statistical evaluation of these ratios was executed in GraphPad Prism 5.03 [115]. An unpaired two-tailed student's *t*-test was applied. *p*-values below 0.05 were regarded as significant, values below 0.001 as highly significant.

2.3.8 Cell penetration assays with peptidic inhibitor

Uptake of rhodamine-labeled peptidic inhibitor was assayed with Hela cells. 5 µM or 50 µM fluorescent inhibitor were added to $2x10^5$ cells in 12 well plates. Cells were either cultivated in medium with or without serum and fixated 1 or 5 hours after addition of the inhibitor. Fluorescence microscopy images were taken as described above (section 2.3.7) using the RFP channel and the fluorescence intensity of the cells was compared to the autofluorescence of untreated cells using ImageJ. For statistical evaluation, an unpaired two-tailed student's *t*-test was applied using GraphPad Prism.

2.4 Biochemical methods

2.4.1 Bacterial cell lysis

Bacterial pellets were thawed rapidly in a water bath and 1 mM of the protease inhibitor PMSF was added, as well as a spatula tip of lysozyme and 0.001 % antifoam. After stirring for 60 minutes at 4 °C, cells were lysed by sonification. For this, the cell suspension underwent 3 pulses of sonification (30 seconds each, 60 % intensity) on ice with 1 minute intervals to avoid excessive heat. Cell fragments and insoluble proteins were pelleted by ultracentrifugation for 70 minutes at 142000 g, 4 °C and the supernatant was collected. After filtration through a 0.22 µm filter, the volume was adjusted to 150 ml and loaded into a Superloop (GE Healthcare, Solingen).

2.4.2 Protein purification of His-tagged Taspase

Affinity chromatography was performed with an Äkta-FPLC system (GE Healthcare, Solingen) using a HisTrap HP 5 ml NiNTA column (GE Healthcare) equilibrated with 50 mM NaH_2PO_4, 450 mM NaCl, 10 mM imidazole, pH 8.0. The detailed buffers, volumes and flow rates used for affinity purification are listed in table 2.20. In short, the His-tagged protein was allowed to bind to the column matrix, before non-target proteins were washed away. For elution, the concentration of imidazole was gradually increased to a maximum of 250 mM imidazole.

Table 2.20 Program used for NiNTA affinity purification with a HisTrap HP 5 ml NiNTA column.

Step	Buffer	Volume	Flow rate	Size of collected fractions
Equilibration	NiNTA equilibration buffer	25 ml	1.5 ml/ml	-
Application of supernatant	Supernatant (in NiNTA equilibration buffer)	150 ml	1 ml/min	-
Wash	NiNTA wash buffer	50 ml	1 ml/min	-
Elution gradient	Gradient from NiNTA wash buffer to NiNTA elution buffer	100 ml	1 ml/min	3 ml
Final elution	NiNTA elution buffer	20 ml	1 ml/min	5 ml

Elution fractions containing protein were identified via absorbance at 280 nm and the correct size of the protein was checked by SDS-PAGE. For this purpose, 20 µl of an elution fraction was added to 20 µl of 2x SDS sample buffer and separated in a 15 % SDS gel. All fractions containing Taspase were concentrated in a Centricon with 30 kDa cut-off to a volume of 2 ml and used for gel filtration. Preparative gel filtrations were performed on an Äkta FPLC system with a Superdex 200 HiLoad 16/600 gel filtration column (GE Healthcare) to remove soluble aggregates and imidazole. The gel filtration buffer contained 50 mM NaH_2PO_4, 450 mM NaCl, 1 mM DTT at pH 7.7. Flow rates and fraction sizes used in the program are listed in table 2.21. The eluted protein was concentrated in Centricons with 30 kDa cut-off, aliquots were shock frozen in liquid nitrogen and stored at -20 °C.

Table 2.21 Program used for gel filtration with a Superdex 200 16/600 gel filtration column.

Step	Buffer	Volume	Flow rate	Size of collected fractions
Equilibration	Gel filtration buffer	130 ml	1.5 ml/ml	-

Sample injection	Concentrated Taspase (in 50 mM NaH_2PO_4 450 mM NaCl ~125 mM imidazole pH 8.0)	5 ml	1 ml/min	-
Elution	Gel filtration buffer	130 ml	1 ml/min	3 ml

2.4.3 Protein purification of the GST-tagged Taspase loop

A 20 ml GSTrap column (GE Healthcare, Solingen) was equilibrated with an Äkta-FPLC system (GE Healthcare) with 50 mM NaH_2PO_4, 450 mM NaCl, 1 mM DTT, 1 % Triton X-100, pH 7.0, before the GST-tagged Taspase loop was bound, washed and eluted with glutathione buffer. The detailed buffers, volumes and flow rates are listed in table 2.22.

Table 2.22 Program used for GST affinity purification with a 20 ml GSTrap column.

Step	Buffer	Volume	Flow rate	Size of collected fractions
Equilibration	GST equilibration buffer	100 ml	1.5 ml/ml	-
Application of supernatant	Supernatant (in GST equilibration buffer)	150 ml	1 ml/min	-
Wash	GST wash buffer	100 ml	1 ml/min	-
Elution	GST elution buffer	100 ml	1 ml/min	3 ml

Although the Taspase loop itself does not absorb light at 280 nm due to its lack of tyrosines and tryptophans, the absorbance of the GST tag can be used to identify protein containing elution fractions. These fractions were concentrated in a Centricon with 10 kDa cut-off to a final volume of 5 ml. Protein concentration was determined using UV/Vis spectroscopy, assuming an extinction coefficient for the GST-loop fusion protein of 42860 M^{-1} cm^{-1}. The PreScission cleavage site between the GST tag and the Taspase loop allowed specific removal of the tag by addition of 20 µg PreScission protease per 6 mg fusion protein and incubation over night at 4 °C. This renders the cleaved Taspase loop with an N-terminal Gly-Pro extension from the GST tag.

Filtration through a Centricon with 10 kDa cut-off resulted in a retention of the 28 kDa GST tag, while the 6.5 kDa Taspase loop could pass through the membrane. Hence, the flow-through was collected and concentrated in another Centricon with 3 kDa cut-off. Protein concentration was determined using the Bradford assay, aliquots were shock frozen in liquid nitrogen and stored at -20 °C.

2.4.4 Quantification of protein, peptide and DNA concentrations

Protein concentrations of purified protein were determined via UV/Vis spectroscopy using the Lambert-Beer law. Extinction coefficients at 280 nm were calculated using the online tool

Protparam [119] and are listed in table 2.23. Absorbance spectra were recorded with a NanoDrop ND 1000.

Protein concentrations of eukaryotic cell lysates were determined in a Bradford assay. 1 µl of sample was incubated with 999 µl Bradford reagent for 5 minutes and absorbance was measured at 595 nm and a blank value was subtracted. Calibration with a bovine serum albumin (BSA) standard curve allowed an estimation of the protein concentration in the sample.

For the quantification of inhibitors containing an Fmoc moiety, the extinction coefficient of Fmoc was determined experimentally. For this, the absorbance of a serial dilution of Fmoc-valine was measured at 300 nm wavelength. Linear regression of the standard curve yielded an extinction coefficient of 4985 M^{-1} cm^{-1}. This value was used to convert the absorbance at 300 nm to inhibitor concentrations.

The concentration of overexpressed GFP-Taspase in eukaryotic cell lysates was obtained using a combination of absorbance and fluorescence spectroscopy. This was necessary, because the concentrations were too low to be detected by absorbance spectroscopy. In a first step, cells transfected with only GFP were lysed and the GFP concentration in the lysate was determined with a Nanodrop ND 1000 applying an extinction coefficient of 9500 M^{-1} cm^{-1} at 475 nm. Transfection and expression is much more efficient for GFP than for GFP-Taspase and a concentration of 15.8 µM GFP in the cell lysate was calculated. From this lysate, a standard curve for fluorescence emission at 509 nm was created (excitation wavelength: 395 nm; excitation/emission slits: 10/10 nm; PMT: 600 V). In a second step, the fluorescence emission of a lysate with overexpressed GFP-Taspase was measured. With the help of the standard curve, this value could be converted to a GFP-Taspase concentration of 370 nM.

Concentrations of the peptidic substrate used in the kinetic assays were determined via the absorbance of the anthranilic acid. An extinction coefficient of 14650 M^{-1} cm^{-1} at 355 nm wavelength was used. The concentration of the rhodamine-labeled inhibitor was determined likewise, assuming an extinction coefficient of 80000 M^{-1} cm^{-1} at 555 nm [123].

DNA concentrations were determined with a Nanodrop ND 1000, assuming an extinction coefficient at 360 nm of 0.02 µg ml^{-1} cm^{-1}.

Table 2.23 Calculated parameters of Taspase proteins.

Protein	Extinction coefficient at 280 nm (ε_{280})	Molecular weight	Amino acids
wt Taspase	26930 M^{-1} cm^{-1}	45 278 Da	420
Inactive Taspase	26930 M^{-1} cm^{-1}	45 204 Da	420
Active Taspase	26930 M^{-1} cm^{-1}	42 082 Da	399
Taspase loop	0 M^{-1} cm^{-1}	6 611 Da	58

2.4.5 SDS-PAGE

The composition of polyacrylamide gels for sodium dodecyl sulfate polyacrylamide gel electrophoresis (SDS-PAGE) is given in table 2.24. Proteins were separated for about 90 minutes at 150 V and stained with Coomassie. For this, the gel was immersed in staining solution (section 2.1.3), microwaved briefly and shaken for 10 minutes. After this, the gel was transferred to destaining solution, microwaved briefly and shaken for another 10 minutes.

Table 2.24 Composition of polyacrylamide gels used for SDS-PAGE.

Component	Stacking gel (5x)	Separating gel (4x)
0.5 M Tris, pH 6.8	500 µl	-
1.5 M Tris, pH 8.0	-	4.4 ml
10 % SDS	50 µl	200 µl
Acrylamide/Bis-acrylamide	850 µl	10 ml
10 % Ammonium peroxydisulfate (APS)	50 µl	200 µl
TEMED	5 µl	8 µl
ddH$_2$O	3.5 ml	5.2 ml

2.4.6 Analytical gel filtration

Analytical gel filtrations were performed with a BioRad DuoFlow FPLC system on a Superdex 200 10/300 gel filtration column (GE Healthcare, Solingen). The column was equilibrated with 30 ml of 50 mM NaH_2PO_4, 450 mM NaCl, 1 mM DTT, pH 8. 180 µg Taspase was loaded into a 140 µl loop and separated with 0.5 ml/min flow rate. Due to the low protein concentration, the absorbance of the peptide bond at 214 nm was used to evaluate the retention times. For calibration, ferritin (450 kDa), aldolase (161 kDa), conalbumin (75 kDa), α-amylase (54 kDa) and ribonuclease A (13.7 kDa) were used. The retention times were plotted against the logarithmic molecular weight for linear regression.

2.4.7 Labeling of Taspase with Atto594-NHS

The wild type protein of Taspase and the inactive mutant were independently labeled at the C-terminus with Atto594. 1 mg of Taspase was diluted in 1 ml of 50 mM NaH_2PO_4, 450 mM NaCl, 1 mM DTT, pH 8. Afterwards, a 1.2-fold molar excess of Atto594 (dissolved in DMSO) was added and the solution was incubated for 60 minutes at room temperature in the dark. Unbound dye was removed with the help of a PD-10 column and the conjugate was concentrated in a Centricon. To determine the protein concentration (c) and degree of labeling (DOL), the absorbance at 280 nm and 601 nm was measured using a NanoDrop ND 1000 and converted as follows:

$$DOL = \frac{A_{501} \cdot 26930\ M^{-1}\ cm^{-1}}{(A_{280} - A_{501} \cdot 0.51) \cdot 120000\ M^{-1}\ cm^{-1}}$$

$$c = \frac{A_{280} - A_{501} \cdot 0.51}{1\ cm\ \cdot 26930\ M^{-1}\ cm^{-1}}$$

These calculations yielded for wild type Taspase a protein concentration of 551 µM and a DOL of 1.0 and for the inactive mutant a concentration of 87 µM with a DOL of 1.01. Aliquots of the conjugates were shock frozen and stored at -20 °C.

2.4.8 Labeling of Taspase with Atto488-maleimide

Wild type Taspase was labeled with the cysteine reactive dye Atto488-maleimide. The buffer was changed for labeling to 50 mM NaH_2PO_4, 450 mM NaCl, pH 7.4 by repeated dilution and concentration in a 30 kDa cut-off Centricon. A 2.5-fold molar excess of Atto488 was used for labeling. Labeling and removal of unbound dye was performed as described for labeling with Atto594-NHS (section 2.4.7). DOL and protein concentration were determined using the following formula:

$$DOL = \frac{A_{501} \cdot 26930\ M^{-1}\ cm^{-1}}{(A_{280} - A_{501} \cdot 0.1) \cdot 90000\ M^{-1}\ cm^{-1}}$$

$$c = \frac{A_{280} - A_{501} \cdot 0.1}{1\ cm\ \cdot\ 26930\ M^{-1}\ l^{-1}}$$

After labeling was completed, the buffer was changed to the previous storage buffer (50 mM NaH_2PO_4, 450 mM NaCl, 1 mM DTT, pH 8.0). This procedure resulted in a final concentration of 84 µM conjugate with a DOL of 2.45. Aliquots of the conjugate were shock frozen and stored at -20 °C.

2.4.9 Assay for autocatalytic activation of Taspase

Spontaneous cleavage of full-length Taspase between D233 and T234 into α- and β-subunit was visualized with SDS-PAGE. First, 9 µM purified Taspase was incubated in different buffers at 30 °C. Samples were taken after a certain period of time, prepared for SDS-PAGE and stored at -20 °C to stop the cleavage process. The two subunits were separated via SDS-PAGE in gels with 15 % acrylamide.

2.4.10 Limited proteolysis assay with proteinase K

Limited proteolysis with proteinase K was performed in gel filtration buffer (section 2.1.3). 5 µg/ml proteinase K was used to digest 6.4 µg Taspase in a total volume of 20 µl for 10 minutes at 21 °C, before 5 mM PMSF was added to stop the reaction. Samples were mixed with SDS sample buffer and separated by SDS-PAGE.

2.5 Spectroscopic methods

2.5.1 Taspase enzyme activity assay

For the determination of catalytic activity of Taspase, a fluorogenic assay was designed [56]. The substrate contains the CS2 cleavage sequence as it occurs in the Taspase target protein MLL, with an additional anthranilic acid coupled to the N-terminus and dinitrophenol-conjugated lysine coupled to the C-terminus of the peptide (CASLO ApS, Lyngby). The fluorescent dye anthranilic acid can be quenched by dinitrophenol. Since during the quenching process the excited electron transfers its excess energy to an electron of the quencher molecule, the quenching efficiency depends on the distance between dye and quencher. The intact peptide is quenched very effectively, i.e. 90 % of the energy absorbed by anthranilic acid is transferred to dinitrophenol and dissipated as heat (figure 2.4a). Cleavage by Taspase separates dye and quencher and the quenched fluorescence of the dye is recovered in a rate directly related to the catalytic activity of Taspase (figure 2.4b).

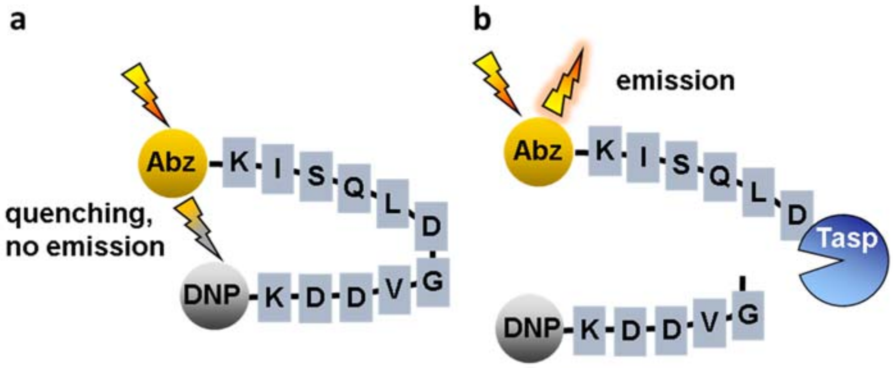

Figure 2.4 Principle of the fluorogenic Taspase activity assay.

a The model substrate contains the cleavage site for Taspase, an N-terminal anthranilic acid (Abz) and a C-terminal dinitrophenol moiety (DNP). After excitation of the Abz dye, the energy is transferred to the DNP and the fluorescence is quenched. **b** Upon cleavage by Taspase, Abz dye and quencher are separated. Hence, Abz is no longer quenched and can emit photons.

As long as the substrate concentration is at saturating levels, the increase in fluorescence is linear and mirrors the initial rate. Hence, the change in fluorescence during the first 180 seconds was fitted with linear regression and converted to enzyme activity. As fluorescence is measured in arbitrary values, a quantification of the kinetics with absolute values was not trivial. One prerequisite for this was that all measurements were taken with the same parameters with respect to temperature, pH, excitation slit width, emission slit width, PMT voltage and sample purity. Furthermore, the substrate concentration had to be low to avoid inner filter effects and allow the assumption of a linear correlation of intensity change and substrate cleavage. 8 µM proved to be a suitable substrate concentration with an absorbance well below 0.1, while still high enough to yield an adequate time to measure the reaction before substrate depletion began.

Unless specified otherwise, all samples were measured in 3 mm cuvettes with a Varian Cary Eclipse spectrofluorimeter equipped with a peltier element. For each assay, 300 nM Taspase was added to 8 µM substrate in a total volume of 60 µl with buffer containing 100 mM HEPES, 10 % sucrose, 10 mM DTT, pH 7.9. The temperature was adjusted to 37 °C and measurements were taken for 10 minutes with the settings provided in table 2.25.

Table 2.25 Parameters used for kinetic measurements with the fluorogenic assay.

Parameter	Value
Excitation wavelength	320 nm
Emission wavelengths	420 nm
Excitation slit width	20 nm
Emission slit width	20 nm
PMT voltage	480 V
Average time	5 s
Temperature	37 °C

Fluorescence intensities were recorded for 8 µM of the intact and the completely cleaved substrate. The measured intensities (I) in arbitrary units were converted to substrate concentrations (c) according to the following equation

$$c = 8\ \mu M \frac{I - I_{intact}}{I_{cleaved} - I_{intact}}$$

where c is the concentration of cleaved substrate, I is the measured fluorescence intensity, I_{intact} is the intensity of the intact substrate and $I_{cleaved}$ represents the intensity of the cleaved substrate.

The change in concentration over time (Δc/Δd) corresponds to the enzymatic activity of Taspase. Hence, the specific catalytic activity could be calculated using the formula below.

$$a_{spec} = \frac{\Delta c}{\min \cdot [Taspase]} \qquad [\frac{\mu mol}{\min \cdot mg}]$$

a_{spec} represents the specific catalytic activity in µmol cleavage per minute and mg Taspase, Δc is the concentration of substrate consumed in 1 minute in µM and [Taspase] is the concentration of Taspase in mg/ml.

For the determination of the Michaelis constant K_M, the initial velocities (v) were measured at different substrate concentrations [S]. Nonlinear regression using least squares fitting to the

Michaelis-Menten equation given below using Prism software [115] yielded maximum velocity v_{max} and Michaelis constant K_m.

$$v = \frac{v_{\max} \cdot [S]}{K_m + [S]}$$

Taspase requires high salt concentrations (>300 mM) for stability. However, salt inhibits the catalytic activity. A reasonable compromise between stability and activity is a buffer containing sucrose, which was used for kinetic assays. In a buffer containing 10 % sucrose, the half-life of Taspase was long enough to perform kinetic measurements without losing activity due to protein denaturation. Despite the stabilizing effect of sucrose, the half-life was too short for a complete test series, such as a titration curve. To circumvent this problem and maximize reproducibility, aliquots of 300 nM Taspase in sucrose were flash frozen and stored at -80 °C. For each measurement, an aliquot was thawed rapidly in a thermomixer at 37 °C and incubated for exactly 5 minutes at 500 rpm to ensure a homogeneous temperature. After the incubation time, preheated Taspase was added to the equally preheated substrate mixed with inhibitor or buffer and immediately filled into cuvettes preheated to 37 °C. The first data point of each trace was measured 10 seconds after the reaction had started.

With this assay, several compounds were tested for inhibitory effects on Taspase activity. Together with the substrate, the compounds were briefly incubated at 37 °C as described above before Taspase was added. Some of the inhibitors tested were insoluble in water at higher concentrations and required dissolving in DMSO. After dilution in sucrose buffer, the DMSO concentration was below 3 % and all measurements were referenced to the buffer controls with respective DMSO concentrations.

Inhibition constant (K_i) and IC_{50} values were obtained by applying nonlinear least squares fitting. For IC_{50} fits, enzymatic activity of Taspase was plotted against logarithmic inhibitor concentrations and fitted to the following model.

$$v = Bottom + \frac{Top - Bottom}{1 + 10^{X - \log(IC50)}}$$

Bottom and Top represent the inhibition at very low and very high inhibitor concentrations, respectively and IC_{50} is the concentration at which 50 % of the effect is observed.

For the experimental estimation of K_i values, the enzyme activity was measured at several combinations of substrate and inhibitor concentration and data was fitted to the following equation.

$$v = \frac{\frac{v_{max}}{1 + \frac{[I]}{\alpha\ \cdot K_i}} \cdot [S]}{\frac{K_m \cdot (1 + \frac{[I]}{K_i})}{\frac{1 + [I]}{\alpha\ \cdot K_i}} + \ [S]}$$

Where v is the observed velocity, v_{max} is the maximum enzyme velocity without inhibitor, K_m is the Michaelis constant, K_i is the inhibition constant, [S] is the substrate concentration, [I] is the inhibitor concentration and α describes the mechanism of inhibition. Very small α values indicate uncompetitive inhibition, very large α values indicate competitive inhibition and a value of 1 is seen for noncompetitive inhibition. If K_m and substrate concentration [S] is known, it is also possible to derive the K_i value from IC_{50} values using the Cheng-Prusoff equation [124].

$$K_i = \frac{IC_{50}}{1 + \frac{[S]}{K_M}}$$

The values obtained from experimental determination and the values gained by mathematical conversion from IC_{50} values were similar. For this reason, most of the K_i values reported are converted from IC_{50} values, which are easier to measure practically.

As negative control, the amino acids at the cleavage site of the substrate were exchanged against alanine, yielding [Abz]-KISQL<u>AA</u>VDDK-[DNP] (Abz: anthranilic acid; DNP: dinitrophenol; CASLO ApS, Lyngby). Another negative control was performed with inactive Taspase using identical parameters. For positive controls, a peptide comprising the CS1 cleavage site of MLL was synthesized with 7-amino-4-methylcoumarin (MCA) as N-terminal fluorescent dye ([MCA]-GKGQVDGADDK-[DNP]; China Peptides, Shanghai). Concentrations of this peptide were determined using an extinction coefficient of 15000 M^{-1} cm^{-1} at 350 nm. Measurements were taken with excitation and emission wavelength of 320 and 400 nm, respectively.

The activity of eukaryotic cell lysates was measured under slightly different conditions. Measurements were taken in lysis buffer (25 mM Tris pH 7.4, 150 mM KCl, 5 mM MgCl2, 5 % glycerol, 1 % triton X-100, 2 mM 2-mercaptoethanol, 1 mM PMSF, 1 cOmplete tablet) with 8 µM substrate added. The cOmplete Protease Inhibitor Cocktail precipitates at 37 °C. Hence, the assay temperature was lowered to 30 °C to minimize precipitation.

2.5.2 Binding studies with detection of fluorescence anisotropy

The principle of fluorescence anisotropy is based on photoselection. This means that after excitation with linear polarized light, fluorophores with an excitation dipole moment parallel to the electric vector of the incident light, are preferentially excited. In the excited state, the fluorophore rotates due to Brownian motion. The degree of rotation before emission depends of rotation correlation time and fluorescence lifetime. Emission occurs with an electric vector parallel to the emission dipole of the fluorophore. Hence, the emitted light of a fast rotating fluorophore is less polarized and the molecule has a lower anisotropy than the emission of a slowly rotating fluorophore. For globular proteins, the rotation correlation time θ depends on the molecular weight as described by the Perrin equation.

$$\theta = \frac{\eta \cdot M}{RT} (\bar{v} + h)$$

Where θ is the rotation correlation time, η is the viscosity of the sample (0.01 poise for water, 0.011 poise for 10 % sucrose), M is the molecular weight, R is the gas constant, T represents the temperature, $\bar{v}$ is the specific volume (typically near 0.73 ml/g) and h is the hydration (typically near 0.23 mg H_2O per mg of protein). The theory of anisotropy explained above shows that binding of a small fluorescent ligand to a protein causes an increase in anisotropy.

Measurements were taken with a Varian Cary Eclipse equipped with polarizer wheels and a peltier element. Unless specified otherwise, the sample volume was 60 µl in 3 mm cuvettes and readings were averaged over 5 minutes at 20 °C with the parameters stated in table 2.26.

Table 2.26 Parameters used for anisotropy measurements.

Parameter	Atto488	Atto594	Rhodamine	Tryptophan	Anthranilic acid
Excitation wavelength	501 nm	601 nm	555 nm	280 nm	320 nm
Emission wavelengths	523 nm	627 nm	582 nm	340 nm	420 nm
Excitation slit width	10 nm	20 nm	5 nm	10 nm	20 nm
Emission slit width	20 nm	20 nm	10 nm	20 nm	20 nm
PMT voltage	400 V	400 V	500 V	600 V	600 V
Average time	5 s	5 s	5 s	5 s	5 s
Temperature	20 °C	20 °C	20 °C	20 °C	20 °C
G factor	1.6724	2.1338	1.9587	0.6537	1.1373
Concentration	1 µM	1 µM	500 nM	10 µM	1 µM

G factors were applied to compensate different transmission efficiency of the polarizers for horizontally and vertically polarized light. To obtain these values, the emission of every fluorophore used was recorded consecutively with polarizers oriented horizontally and vertically and the ratio of the intensities yielded the G factor. The samples were excited with vertically polarized light and emission intensities of horizontally (I_H) and vertically (I_V) polarized light were recorded separately. With these values the anisotropy (r) was calculated.

$$r = \frac{I_V - G \cdot I_H}{I_V + 2G \cdot I_H}$$

The increase in anisotropy was plotted against ligand concentration and binding constants were derived from nonlinear curve fitting using Prism software [115] with an equation for saturation binding.

$$\Delta r = \frac{r_{max} \cdot [ligand]}{K_d + [ligand]}$$

Where Δr is the increase in anisotropy, r_{max} is the increase in anisotropy at saturating ligand concentrations and K_d is the dissociation constant.

2.5.3 Binding detected with microscale thermophoresis

Thermophoresis is the directed movement of particles due to a temperature gradient. In most cases, this movement occurs from hot to cold and depends on the hydration shell, charge and size of the molecules. If binding of another molecule changes any of these three parameters, this can be detected by microscale thermophoresis (MST; NanoTemper, Munich). The temperature gradient is generated by an infrared laser and the movement of the molecules is followed by change in local fluorescence intensity inside a capillary.

Binding of Taspase to nanoparticles was assessed in standard glass capillaries with a Monolith NT.115 during a MST demonstration course. Taspase was labeled with Atto488 and 50 nM labeled protein was added to a 16-step serial dilution of nanoparticles, ranging from 200 µg/ml to 12 ng/ml. To avoid adsorption of Taspase to the capillary walls, 0.1 % Tween was added to a buffer containing 50 mM NaH_2PO_4, 450 mM NaCl, 1 mM DTT, pH 8.0 in a final volume of 40 µl. Binding of the peptidic Taspase inhibitor Comp9 was assessed under label-free conditions, using intrinsic tryptophan fluorescence for detection with a Monolith NT.115LabelFree. 1 µM of Taspase was added to a serial dilution of 400 µM to 12 nM Comp9 in 50 mM NaH_2PO_4, 450 mM NaCl, 1 mM DTT, 0.1 % Tween, pH 8.0. Data analysis and determination of K_d values was performed with the software tools implemented in the NanoTemper Analysis software.

2.5.4 Determination of inhibitor stability with fluorescence anisotropy

Fluorescence anisotropy is sensitive to changes in the hydrodynamic radius, as explicated in section 2.5.2. Therefore, it can be used as a measure for the cleavage of fluorescent substrates. The stability of the peptidic rhodamine-labeled inhibitor was assayed in the presence of 1 µM Taspase and compared to the regular fluorescent substrate (section 2.5.1) as positive control. Measurements were taken in 200 µl of 50 mM NaH_2PO_4, 450 mM NaCl, 1 mM DTT, pH 8.0 in 3 mm cells. Inhibitor or substrate concentrations amounted to 8 µM and readings were performed with a Varian Cary Eclipse fluorescence spectrometer using the settings listed in table 2.27.

Table 2.27 Parameters used to measure inhibitor stability with anisotropy.

Parameter	Substrate	Inhibitor
Excitation wavelength	320 nm	495 nm
Emission wavelength	420 nm	582 nm
Excitation slit width	20 nm	20 nm
Emission slit width	20 nm	20 nm
PMT voltage	600 V	600 V
Average time	5 s	5 s
Interval	10 min	10 min
Temperature	20 °C	20 °C
G factor	1.1373	1.9640

Curves were fitted to a model for mono-exponential decay with GraphPad Prism:

$$r = (r_{intact} - r_{cleaved})^{-K \cdot t} + r_{cleaved}$$

where r represents the anisotropy, r_{intact} is the anisotropy value of the uncleaved state, $r_{cleaved}$ is the anisotropy value in the cleaved state, t is the time and K the rate constant. The half-life $t_{0.5}$ can be calculated as

$$t_{0.5} = \frac{ln2}{K}$$

2.5.5 CD spectroscopy

CD spectra and melting curves were recorded with a Jasco J-710 CD spectropolarimeter (Jasco, Gross-Umstadt). Far-UV spectra were recorded in 0.1 cm cuvettes (Hellma Analytics, Müllheim). For Taspase and Taspase mutants the buffer contained 50 mM potassium phosphate buffer at pH 6.5, while the synthetic loop peptide was dissolved in 50 mM potassium phosphate, pH 6.0. The protein concentration was determined precisely and 200 µl of a 0.2 mg/ml solution were measured with the parameters given in table 2.28.

To correct the y-drift of the device, all spectra were shifted so that the ellipticity between 250 and 260 nm was zero. From each protein spectrum a buffer spectrum was subtracted and the mdeg units were converted to molar ellipticity using path length and protein concentration.

$$\psi_{spec} = \frac{\psi}{l_{cm} \cdot c_{mg/ml}}$$

where ψ_{spec} is the specific ellipticity in deg cm^3 dm^{-1} per gram of amino acid, ψ is the observed ellipticity in mdeg, l is the path length in cm and c is the concentration in mg/ml.

These spectra show if the purified protein is folded and allow an estimation of helix, sheet, turn and random coil content. For the estimation of secondary structure content by deconvolution, the CDSSTR algorithm [125] was used.

Melting curves were recorded in a 1 cm cuvettes sealed with a stopper (Hellma Analytics, Müllheim) with 0.05 mg/ml protein in 50 mM potassium phosphate buffer at pH 6.5. The set of parameters used to obtain the melting curves is listed in table 2.28. Nonlinear curve fitting to obtain melting temperatures was performed with the Jasco Spectra Manager 2.0 software package.

Table 2.28 Parameters used to record far-UV CD spectra with a Jasco J-710.

Far-UV spectra		Melting curves	
Parameter	**Value**	**Parameter**	**value**
Start	260	**Wavelength**	225 nm
End	200	**Temperature slope**	1 °C/min
Scanning mode	Continuous	**Delay time**	180 s
Response time	0.5 s	**Response time**	8 s
Bandwidth	2 nm	**Bandwidth**	1 nm
Data pitch	0.2 nm	**Data pitch**	0.1 °C
Temperature	21 °C	**Temperature**	20-85 °C
Accumulations	20		
Scanning speed	100 nm/min		

2.5.6 Fluorescence melting curves

For fluorescence melting curves of Taspase, the solvatochromism of tryptophan is exploited. The emission maximum of tryptophan depends on the polarity of the environment, because two different electron transitions can occur when the fluorescent indole ring absorbs a photon. These two perpendicular electronic transitions are referred to as ^1L_a and ^1L_b and differ in their energy levels. For a tryptophan in the protein core, ^1L_b has lower energy than ^1L_a and is the predominant transition. Since the ^1L_a transition is directed through the ring-NH group, it can have dipole-dipole interactions with polar solvent molecules and is therefore the lowest energy transition for surface exposed tryptophans. As emission from ^1L_b occurs from a higher energy level than emission from ^1L_a, the tryptophan emission undergoes a bathochromic shift during protein unfolding.

Accurate determination of the emission maximum to one nanometer is challenging, because of the broad emission spectrum of tryptophan. In order to increase the accuracy of the measurement, the intensity at two wavelengths with considerable changes in intensity during unfolding were observed during unfolding. This procedure also allowed a mathematical elimination of the thermal quenching occurring during the measurement via division by the sum of the intensities.

Measurements were taken in 3 mm quartz cuvettes with a Varian Cary Eclipse spectrofluorimeter equipped with a peltier element. 10 µM of Taspase in 200 µl was assayed to determine the effect of buffer composition and nanoparticle binding. After excitation at 280 nm, the fluorescence emission intensities at 334 and 376 nm were recorded, while the temperature was increased from 20 to 95 °C. The detailed settings for this assay can be found in table 2.29.

Table 2.29 Parameters used for recording of fluorescence melting curves.

Parameter	Value
Excitation wavelength	280 nm
Emission wavelengths	334 nm and 376 nm
Excitation slit width	20 nm

Emission slit width	10 nm
PMT voltage	480 V
Average time	5 s
Hold time	180 s
Temperature slope	0.5 °C/min
Data interval	0.1 °C
Temperature range	20-95 °C

The intensities measured at 334 nm (I_{334}) and 376 nm (I_{376}) were converted to arbitrary folding units (F) using the following formula.

$$F = \frac{I_{334} - I_{376}}{I_{334} + I_{376}}$$

These values were normalized on a scale from 0 to 1 using the values of the folded and unfolded states as references. The fraction of unfolded protein (U) at a temperature (T) is defined as

$$U(T) = 1 - \frac{F(T) - F_{unfolded}}{F_{folded} - F_{unfolded}}$$

where F(T) represents the value of the folding value (as defined above) at temperature T, while F_{unfolded} and F_{folded} represent folding value of the unfolded and native protein, respectively.

2.5.7 NMR spectroscopy

For NMR spectra of Taspase, the buffer was changed to 50 mM NaH_2PO_4, 300 mM NaCl, 1 mM DTT, pH 7.9 by repeated dilution and concentration in a Centricon and measurements were taken at 30 °C, unless specified otherwise. Sample concentrations ranged between 400 and 600 µM and to all samples 2 % (v/v) deuterium oxide was added as frequency lock, and 50 µM DSS (2,2-dimethyl-2-silaptane-5-sulfonate) to allow a calibration of ^{1}H chemical shifts. The final sample volume of 600 µl was transferred into a 5 mm thin-wall NMR tube.

NMR spectra were recorded with a Bruker Ultrashield 700 NMR spectrometer with inverse triple resonance cryoprobe (Bruker Biospin, Rheinstetten) with constant transmitter frequencies (1H : 700,22 MHz; 15N: 70.952676 MHz; 13C: 176,070459 MHz). Recording and processing of NMR spectra was executed with the Topspin 3.0 software package (Bruker Biospin, Rheinstetten) using the parameters specified in supplemental table 7.1, table 7.2, and table 7.3. All pulse programs used were taken from the Bruker standard library.

2.5.8 Recording and processing of NMR spectra

Free induction decays were Fourier transformed in every dimension (command “xfb” for 2D or “tf3; tf2; tf1” for 3D) and π/4 shifted sine filter functions were used for apodization. A fifth degree polynomial was subtracted for baseline correction in every dimension (commands “abs2.water;

abs1" for 2D or "tabs3; tabs2; tabs1" for 3D). Spectra were phase corrected, with imaginary data added to 2D planes of 3D spectra by Hilbert transformation (command "xht2; xht1") to allow a phase correction of 3D spectra. For the evaluation and peak assignment, CCPN suite 2.3 was used.

2.5.9 Assignment theory

The principle of backbone atom assignment and identification of sequential amino acids is explained here using simplified example spectra (figure 2.5). The assignment was based on a ^{1}H-^{15}N HSQC, which can be regarded as the fingerprint of a protein. This spectrum shows all H-N correlations, which are mainly backbone amide groups (figure 2.5b), but also side-chain H-N groups of tryptophans, asparagines and glutamines are visible. Essentially, every amino acid (except for the N-terminal one and prolines) causes one peak in this spectrum. With only the H-N chemical shifts, it is not possible to identify which type of amino acid the signal belongs to. Hence, these peaks are arbitrarily numbered. This is shown for three amino acids in figure 2.5a.

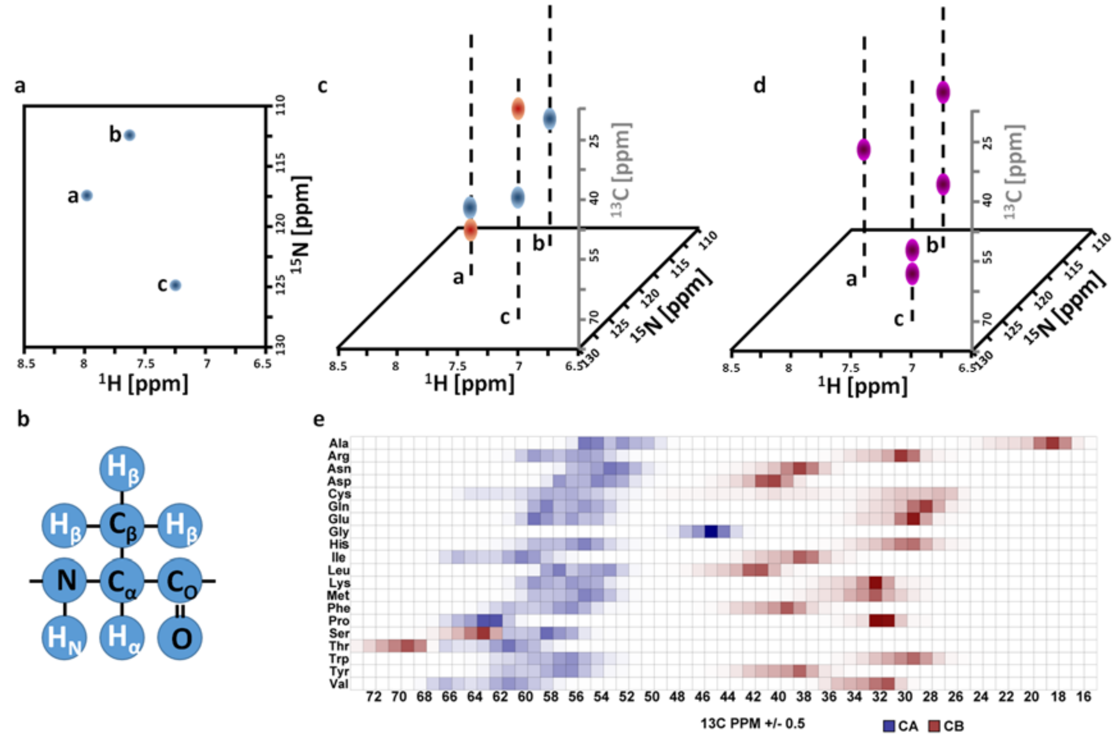

Figure 2.5 Schematic spectra and information for NMR backbone assignment.

a ^{1}H-^{15}NHSQC spectrum showing three amino acids labeled "a", "b" and "c". **b** Naming convention for amino acid atoms, shown for alanine in a polypeptide chain. Heavy atoms are displayed in black, hydrogens in white. **c** 3-dimensional HNCaCb spectrum showing the carbon resonances of the amino acids "a", "b" and "c". Alpha carbon atoms are displayed in blue, beta carbon atoms in red. **d** 3 dimensional CbCaCONH spectrum showing the carbon resonances of the amino acids *preceding* amino acids "a", "b" and "c". Alpha and beta carbon atoms are indistinguishable in this spectrum. **e** Reference chemical shifts for the alpha (blue) and beta (red) carbon atoms of all 20 amino acids. Reference chemical shifts were extracted from CCPN and are based on the RefDB database [126].

To obtain the information needed for an assignment of the amino acid type, information from 3D spectra were recorded. In HSQC-based 3 dimensional spectra, a third axis with information about the chemical shift of carbon atoms is added. In the spectrum shown in figure 2.5c, the chemical shift of the alpha and beta carbon atoms is recorded and can be visualized in columns above the

HSQC spectrum, because the chemical shift of the respective H-N groups is also included in this spectrum. Alpha and beta carbon atoms can be distinguished due to their opposite phase. The chemical shifts of the carbon alpha and beta atoms depend strongly on the amino acid type. Since the combination of C_α and C_β shift values is unique for some amino acid types (figure 2.5e), this allows assigning the residue type. In the example shown in figure 2.5, residue “a” has a C_β with a chemical shift higher than the C_α. As seen in figure 2.5e, this is only the case for serine and threonine. Consequently, residue “a” is probably a serine or threonine. Residue “b” does not have a C_β, but only a C_α. As all amino acids but glycines contain a C_β atom, residue “b” must be a glycine. The C_β shift of residue “c” is with 20 ppm remarkably low. This is typical for alanines, indicating that residue “c” is most likely an alanine.

Proteins usually contain an amino acid type more than once, which prevents an assignment of the position in the polypeptide chain with the information of HSQC and HNCaCb spectra. This means, it is possible to determine that the HSQC peak labeled as residue “b” is a glycine, but it is not possible to determine which glycine in the protein caused this peak. Furthermore, the order of the three amino acids cannot be derived from these spectra.

Information about the sequential arrangement of the amino acids can be obtained with pulse programs, in which the magnetization is transferred from the carbon atoms to the H-N group of the succeeding amino acid (i+1). Figure 2.5d shows such a spectrum (called CbCaCONH), in which the C_α and C_β chemical shift information of the preceding amino acid (i-1) is recorded with the N-H shifts of the amino acid considered. This means that the columns above the HSQC spectrum (figure 2.5d) now represent the chemical shifts of the preceding amino acid.

Looking at the CbCaCONH spectrum (figure 2.5d) of residue “b”, it is noticeable that the chemical shift values in C dimension are identical to those of residue “a” in the HNCaCb spectrum (figure 2.5c). As explained above, this can only be the case, if residue “a” precedes residue “b”. Residue “a” has only one single peak in the CbCaCONH spectrum (figure 2.5d), which has the same chemical carbon shift as the C_α of residue “c” (figure 2.5c). Hence, residue “c” precedes residue “a”. The CbCaCONH peaks of residue “c” indicate the carbon shifts of the amino acid preceding residue “c”. With these three spectra (HSQC, HNCaCb, CbCaCONH) the order of the three residues could be determined as Gly (residue “c”) – Ser/Thr (residue “a”) – Ala (residue “b”). This procedure is called chain tracing.

In many cases, it is possible to localize this short fragment in the protein sequence. If the protein has both Gly-Ser-Ala and Gly-Thr-Ala in its sequence, or the motif occurs multiple times, it is necessary to assign longer fragments, before it can be unambiguously assigned to the protein sequence. Other spectra reveal information about the chemical shifts of side chain hydrogens and/or hydrogens of the preceding amino acids. These values are helpful both to identify the amino acid type and sequential order.

It should be mentioned that spectra are never as perfect as in the example explained above. In the HNCaCb spectrum, the carbon shifts of the preceding amino acid are frequently visible in addition to the carbon shifts of the amino acid itself. Furthermore, usually not all peaks are clearly visible due to overlap, insufficient signal-to-noise ratio, too high or too low correlation times, or terminal degradation. Additionally, small shift differences between two spectra are commonly observed, because of slight conformational changes or minor deviations in sample preparation. If two stable conformations exist, which is often observed as *cis/trans* conformations for amino acids near prolines, both conformations are visible with their signal intensity corresponding to the abundance of the respective conformation.

2.5.10 Lactate dehydrogenase activity assay

As a control for nanoparticle inhibition, lactate dehydrogenase (LDH) was used. The conversion of NADH to NAD^+ during the reduction of pyruvate to lactate was followed by absorbance spectroscopy. The reaction was followed in 1 cm cuvettes at 340 nm wavelength in a Varian Cary 100 spectrophotometer equipped with a peltier element. Measurements were performed with a spectral band width of 1 nm and 5 seconds average time at 20 °C. Prior to each measurement, the blank rate of 250 µM NADH and 1 mM pyruvate in 100 mM sodium phosphate buffer pH 7.4 was measured for 2 minutes. To start the reaction, 100 ng/ml LDH were added and the linear decrease of absorbance was followed over several minutes. With a molar extinction coefficient for NADH of 6220 M^{-1} cm^{-1}, the NADH consumption per minute was calculated and the blank rate was subtracted. To test for inhibition by nanoparticles, Amsil8 and Amsil125 nanoparticles were added to the final reaction volume of 300 µl and incubated briefly, before the activity was assayed.

2.5.11 Chymotrypsin activity assay

Another protease tested for inhibition by nanoparticles was the serine protease chymotrypsin. As substrate, the peptide Succ-Ala-Ala-Pro-Phe-pNA was used, where Succ is succinic acid and pNA is p-nitroaniline. Chymotrypsin cleaves the substrate between Phe and pNA. Free pNA exhibits a strong absorbance, which can be followed by UV/Vis spectroscopy. Measurements were taken at 20 °C with 300 µl of 50 mM NaH_2PO_4, 10 % sucrose, 450 mM NaCl, 1 mM DTT, pH 8.0 in 1 cm cuvettes with a Varian Cary 100. In this assay, the blank rate of 150 µM substrate peptide in presence or absence of nanoparticles was followed at 390 nm for 2 minutes, before the reaction was started by addition of 350 nM chymotrypsin. After baseline subtraction, the comparison of the increase in absorbance with and without nanoparticles allowed a determination of the inhibitory effect.

2.5.12 MALDI-TOF mass spectrometry

Mass spectra of proteins were recorded with an Autoflex speed MALDI-TOF mass spectrometer (Bruker Daltonics, Bremen). The matrix solution was created by dissolving 7.6 mg of 2',5'-dihydroxyacetophenone in 375 µl analytical ethanol and adding it to 125 µl of an 18 mg/ml aqueous solution of ammonium hydrogen citrate. Proteins were desalted with the help of Supel-Tips C18 (Sigma-Aldrich, Seelze) and eluted in 2 µl of a 50:50-mixture (v/v) of acetonitrile and 0.1 % trifluoroacetic acid. 2 µl of 2 % TFA and 2 µl of matrix solution were added to the eluted protein. 0.5 µl of this mixture was spotted on an MTP 384 ground steel target plate (Bruker

Daltonics, Bremen) and allowed to dry. Samples were mounted onto a target frame and analyzed with the standard methods LP_20-50kDa or RP_5-20kDa from the Bruker library.

2.5.13 LC-MS ESI-TOF mass spectrometry

Liquid chromatography-mass spectrometry electrospray ionization time-of-flight mass spectrometry (LC-MS ESI-TOF MS) measurements were taken with an LCQ Fleet ESI spectrometer (Thermo Scientific, Darmstadt) equipped with an Eclipse XDB-C18 column (Agilent, Böblingen). Chromatography was performed with 5 mM ammonium acetate and linear gradient from acetonitrile to water was applied over 10 ml. The flow rate was set to 1 ml/min and absorbance was detected at 210 nm.

2.6 Bioinformatic methods

2.6.1 Generation of Taspase models and preparation for docking

Missing parts of the Taspase crystal structure were added by homology modeling using the available structure (PDB 2a8j) as template. For homology modeling with YASARA, sequence and structure were subjected to the implemented algorithm with the parameters given in table 2.30.

Table 2.30 Parameters for homology modeling in YASARA.

Parameter	Value
PsiBLASTs	1
EValue Max	0.5
Templates Total	5
Templates SameSeq	1
OligoState	4
Alignments	5
LoopSamples	50
TermExtensions	90
Speed	slow

For homology models created with Swiss-Model [122], the automated modeling mode was used with default parameters and 2a8i as template.

As YASARA and Swiss-Model do not support heterodimer modeling, the model of cleaved Taspase was generated in a stepwise approach. First, homology models of the α- and β-subunit were computed independently. Subsequently, both models were aligned to the full-length structure 2a8i, to reconstitute the active αβ-dimer. This dimer was refined in an energy minimization and 1 ns molecular dynamics (MD) simulation using YASARA.

The structures were prepared for docking using UCSF chimera [112] and programs of the DOCK 6 suite [114]. In chimera, solvent molecules were deleted, for alternative atom locations only the highest occupancy was kept and charges were calculated. Next, cavities on the surface were identified using sphgen [127] and the active site was selected as target area for docking. The overlapping spheres are used later in the docking process. As third step, a square box with 50 Å edge length was built around the active site. In this box, two energy grids were computed using grid [128] with the input parameters listed in table 2.31. The bump grid contains information necessary to identify steric overlap of ligand and receptor. The energy grid is used for scoring and holds information about the van der Waals and electrostatic interactions.

Table 2.31 Parameters to calculate the energy grid for docking.

Parameter	Value
grid_spacing	0.3 Å
energy_cutoff_distance	9999 Å
atom_model	a (all atoms, including H)
attractive_exponent	6
repulsive_exponent	12
dielectric_factor	4
bump_overlap	0.75

2.6.2 Compound database for virtual docking

Compounds for the *in silico* virtual screen were obtained from the ZINC database [129]. To reduce the amount of structures and still cover a maximum of different features, compounds with a similar structure were discarded. For this, the structures were converted to chemical hashed fingerprints with ChemAxon [130], the fingerprints of the structures were compared and only compounds that differ from all others by more than 60 % were selected. For this, the compounds were compared pairwise. Both compounds were checked for the presence or absence of certain structural features and the portion of shared features was calculated. This is additionally done for longer fragments, branching points and cyclic patterns. The structures of this subset were downloaded from the ZINC database in mol2 file format.

2.6.3 Virtual Docking

Two docking methods were used consecutively. First, the compounds were screened in a flexible docking process, and then compounds similar to the best fitting compounds were obtained and docked using an AMBER force field [131].

Flexible docking was performed with the Anchor-and-Grow method on 4 processors. This algorithm partitions the compound, which is to be docked, into rigid segments. These segments contain only bonds with double bonds or partial double bond character. The largest rigid fragment is used as anchor and oriented in the active site. This is done by matching the heavy atoms of the fragment with the spheres generated with sphgen (see section 2.6.1) and subsequent energetic optimization. This process is repeated 500 times and 100 orientations with the best docking scores are used for growth. In the growth stage, the flexible parts of the compounds are added one by one and only the conformations with the best binding energies are used for the next growth step. After the last cycle, all the fragments are combined and the original compound is docked in the active site. A final energy calculation is performed to allow a ranking of all the compounds that are docked. Parameters used for this step are listed in table 2.32.

All structures with a docking score below an arbitrarily defined cut-off (-40 kJ/mol) were selected for the following step. For the selected structures, similar structures were searched and used for the next docking round. This second docking round was performed with the same parameters used for the first round (table 2.32) on 8 processors. The docked conformations were processed with the prepare_amber script of the DOCK suite, which adds hydrogens, AMBER force field atom types, charges, topology and coordinates. 31 structures containing cyclobutane moieties could not be parameterized correctly and thus were excluded from the set. The amber input files were used for the final docking round with AMBER scoring. In this docking process, all 26 amino acids within 5 Å around the active site were treated as flexible. The ligand-receptor-complex was subjected an energy minimization with 200 conjugate gradient steps, followed by a 10 picoseconds MD simulation and another energy minimization. These calculations were performed on 8 processors with the input variables given in table 2.33.

Table 2.32 Parameters used for flexible Anchor-and-Grow docking.

Parameter	Value
automated_matching	yes
max_orientations	500
min_anchor_size	40
pruning_max_orients	100
pruning_clustering_cutoff	100
simplex_anchor_max_iterations	500
simplex_growth_max_iterations	500
atom_model	a (all atoms)

Table 2.33 Parameters used for AMBER score docking.

Parameter	Value
amber_score_movable_distance_cutoff	5 Å
amber_score_before_md_minimization_cycles	200
amber_score_after_md_minimization_cycles	200
amber_score_md_steps	10000
amber_score_temperature	300 K
amber_score_nonbonded_cutoff	18 Å

2.6.4 Generation of Taspase loop models

Two models of the isolated Taspase loop were generated. The first model was obtained with conventional homology modeling, as described for the full-length protein (section 2.6.1). Starting point for the second model was a linear peptide chain. After energy minimization and 100 ns MD simulation, the structure reached an energetic minimum, which was considered as stable state.

3 Results

3.1 Cloning and purification of Taspase protein

The DNA for Taspase proteins was cloned in expression vectors and transformed in competent bacterial expression strains. The conditions for protein expression were individually optimized for wild type Taspase, the active mutant and the loop peptide. Affinity tags allowed a purification of heterologously expressed protein in the milligram scale. The pure proteins were used for biochemical characterization in *in vitro* assays.

3.1.1 Cloning of Taspase and its mutants

Isolation of the cDNA of human Taspase from SEM cells and cloning into a pET-22b vector with C-terminal His-tag was performed by Jens Rabenstein [82]. The bicistronic construct for active Taspase with shortened loop (figure 2.3) was designed *in silico*. The DNA was synthesized (GeneArt, Regensburg) and subsequently cloned via NdeI/XhoI restriction sites into a modified pET-41b vector [132,132]. The catalytically inactive mutant D233A/T234A was created by QuikChange according to manufacturer's instructions using the construct for wild type Taspase as template. Vector maps of all bacterial expression constructs can be found in supplemental figure 7.1.

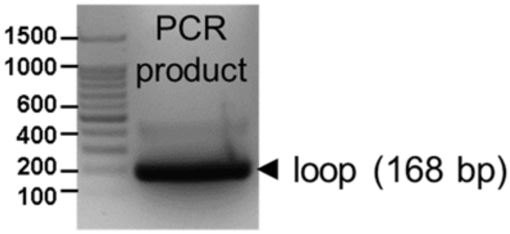

Figure 3.1 Agarose gel after PCR amplification of the Taspase loop.

PCR was performed with wild type Taspase as template. The visible band exhibits the expected size of the Taspase loop of 168 bp.

For cloning of the Taspase loop, the full length Taspase construct was used as template with the primer pair given in table 2.13. After PCR amplification, the PCR product was analyzed in an agarose gel (figure 3.1). A band at approximately 150 bp can be detected, which corresponds to the expected size of 168 bp for the Taspase loop. This band was cut from the gel and the DNA was isolated. Subsequently, both the insert (PCR product) and the vector (pET-41b) were digested separately with ApaI and XhoI. Insert and vector were purified again, before they were ligated (3 to 1 ratio) using T4 ligase. After transformation of the ligation product into shox cells and incubation over night, ten clones were tested in a colony PCR and the result was again controlled in an agarose gel (figure 3.2).

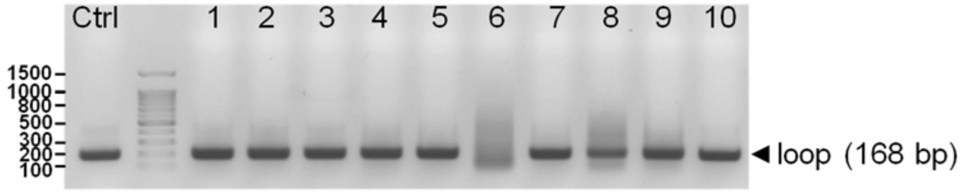

Figure 3.2 Agarose gel after colony PCR for verification of positive clones.

Ten clones were selected after ligation of Taspase loop and modified pET-41b vector. Comparison to a PCR with wild type Taspase plasmid (Ctrl) shows that all clones except for clone 6 exhibit a band at the size of the Taspase loop (168 bp).

All clones except for clone 6 showed a band at the size of the positive control (168 bp). Clones 1 and 3 were selected arbitrarily for DNA isolation and sequencing. Both clones tested possessed the correct sequence and the DNA of clone 1 was transformed into the expression strain BL21(DE3)T1r.

3.1.2 Expression test of wild type Taspase

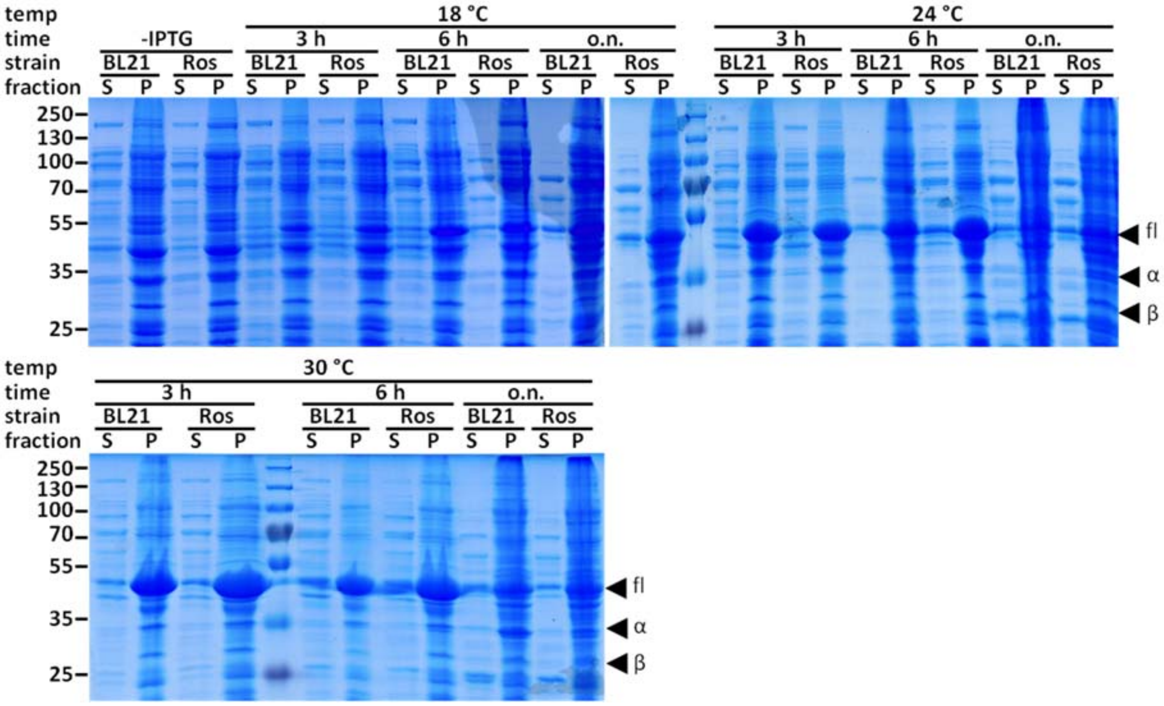

Figure 3.3 SDS-PAGE gels of expression test for wt Taspase.

Expression of wild type Taspase was tested in *E. coli* BL21(DE3)T1r cells (BL21) and Rosetta2 cells (Ros) at 18 °C, 24 °C and 30 °C after 3 h, 6 h and over night (o.n.). Supernatant (S) and pellet fractions (P) were compared to a sample before IPTG-induction (-IPTG). The expected sizes of full-length Taspase (fl), α-subunit (α) and β-subunit (β) are indicated with arrows. Optimum expression conditions are achieved in Rosetta2 cells after 6 h at 30 °C.

Heterologous expression of the His-tagged wild type Taspase protein in *E. coli* was tested in two different strains (BL21(DE3)T1r and Rosetta2) at three different temperatures (18 °C, 24 °C and 30 °C) and for three different expression times (3 h, 6 h, over night) in TB medium. The amount of overexpressed protein was compared to the protein content before addition of IPTG. After lysis and ultracentrifugation, pellet and supernatant proteins were investigated with SDS-PAGE (figure 3.3).

Under most conditions, the major fraction of Taspase can be found in the pellet, while only a small fraction is present in the supernatant. The largest amount of soluble Taspase is achieved after expression for 6 h at 30 °C in Rosetta2 cells. Consequently, these conditions were used for the expression of wild type Taspase, as well as for the expression of the inactive Taspase mutant (D233A/T234A mutant).

3.1.3 Purification of wild type Taspase and inactive Taspase

In figure 3.4, the chromatograms and gels for the purification of wild type Taspase are displayed. The corresponding figures for the inactive mutant can be found in supplemental figure 7.4.

After expression in 2 l under optimized conditions (section 3.1.2), bacteria were resuspended in phosphate buffer and lysed by incubation with lysozyme, followed by sonification. After cell debris and insoluble proteins had been removed by ultracentrifugation and sterile filtration, a NiNTA affinity chromatography was performed and the purity of the eluted fractions was controlled by SDS-PAGE (figure 3.4).

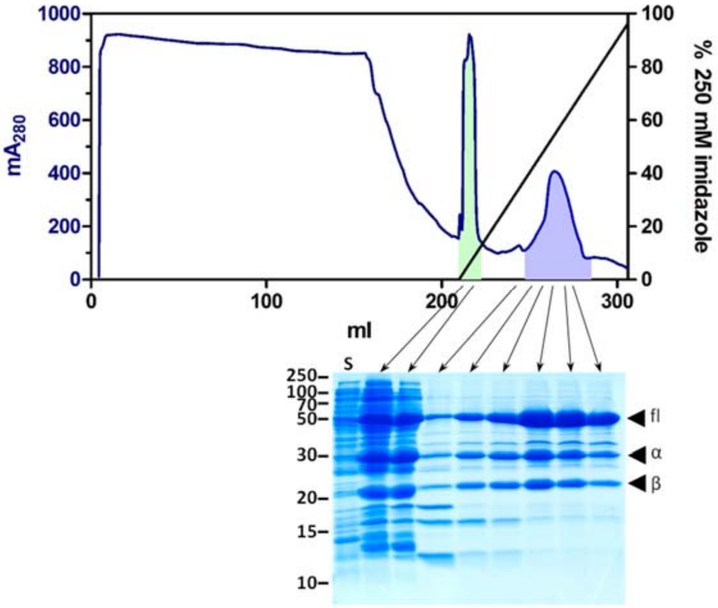

Figure 3.4 NiNTA affinity purification of wild type Taspase.

The upper panel shows the chromatogram of the NiNTA affinity purification including the gradient of elution buffer. Samples for SDS-PAGE were taken from the supernatant before NiNTA purification (S) and from elution fractions indicated with arrows. The corresponding gel (lower panel) reveals fractions containing full-length Taspase (fl), α-subunit (α) and β-subunit (β). Fractions highlighted in blue were pure enough for gel filtration, while the impure fractions highlighted in green were applied to another NiNTA affinity chromatography.

The first elution peak (green in figure 3.4) emerges at low imidazole concentrations (~35 mM) and contains significant amounts of Taspase in addition to severe impurities by *E. coli* proteins. The fractions of this peak were diluted to 100 ml, reducing the imidazole concentration to 10 mM, and applied another time to a NiNTA affinity column. The chromatogram of this purification and the respective gel filtration can be found in supplemental figure 7.5.

The second elution peak at 125 mM imidazole (blue in figure 3.4) contains Taspase with only few impurities at around 35 kDa. This peak was pooled and concentrated to 2 ml, before the protein was subjected to gel filtration on a Superdex 200 column for further purification and removal of imidazole. Two peaks are visible, which were analyzed by SDS-PAGE (figure 3.5).

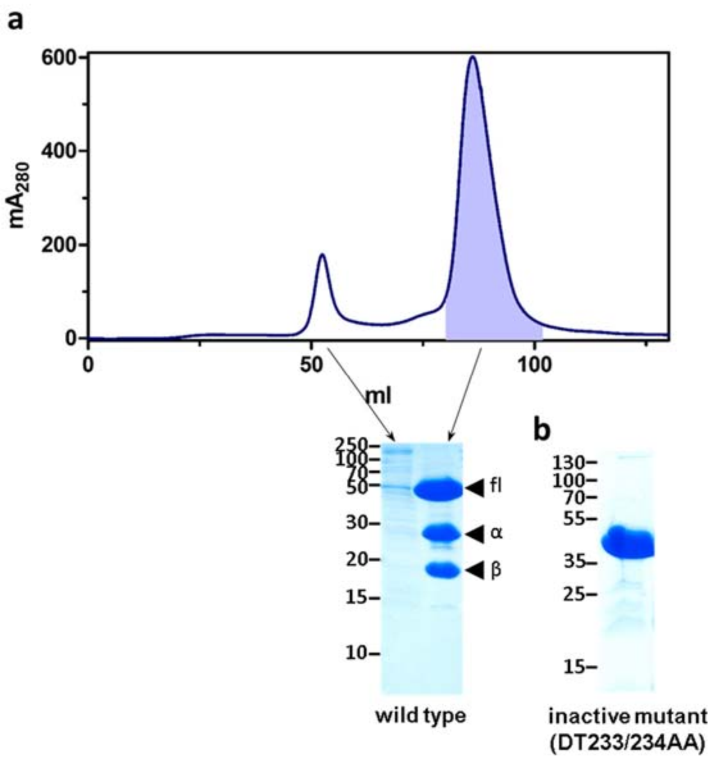

Figure 3.5 Preparative gel filtration of wild type Taspase.

a The upper panel displays the gel filtration chromatogram. The two peaks were analyzed by SDS-PAGE (lower panel), showing that the second peak (highlighted in blue) contains pure full-length Taspase (fl), α-subunit (α) and β-subunit (β). **b** The corresponding gel for the inactive Taspase mutant (D233A/T234A) shows only one band near 45 kDa, corresponding to the full-length enzyme.

The first peak at 50 ml corresponds to the void volume and contains large complexes or aggregates. For wild type Taspase, the major peak (blue in figure 3.5a) contains almost exclusively the proenzyme of full length Taspase or the active form consisting of α- and β-subunits. For the inactive mutant, only the proenzyme was found (figure 3.5b). This peak was concentrated to 18 mg/ml and stored in aliquots at -20 °C. The overall protein yield amounted 25 mg per liter of bacteria culture.

3.1.4 Purification of active Taspase mutant

To express a cleaved Taspase variant, the two subunits were co-expressed in *E. coli* with shortened Taspase loop. This variant is subsequently referred to as active Taspase. The bicistronic construct for active Taspase comprises the amino acids 1 to 206 (His-tagged α-subunit) and amino acids 234 to 420 (β-subunit; figure 2.3). Expression tests indicated maximum protein expression after 6 hours at 37 °C (see supplemental section 7.6). The low amount of overexpressed protein could partially be compensated by increasing the expression culture size to 6 liter. Cell lysis and NiNTA affinity purification were performed as described for the wild type Taspase (section 3.1.3). Although only the α-subunit is His-tagged, the β-subunit can be co-purified due to dimerization of the subunits. The chromatograms of the NiNTA affinity chromatogram and the subsequent gel filtration are displayed in figure 3.6.

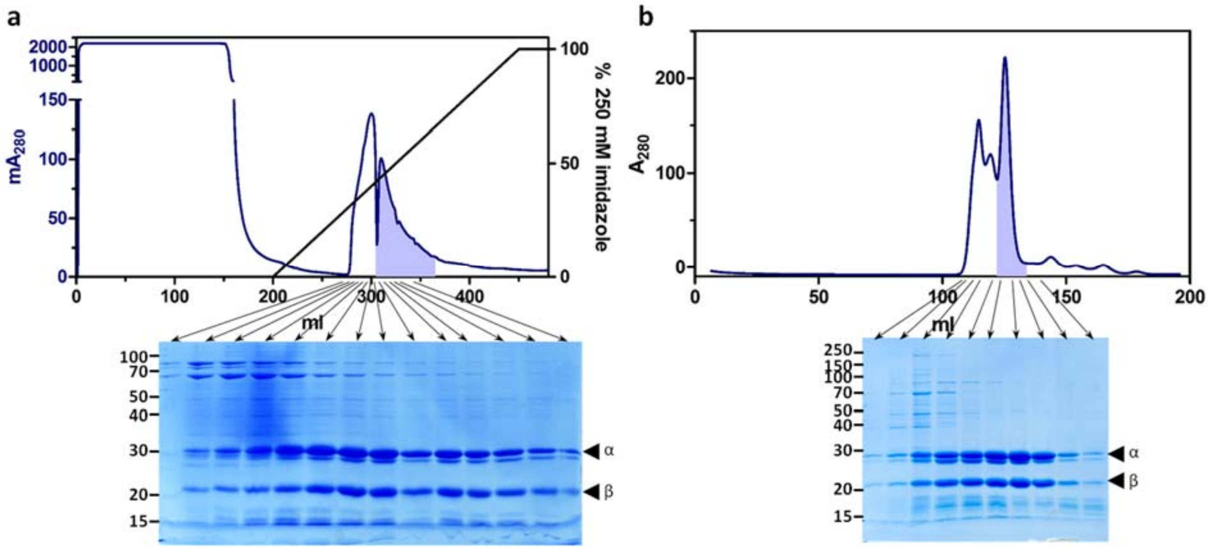

Figure 3.6 Purification of active Taspase by affinity chromatography and gel filtration.

a NiNTA affinity purification of active Taspase. The His-tagged α-subunit and the untagged β-subunit were co-purified. The top panel shows the chromatogram including the elution gradient. The SDS gel of protein containing elution fractions is shown in the lower panel. The second peak (highlighted in blue) contains α-subunit (α) and β-subunit (β) with few impurities and was used for subsequent gel filtration. **b** Gel filtration of active Taspase. The upper panel displays the chromatogram. The SDS-PAGE gel of protein containing fractions is shown in the lower panel. The third peak (highlighted in blue) contains pure active Taspase.

The first elution peak of the NiNTA column (figure 3.6a) between 275 and 300 ml contains Taspase, but also a significant amount of impurities. Hence, only the second elution peak (blue in figure 3.6a) was concentrated and used for gel filtration. The gel filtration chromatogram (figure 3.6b) exhibits three prominent peaks. The left peak corresponds to the void volume and contains aggregated protein. The middle peak contains Taspase with impurities of larger proteins and the right peak (blue in figure 3.6b) contains Taspase with some impurities below 20 kDa. These proteins were probably degradation products and could be successfully removed by using a filter with 30 kDa cut-off for final concentration to 15 mg/ml. The overall yields of active Taspase ranged from 1 to 2 mg per liter of bacteria culture.

3.2 Characterization of Taspase and its mutants

With purified wild type, active and inactive Taspase available, a detailed biochemical comparison and characterization was accomplished. Dimerization was assessed by analytical gel filtration, while CD as well as fluorescence spectroscopy gave insight into the stabilization by sodium chloride. Possible posttranslational modifications could be excluded with the help of mass spectrometry, and the autocatalytic processing was followed by SDS-PAGE and NMR spectroscopy. Furthermore, first structural information about the loop region, which is not resolved in the crystal structures, was obtained by NMR and CD spectroscopy.

3.2.1 CD spectroscopic studies

In order to analyze the secondary structure of the Taspase mutants, far-UV CD spectra were recorded (figure 3.7a).

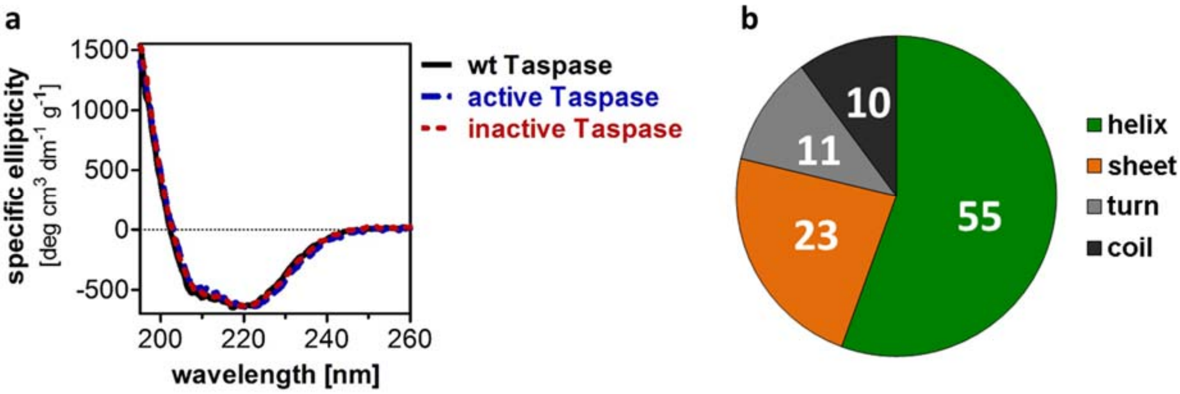

Figure 3.7 Far-UV CD spectra of Taspase.

a Far-UV CD spectra of wild type Taspase (wt), active Taspase (with shortened loop) and inactive Taspase (D233A/T234A) indicate a similar secondary structure composition of all three proteins. The shape of the spectrum, especially the minima at 222 nm and 208 nm hint at a helix-rich protein with beta-stand portions. **b** Secondary structure deconvolution of the wt CD spectrum using the CDSSTR algorithm confirm 55 % helix, 23 % sheet, 11 % turn and 10 % random coil elements. Numbers indicate percent values.

All three CD spectra for wild type, active and inactive Taspase are similar and exhibit minima at 220 nm and 208 nm with the 220 nm minimum exhibiting the lowest ellipticity. Comparison with a reference data set with the CDSSTR algorithm yielded 55 % helix and 23 % sheet content (figure 3.7b).

3.2.2 Stability of Taspase

Secondary structure is lost, when proteins are unfolded. Hence, CD spectroscopy can be used to monitor thermal unfolding of proteins (figure 3.8a). To find suitable buffer conditions for subsequent assays, Taspase stability was measured in different buffers. As CD spectroscopy is limited with respect to chloride and sucrose concentration, tryptophan unfolding via fluorescence spectroscopy was employed as orthogonal method (figure 3.8b).

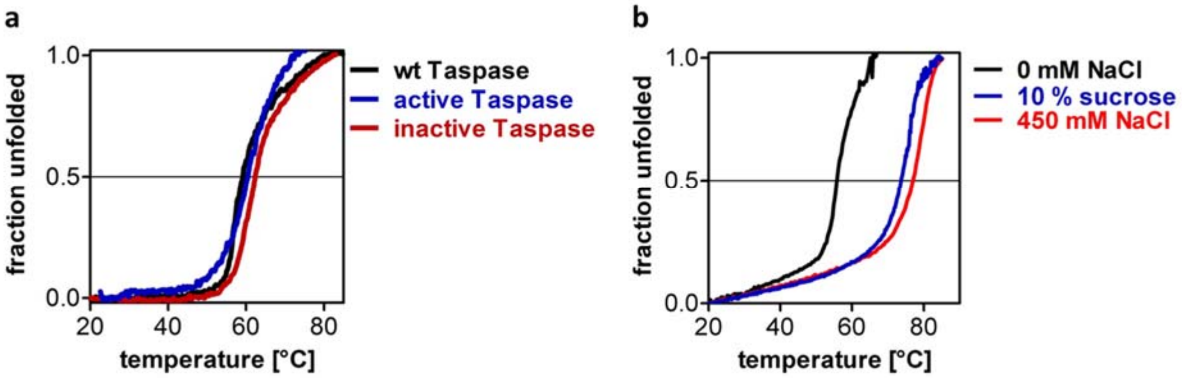

Figure 3.8 Melting curves of Taspase.

a CD melting curves of wild type Taspase (wt Taspase; black; T_m = 59 °C), active Taspase (blue; T_m = 60 °C) and inactive Taspase (red; T_m = 63 °C) in 50 mM phosphate buffer. **b** Tryptophan fluorescence melting curves show that wild type Taspase in 50 mM phosphate buffer (black; T_m = 56 °C) can be stabilized by addition of 10 % sucrose (blue; T_m = 73 °C) or 450 mM NaCl (red; T_m = 77 °C).

CD spectroscopy in phosphate buffer reveals a melting temperature (T_m) of 59 °C for wild type Taspase, which consists of α- and β-subunit and a T_m of 60 °C for the active Taspase with shortened loop. In contrast, the inactive mutant is made up of a continuous polypeptide chain and is somewhat more stable with a melting temperature of 63 °C. Fluorescence spectroscopy yielded a melting temperature of 56 °C for wild type Taspase. Khan *et al.* [56] used chloride and sucrose in their buffers, which was tested here for a stabilizing effect. Addition of 10 % sucrose (292 mM) elevates the melting temperature by 17 °C to a T_m of 73 °C. A similar effect could be seen for 450 mM NaCl, which stabilized Taspase by 21 °C to 77 °C.

3.2.3 MALDI-MS analysis

Mass spectrometry allows a precise determination of the molecular weight of proteins. Spectra were recorded for masses between 15 and 50 kDa, which covers the mass of the proenzyme, as well as the masses of the subunits (figure 3.9).

For the wild type enzyme (black in figure 3.9), four major peaks are visible. They correspond to the proenzyme (T2-H428) with a sodium and potassium ion as adduct (Δm/z = 0.01 %), the α-subunit (T2-D233) with a potassium ion as adduct (Δm/z = -0.01 %) and the β-subunit (T234-H428) with a sodium ion as adduct (Δm/z = -0.05 %). The double charged proenzyme causes the fourth peak at exactly half the mass of the proenzyme (22722 Da).

The active Taspase (blue in figure 3.9) exhibits two main peaks in the mass spectrum. They correspond to the α-subunit (H1-A212) with a potassium ion as adduct (Δm/z = -0.05 %) and the β-subunit (T234-E420) with a sodium ion as adduct (Δm/z = 0.01 %).

The inactive mutant (red in figure 3.9) exhibits three major peaks, corresponding to the proenzyme with potassium and sodium ions as adduct (Δm/z = -0.1 %), as well as the double and triple charged proenzyme.

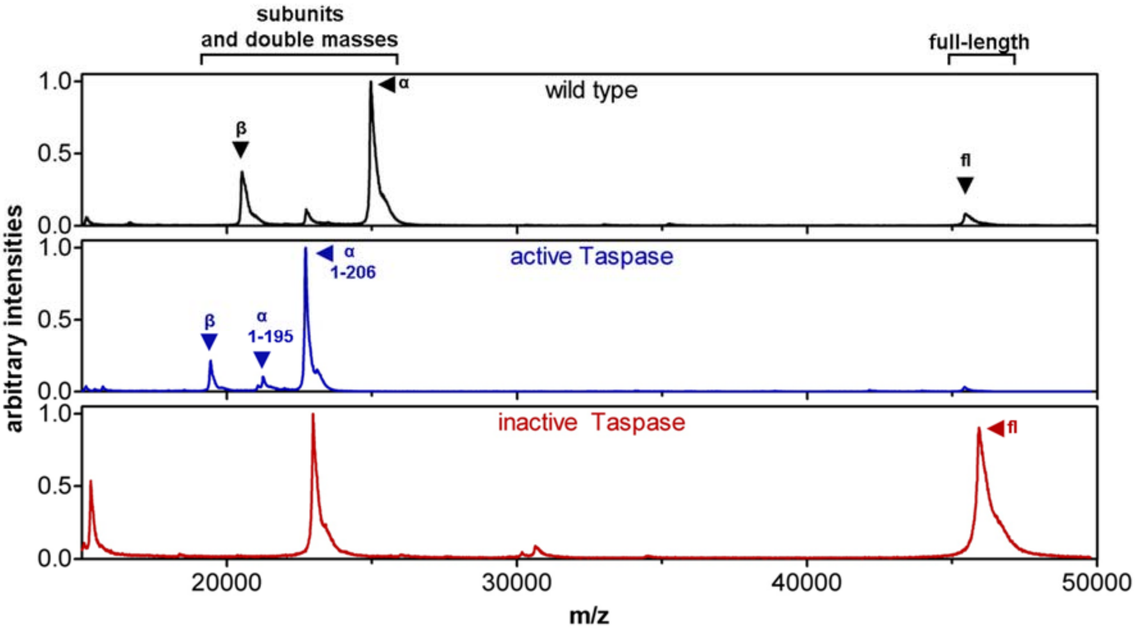

Figure 3.9 MALDI-TOF mass spectra of Taspase.

Mass spectra of wild type Taspase (top panel), active Taspase (middle panel) and ^{15}N-labeled inactive Taspase (lower panel) were recorded in the range of 15 to 50 kDa. The arbitrary intensity units were rescaled. Arrows indicate masses of the respective full-length protein (fl), α-subunit (α), β-subunit (β), and shortened α-subunit (amino acids 1-206 or 1-195). For improved clarity, double and triple charged masses are not labeled.

3.2.4 Analytical gel filtration

Analytical gel filtration was performed to test for Taspase multimerization. The calibration range covers the subunits (22 kDa), the dimer (45 kDa) as well as the tetramer (90 kDa) and can be found in supplemental figure 7.7. Gel filtration runs of 1 to 400 µM Taspase and inactive Taspase (D233A/T234A) in the presence of 450 mM NaCl on a Superdex 200 column are displayed in figure 3.10.

Both wild type Taspase and the inactive mutant elute in the range of a tetramer (90-110 kDa; gray area in figure 3.10) independent of the protein concentration. The expected range for the αβ-dimer (45-55 kDa) is highlighted in green. No peak can be detected in this area for the wild type or the inactive mutant. Consistent with this, no peak for the separate α- or β-subunit can be detected at 19 ml retention volume.

The result is essentially the same at lower salt concentrations (100 mM NaCl): Wild type Taspase, active and inactive Taspase elute as tetramer with apparent molecular weights around 100 kDa (supplemental figure 7.8).

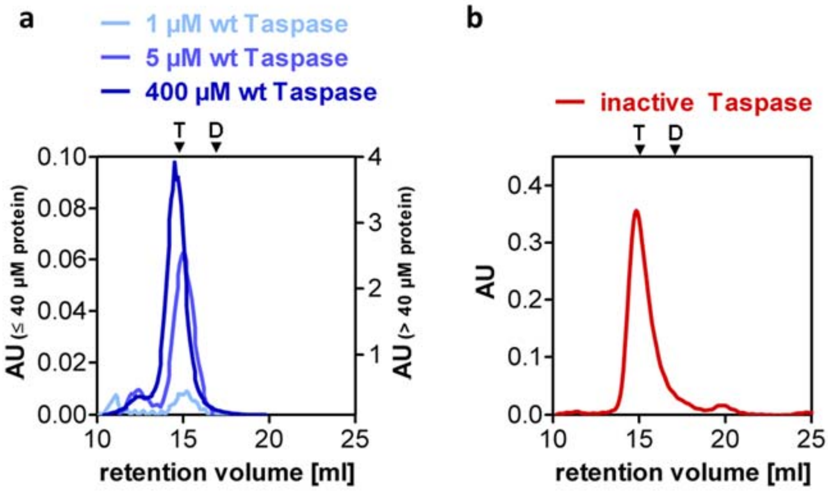

Figure 3.10 Analytical gel filtration of Taspase.

Analytical gel filtration chromatograms of a calibrated Superdex 200 column reveal that wild type Taspase (**a**) and inactive Taspase (**b**) elute in the range of 90-110 kDa (labeled T), corresponding to a hetero-tetramer. At the expected dimer size of 45-55 kDa (labeled D), no peak is visible.

3.2.5 Autocatalytic processing of the Taspase proenzyme

The Taspase proenzyme undergoes spontaneous intramolecular autocatalytic processing. In this process, the polypeptide chain opens between Asp233 and Thr234, yielding the catalytic active Thr234 with free hydroxyl group. This process is time dependent and can be visualized by a separation of the subunits by SDS-PAGE (figure 3.11a).

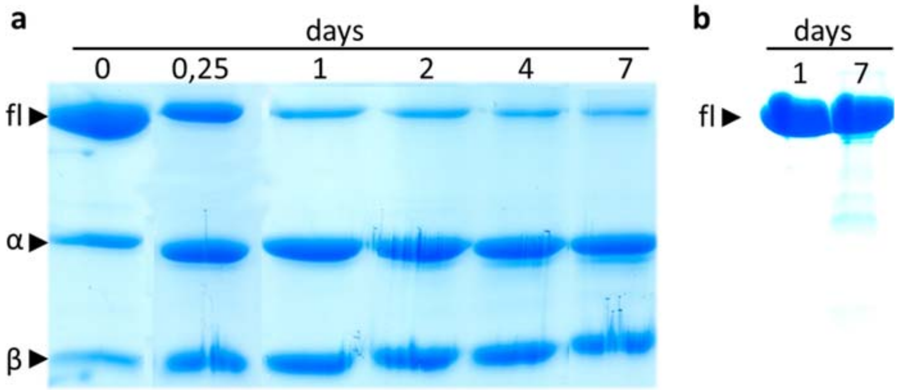

Figure 3.11 Autocatalytic processing of Taspase.

a 10 µM wild type Taspase was incubated in gel filtration buffer at 37 °C. At indicated time points, samples were taken for SDS-PAGE. The expected sizes of full-length Taspase (fl), α-subunit (α) and β-subunit (β) are marked with arrows in the 15 % SDS-PAGE gel. **b** No autocatalytic processing was observed for the inactive Taspase mutant after 7 days.

Six hours incubation at 37 °C caused an attenuation of the band for the full-length enzyme, while the bands for α- and β-subunit gained intensity. After one day, the band for the full-length enzyme is diminished, while both subunit bands became stronger. The weak band for the full-length enzyme is visible even after one week. In contrast, incubation of the inactive mutant for one week resulted in a single band for the full-length enzyme (figure 3.11b).

3.2.6 NMR spectroscopic analysis of Taspase

For the first time, Taspase was analyzed by NMR spectroscopy in this project to gain information about the flexible parts, which are not resolved in the crystal structures. A ^{1}H-^{15}N HSQC spectrum of ^{15}N-labeled wild type Taspase was recorded at 30 °C (figure 3.12a).

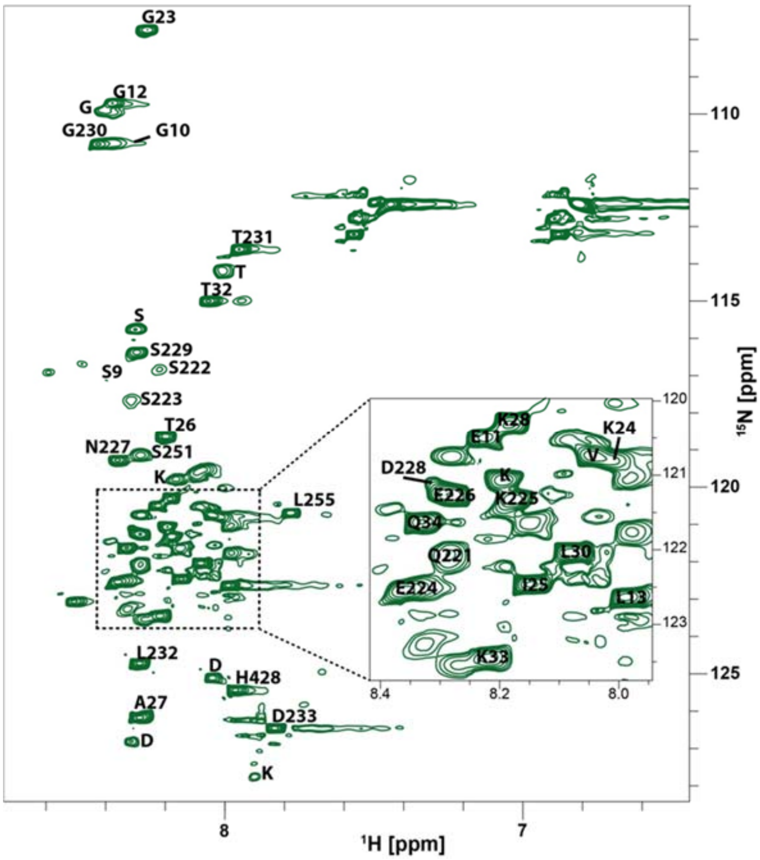

Figure 3.12 ^{1}H-^{15}N HSQC spectrum assignment.

^{1}H-^{15}N HSQC spectrum of wild type Taspase after one week at 30 °C in gel filtration buffer. The crowded region in the center of the spectrum (dashed lines) is magnified. For amino acids labeled with letters without numbers, only the residue type could be determined unambiguously.

The His-tagged protein comprises 428 amino acids, including 15 prolines, which results in 412 backbone peaks theoretically visible in a ^{1}H-^{15}N HSQC spectrum. However, only 56 backbone peaks are visible in the ^{1}H-^{15}N HSQC spectrum.

These peaks were assigned to the corresponding amino acids using backbone (HNCaCb, CbCaCONH, HNCOCa) and side chain spectra (^{15}N-TOCSY-HSQC, ^{15}N-COSY-HSQC, HbHaNH, HbHaCONH, HCCH-TOCSY) recorded with ^{15}N and ^{13}C labeled protein (supplementary table 7.4). This allowed an assignment of 40 residue types (71 %), of which 32 (55 %) could be assigned to specific amino acid positions. Moreover, a spectrum recorded at pH 6.5 (data not shown) showed only marginal shifts and the same number of peaks compared to the spectrum at pH 7.9 shown in figure 3.12a.

Another striking observation was a time dependent appearance of peaks in the HSQC spectrum. The spectrum of a Taspase sample recorded immediately after purification exhibits only 22 backbone NH peaks (supplemental figure 7.9). The other 34 peaks become visible by and by during the incubation for five to seven days. A spectrum of a sample incubated for 30 days (data not shown) still shows the 56 peaks seen after seven days and only few signs of terminal degradation, indicating that the underlying process is completed after seven days. The amino acids initially visible in the HSQC spectrum could be assigned to the N-terminus (5 residues), the flexible loop (3 residues) and a loop near the active site (1 residue).

The inactive mutant lacking the ability of autocatalytic activation due to a double mutation of the active site (D233A/T234A) was ^{15}N isotopic labeled and ^{1}H-^{15}N HSQC spectra were recorded (supplemental figure 7.10) under the same conditions used for wild type protein. Both proteins were incubated for 7 days at 30 °C before spectra were recorded. Compared with the wild type spectrum, 9 backbone peaks of amino acids located in the flexible loop (S222-D233) and the peak of Glu34 in the N-terminus are missing.

3.2.7 Characterization of the Taspase loop

***In silico* studies**

The Taspase loop is released at the C-terminal end by an autocatalytic event, which creates the catalytically active Thr234 at the N-terminus of the β-subunit. Suitable algorithms, such as JNet, CFSSP or the YASARA tool, can predict the secondary structure elements of the loop based on the amino acid sequence (figure 3.13a).

All three algorithms consistently predict a helical content around 50 % and the rest as unstructured. Both N- and C-terminus are predicted as random coil regions, while the central part (N185-S223) is predicted to form helices.

To investigate if the loop conformation changes after the autocatalytic cleavage, releasing the loop at the C-terminus, homology models of the proenzyme and active Taspase were generated (figure 3.13c and d). In both models, the loop region comprises two interacting helices. The conformation of the loop, however, differs between the proenzyme and active Taspase. While in the proenzyme the loop is attached to the active site and therefore blocking the catalytic center, in the model of active Taspase the loop is located outside the active site, rendering the catalytic Thr234 accessible for substrates.

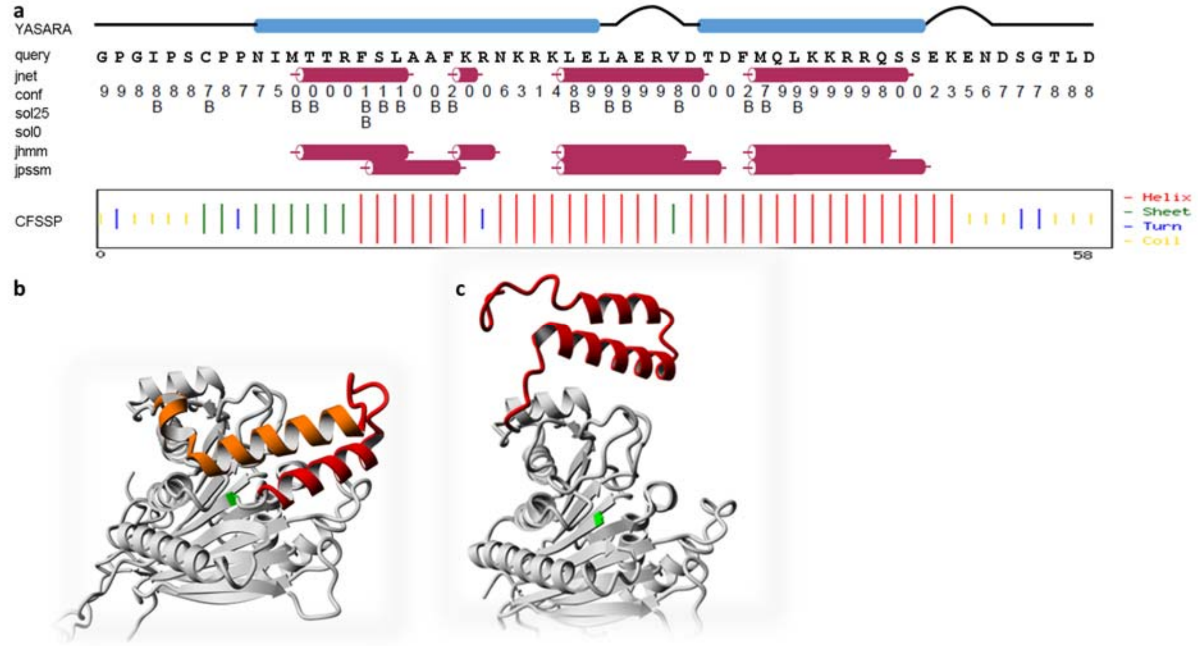

Figure 3.13 Secondary and tertiary structure prediction of the Taspase loop.

a Primary sequence based secondary structure prediction of the loop region G178-D233, which is missing in the crystal structure of active Taspase (PDB 2a8j). The algorithms predict a stretch of helices between N185 and S223. For the YASARA model and the JNet prediction, cylinders represent helical areas, lines represent random coil and loops are represented as curves. Confidence (conf) values range from 0 (uncertain) to 9 (confident). Residues predicted as buried by sol25 and sol0 are labeled (B). Note that the N-terminal GP originates from the GST tag. **b** In the proenzyme, the loop (red and orange) is covalently attached to the active site (green). The model is based on the crystal structure of the proenzyme (PDB 2a8i). The loop amino acids that are structured in the crystal structure of the proenzyme, but not in the processed protein are colored in orange. Newly modeled amino acids are displayed in red. **c** After autocatalytic activation, the loop (red) can leave the active site (green). The model is based on the structure of active Taspase (PDB 2a8j).

In vitro experiments

Testing this *in silico* model *in vitro* requires purified loop peptide. For this, the 56 amino acid loop fragment was obtained by recombinant expression in *E. coli*. In addition, a shorter loop fragment of 42 amino acids covering only the two helices was synthesized (CASLO ApS, Lyngby). Recombinant expression of the short fragment was considered ineffective, as short peptide fragments are typically prone to degradation, even if long tags, such as GST, are used.

Expression tests of the long loop in *E. coli* (supplemental figure 7.11) indicated optimum expression conditions of 25 °C over night in LB medium and addition of 1 % Triton X-100 to the buffer in which the pellet was resuspended. The GST fusion protein was purified by GSH affinity chromatography (figure 3.14a).

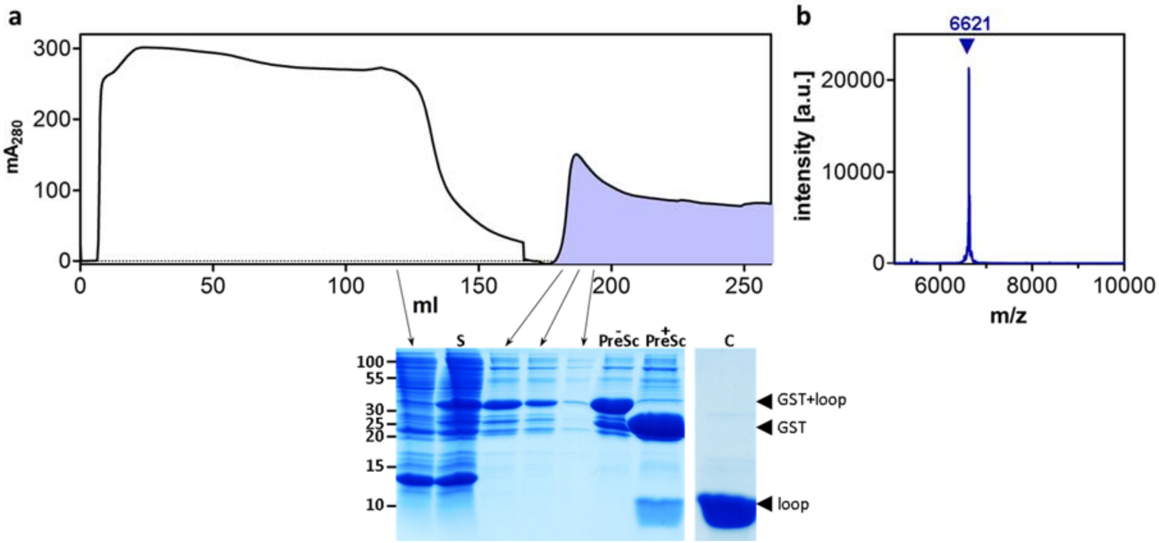

Figure 3.14 Purification of the Taspase loop.

a GSH affinity chromatogram (top panel) and the SDS-PAGE gel of the fractions indicated by arrows. The overexpressed GST-loop fusion protein visible in the supernatant before affinity chromatography (S) is bound to the column and thereby removed from the flow-through (first lane). After washing, the GST-loop is eluted and concentrated (-PreSc). PreScission (+PreSc) removes the GST tag and removal of GST in a 10 kDa cut-off Centricon with subsequent concentration of the flow-through yielded pure loop protein. **b** The correct size of the loop protein (6621 Da) was confirmed by MALDI-MS.

The supernatant after ultracentrifugation with the overexpressed GST-loop (S in figure 3.14a) was applied to a GSH column. Efficient binding to the column is confirmed by the absence of the target protein in the flow-through. The elution fractions contain GST-loop, which is still impurified by additional proteins. The GST-tag was removed by PreScission protease treatment (+ PreSc in figure 3.14a) and filtration through a 10 kDa membrane yielded pure loop peptide (C in figure 3.14a). The GST tag and other impurities were retained. The correct mass of the peptide was confirmed by MALDI-MS (figure 3.14b). With the two variants of the loop peptide available, the secondary structure was analyzed by CD spectroscopy (figure 3.15a).

The short and long loop differ in their secondary structure, indicating a strong influence of the 16 additional amino acids present in the longer loop (5 N-terminal; 11 C-terminal). The spectrum of the short loop peptide exhibits unambiguous features of an unstructured random coil protein, such as positive ellipticity at 220 nm and a minimum at 200 nm. In contrast, the long loop possesses a minimum at 222 nm and increasing ellipticity below 200 nm, which is typical for helices. Nevertheless, the minimum at 200 nm is a clear sign for random coil regions in the long loop. Deconvolution of the CD spectra (figure 3.15b) yields a helix content of 58 % for the long loop and only 19 % for the short loop.

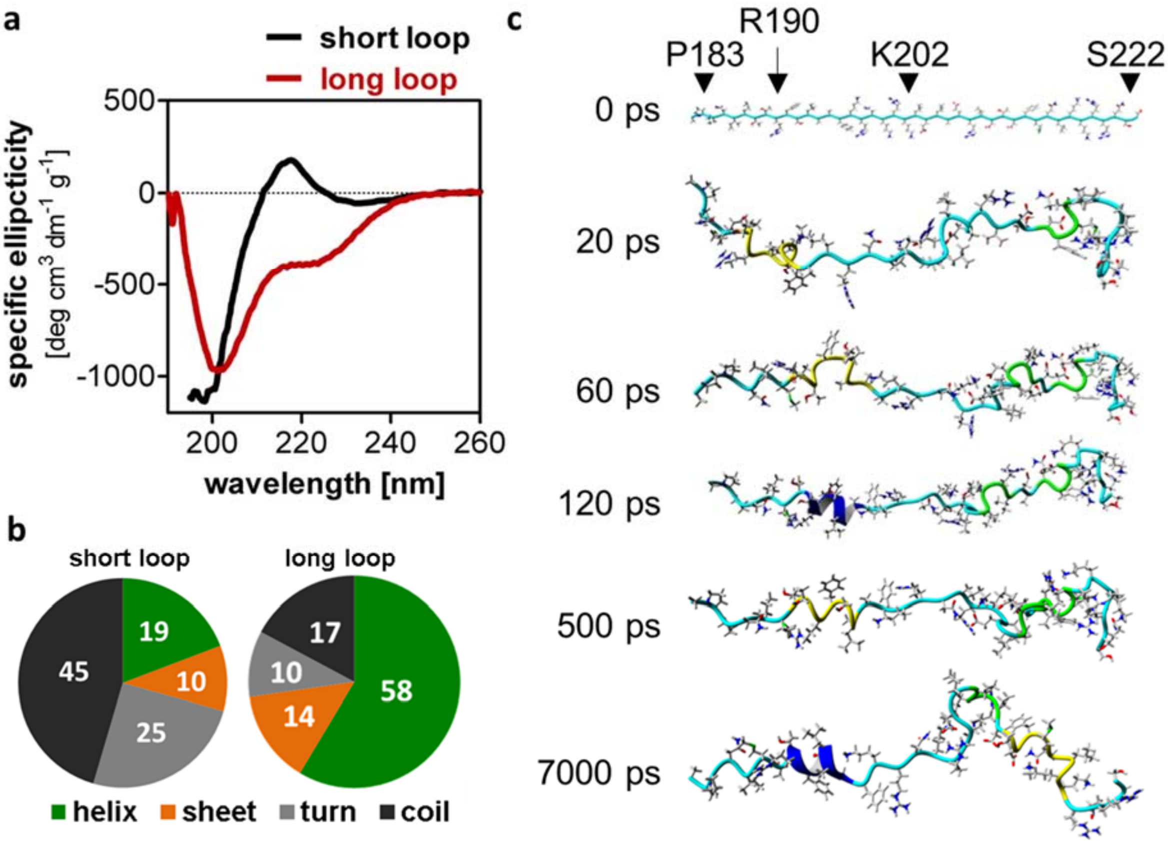

Figure 3.15 Spectroscopic analysis and MD simulation of the Taspase loop.

a CD spectra of the short (P183-S222; black) and long Taspase loop (G178-D233; red) show more helical structure for the long loop. **b** CD spectrum based secondary structure deconvolution using CDSSTR and CONTIN confirm a higher helical content (blue) in the long loop compared with the short loop. Numbers are given in percent. **c** 7 ns molecular dynamics simulation starting with a linear loop indicates formation of transient helices, especially around Arg190.

To investigate how the short loop peptide behaves in solution, a 7 nanoseconds MD simulation was performed (figure 3.15c). Analysis of the adopted conformations over time reveals the formation and disorganization of short helical areas. Most prone for helix formation is the stretch around Arg190, while in the terminal regions and the central part around Lys202 no helix formation could be observed during the simulation.

3.3 Catalytic activity of Taspase

Qualitative assays of Taspase activity have been published before [56,63,69]. In this thesis, an improved assay is presented. It allowed quantification of the specific activity for the first time and revealed different catalytic rates with respect to the two MLL cleavage sites. For this, the oppositional role of sodium chloride, which is required for stability but inhibits Taspase activity [56], had to be overcome. Furthermore, a modification of the assay facilitated a determination of specific Taspase activity in cell lysates.

3.3.1 Quantitative Taspase activity assay

The catalytic activity of Taspase was assayed with the help of a model substrate comprising the Taspase target sequence. In the intact peptide, an N-terminal fluorophor is quenched by a C-terminal dinitrophenol moiety, which is removed upon cleavage. After the reaction is started by addition of Taspase, the intensity increases linearly as long as saturating substrate concentrations are present (figure 3.16). With decreasing substrate concentrations, the reaction rate drops until all substrate is consumed and a plateau is reached. If the two amino acids adjacent to the cleavage site of the substrate peptide are substituted by alanines, no increase in fluorescence intensity is observed after addition of Taspase.

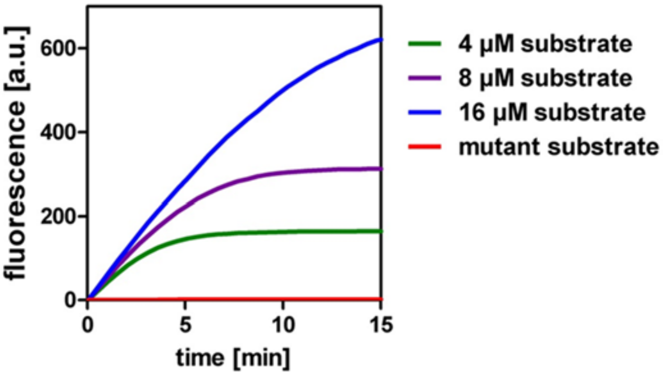

Figure 3.16 Taspase activity assay.

Emission of the fluorogenic substrate increases over time in presence of Taspase. The initial rate and plateau at substrate depletion increase with substrate concentration. Substrate with mutated cleavage site (red) shows no increase in fluorescence.

As explicated in the sections above, sodium chloride stabilizes Taspase and prevents precipitation. However, chloride inhibits Taspase activity with an IC_{50} value of 68 ± 7 mM (supplemental figure 7.12). Hence, chloride was omitted from the buffer and all activity measurements were taken in 10 % sucrose.

Wild type Taspase was incubated in a buffer with 10 % sucrose at 37 °C and the activity was measured after different incubation times to test for a potential loss of activity (figure 3.17).

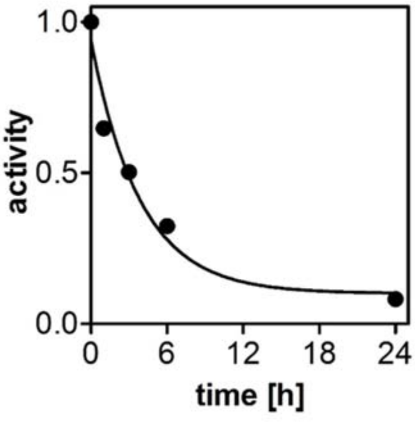

Figure 3.17 Loss of Taspase activity over time.

Incubation of wild type Taspase at 37 °C in measurement buffer containing 10 % sucrose shows a loss of activity over time. Nonlinear fit yields a half-life around 2.5 hours.

After 24 hours, the residual activity of Taspase is less than 10 % compared to the activity immediately after thawing. The calculated half-life of Taspase activity is near 2.5 hours. Although sucrose and salt show a similar increase of the melting temperature (figure 3.8b), incubation for 24 hours in a buffer with 450 mM NaCl resulted in no detectable loss of activity (data not shown). To overcome the instability in measurement buffer, fresh Taspase aliquots were thawed for each assay. This approach enabled a reproducible quantitative measurement of Taspase activity.

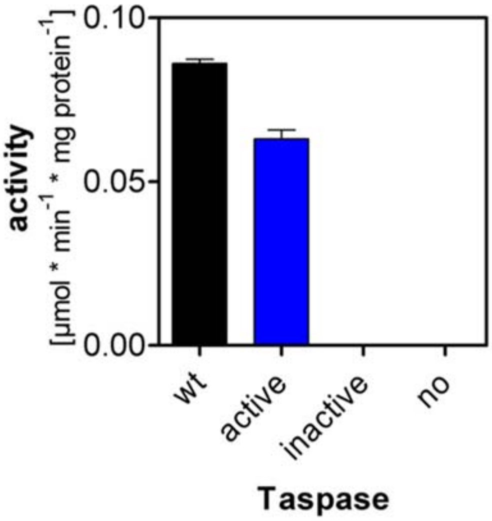

Figure 3.18 Activity of the Taspase variants.

Specific activity of wild type Taspase (wt, black, 0.086 ± 0.0009 µmol * min^{-1} * mg^{-1}), active Taspase (shortened loop, blue, 0.063 ± 0.002 µmol * min^{-1} * mg^{-1}), inactive Taspase (D233A/T234A mutant, 0.00003 µmol * min^{-1} * mg^{-1}) and buffer control (no, 0.00006 µmol * min^{-1} * mg^{-1}) in the presence of 8 µM substrate. For the inactive mutant and the buffer control no activity was observed. Error bars indicate standard deviations.

Wild type Taspase, active Taspase and the inactive mutant were used in equal concentrations of 300 nM for activity assays with 8 µM substrate (figure 3.18). The active mutant exhibits 75 % of the activity measured for wild type Taspase. In contrast, the inactive Taspase mutant has no catalytic activity, which also applies to the buffer control without Taspase.

3.3.2 Cleavage sequence specificity of Taspase

A natural substrate of Taspase is the MLL protein. Taspase cleaves MLL at two cleavage sites, called CS1 and CS2. 50 % of the amino acids are identical for the two sequences (table 3.1). Here, kinetic constants for CS1 (GKGQVDGADDK) and CS2 (KISQLDGVDDK) peptides are reported for the first time (figure 3.19).

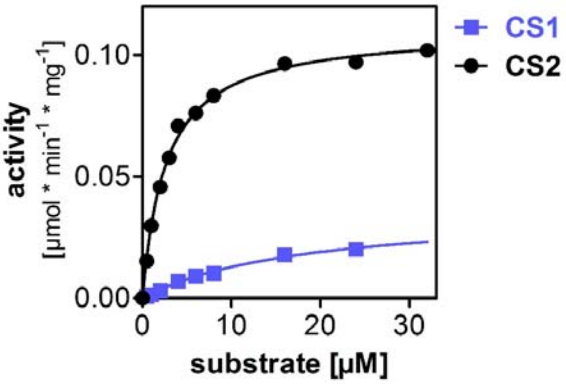

Figure 3.19 Substrate specificity of Taspase.

Michaelis-Menten plots at 37 °C for the two Taspase peptides with the cleavage sites CS1 (blue squares) and CS2 (black circles) of the MLL protein. Catalytic parameters obtained by nonlinear fitting can be found in table 3.1.

Taspase has an affinity in the low-micromolar range for both target sequences, with a sevenfold higher affinity for the CS2 peptide (18 μM), compared to the CS1 peptide (2.7 μM). Furthermore, the maximum reaction velocity (v_{max}) and, hence, also the turnover number (k_{cat}) differs between the two substrates. Both values are about 3 times higher for CS2 than for CS1 (CS1: v_{max} = 0.03 ± 0.003 μmol min^{-1} mg^{-1}, k_{cat} = 0.0274 s-1; CS2: v_{max} = 0.11 ± 0.002 μmol min^{-1} mg^{-1}, k_{cat} = 0.083 s^{-1}). A significant difference can be seen if the specificity constants (k_{cat}/K_m) are compared. Here, cleavage of the CS2 peptide is more than 20-fold more efficient than CS1 cleavage.

Table 3.1 Catalytic parameters of Taspase target sequences at 37 °C.

	CS1 [Mca]-GKGQVDGADDK-[DNP]	**CS2** [Abz]-KISQLDGVDDK-[DNP]
K_m (μM)	18.4 ± 2.8	2.7 ± 0.1
v_{max} (μmol min^{-1} mg^{-1})	0.03 ± 0.003	0.11 ± 0.002
k_{cat} (s^{-1})	0.0274	0.083
k_{cat}/K_m (l mol^{-1} s^{-1})	1487	31190

[Mca]: 7-amino-4-methylcoumarin; [DNP]: dinitrophenol; [Abz]: anthranilic acid

3.3.3 Taspase activity in human cell lysates

Taspase levels in eukaryotic Hela, HEK and HCT 116 cells are low and therefore below detection levels the western blots performed in this project (supplemental figure 7.13). Consequently, Taspase levels had to be increased by overexpression. To allow a subsequent quantification of Taspase concentration, a GFP tag was added, which does not impair the catalytic activity [70]. This approach yielded Taspase concentrations of 370 nM in Hela cell lysates. Additionally, the assay temperature had to be lowered from 37 °C to 30 °C to prevent precipitation of the lysis buffer after supplemented with PMSF. To compare the activity of Hela lysates with overexpressed Taspase and Taspase isolated from *E. coli*, measurements were taken under identical conditions (figure 3.20).

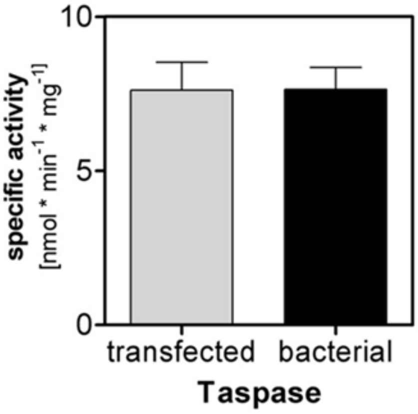

Figure 3.20 Specific activity of eukaryotic Taspase.

Specific activity at 30 °C in the presence of 8 µM substrate of Hela lysates with overexpressed Taspase-GFP fusion protein (transfected) and purified Taspase after heterologous bacterial expression (bacterial). Both Taspase species show a similar specific activity.

Hela lysates and Hela controls transfected with an empty PC3 vector showed no measurable Taspase activity (data not shown). In contrast, the lysate with overexpressed GFP-Taspase is able to cleave the substrate peptide. Compared with bacterially expressed and purified Taspase, the specific activity of overexpressed Taspase in Hela lysates is nearly identical.

3.3.4 Taspase inhibition test using NSC48300

With this assay in hands, the only available Taspase inhibitor NSC48300 described by Chen *et al*. [63], which has been controversially discussed [133], could be tested (figure 3.21).

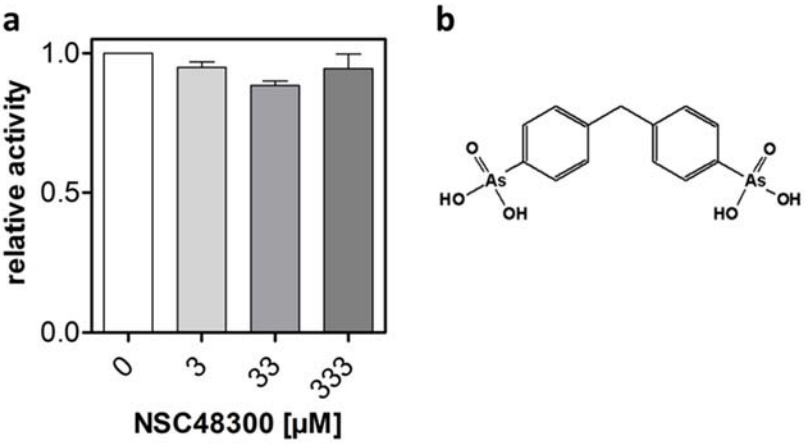

Figure 3.21 Inhibition test with the reported Taspase inhibitor NSC48300.

a The reported Taspase inhibitor NSC48300 exhibits no inhibitory activity at concentrations up to 333 µM, compared to DMSO controls. Note that the reported K_i is 4.22 µM. **b** Structure of NSC48300.

In the *in vitro* activity assay, the inhibitory effect observed by Chen *et al*. [63] could not be confirmed. NSC48300 yielded no decrease in catalytic activity, even at concentrations of 333 µM, which exceeds the reported K_i more than 70-fold. The presence and purity of NSC48300 was confirmed by ESI-LC-MS analysis (supplemental figure 7.14).

3.4 Exploration of Taspase inhibitors by virtual docking

In this project, different approaches were followed to find novel Taspase inhibitors. One of these approaches was a virtual docking of a large compound library. Subsequently, the top binding candidates were purchased and tested for inhibition *in vitro*. All tested candidates failed to exhibit an inhibitory effect.

3.4.1 Model preparation

Virtual docking basically requires two molecules, termed ligand and receptor. As receptor, two different states of Taspase were used: On the one hand the proenzyme, where binding of a small molecule could interfere with the autocatalytic activation process and, thereby, keep Taspase in the inactive proenzyme state and on the other hand the active Taspase protein, where a small molecule could inhibit the catalytic activity by blocking the active site.
In a first step, the missing loop areas were added to the monomers of the crystal structures (figure 3.22a) to include the N-terminus (M1-R40), the Taspase loop (A206-S229) and a short loop in the β-subunit (S352-Q362). The corresponding model quality statistics can be found in supplemental figure 7.15.

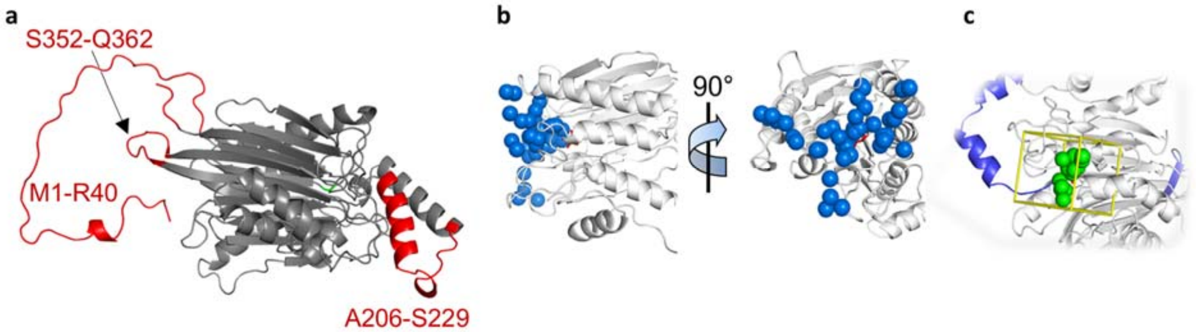

Figure 3.22 Preparation of Taspase models for virtual docking.

a Model of wild type Taspase proenzyme based on PDB 2a8i with missing loops (red) modeled. YASARA homology modeling was used to add the N-terminus (M1-R40), the Taspase loop (A206-229) and a short loop in the β-subunit (S352-Q362). These residues were not defined in the crystal structure. **b** Sphere cluster (blue) generated by sphgen. The cluster covers the catalytic Thr234 (red). **c** The active site (green) was surrounded with a cube (yellow), in which the energy grids were precomputed. In this area, the space was performed.

Partial charges were calculated with the help of Chimera [112] and suitable target areas for docking were identified by the sphgen algorithm (figure 3.22b). The area covering the site was selected as ligand binding site and in a cube with 30 Å edge length the energy grids for rigid docking were precomputed (figure 3.22c).

For the ligand database, a large variety of compounds and availability of the compounds for *in vitro* use was required. The ZINC database [129] met both criteria, with 12 million purchasable compounds available. To reduce the number of compounds to a reasonable amount for docking and still cover a maximum of different conformations, chemically different molecules were selected with the help of the SUBSET algorithm [130]. Only molecules which differ from all other by at least 60 % were used for docking. With this approach, the number of compounds was reduced from 12 million to 15865.

3.4.2 Virtual docking of ZINC database compounds

As a first step, the compounds of the ZINC database were treated as flexible and docked with an anchor-and-grow algorithm (section 2.6.3). Taspase residues within 5 Å of the active site were regarded as flexible, as well. This allowed a fast and yet sufficiently accurate exploration of several hundred different binding conformations for each compound. The free binding energy for the top pose of each ligand was computed with a precomputed grid, which includes van der Waals and electrostatic components. A distribution of the binding energies is shown in figure 3.23.

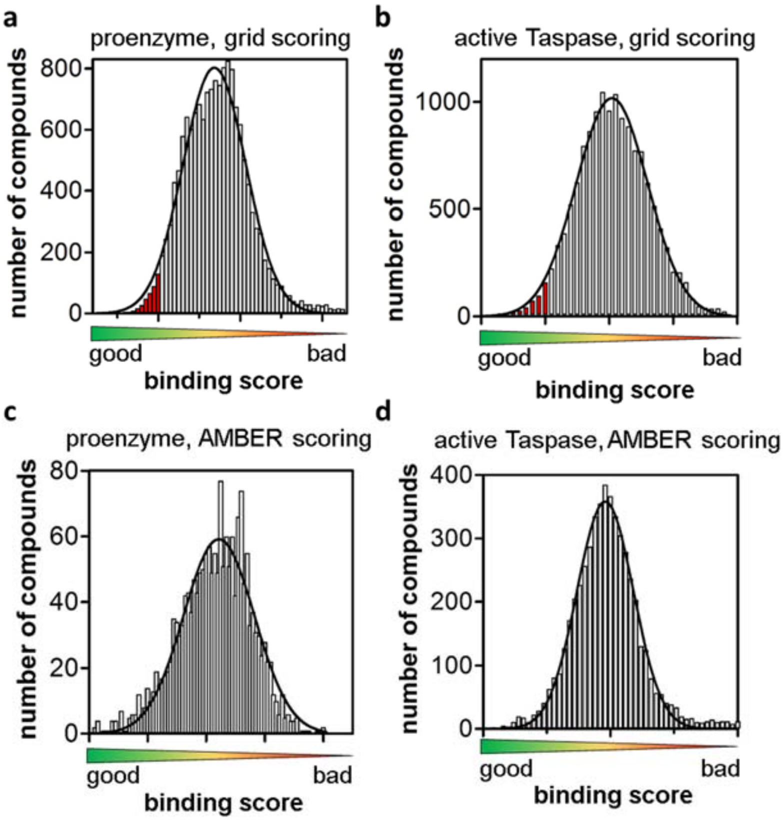

Figure 3.23 Energy distribution of the docked compounds.

a+b 15865 compounds of the ZINC database were docked on the proenzyme (**a**) or active Taspase (**b**) with an anchor-and-grow algorithm. A ranking of the free binding energies follows a Gaussian distribution (black lines). For compounds with binding energy below 40 kcal/mol (red), similar compounds were searched. **c+d** These similar compounds were docked in a second round on the proenzyme (**c**) or active Taspase (**d**) and an AMBER scoring function was used for ranking after a short MD simulation.

The sample size of 15865 compounds was large enough to obtain a Gaussian distribution of binding scores (figure 3.23a and b) with a mean binding energy of 26 kcal/mol for the proenzyme and 30 kcal/mol for the active Taspase. The best binding compounds were used for the subsequent docking round. As threshold, twice the standard deviation was used, which resulted in a cut-off binding energy of 40 kcal/mol. This criterion was met by 1 % of the proenzyme dataset and 2 % of the active Taspase dataset.

Since a filtered dataset was used, in which only compounds that differ from each other by at least 60 % were present, the data set of the top compounds was expanded by the inclusion of similar molecules. For this, the ZINC database was searched for compounds with at least 70 % similarity to the top compounds. This approach increased the number of compounds to 1925 (from 363 compounds for the proenzyme) and 7313 (from 1817 compounds for active Taspase) and ensured that derivatives of the top compounds were included in the next docking round.

To increase the reliability of the binding score, an energy minimization and short MD simulation was performed for each compound after docking, before the binding energy was calculated using an AMBER force field scoring. The scoring distributions for the proenzyme and active Taspase are shown in Figure 3.23c and d, respectively. Again, a Gaussian distribution is almost obtained indicating a sufficient sample size.

3.4.3 Inhibition tests with compounds obtained by virtual docking

For both datasets (proenzyme and active Taspase), the top poses of the modeled Taspase-inhibitor-complexes were inspected, the respective compounds were reviewed for toxicity and availability. Figure 3.24a and b shows the docked conformations of two top candidates found for the proenzyme, referred to as ZINC52513265 and ZINC19323748, respectively. Both compounds block the catalytic Thr234 (cyan in figure 3.24a and b) and have contact to the surrounding residues (pale orange in figure 3.24a and b).

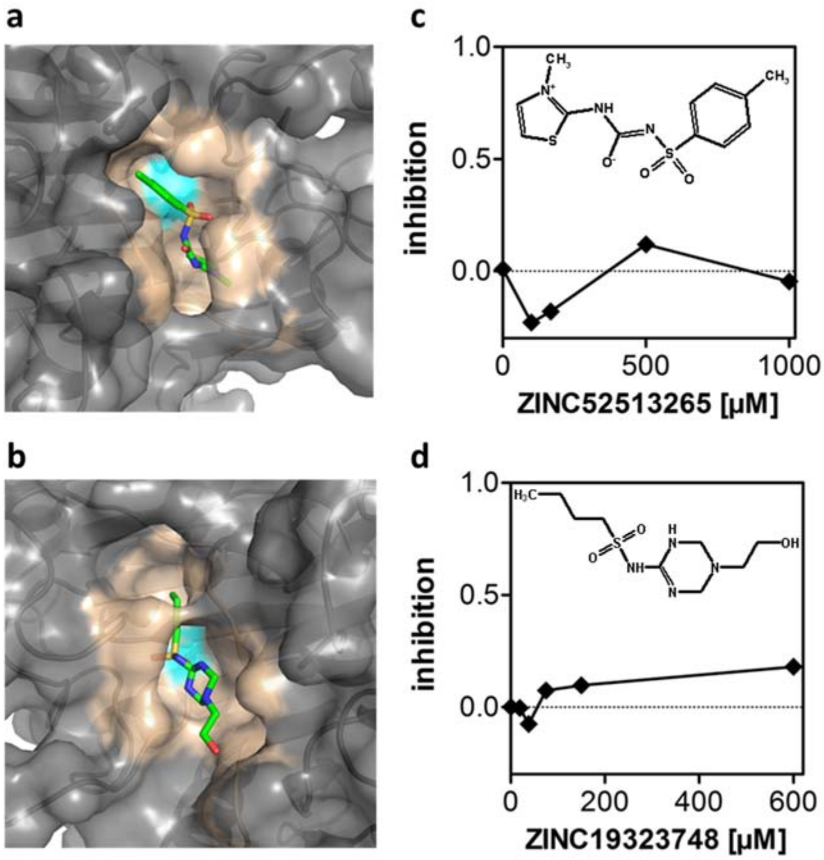

Figure 3.24 Docked conformation and inhibition test of putative proenzyme inhibitors.

a+b Docked poses of ZINC52513265 (**a**) and ZINC19323748 (**b**) with the proenzyme. The catalytic Thr234 is highlighted in cyan and interacting Taspase residues in pale orange. **c+d** Addition of ZINC52513265 (**c**) or ZINC19323748 (**d**) shows no significant inhibition of Taspase activity. The structures of the two compounds are inserted.

A shared feature of these two compounds is the sulfate group, which interacts with the Thr234. An overlay of the docked poses of the top ten compounds reveals that this interaction of a sulfate group with the Thr234 is a shared feature among these compounds (figure 3.25).

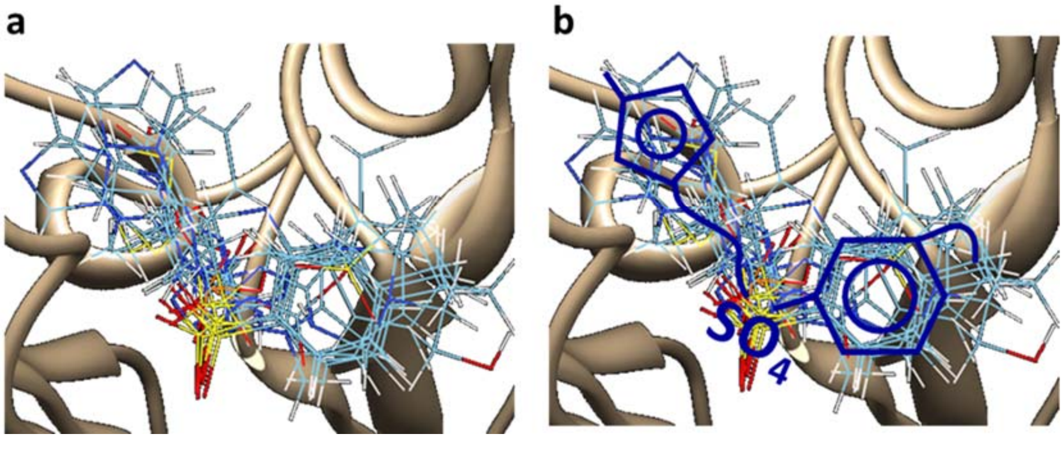

Figure 3.25 Shared features among top candidates.

a An overlay of the ten compounds with best binding scores reveals common features. **b** Additionally to a central sulfate moiety, two aromatic rings (5- and 6-membered) are present in most structures.

This common framework is diversified by different moieties at the aromatic rings and different linkers from the sulfate moiety to the rings. For this reason, two compounds were selected, which contain a central sulfate group but differ in most of the other moieties. These compounds were purchased, incubated at a concentration of 200 µM with Taspase for 6 h to allow an inhibition of the autocatalytic activation, and were tested in the fluorogenic assay. However, the proteolytic Taspase activity is not inhibited in presence of up to 1 mM ZINC52513265 (figure 3.24c) or 600 µM ZINC19323748 (figure 3.24d).

Evaluation of the best binding compounds in the dataset for active Taspase showed a more heterogeneous group of inhibitors than the proenzyme dataset. A sulfate group is present in some inhibitors, as well, but an overlay of the top inhibitors revealed no striking common framework. Hence, three compounds (ZINC63428205, ZINC21096526, and ZINC21096535) were selected randomly for *in vitro* analysis (figure 3.26a-c).

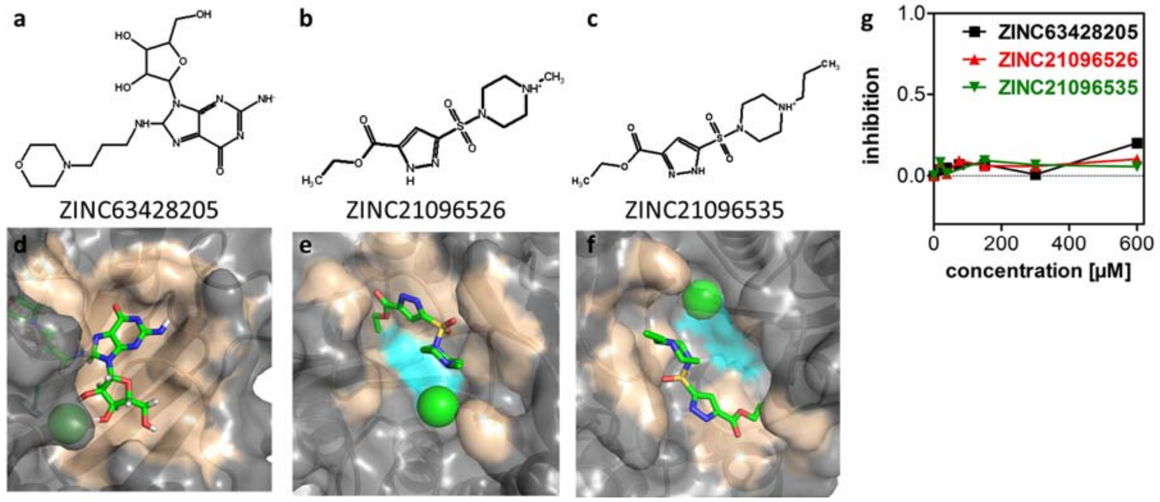

Figure 3.26 Docked conformation and inhibition of putative active Taspase inhibitors.

a-c Structures of ZINC63428205 (**a**), ZINC21096526 (**b**) and ZINC21096535 (**c**). **d-f** Docked poses of ZINC63428205 (**d**), ZINC21096526 (**e**) and ZINC21096535 (**f**) with active Taspase. The catalytic Thr234 is highlighted in cyan, interacting Taspase residues in pale orange and the chloride ion in green. **g** All three ZINC compounds exhibit no inhibitory effect in the Taspase activity assay.

All three compounds cage the chloride ion in the active site and do not directly interact with the catalytic Thr234 (figure 3.26d-f). Interestingly, the compounds shown in figure 3.26e and f cage the chloride ion at different positions, despite their close structural similarity. In the Taspase activity assay, however, all three compounds exert no inhibitory effect in concentrations up to 600 µM (figure 3.26g).

3.5 Inhibition of Taspase by nanoparticles

Recent studies disclosed binding of serum proteins to nanoparticles [99]. Furthermore, silica nanoparticles can inhibit the proteasome, the only other N-terminal nucleophile (Ntn) threonine protease (Shirley Knauer, personal communication). Hence, binding of Taspase to silica nanoparticles and their effect on the proteolytic activity was tested. Three different sizes of nanoparticles inhibited Taspase at low nanomolar concentrations, while the activities of three control enzymes were not impaired.

3.5.1 Nanoparticles bind and inhibit Taspase *in vitro*

Binding of Taspase to silica nanoparticles was observed in a preliminary experiment during a microscale thermophoresis (MST) demonstration course. Here, Taspase was added to nanoparticles with 8 or 125 nm diameter, and binding was observed label-free in solution (figure 3.27a).

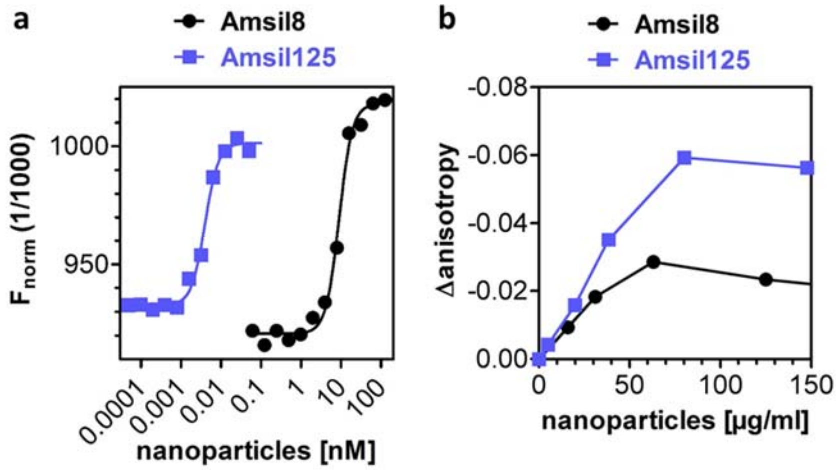

Figure 3.27 Nanoparticles bind Taspase.

a Microscale thermophoresis (MST) titrations reveal binding of Taspase to nanoparticles. For 8 nm (Amsil8) and 125 nm (Amsil125) silica nanoparticles EC_{50} values of 35 nM ± 0.5 nM and 10 pM ± 0.4 pM were obtained. **b** Fluorescence anisotropy titrations with 1 µM Atto488-labeled Taspase yield a stoichiometry of some 10 µmol/mg nanoparticles. This corresponds to roughly 5000 Taspase molecules per Amsil125 nanoparticle and 6 Taspase molecules per Amsil8 nanoparticle.

Both sizes of nanoparticles were able to bind Taspase with high affinity. The obtained EC_{50} concentrations were in the nanomolar range for Amsil8 (35 nM ± 0.5 nM) and in the picomolar range for Amsil125 (10 pM ± 0.4 pM). Active site fluorescence anisotropy titrations with Atto488-labeled Taspase confirmed the ranges of binding affinities detected by MST and displayed a higher change in anisotropy upon binding for Amsil125 than for Amsil8 due to the higher molecular weight. Based on these data, a stoichiometry of roughly 10 nmol per mg nanoparticles was calculated for both Amsil8 and Amsil125 (figure 3.27b). This corresponds to approximately six Taspase molecules bound per Amsil8 nanoparticle and 5000 Taspase molecules per Amsil125 nanoparticle. To explore possible consequences of nanoparticles for Taspase activity, this was tested in an *in vitro* assay (figure 3.28).

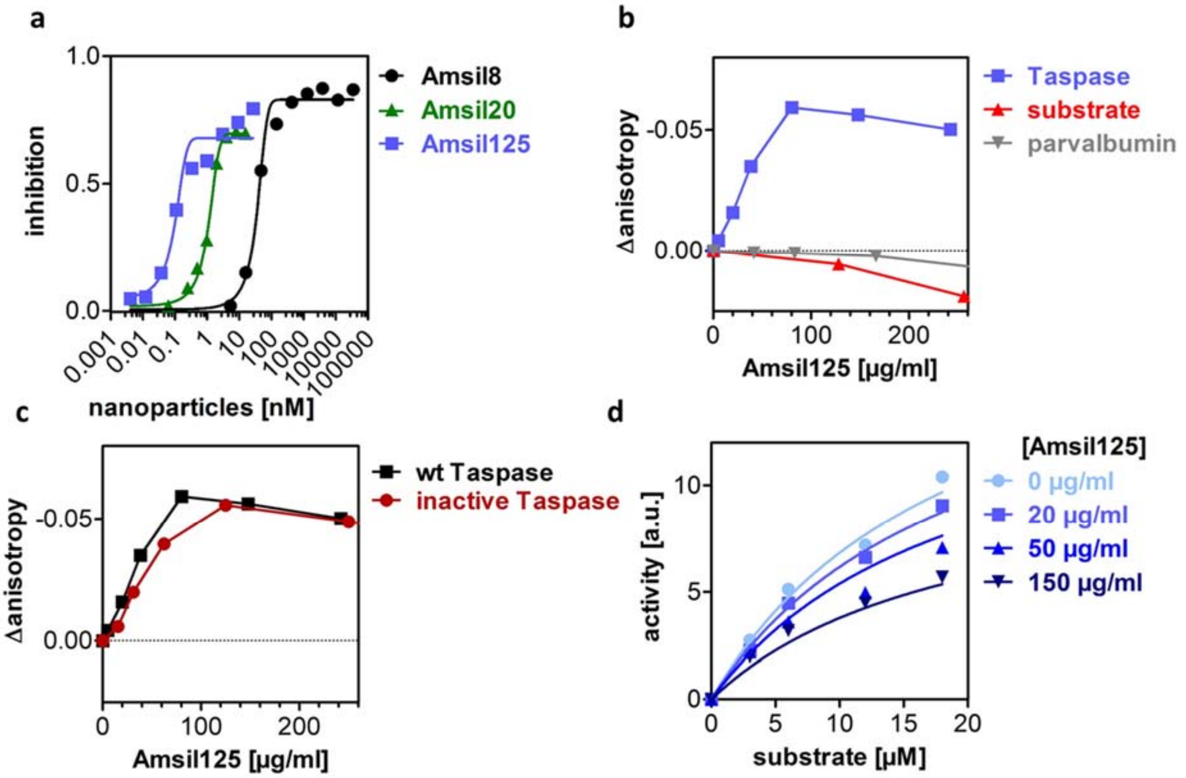

Figure 3.28 Nanoparticles inhibit Taspase activity noncompetitively.

a Silica nanoparticles with 8 nm (Amsil8) 20 nm (Amsil20) and 125 nm (Amsil125) diameter inhibit Taspase activity. EC_{50} values of 41 ± 9 nM, 1.4 ± 0.3 nM and 119 ± 21 pM were calculated for Amsil8, Amsil20 and Amsil125, respectively. **b** Fluorescence anisotropy of Atto488-labeled changes in the presence of Amsil125, while the anisotropy of the fluorogenic substrate and the Atto488-labeled control protein parvalbumin alters only marginally. **c** The change in anisotropy upon addition of Amsil125 nanoparticles is the same for wild type Taspase (wt) and the inactive Taspase mutant (red), indicating that they bind to nanoparticles in the same manner. Wild type and inactive Taspase proteins were labeled with Atto488. **d** Titrations with Amsil125 at different substrate concentrations pinpoint a noncompetitive inhibition mechanism (R^2 = 0.98). A K_i value of 380 ± 55 pM was calculated.

All three sizes of silica nanoparticles tested (8, 20 and 125 nm diameter) inhibited the Taspase activity already at low concentrations. As observed for binding to nanoparticles, the EC_{50} concentrations are negatively correlated with the nanoparticle diameter. Hence, Amsil125 has the highest affinity with 119 ± 21 pM, while Amsil20 and Amsil8 bind Taspase at nanomolar concentrations (EC_{50} = 1.4 ± 0.3 nM and 41 ± 9 nM, respectively).

However, nanoparticles would artificially lower Taspase activity, if they bind the fluorescent substrate and render it unavailable for Taspase cleavage. To this end, binding of the substrate to Amsil125 nanoparticles was analyzed by fluorescence anisotropy and compared to Taspase binding (figure 3.28b). Since only the anisotropy of Taspase changed in the presence of nanoparticles, while the anisotropy of the substrate remained virtually constant, binding of the substrate to nanoparticles can be excluded as an explanation for the inhibition of Taspase activity. Interestingly, the proenzyme binds to Amsil125 comparably to the wild type enzyme. For this experiment, the titration was performed with Atto488-labeled inactive Taspase mutant (figure 3.28c). Furthermore, the constant anisotropy of the Atto488-labeled control protein parvalbumin excludes an Atto488-dependent binding to nanoparticles. Only at high concentrations, a binding of parvalbumin to nanoparticles could be observed (supplementary figure 7.16). However, the EC_{50} value of 3 ± 0.8 µM determined for this interaction is 300 000-fold higher compared to Taspase.

To gain a first insight into the inhibitory mechanism, the inhibition type was determined for Amsil125 by a variation of both substrate and nanoparticle concentrations (figure 3.28d). Nonlinear fitting reveals a reversible noncompetitive inhibition with a K_i value of 380 ± 55 pM.

One possible explanation for the observed inhibition is a destabilization of Taspase by nanoparticles, which causes unfolding and thereby reduces the activity. Hence, the impact of nanoparticles on the secondary and tertiary structure of Taspase was analyzed. To this end, CD spectra were recorded to assess the secondary structure (figure 3.29a).

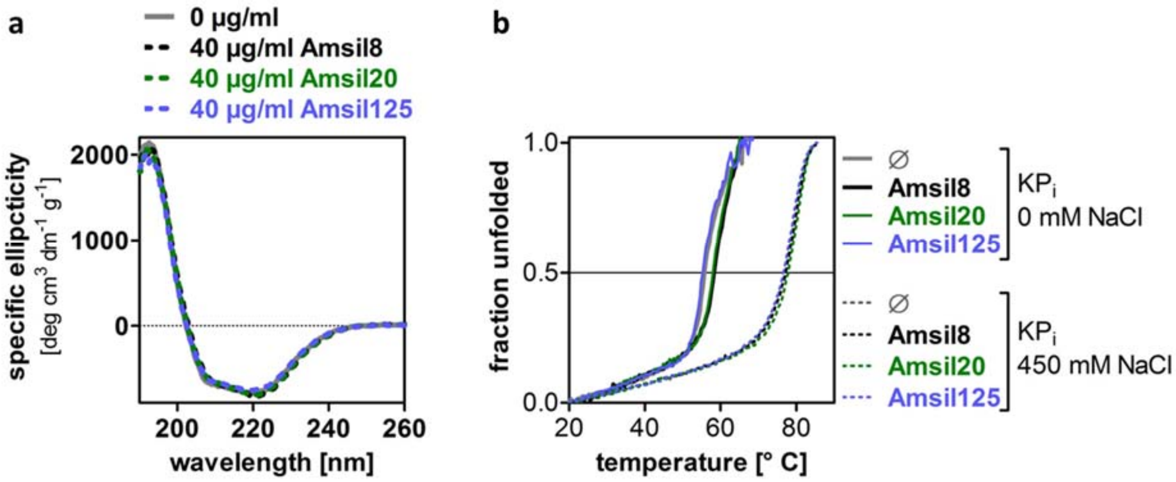

Figure 3.29 Nanoparticles do not alter secondary structure or stability.

a CD spectra in the presence of nanoparticles with 8 nm (Amsil8) 20 nm (Amsil20) and 125 nm (Amsil125) diameter show no change in secondary structure content of Taspase. **b** Tryptophan fluorescence melting curves reveal no alteration of Taspase stability. Melting points in phosphate buffer without NaCl (solid lines) are near 56 °C and with 450 mM NaCl near 77 °C (dashed lines), both in the presence and absence of 100 µg/ml nanoparticles with 8 nm (Amsil8) 20 nm (Amsil20) and 125 nm (Amsil125) diameter.

The obtained spectra in the presence and absence of nanoparticles are indistinguishable, indicating that neither nanoparticle type caused a change in secondary structure content at inhibitory concentrations of 40 µg/ml. However, a change in the tertiary structure, such as a movement or torsion of a whole subunit, cannot be excluded by these data.

Consequently, fluorescence tryptophan melting curves were recorded to get insight into the tertiary structure, as well as the overall folding state and stability of Taspase (figure 3.29b). As explicated in section 3.2.2, Taspase has a melting temperature near 56 °C and 77 °C in buffer without and with 450 mM NaCl, respectively. These values do not change in the presence of 100 µg/ml nanoparticles (= 266 nM Amsil8; 16 nM Amsil20; 204 pM Amsil125).

Taken together, these data argue against changes in secondary or tertiary structure and indicate that the inhibition by nanoparticles is not caused by a destabilization of Taspase.

3.5.2 Enzyme inhibition is no general feature of nanoparticles

So far, inhibition of enzyme activity could be not only restricted to Taspase, but instead be a general feature of nanoparticles. To test the hypothesis of a general inhibitory effect of nanoparticles on enzyme activity, three control enzymes were studied in activity assays, measuring either lactate formation by lactate dehydrogenase (LDH) or proteolytic activity of the serine endopeptidase chymotrypsin and of the serine endo- and exopeptidase proteinase K (figure 3.30).

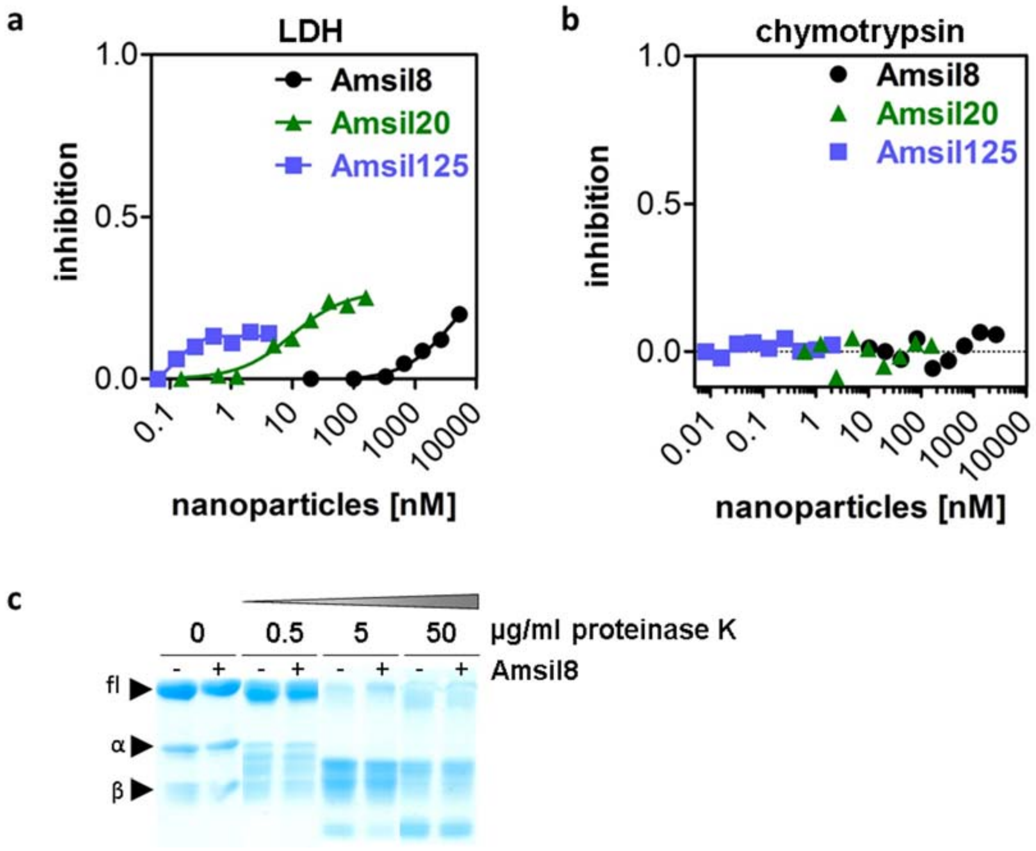

Figure 3.30 LDH, chymotrypsin and proteinase K are weakly inhibited by nanoparticles.

a Lactate dehydrogenase (LDH) activity was assayed in the presence of silica nanoparticles with 8 nm (Amsil8) 20 nm (Amsil20) and 125 nm (Amsil125) diameter. Amsil8 shows weak inhibition at high concentrations (3 mg/ml). Amsil20 inhibits the activity by up to 25 % with a nanomolar EC_{50}. Amsil125 reduces the activity by up to 15 %. **b** Chymotrypsin activity is not inhibited by nanoparticles with 8 nm (Amsil8) 20 nm (Amsil20) and 125 nm (Amsil125) diameter. **c** Proteinase K activity is not influenced in the presence of 100 µg/ml Amsil8. For concentrations between 0.05 and 50 µg/ml proteinase K, the digestion pattern does not change in the presence of nanoparticles. fl, α and β represent the size of full-length Taspase, α- and β-subunit, respectively.

Amsil125 inhibits LDH activity by up to 15 % at low nanomolar concentrations (figure 3.30a; blue). Higher concentrations cause no further reduction of LDH activity. For Amsil20, inhibition is not seen in the picomolar range, where Taspase is already significantly inhibited. However, higher concentrations can reduce LDH activity by up to 25 %. Similarly, micromolar concentrations of

Amsil8 are required to inhibit LDH activity by 10 %, which is two orders of magnitude more than for Taspase with an EC_{50} value of 41 nM.

Concerning the second control enzyme chymotrypsin, the enzymatic activity is not altered by nanoparticles (figure 3.30b). Neither of the nanoparticles could reduce the proteolytic activity, even if the concentrations exceeded the EC_{50} of Taspase by two orders of magnitude.

To assay the activity of the third control enzyme proteinase K, the Taspase digestion pattern was analyzed by SDS-PAGE after limited proteolysis by proteinase K (figure 3.30c). The digestion bands below both the full-length enzyme and the two subunits indicate that high concentrations of proteinase K can degrade all three Taspase species. A comparison of the degradation pattern in the presence and absence of 100 µg/ml Amsi8 reveal no inhibition for all 11 proteinase K concentrations tested.

3.5.3 Nanoparticles inhibit Taspase in cell lysates and in cells

Studies with three control enzymes indicated that inhibition of enzyme activity seemed to be no general feature of nanoparticles. Hence, the selective inhibition of Taspase activity by nanoparticles could also be possible in cell lysates. This hypothesis was tested in Hela cell lysates with overexpressed GFP-Taspase (figure 3.31).

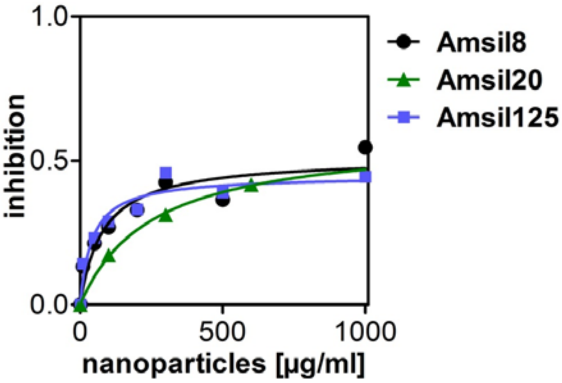

Figure 3.31 Nanoparticles inhibit Taspase activity in cell lysates.

Taspase activity was assayed in Hela cell lysates in the presence of nanoparticles with 8 nm (Amsil8) 20 nm (Amsil20) and 125 nm (Amsil125) diameter. Nonlinear fitting yielded EC_{50} values of 80 ± 34 µg/ml (= 213 ± 90 nM) for Amsil8, 251 ± 24 µg/ml (= 40 ± 4 nM) for Amsil20 and 42 ± 15 µg/ml (= 86 ± 31 pM) for Amsil125.

One striking finding is that nanoparticles reduce Taspase activity only by up to 50 % in lysates. Moreover, the EC_{50} values (40-250 µg/ml) are somewhat higher than for pure Taspase (8-60 µg/ml), which additionally reduces the inhibitory effect in cell lysates.

However, the inhibitory concentrations in lysates were still in the nanomolar and sub-nanomolar range. Since nanoparticles can be taken up by cells [99], the consequent experiment was to test the effect of nanoparticles on cellular Taspase activity. This endeavor required a cell-based activity assay, in which a fluorescent reporter substrate, called BioTasp [71], with nuclear import and export sequences was used (figure 3.32a).

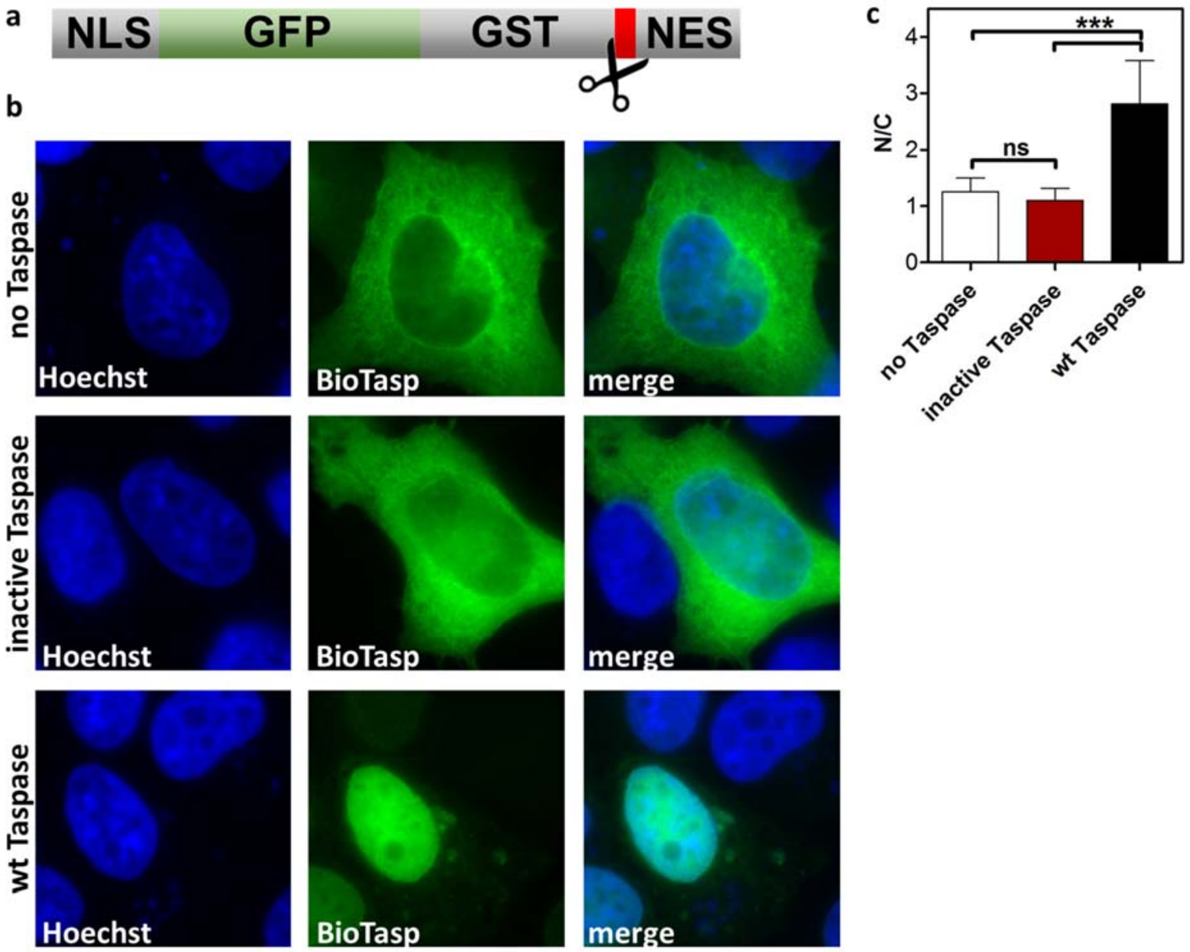

Figure 3.32 Cellular Taspase activity assay.

a The BioTasp reporter substrate comprises an N-terminal nuclear localization signal (NLS) eGFP (green), glutathione S-transferase (GST), Taspase cleavage sites (red; scissors) and a reverse nuclear export signal (NES). **b** BioTasp (green; second column) is found equally distributed in nucleus and cytoplasm in Hela cells without Taspase (first row) and Hela cells transfected with inactive Taspase (second row) due to the presence of both nuclear localization and export signal (NLS and NES, respectively). Nuclei were stained with Hoechst (blue; first column). In the presence of wild type Taspase (wt Taspase; third row), the nucleus export signal (NES) is cleaved and the nuclear localization signal (NLS) causes an accumulation of BioTasp in the nucleus. **c** Statistical analysis shows no significant (ns) difference in the nucleus to cytoplasm ratio (N/C) of BioTasp between untransfected cells and cells with inactive Taspase. In contrast, the N/C ratio is significantly higher in cells with wild type Taspase. 50 cells from 3 independent experiments were counted. *** indicate *p*-values < 0.001.

BioTasp contains a green fluorescent protein (GFP) fused to a GST to prevent passive diffusion through the nuclear pores. The sensor shuttles between nucleus and cytoplasm by its NLS and NES. Due to a well-considered combination of signal strength, the steady state of the sensor is an even distribution throughout the cell (figure 3.32b). The localization of BioTasp changes, if Taspase is overexpressed. Taspase cleaves BioTasp at the integrated CS2 cleavage site from MLL and removes the NES, which leads to an accumulation of BioTasp in the nucleus. Controls with overexpressed inactive Taspase show a distribution similar to cells without Taspase. Statistical evaluation confirmed a significantly increased nuclear localization in cells with wild type Taspase compared to cells with inactive or no Taspase (figure 3.32c; N/C ratios for no Taspase: 1.25 ± 0.03, inactive Taspase: 1.03 ± 0.03, wild type Taspase: 2.81 ± 0.1).

With this assay, the silica nanoparticles of 8, 20 and 125 nm diameter were tested. For this, cells were challenged with 200 µg/ml nanoparticles 3 hours after transfection. The presence of nanoparticles had no visible effect on the cell viability or morphology (supplementary figure 7.17). The BioTasp localization was analyzed after 18 hours incubation (figure 3.33).

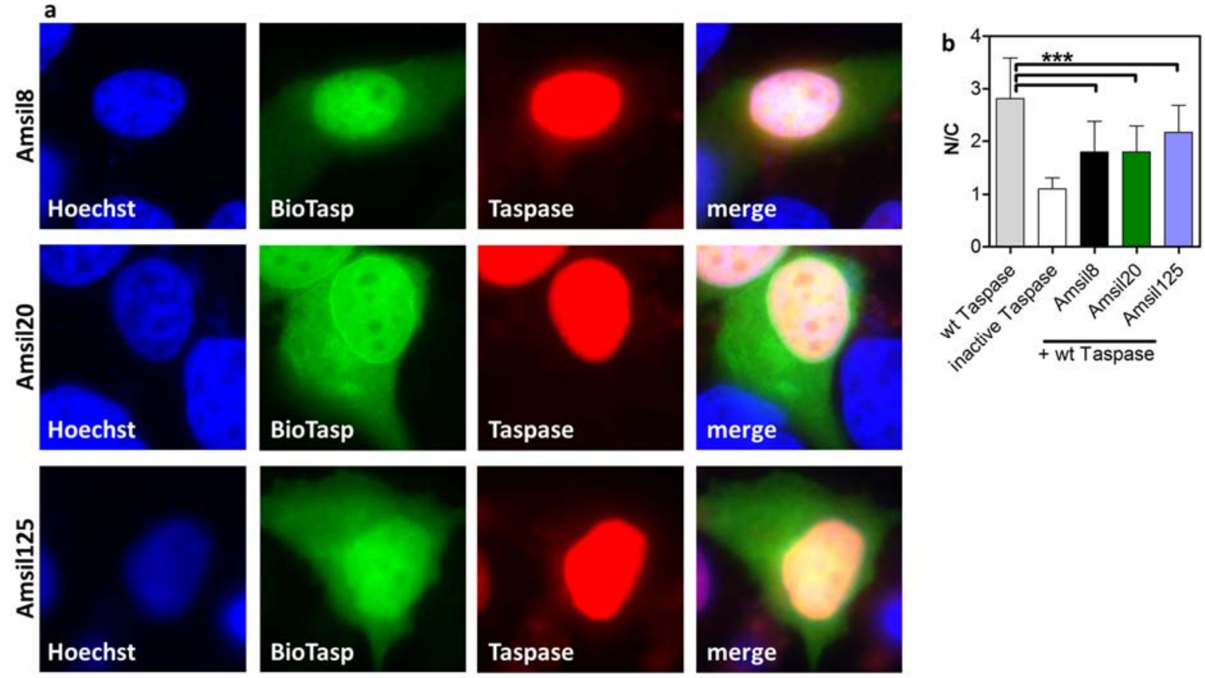

Figure 3.33 Nanoparticles inhibit Taspase activity in cells.

a Hela cells transfected with Taspase (red; mCherry) and the BioTasp reporter substrate (green; GFP) were stained with Hoechst (blue) after treatment with 200 µg/ml Amsil8 (first row), Amsil20 (second rwo) or Amsil125 (third row) for 18 h. The equal distribution of the green BioTasp reporter substrate indicates low Taspase activity in presence of nanoparticles. Hoechst, GFP and mCherry channels are displayed separately in columns 1-3, respectively, and merged in column 4. **b** Statistical analysis of the nuclear to cytoplasm ratio (N/C) shows a significantly reduced N/C ratio in the presence of nanoparticles compared to untreated controls. 50 cells from 3 independent experiments were counted. *** indicate *p*-values < 0.001.

Figure 3.33a shows an even distribution of BioTasp throughout the whole cell after nanoparticle challenge. The red fluorescence confirms the successful overexpression of wild type Taspase and its perfect overlap with the Hoechst staining indicates an exclusively nuclear localization. Statistical evaluation reveals that all three types of nanoparticles significantly reduce the nuclear localization of BioTasp to a level midway between cells with wild type and inactive Taspase (figure 3.33b). Since the control cells with wild type Taspase can be regarded as 100 % activity and the cells with inactive Taspase as 0 % activity, nanoparticles reduce the Taspase activity in cells by roughly 50 % at 200 µg/ml. Furthermore, the inhibitory effect of Amsil125 seems to be somewhat lower compared to Amsil8 and Amsil20.

In summary, inhibition of Taspase activity in cell lysates and cells was observed for all three nanoparticles at nanomolar concentrations.

3.6 Inhibition of Taspase by peptidyl-succinimidyl peptides

Besides nanoparticles and compounds obtained by virtual docking, substrate analog Taspase inhibitors designed by Prof. Markus Kaiser were tested in this project. Starting point for this endeavor was the proteolytic cleavage mechanism proposed by the Bogyo group [69]. This mechanism involves the formation of a succinimide-hydrate intermediate (figure 3.34), which facilitates the peptide bond transfer of the protein backbone to the aspartate side chain of the substrate.

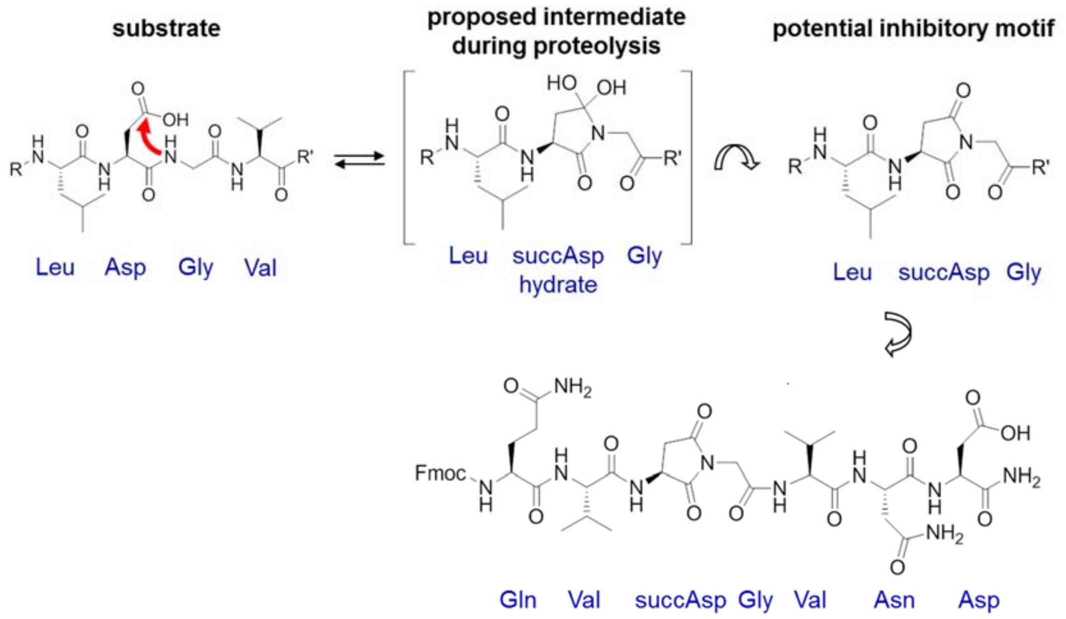

Figure 3.34 Design of the peptidyl-succinimidyl peptide.

In the proposed cleavage mechanism [69], the aspartate side chain attacks the following glycine (red arrow). This reaction yields a succinimide-hydrate intermediate (top panel; succAsp hydrate), which was used as starting point for substrate analog Taspase inhibitors. The potential inhibitor motif peptidyl-succinimidyl (succAsp) is shown in the top right panel. In the test compound Comp2 (bottom panel), the Leu at P2 was substituted by Val to reduce the polarity. The Fmoc protection group was left for detection by UV absorption. This figure was taken from [134].

The novel class of substrate analog inhibitors developed for this thesis features a succinimide moiety (figure 3.34). Optimization of the initial inhibitors yielded the most potent Taspase inhibitor so far with a K_i of 0.4 ± 0.1 µM *in vitro*. Moreover, this compound was active in cell lysates, albeit the affinity is 30-fold attenuated. Furthermore, the developed inhibitors can enter the cell, however, the achieved intracellular concentrations were too low for a measurable inhibition of Taspase activity. This project was accomplished in cooperation with the Kaiser group, who designed and synthesized the compounds.

3.6.1 Peptidyl-succinimidyl peptides inhibit Taspase *in vitro*.

The peptidyl-succinimidyl peptides were synthesized by the Kaiser group using Fmoc/*t*Bu solid phase peptide synthesis. Leaving the N-terminal fluorenylmethyloxycarbonyl (Fmoc) group on the final product allowed an exact spectroscopic determination of the concentration. However, this additional aromatic moiety could change the inhibitory properties of the compound. To rule out an inhibition by the Fmoc group, the inhibitory effect of Fmoc-valine (Comp1) was tested in the *in vitro* assay (supplemental figure 7.18a). This titration resulted in a negligible effect on Taspase activity, even at high Fmoc-Val concentrations.

In the next step, the designed inhibitor (figure 3.34) as well as eight derivatives were titrated to determine IC_{50} and K_i values (table 3.2 and supplemental figure 7.18).

Table 3.2 Inhibitory potential of the succinimidyl peptides and their derivatives.
Deviations from the common inhibitor scaffold are highlighted in yellow.

Compound	Sequence*	IC_{50} [µM]	K_i [µM]
Comp1	Fmoc-Val	> 1000	n.d.
Comp2	Fmoc-Gln-Val-succAsp-Gly-Val-Asn-Asp-NH2	38.7 ± 12.1	4.3 ± 1.3
Comp3	Fmoc-Gln-Val-piperidineAsp-Gly-Val-Asn-Asp-NH2	30.1 ± 10.6	3.3 ± 1.2
Comp4	Fmoc-Gln-Val-allocAsp-Gly-Val-Asn-Asp-NH2	143 ± 39	15.9 ± 4.3
Comp5	Fmoc-Gln-Val-succAsp-βAla-Val-Asn-Asp-NH2	61 ± 9.5	6.8 ± 1.1
Comp6	Fmoc-Gln-Val-succGlu-Gly-Val-Asn-Asp-NH2	14.4 ± 2.8	1.6 ± 0.3
Comp7	Fmoc-Gln-Val-Asp-Gly-Val-Asn-Asp-NH2	> 1000	n.d.
Comp8	Fmoc-Gln-Val-isoAsp-Gly-Val-Asn-Asp-NH2	424 ± 58	47 ± 6.4
Comp9	Fmoc-Prg-Bpa-Gln-Val-succAsp-Gly-Val-Asn-Asp-NH2	3.6 ± 0.8	0.4 ± 0.09
Comp10	Rhd-Gln-Val-succAsp-Gly-Val-Asn-Asp-NH2	373 ± 23	41 ± 2.6

* Fmoc: fluorenylmethyloxycarbonyl; succAsp: succinimide; piperidineAsp: Asp with piperidine protection group; allocAsp: Asp with alloc protection group; βAla: β-alanine; succGlu: glutarimide; isoAsp: isoaspartate; Prg: propargyl glycine; Bpa: benzophenone alanine; Rhd: rhodamine B

Comp2 exhibited a promising inhibitory effect in the low micromolar range (K_i = 4.3 ± 1.3 µM). To ensure that the inhibitor was not simply used as competitive substrate and cleaved by Taspase, the succinimide moiety was omitted, yielding a peptidic Taspase substrate (Comp7 in table 3.2). In contrast, this compound was degraded without a reduction of Taspase activity. This indicates that Comp7 is degraded rapidly, while the succinimide moiety in Comp2 truly acts as an inhibitor and cannot be degraded by Taspase.

During synthesis, a side product with an LC-MS mass equivalent to a piperidine addition product could be isolated (Comp3). Although not further analyzed, this compound was presumably generated by an addition of piperidine to the succinimide residue. The K_i and IC_{50} values of Comp3 are similar to those of Comp2 (K_i = 3.3 ± 1.2 µM). Another side product occurring during synthesis displayed an LC-MS mass corresponding to a compound with alloc-protected Asp (Comp4). However, compared with Comp3, the inhibitory effect of Comp4 was fivefold lower (K_i = 15.9 ± 4.3 µM).

In the proposed cleavage mechanism [69], the protein backbone of the substrate is transferred to the aspartate side chain, forming an isoaspartate intermediate (figure 3.35).

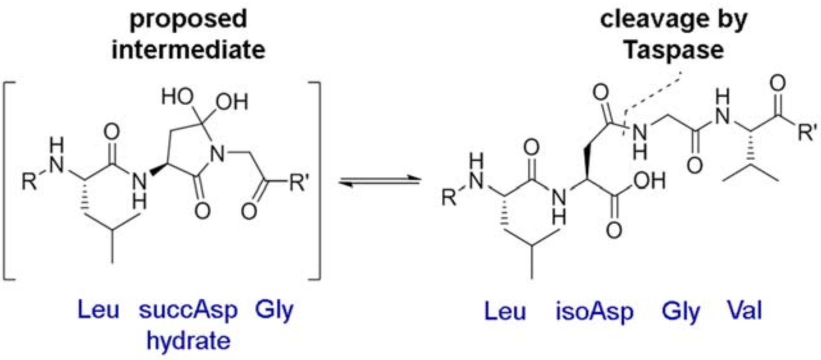

Figure 3.35 Isoaspartate intermediate during proteolysis.

In the proposed catalytic mechanism, the succinimide-hydrate intermediate (succAsp hydrate) is used to transfer the protein backbone to the aspartate side chain. This yields an isoaspartate (isoAsp), which is needed for Taspase cleavage.

To test if isoaspartate can truly be cleaved by Taspase or inhibits the reaction, a substrate with isoaspartate instead of aspartate was synthesized (Comp8). This compound exhibited a tenfold weaker inhibition of Taspase than the succinimide compound Comp2 (IC_{50} = 424 ± 58 µM), which excluded isoaspartate as inhibitory moiety for Taspase.

For further improvement of the binding affinity, the role of the S' site of Taspase for inhibitor binding was explored. To this end, the P' residue glycine was replaced by β-alanine (Comp5). This small structural change caused a minor reduction of the binding affinity (K_i = 6.8 ± 1.1 µM).

For an extension of the 5-membered succinimide ring to a 6-membered ring, the succinimide was replaced by a glutarimide (Comp6). This change slightly improved the affinity to a K_i of 1.6 ± 0.3 µM.

The most promising compound was the photoreactive inhibitor Comp9, which possesses an additional N-terminal benzophenone as well as a propargyl glycine group. With a K_i in the nanomolar range (0.4 ± 0.09 µM) this compound showed a tenfold higher inhibitory potential than the best published Taspase inhibitor. Binding of Comp9 was confirmed by microscale thermophoresis (MST) as alternative method (figure 3.36a).

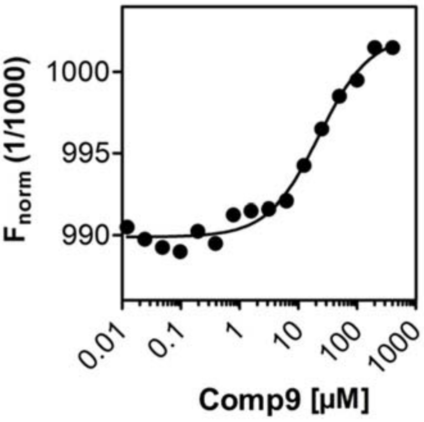

Figure 3.36 Binding of the peptidyl-succinimidyl peptide inhibitors.

Binding of Comp9 was verified by microscale thermophoresis (MST) titrations. A K_d value of 22.1 ± 0.6 µM was obtained.

In contrast to the activity assay, MST allows the determination of binding constants in the presence of NaCl. Hence, the MST measurements were performed in the presence of 450 mM NaCl to maintain Taspase stability. This procedure allows inspecting if the inhibitor binds in the active site and competes with the chloride ion, which was found in the active site [56].

A comparison of the affinity of Comp9 in the presence (22.1 ± 0.6 µM; MST) and absence of NaCl (0.4 ± 0.09 µM; activity assay) reveals 50-fold weaker binding in the presence of NaCl. This finding supports that binding is competitive with respect to chloride. This was also found for the substrate, indicating a similar binding mode of substrate and inhibitor.

3.6.2 Peptidyl-succinimide peptides are resistant against Taspase cleavage

To verify the competitive type of inhibition, Taspase inhibition by Comp2 was assayed in the presence of different substrate concentrations (figure 3.37a). Nonlinear fitting of the data with a model for competitive inhibition confirms that Comp2 truly acts as a reversible competitive inhibitor.

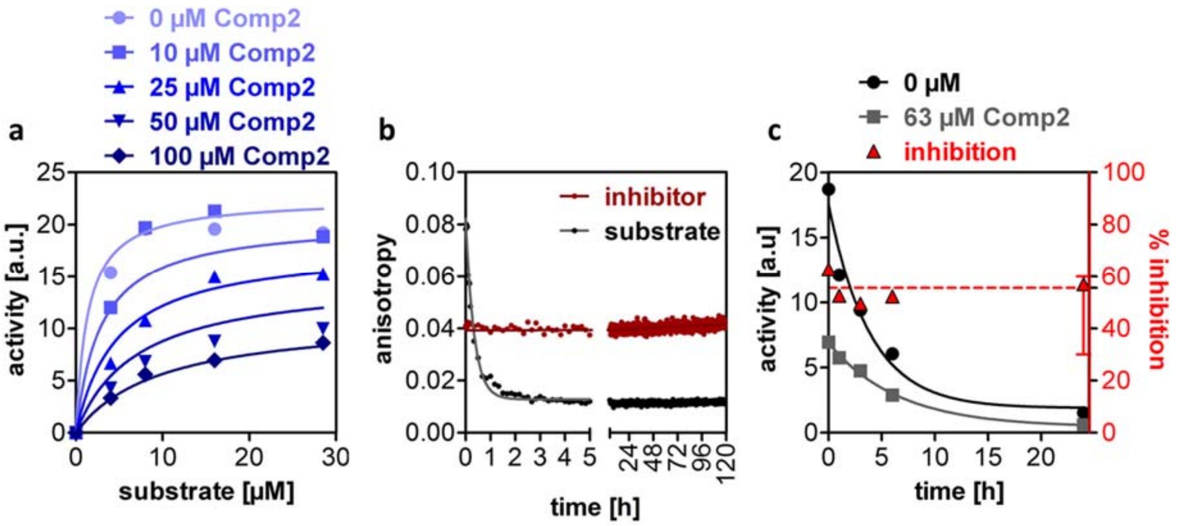

Figure 3.37 Stability of competitive peptidyl-succinimidyl peptides.

a Competitive inhibition of peptidyl-succinimidyl peptides was confirmed with Comp2. A K_i of 2.5 ± 2 µM was obtained by nonlinear fitting. **b** Rhodamine-labeled inhibitor was incubated with 1 µM Taspase to assay stability. The inhibitor shows no decrease in anisotropy, while the anisotropy of the substrate control drops due to cleavage. **c** Taspase was incubated with and without 63 µM Comp2, before activity was assayed. The calculated inhibition reflects the ratio of the activities in the presence and absence of the inhibitor after certain incubation times. Constant inhibition by roughly 60 % indicates a sufficiently high stability of the inhibitor against degradation. Bars indicate standard errors.

Competitive inhibition of a protease, however, carries the risk of proteolytic degradation of the inhibitor due to its substrate analog nature. Hence, the stability of the succinimide motif against Taspase mediated proteolysis was tested. This required the synthesis of a fluorescent derivative of the inhibitor (Comp10). Although the incorporation of a bulky rhodamine dye reduce the K_i twentyfold (K_i = 41 ± 2.6 µM), the affinity was still sufficiently high for stability tests. The fluorescent dye allowed following the degradation over time by fluorescence anisotropy (figure

3.37b). The anisotropy obtained for Comp10 in the presence of Taspase was constant over 5 days. In contrast, the anisotropy of the substrate drops rapidly due to proteolytic cleavage.

To exclude an influence of the fluorescent dye attached to Comp10, Taspase was incubated with 63 µM Comp2, and the activity was assayed after defined times (figure 3.37c). The initial inhibition by roughly 60 % remained constant even after incubation for 24 hours. However, the overall Taspase activity was reduced over time due to the instability of Taspase in the assay buffer (see section 3.2.2).

Altogether, these experiments demonstrate the stability of peptidyl-succinimide inhibitors against proteolytic cleavage by Taspase.

3.6.3 Peptidyl-succinimide peptides bind and inhibit Taspase in cell lysates

The next step towards *in vivo* experiments was to test the inhibitory potential of the developed peptidyl-succinimide peptides in cell lysates. To this end, Hela cell lysate was supplemented with recombinant Taspase and incubated with the photoreactive compound Comp9. Irradiation with UV light cross-linked the inhibitor with the bound protein. A subsequent addition of a rhodamine azide via click reaction allowed visualization by fluorescence imaging (figure 3.38).

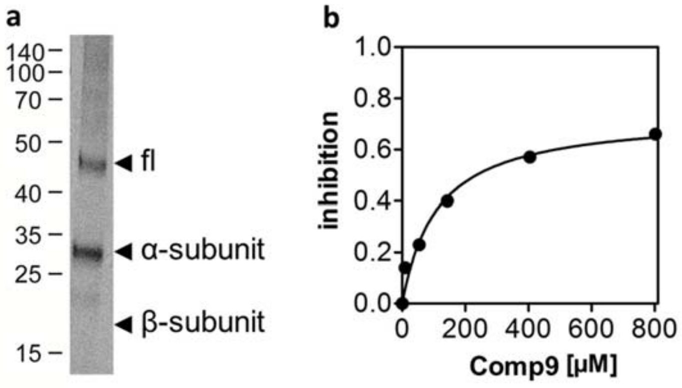

Figure 3.38 Photolabeling and lysate inhibition with peptidyl-succinimide peptides.

a Taspase (5 µM) was added to Hela cell lysates and subsequently cross-linked with 5 µM of the UV-reactive Comp9 inhibitor. A click reaction with rhodamine amide allowed detection via fluorescence. The α-subunit and the band for the full-length (fl) Taspase are visible in the gel, but not the β-subunit. Cross-linking, click reaction and fluorescence gel imaging was performed by Susanne Zweerink, Kaiser group. **b** Comp9 inhibits the activity of overexpressed Taspase in Hela lysates with an IC_{50} of 111 ± 30 µM.

The fluorescent bands at 45 kDa and 28 kDa correspond to full-length Taspase and the α-subunit, respectively. This indicates that the inhibitor binds to the α-subunit of Taspase, while no interaction with the β-subunit is visible. Furthermore, no interaction above background with other proteins in the lysate was observed. However, the comparatively high concentration of recombinant Taspase (5 µM) added to the lysates should be considered in the interpretation of this finding.

The inhibitory potential was assayed in Hela lysates transfected with GFP-Taspase. The assay was performed in lysis buffer containing 150 mM NaCl. Under these conditions, the inhibition is roughly 30-times weaker (IC_{50} = 111 ± 30 µM) than for recombinant Taspase in the *in vitro* assay.

3.6.4 Peptidyl-succinimidyl peptides enter the cell

Although the molecular weight of the peptidyl-succinimide peptides of nearly 1 kDa is rather large to enter the cell, their ability to cross the cell membrane was tested. For this, Hela cells were treated with the fluorescent compound Comp10. After defined incubation times, the cells were washed and the intracellular fluorescence was used as a measure for cellular uptake of the compound (figure 3.39a-c).

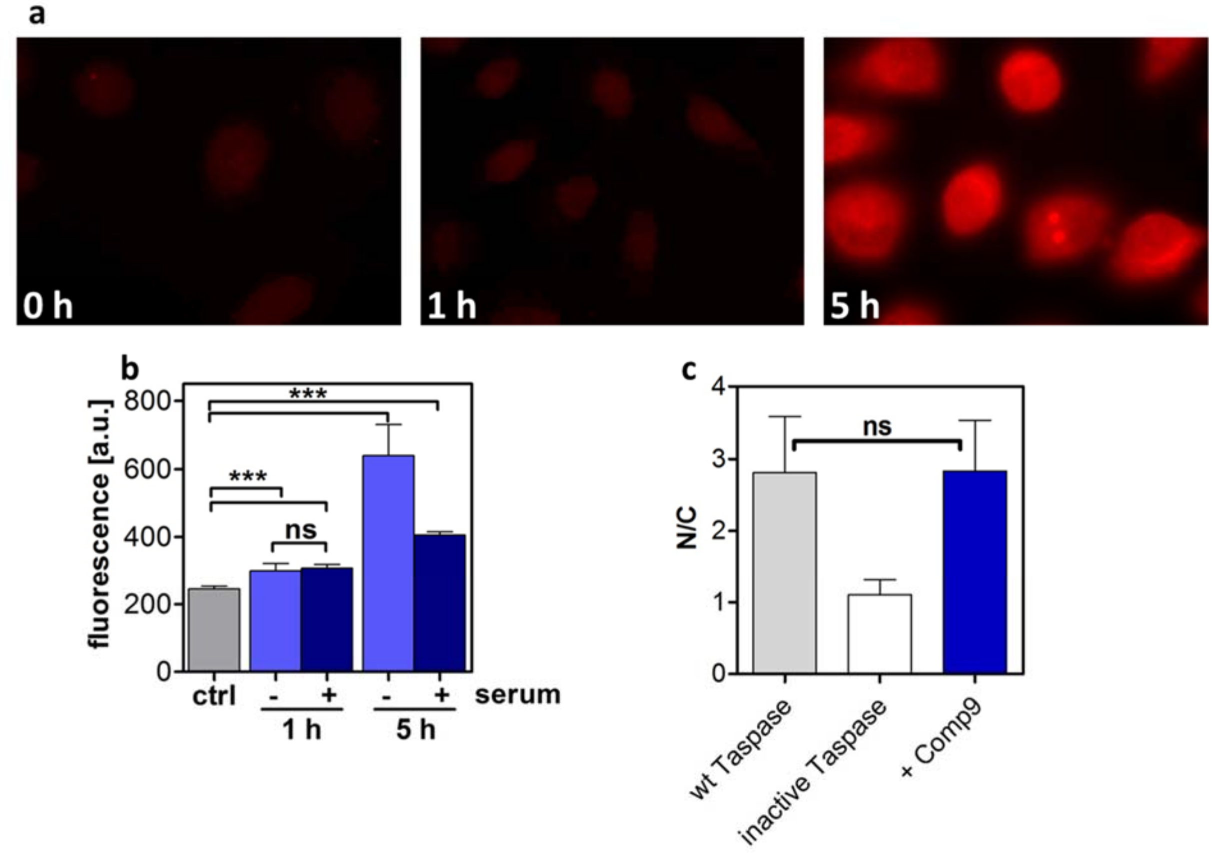

Figure 3.39 The peptidic inhibitors enter the cell but exhibit no Taspase inhibition.

a The fluorescence labeled peptidic inhibitor can enter Hela cells. The intracellular fluorescence intensity is increased after 1 h (middle panel) and 5 h (right panel) compared to the background intensity (left panel). **b** Statistical analysis confirms elevated fluorescence due to inhibitor entry after 1 and 5 hours. The inhibitor uptake is increased by incubation in the absence of serum. **c** Hela cells treated with 50 µM Comp9 for 20 h show no significant (ns) inhibition of Taspase activity in comparison to untreated cells (wt Taspase). In this cellular Taspase activity assay, the nucleus to cytoplasm ratio (N/C) corresponds to the Taspase activity. 20 (**c**) or 50 (**e**) cells from 3 independent experiments were evaluated. *** indicate *p*-values < 0.001.

Untreated Hela cells show a very low background fluorescence in the RFP channel (figure 3.39a). After treatment for 5 hours with the peptide, the cells show a distinct red fluorescence evenly distributed throughout the cell, indicating a cellular uptake of the fluorescent inhibitor. Statistical evaluation of the samples reveals that the increase in fluorescence is highly significant (figure 3.39b). Even after incubation for 1 hour, the cells display an increased fluorescence, which is not visible by eye (figure 3.39a). Notably, the incubation in serum-free medium increased the uptake of the inhibitor more than twofold in the samples treated for 5 hours. With fluorescence microscopy, a determination of the intracellular concentration of the inhibitor was not possible. Therefore, the uptake could only be confirmed qualitatively.

Nevertheless, the inhibitory effect of the peptidyl-succinimide inhibitor was tested in Hela cells using a cell-based activity assay (section 3.5.3). To this end, Hela cells were treated with 50 µM Comp9 for 18 hours, before cells were fixated and the localization of the reporter substrate was evaluated (figure 3.39c). However, cells treated with Comp9 displayed the same Taspase activity as untreated cells.

In summary, the peptidyl-succinimide peptides successfully inhibited recombinant Taspase and cell lysates, but showed no inhibitory effect in the cellular activity assay despite cellular uptake of the compounds.

4 Discussion

Proteolytic activation is a common regulatory mechanism for various cellular processes. In the case of a t(4;11) translocation, Taspase is the key enzyme for the proteolytic activation of the oncogenic MLL protein. Consequently, inhibition of Taspase could prevent the malignant transformation of cells with t(4;11) translocation and probably also solid tumors.

For the development of new inhibitors, a detailed understanding of the biochemical properties, the catalytic mechanism and the structure of the target enzyme are of tremendous value. Therefore, Taspase was subjected to extensive biochemical characterization with respect to structure, stability, autocatalytic activation, posttranslational modification and substrate specificity. With this knowledge, novel Taspase inhibitors were evaluated *in vitro*, in cell lysates and in cells. This approach yielded two novel classes of Taspase inhibitors: Silica nanoparticles and substrate analog succinimide peptides.

4.1 Taspase is a unique protease and requires unique inhibitors

Taspase belongs to the type II asparaginase family and shares the typical αββα asparaginase fold, an autocatalytic activation process, as well as an N-terminal nucleophile (Ntn) at the β-subunit. However, despite these similarities, Taspase differs from other type II asparaginases in some key properties, which were analyzed in detail.

4.1.1 Catalytic constants of Taspase

The MLL protein possesses two similar Taspase cleavage sites (CS1 and CS2; table 3.1) with CS2 being more conserved and optimal for cleavage [57]. With a quantitative activity assay in hand, this cleavage site specificity could be quantified for the first time (figure 3.19). Although the CS1 and CS2 model substrates used for the *in vitro* assay differ slightly in the fluorescent dyes attached at the N-terminus, the effect on the catalytic activity is expected to be negligible due to sufficient distance to the cleavage site. The resulting catalytic constants revealed low micromolar affinities of the CS1 and CS2 substrates (K_m = 18 and 3 µM, respectively), which is in good agreement with the previously published affinity for CS1 (12 µM; [56]). The turnover numbers for CS1 and CS2 cleavage were quantified for the first time (0.03 and 0.08 s^{-1}, respectively) and are rather low compared to other asparaginases, for example from the enterobacterial *Pectobactrium carotovorum* (120 s^{-1}; [135]), from *Yersinia pseudotuberculosis* (0.22 s^{-1}; [136]), or from the hyperthermophilic *Pyrococcus furiosus* (888 s^{-1} at 80 °C; [137]). The resulting specificity constant confirms a twentyfold higher cleavage preference of CS2 over CS1.

Post-translational modifications are a common mechanism for the regulation of enzyme activity and have also been speculated for Taspase [71]. For Taspase protein expressed heterologously in *E. coli*, post-translational modifications could not be detected by MALDI-MS (figure 3.9). While methylation and acetylation have been described for *E. coli* [138], enzymatic regulation by phosphorylation is common in eukaryotes, but rarely observed in *E. coli*. However, the fact that

Taspase expressed in bacteria and eukaryotic cells exhibit the same specific activity (figure 3.20), suggests that Taspase activity does not need activation by post-translational modifications in eukaryotic cells. However, modifications under stress conditions such as phosphorylation cannot be excluded with these data. Note that the GFP-tag needed for this experiment is reported to have no influence on the activity [71].

Moreover, these data rule out the hypothesis that bacterially expressed Taspase displays only an attenuated activity [71]. Additionally, the enzyme/substrate ratio required for efficient substrate cleavage is below 1:500, which is more than two orders of magnitude more efficient than published [71]. One plausible explanation that the catalytic activity *in vitro* is higher than published before refers to the instability of Taspase in the assay buffer. In this regard, the requirement of salt for stability was pinpointed (figure 3.8) and NaCl concentrations below 450 mM caused precipitation of Taspase (data not shown). To avoid inhibition by chloride, Taspase was stabilized by sucrose for activity measurements and it was demonstrated for the first time that albeit sucrose stabilizes Taspase, the half-life is still only near 2.5 hours. Hence, Taspase requires fast purification with high salt concentrations and short incubation times to maintain its catalytic activity. Insufficient consideration of any of these requirements was found to result in a dramatic loss of activity (figure 3.17 and figure 3.8).

4.1.2 Autocatalytic processing of Taspase takes several days

While the general principle of autocatalytic processing of a proenzyme is shared among asparaginases, the kinetics of the activation rates varies significantly between different asparaginases (table 4.1). For instance, activation of *E. coli* asparaginase takes less than one day [62], contrary to the fivefold slower activation of *Flavobacterium meningosepticum* asparaginase [139]. The slowest activation rate was reported for human asparaginase with 90 days. For Taspase, the only reported value is that it takes longer than 6 hours [63].

Table 4.1 Properties of Taspase-homolog proteins.

	Homology		**Oligomeric state**		
Protein	**sequence**	**structure**	**Xtal**	**solution**	**Autocatalysis**
Taspase	100 %	0 Å	dimer	dimer	3 days
Asparaginase	36 %	0.9 Å	dimer	dimer + monomer	90 days
***F. m.* Glycoamidase**	27 %	1.1 Å	dimer	monomer	< 5 days
***E. c.* Asparaginase**	21 %	1.5 Å	dimer	dimer	< 1 days
Proteasome	14 %	4.7 Å	heptamer	heptamer	α-SU-dependent

A detailed study of the autocatalytic process provided for the first time information about the Taspase activation rate. Separation of the active subunits from the proenzyme by SDS-PAGE indicates that the activation process takes approximately one day (figure 3.11). Importantly, the activation of Taspase does not begin at the start of the assay, but already during the purification process of the protein. This becomes clear by comparison of the SDS gels of the bacterial lysate (figure 3.3; almost only proenzyme), after affinity purification (figure 3.4; predominantly proenzyme) and after gel filtration (figure 3.5; ca. 50 % proenzyme). Hence, the two days needed for protein purification have to be added to the activation time determined in the assay, yielding a total activation time of three days. Moreover, the high amount of proenzyme in the bacterial lysates after expression over night could hint at a lower processing in cells compared to buffer conditions.

Interestingly, the band for the proenzyme loses intensity over time, but does not disappear even after seven days. Two explanations are possible for this phenomenon. Either a fraction of Taspase is still in the proenzyme form, or the band is caused by an SDS-resistant dimer of the two subunits. Since the autocatalytic processing is an irreversible spontaneous event and no equilibrium reaction, a stagnation of this process is unlikely. Additionally, the presence of an SDS-resistant αβ-dimer is in agreement with the high affinity of the subunits discussed below.

Moreover, Nomme and colleagues reported an acceleration of the human asparaginase activation process by addition of glycine [66]. However, Taspase activation was independent of glycine, salt, sucrose or malate (data not shown).

To gain further insight into this activation process, time-dependent NMR studies were applied. With this technique, the activation can be followed more detailed than with SDS-PAGE at the atomic level. The NMR peak intensities of the amino acids in the fragment released by the autocatalytic activation event (referred to as Taspase loop) increased over time (supplemental figure 7.9). Since the assigned peaks in the ^{1}H-^{15}N-HSQC spectrum of Taspase correspond to flexible loop regions and disordered regions (see section 4.1.4 for detailed explanation), the appearance of peaks correlates with an increased flexibility of the corresponding amino acids. Therefore, the increasing flexibility of the loop residues reflects the autocatalytic activation of Taspase.

The peak intensities of the loop residues reach their maximum after approximately seven days, indicating that the autocatalytic activation is completed after this period. Hence, compared to the SDS-PAGE-based analysis of the autocatalytic activation, the NMR experiments indicate a somewhat slower activation rate. This difference can presumably be attributed to the lower incubation temperature during the NMR experiment (30 °C) compared to the SDS-PAGE experiment (37 °C), as the probability for a nucleophilic attack, which is needed for the activation process, is usually temperature dependent as described for the activation of other Ntn-hydrolases [139]. Additionally, both experiments are only qualitative.

In summary, these first data of the Taspase maturation process reveal that Taspase activation *in vitro* takes approximately three days, which is significantly shorter than its closest structural homolog, human asparaginase (90 days).

4.1.3 Taspase is a hetero-tetramer with high affinity

After autoproteolysis, the subunits of asparaginase type II family proteins assemble to an αβ-heterodimer. In Taspase, the αβ-heterodimer displays a remarkably high stability. This high affinity of the subunits allowed a co-purification with a His-tag only present at the α-subunit (section 3.1.4). Furthermore, the two subunits were retained by a 30 kDa filter membrane during purification, although each subunit is small enough for passage (25 and 20 kDa). Accordingly, a FRET-based assay, in which Atto488-labeled Taspase was mixed with Atto594-labeled Taspase, failed to detect an exchange of the subunits indicating no or slow subunit exchange (data not shown). A look at the crystal structure reveals that the high affinity of the subunits is based on a large hydrophobic interface with a positively charged patch of the α-subunit buried in a negatively charged groove in the β-subunit (figure 4.1).

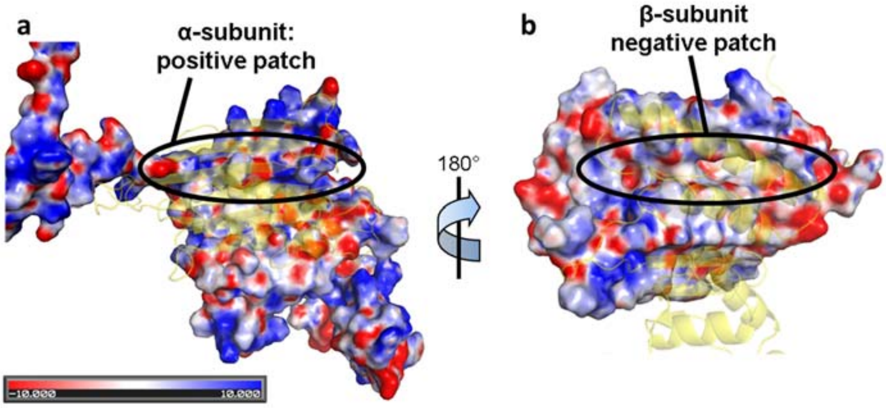

Figure 4.1 Interface of the two Taspase subunits.

a The α-subunit possesses a positively charged patch (blue) at the interface to the β-subunit (yellow). **b** Conversely, the β-subunit shows a negatively charged patch (red), which allows interaction with the α-subunit (yellow). Charges were mapped on a model based on PDB 2a8j.

While the αβ-dimer is generally accepted for Taspase, the hetero-tetrameric oligomer of Taspase seen in all asparaginase-like crystal structures [56,66,139,140] is, however, discussed controversially. On the one hand, Taspase unambiguously adopts a hetero-tetrameric structure upon crystallization and the large hydrophobic interface between the two αβ-dimers suggests a high stability of the complex [56]. On the other hand, pull-down experiments and gel filtrations indicated only a low affinity of the two αβ-heterodimers in solution [68]. Nevertheless, these contradictory experiments can be brought in line by a consideration of the Taspase concentrations. At high concentrations used for crystallography, Taspase is a hetero-tetramer, whereas the low concentrations used in the biochemical assays favor the αβ-dimer. Accordingly, also the homolog *F. meningosepticum* glycosylasparaginase is a dimer in solution, despite showing a heterotetramer in the crystal structure (table 4.1 and [140]).

For the first time, concentration dependent gel filtrations were performed with Taspase to shed light on the oligomeric state of Taspase in solution. For concentrations between 1 and 400 µM Taspase was exclusively found as αββα-heterotetramer (section 3.2.4). Cellular concentrations of Taspase are assumed to be much lower, but could not be assessed by gel filtration, as they fall below the detection limit of the UV detector [68]. However, the fact that the 90 kDa Taspase hetero-tetramer can pass a 50 kDa filter membrane (supplemental figure 7.19) indicates that the complex is not as stable as proposed by Khan and colleagues based on the dimer interface area in the crystal structure [56].

4.1.4 Structure of the Taspase loop

In the previous sections, the autocatalytic maturation of the Taspase proenzyme was discussed. This process yields a C-terminal stretch at the α-subunit of all Ntn-hydrolases, which is missing in all available crystal structures due to a lack of electron density for this region (figure 4.3b). In the case of Taspase, this region comprises 56 amino acids (G178-D233) and is referred to as Taspase loop. As crystallography failed to provide information about this part of the protein, NMR and CD spectroscopy were used as complementary methods to gain first information about the flexible Taspase loop.

The first striking finding was that the ^{1}H-^{15}N HSQC spectrum of full-length Taspase shows low ^{1}H signal dispersion of 0.8 ppm (between 7.8 and 8.6 ppm), which is typical for unstructured regions [141–143]. To map these residues, the respective areas in the model were added by homology modeling (figure 4.2).

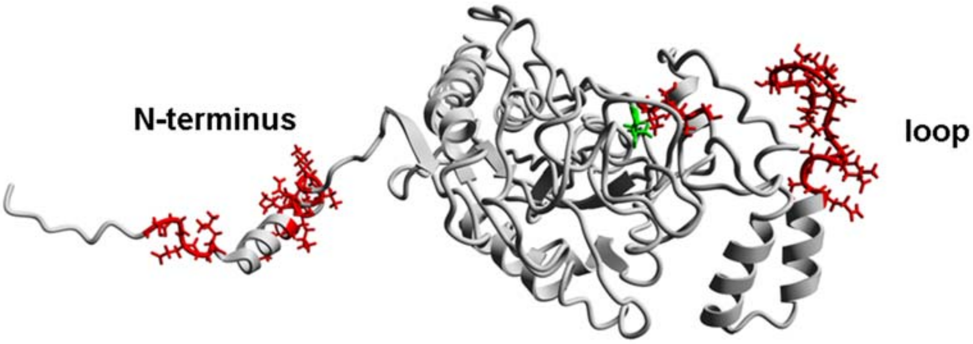

Figure 4.2 Mapping of the ^{1}H-^{15}N HSQC signals.

Mapping of the assigned residues on a model of wild-type Taspase based on the structure PDB 2a8j. Assigned residues are highlighted in red; the active site is marked in green. Most of the assigned residues can be found in the flexible N-terminus and the flexible Taspase loop.

Indeed, the assigned signals in the spectrum correspond to flexible regions in the N-terminus (15 residues) or the Taspase loop (12 residues), while the rigid parts with a defined secondary structure remain invisible. Hence, the missing regions of the Taspase crystal structure can be selectively investigated by NMR spectroscopy. An important factor for the signal intensity in NMR spectroscopy is the rotation correlation time of the protein, which correlates with the protein size. This rotational correlation time is related to both the longitudinal (T1) and transversal (T2) relaxation times. Large proteins like Taspase exhibit long T1 and short T2 times, which results in line-broadening in the resultant NMR spectrum due to a loss of magnetization and renders the peaks invisible. However, the large loop regions of Taspase obviously behave like separate disordered domains with independent rotational correlation times. Thus, the rigid core region loses its magnetization quickly, while the flexible regions possess lower rotation correlation times and the signals can be recorded before the magnetization is lost. Conversely, the inactive mutant does not cleave itself, so that the loop retains the rotational correlation time of the core and is therefore invisible in the NMR spectra of inactive Taspase (figure 7.10).

Thus, according to NMR spectroscopic studies the Taspase loop seems to be flexible. Furthermore, these data are in line with the helix-turn-helix model generated by homology modeling (figure 3.13). Essentially, the amino acids preceding Ser222 were not visible in the NMR spectra, whereas the region C-terminal of Ser222 was seen in the NMR spectra. This strongly supports the occurrence of a more rigid secondary structure ending at Glu221.

Based on these data, the first structural model was generated for the loop region missing in the crystal structure of Taspase and all other asparaginases. The model fulfils the criteria mentioned above, namely a central region of discontinuous helices, as well as a defined structure C-terminal of Ser222.

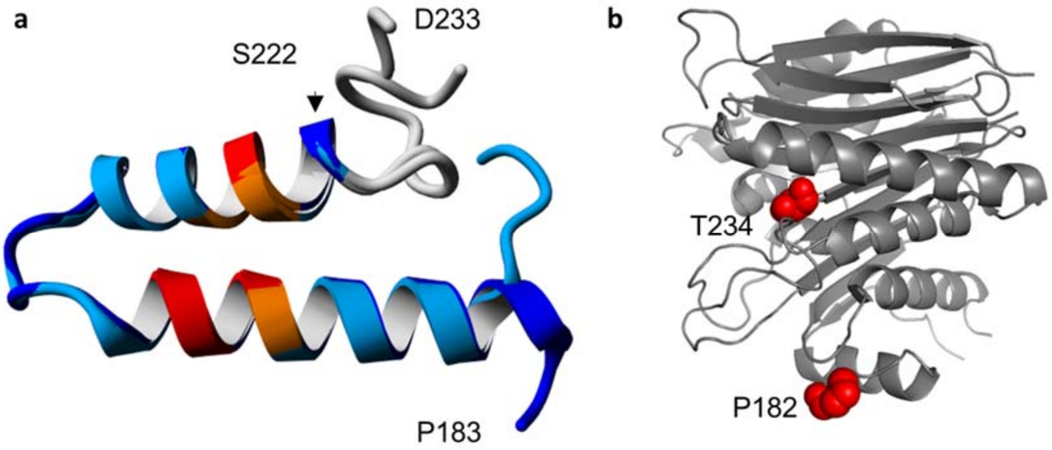

Figure 4.3 Proposed structure of the Taspase loop.

a The proposed structure is based on NMR and CD spectroscopy data as well as secondary structure prediction. The model shows a helix-turn-helix motif. NLS amino acids are highlighted in orange, critical NLS residues are displayed in red. The overlay of two possible conformations indicates flexibility of the termini. **b** Location of the loop in the Taspase protein (PDB 2a8j).

The 3D model generated by YASARA displays the proposed helix-turn-helix structure of the Taspase loop with flexible termini (figure 4.3a). Interestingly, the helix-turn-helix motif ends at Glu221 and allows the interaction of the two helices, so that the bipartite basic NLS [74] forms a continuous patch (red in figure 4.3a). Furthermore, the interaction of the two helices agrees with the interface visible in the wheel projections (data not shown).

As mentioned before, all other type II asparaginases comprise a flexible loop region N-terminal of the catalytic site that is disordered in the crystal structures of human glycosylasparaginase, human asparaginase, plant asparaginase, *E. coli* asparaginase, and *F. meningosepticum* glycosylasparaginase. Sequence-based models of the loop for these Taspase homologs (figure 4.4) reveal that only the Taspase loop is predicted to be predominantly helical. In contrast, the other loops are predicted as pure random coil (human asparaginase, *E. c.* asparaginase, and *F. m.* glycosylasparaginase) or random coil interspersed with short helices (human glycosylasparaginase and plant asparaginase).

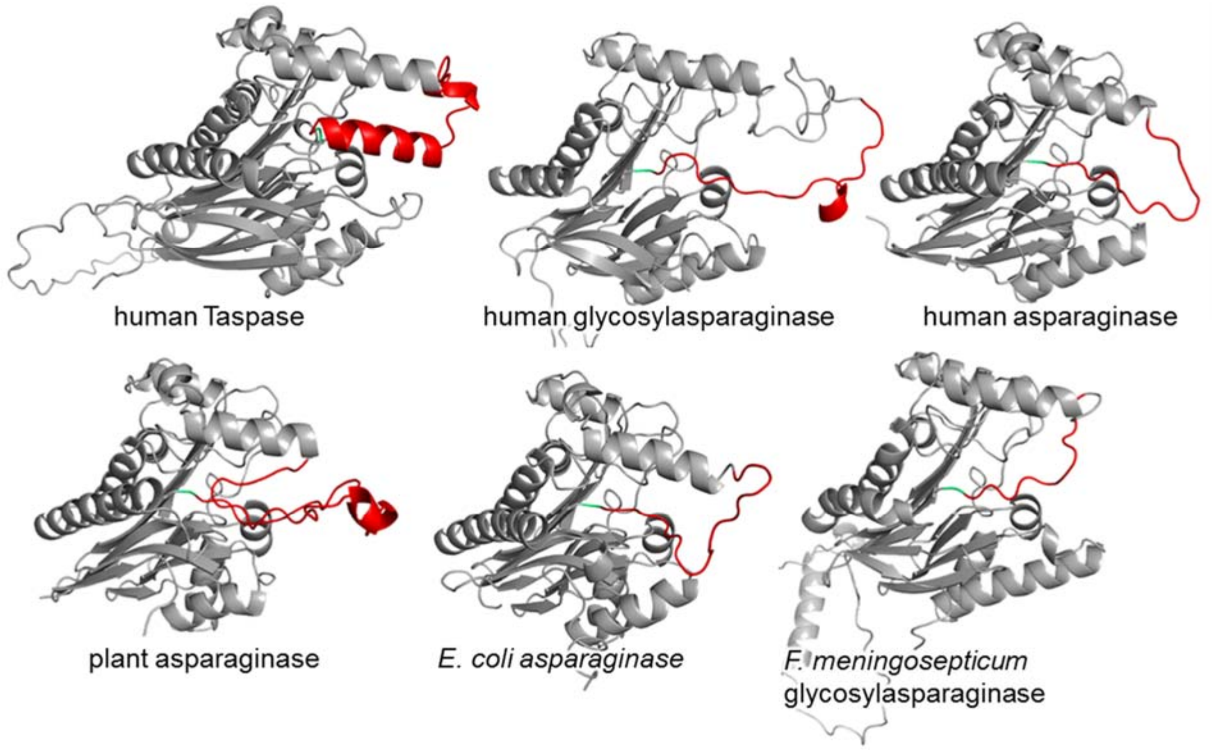

Figure 4.4 Asparaginase type II loop models.

Modeled structures of the Taspase loop homologous regions in other type II asparaginases. The loop of human Taspase (template PDB 2a8i; loop length: 25 aa) is predicted as predominantly helical, while for human glycosylasparaginase (template PDB 1apy; loop length: 20 aa), human asparaginase (template PDB 4pvs; loop length: 14 aa), plant asparaginase (template PDB 2gez; loop length: 33 aa), *Escherichia coli* asparaginase (template PDB 2zal; loop length: 17 aa), and *Flavobacterium meningosepticum* glycosylasparaginase (template PDB 1ayy; loop length: 10 aa) mainly random coil elements are predicted. The modeled loop regions are highlighted in red; the active site Thr234 is highlighted in green.

Although loops shorter than the 25 amino acids Taspase loop are unstructured (*F. m.* glycosylasparaginase: 10 amino acids; human asparaginase: 14 amino acids; human glycosylasparaginase: 20 amino acids), also the longer plant asparaginase loop (33 amino acids) possesses predominantly random coil elements.

Further analyses with the isolated loop protein confirmed the helical structure of the Taspase loop and revealed that the terminal loop region are required for helix formation (figure 3.15a). Moreover, MD simulations of the loop without the termini indicate that although short helices can form, they are only transient and cannot establish a defined tertiary structure (figure 3.15c).

4.1.5 Inhibition strategies for Taspase

Due to the key role of Taspase in the activation of the oncogenic MLL protein associated with t(4;11) leukemias, Taspase inhibitors are of high demand. However, although several strategies have been followed to find inhibitors, a breakthrough is still awaited and novel Taspase inhibitors are urgently required.

In contrast, inhibition of the homolog enzyme asparaginase is undesired for medical purposes. Rather, high asparaginase activity is desired for cancer treatment, since asparagine is essential for leukemic cells. Consequently, depletion of asparagine by asparaginase leads to inhibition of protein synthesis and subsequent cell death [144]. Thus, asparaginase is successfully used as chemotherapeutic and was released as *E. coli* asparaginase (Elspar™), PEGylated *E. coli* asparaginase (Oncaspar™), or *Erwinia chrysanthemi* asparaginase (Erwinase™) for the treatment of childhood ALL [145].

As explicated in the previous sections, Taspase differs from all other type II asparaginases in its substrate specificity and the catalytic mechanism. This is assumed to be the reason, why commercial protease inhibitors, such as the serine protease inhibitor PMSF or the cOmplete™ inhibitor cocktail, but also the threonine protease inhibitor bortezomib [63], do not inhibit Taspase. However, this unique position of Taspase offers various ways for new inhibitors, some of which have already been mentioned in the introduction (section 1.3.4):

Compound screening yielded an allosteric arsenic inhibitor (NSC48300) with a K_i of 4.2 µM [63]. However, this compound is not specific for Taspase and was initially identified as an anti-angiogenic drug. Besides the toxicity of the arsenic moiety, this compound has been under discussion, since inhibition could not be reproduced in a cellular assay [133]. This lack of inhibition by NSC48300 was here confirmed *in vitro* (figure 3.21), which questions the potential of the compound even more.

Virtual docking by Knauer and colleagues resulted in two compounds (CHC-A4 and DHC-C1) with weak inhibitory potential [71]. The authors discussed the missing parts in the Taspase crystal structure and limited cell entry of the compounds as possible causes for the poor screening output. Furthermore, the comparatively small size of the compound database might also have lowered the number of hits.

For these reasons, the virtual docking was repeated with an improved Taspase model including the missing loop regions and a fiftyfold larger compound library (section 3.4.2). Additionally, the hurdle of crossing the cell membrane was eliminated by using an *in vitro* assay for the readout. Nevertheless, the resulting compounds displayed no inhibition of Taspase activity. This supports the theory that Taspase undergoes a structural change upon substrate binding, which would limit the value of the crystal structure for virtual docking approaches.

Substrate analogs were first tested by Lee and colleagues with a series of substrate-derived vinyl sulfone and vinyl ketone derivatives [69]. Despite the moderate inhibitory potential (IC_{50} near 30 µM for the best compound yzm18), these studies proved helpful for the design of new substrate analog compounds. These succinimide peptides tested in this thesis are discussed separately below (section 4.3).

Enforced dimerization by the fusion of Jun- and Fos-tags to the C-terminus of Taspase resulted in a loss of catalytic activity [68]. This finding seems to be in contrast to the catalytic activity obtained with Taspase at concentration where the dimer is the predominant oligomeric state (figure 3.37b). A simple explanation for these contradictory findings is that the enforced dimer adopts a different conformation than the natural dimer. Particularly, the C-terminally attached dimer tags presumably bring the C-termini in close proximity in the enforced dimer. However, the

C-termini of the natural dimer are more than 60 Å apart on the opposite ends of the hetero-tetramer (figure 7.20). In the enforced dimer, a steric hindrance could therefore prevent substrate binding and thus abolish catalytic activity. Furthermore, the artificial generation of higher oligomeric Taspase species by Jun/Fos mediated dimerization was not excluded, which might be another reason for the missing activity.

Molecular plugs are a comparatively new mechanism to occlude the active site by artificial ligands. The Schmuck group achieved an inhibition of the serine protease β-tryptase with nanomolar K_i using a four-armed ligand to block the active site noncompetitively [146,147]. This approach could also be applicable to Taspase, if the compounds sterically prevent substrate binding. Consequently, 41 of these molecular plug derivatives were obtained from the Schmuck group and tested for Taspase inhibition. Although these compounds covered combinations of different charges, lengths and hydrophobicity, none of them was able to inhibit Taspase (supplemental figure 7.21 and figure 7.22).

4.2 Nanoparticles as novel inhibitors

Owing to their high surface to volume ratio, nanoparticles possess a high free surface energy, which allows the adsorbance of other molecules [148]. The interaction of nanoparticles with biomolecules is already used for a broad range of diagnostic and therapeutic methods in medicine [149]. Recent studies revealed that the proteasome, the only other Ntn-type threonine protease, binds to silica nanoparticles (Shirley Knauer, unpublished data). For this reason, Taspase binding to silica based nanoparticles was investigated.

4.2.1 Taspase binding depends on nanoparticle size

Indeed, microscale thermophoresis and fluorescence anisotropy experiments showed binding of Taspase to silica nanoparticles at low nanomolar concentrations (section 3.5.1). Furthermore, in contrast to Taspase, the control protein parvalbumin showed a 300 000-fold weaker affinity. To understand why some proteins bind to nanoparticles, while others are rejected, the protein-nanoparticle interface needs to be examined in more detail. However, the interactions of nanoparticles with biomolecules are still not fully elucidated, despite extensive research in recent years. Nevertheless, some concepts emerged from these efforts, which help to understand the influence of nanoparticles on proteins [92]. Some of the possible interactions are displayed in figure 4.5.

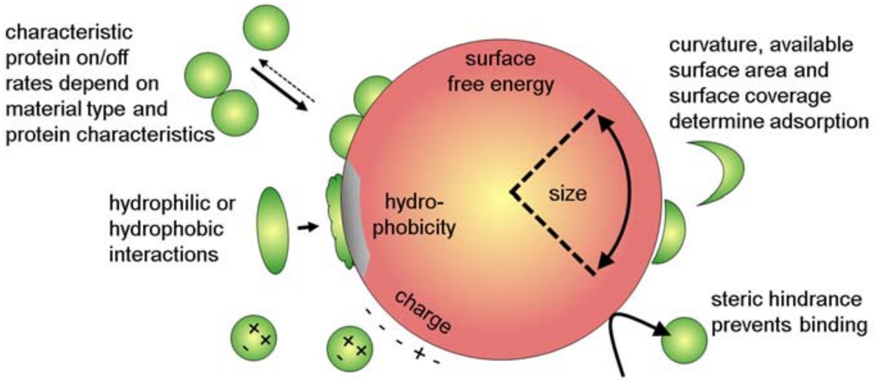

Figure 4.5 Interactions of proteins with nanoparticles.

Binding to nanoparticles (red) is dependent on protein-specific on/off rates, as well as hydrophobicity, size and charge of the particles themselves. The green circles represent various proteins. Modified according to [92].

Obvious factors that rule the interactions are charge and hydrophobicity of the particle and the protein. Surprisingly, a recent study revealed that negatively charged proteins show increased binding to nanoparticles, irrespective of their net charge [99]. Other important determinants are the size and curvature of the nanoparticles and steric factors. The protein layer surrounding the nanoparticles is called corona. Due to the parameters outlined in figure 4.5, this corona is specific for each type of nanoparticle and establishes rapidly. Hence, nanoparticles interact selectively with only some proteins and do not bind every protein [99,150]. This is in agreement with the binding of Taspase to silica nanoparticles, while parvalbumin is rejected (section 3.5.1).

For the interaction of Taspase with negatively charged amorphous silica particles (Amsil), the surface area and curvature showed a great influence on Taspase binding affinity and capacity (figure 3.27). The EC_{50} of nanoparticles with 125 nm diameter (Amsil125) is 3500-fold lower compared with nanoparticles of 8 nm diameter (Amsil8). This is also reflected in the stoichiometry of roughly 5000 and 6 Taspase molecule per Amsil125 and Amsil8 nanoparticle, respectively, which is in good agreement with the stoichiometry of 620:1 reported for HSA with 70 nm NIPAM/BAM-nanoparticles [151]. Notably, an Amsil8 particle binds roughly 800 times less Taspase molecules than an Amsil125 particle, although the surface area is only roughly 250 times smaller for Amsil8. This is probably the case because Taspase is able to bind with higher density to a surface with low curvature (Amsil125) compared to high curvature surfaces (Amsil8).

4.2.2 Possible inhibitory mechanisms

Here, for the first time silica nanoparticles were found not only to bind, but also to inhibit Taspase (figure 3.28). Notably, binding and inhibition occur at similar nanoparticle concentrations (figure 3.27 and figure 3.28), indicating that every Taspase molecule bound to nanoparticles loses its activity. However, the inhibition of enzymes by nanoparticles is poorly investigated and scarcely described. One example is the inhibition of chymotrypsin multi-walled carbon nanotubes, which were specifically imprinted to enable chymotrypsin binding [152], which was also applied to trypsin by an independent group [153]. Another study investigated the influence of single-walled carbon nanotubes on soybean peroxidase and chymotrypsin activity [109]. They found an irreversible inhibition of chymotrypsin activity and more than 90 % inhibition of soybean peroxidase activity. For the inhibition mechanism of chymotrypsin, the authors suggested a denaturation of the protein, while the inhibitory mechanism for soybean peroxidase remained unresolved. Further possible models for enzyme inhibition by nanoparticles are displayed for Taspase in figure 4.5 [92].

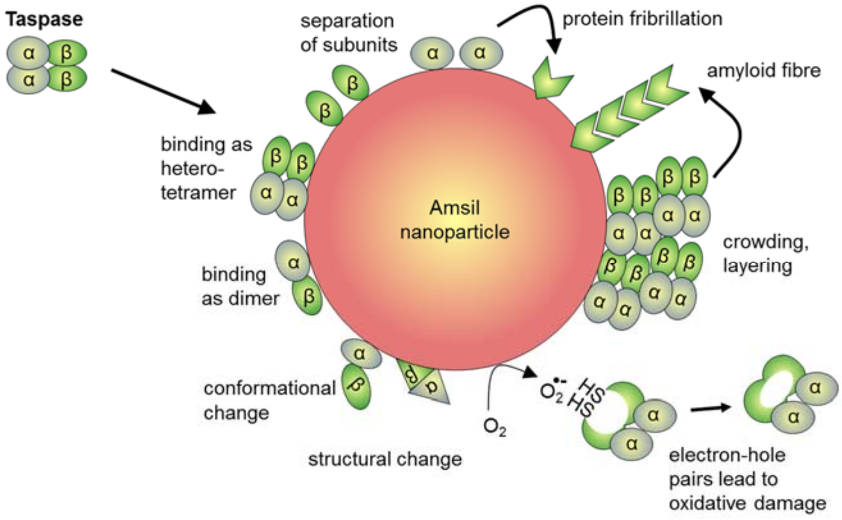

Figure 4.6 Structural changes of proteins bound on nanoparticles.

Interaction with nanoparticles can change the protein structure and function. The green circles represent Taspase subunits. Models for Taspase inhibition by nanoparticles include steric occlusion of the active site after binding as hetero-tetramer or dimer, separation of the subunits, as well as structural or conformational changes, crowding effects, fibrillation and oxidation. Modified according to [92].

Structural changes have been described for the human β_2-microglubulin upon binding to copolymer particles, cerium oxide particles, quantum dots and nanotubes [154]. In the case of β_2-microglubulin, nanoparticles increase the probability of nucleation of protein fibrils and thereby induce amyloid formation. This fibrillation process is accompanied by a transition from a helix to a sheet and thus significant changes in the protein structure. However, the secondary structure of Taspase is not altered upon binding to nanoparticles (figure 3.29a), which rules out fibrillation as explanation for inhibition. In addition, the reversibility of the inhibition does not agree with an irreversible fibrillation and aggregation process.

Moreover, the stability of enzymes bound to nanoparticles can differ from the enzyme in solution [109,155]. Interestingly, this effect can either be stabilizing or destabilizing, depending on both the nanoparticle and the protein investigated. For instance, soybean peroxidase and subtilisin Carlsberg were stabilized by spherical nanoparticles such as C_{60} fullerenes, silica or gold nanoparticles [155], while chymotrypsin unfolds upon binding to carbon nanotubes [109]. Additionally, the storage stability of glucose oxidase was significantly increased after binding to silica-encapsulated magnetic nanoparticles [156]. Nevertheless, both stabilization and destabilization can be excluded as the cause for Taspase inhibition, since the stability is not altered by nanoparticles (figure 3.29).

Another mechanism is the oxidation of biomolecules catalyzed by nanoparticles, which has been demonstrated for DNA in the presence of TiO_2 nanoparticles [157], but can also affect proteins and other biomolecules [93,158]. Indeed, Taspase possesses at least six cysteins and two methionines with sufficient solvent accessibility for oxidation and especially methionine oxidation was found to be important for inhibition for example in the case of catalase [159]. However, oxidation of Taspase is unlikely due to the highly reducing milieu in the buffer containing 10 mM DTT.

Moreover, binding of proteins to nanoparticles can greatly increase the local protein concentration in the nanoparticle corona and cause layering or crowding effects, which are known to promote aggregation [160,161]. Indeed, the stoichiometry of 6 and 5000 Taspase molecules per Amsil8 and Amsil125 nanoparticle (figure 3.27b), respectively, indicate high local Taspase concentrations. However, the CD spectra in the presence of nanoparticles contradict the aggregation of Taspase. Moreover, assuming an interface size of 35 x 42 Å per Taspase monomer and perfect steric packing, the surface coverage of Amsil8 is below 50 % and roughly 150 % for Amsil125. This suggests that a heavily curved surface can bind less Taspase molecules compared to flatter surfaces (figure 4.7). However, a burying of Taspase by multiple layers in the nanoparticle corona is probably not the cause for the reduced activity.

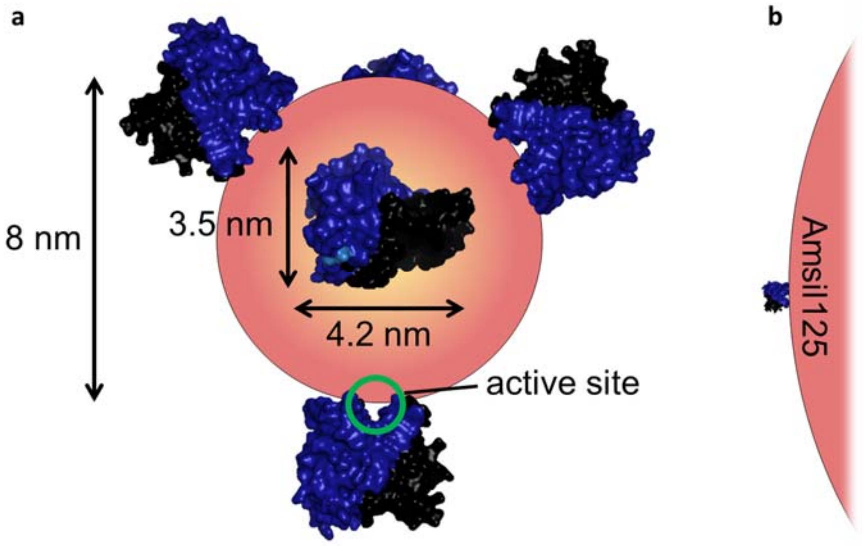

Figure 4.7 True-to-scale model of Taspase bound to nanoparticles.

a Scaled model of Taspase bound to Amsil8 nanoparticles (red) as αβ-heterodimer (black and blue, respectively). The active site (green circle) is occluded in the bound state. The calculated stoichiometry of 6:1 is displayed. **b** Size comparison of Taspase and Amsil125.

Hence, Taspase is likely to bind to nanoparticles in a single layer without major conformational changes. For this it is important to consider the oligomeric state of Taspase. If Taspase binds as hetero-tetramer, the two active sites are located at opposite ends and cannot be covered simultaneously by one nanoparticle. As inactivation of one protomer has no effect on the other protomer [85], one protomer is likely to be active if Taspase binds as hetero-tetramer, unless small conformational changes undetectable by CD and fluorescence spectroscopy occur.

With the current data, the most plausible explanation for Taspase inhibition by nanoparticles is binding as an αβ-dimer in a single layer without conformational change as shown in figure 4.7a. This either results in noncompetitive inhibition (figure 3.28) that is either allostery-like or occludes the active site. However, the latter mechanism is more likely, since the positively charged active site is probably part of the binding interface for the strongly negatively charged nanoparticles. As a result, the active site is reversibly occluded and inaccessible for the substrate. Given the fact that the inactive mutant can still bind nanoparticles, the positively charged Taspase loop (pI = 9.8) probably supports binding, while the location does probably not influence binding strength.

Finally, binding of only one subunit and separation of the highly affine αβ-dimer can be ruled out, as this would result in free α- or β-subunits, which again can be excluded since neither subunit is found after filtration through a 30 kDa membrane (data not shown). However, a separation of the two subunits and binding of both subunits to nanoparticles is another plausible explanation for the inhibitory effect.

Importantly, control experiments with lactate dehydrogenase, chymotrypsin and proteinase K showed no or low inhibition of the respective enzyme activity at nanoparticle concentrations needed for Taspase inhibition (figure 3.30). In summary, the nanoparticle concentrations required for LDH inhibition are 1-2 orders of magnitude higher than for Taspase, and no inhibitory effect was found for chymotrypsin and proteinase K. Moreover, nanoparticles cannot reduce LDH activity by more than 25 %, in contrast to the 90 % inhibition seen with Taspase. This pinpoints that silica nanoparticles do not inhibit enzymes in general. While silica nanoparticles displayed an inhibitory effect on the threonine proteases Taspase and the proteasome, they failed to inhibit the serine proteases chymotrypsin and proteinase K. This is in agreement with the finding that nanoparticles bind a selective set of proteins [99]. However, for a prediction whether an enzyme is inhibited by nanoparticles, further studies are required to gain a deeper understanding of these interactions.

4.2.3 *In vivo* effects of nanoparticles on Taspase

In contrast to *in vitro* assays with purified protein, nanoparticles face a large variety of different proteins *in vivo*. Hence, the nanoparticle corona will consist of a diverse mixture of proteins that compete for binding. To test Taspase binding under such conditions, Hela cell lysates with overexpressed GFP-Taspase were tested for Taspase activity in the presence of silica nanoparticles.

While nanoparticles were able to inhibit Taspase by up to 90 % *in vitro*, the maximum inhibitory effect is limited to 50 % in cell lysates (figure 3.31). Consequently, the nanoparticle surface is probably partly occupied by other cellular proteins, which reduce the inhibitory potential with respect to Taspase. Nevertheless, the nanomolar affinity was still good enough to investigate Taspase inhibition in cells.

Owing to their large size, nanoparticles cannot enter the cell passively, but must be taken up actively by the cell. However, the efficiency of this cellular uptake again depends on size and shape of the nanoparticle [162]. The current model for the uptake mechanism involves energy-dependent wrapping of the nanoparticle with the help of clathrin and the cytoskeleton [92]. In a recent study, tissue-specific targeting of compounds was achieved by coating nanoparticles with a lung-targeting peptide, which resulted in an enrichment of these nanoparticles in the lung after venous injection in mice [163]. Even targeting of cellular compartments was successfully shown in living cells with nanoparticles conjugated to a small signal peptide. With this approach, fluorescent nanocrystal quantum dots accumulated selectively in the mitochondria or the nucleus within 15 minutes [164].

Some nanoparticles pose a risk to cells due to their toxic potential. For instance, ZnO nanoparticles were tested for cytotoxicity against human immune cells and monocytes were found to be particularly susceptible to the reactive oxygen species induced by the nanoparticles [165]. Especially crystalline silica (SiO_2) is known to induce chronic inflammation, fibrosis and lung cancer upon inhalation [166,167]. In stark contrast to the high toxicity of crystalline silica, amorphous silica nanoparticles are regarded to be safe without displaying chronic effects, as studied in rats [168]. This is in agreement with the good viability of the cells after Amsil nanoparticle challenge with normal proliferation, cell size and morphology (figure 3.33).

Using fluorescently labeled nanoparticles, Tenzer and colleagues cold confirm that the silica nanoparticles used in this project are readily taken up within roughly one hour [99]. Furthermore, the cellular uptake rate was increased in the presence of serum, compared to serum-free incubation.

Taspase does not reside in the cytoplasm, but is located mainly inside the nucleus [74]. Notably, this nuclear localization is not static, but Taspase shuttles between nucleus and cytoplasm in an importin-α/nucleophosmin-dependent manner [74]. Importantly, the nuclear localization is retained in the presence of nanoparticles, which are unlikely to be shuttled actively between nucleus and cytoplasm (figure 3.33a). This finding excludes that nanoparticles bind Taspase in the cytoplasm and prevent the nuclear import, as this would be reflected in a distinct accumulation of Taspase at the nuclear envelope and in the cytoplasm. Hence, this suggests that nanoparticles have access to the nucleus, where Taspase binding and inhibition occurs. The diameter of the central channel of the nuclear pore complex (NPC) is with 40 nm large enough for the passage of nanoparticles [169,170]. Indeed, nanoparticles can enter the nucleus [164], which was also shown for silica nanoparticles [99]. Since proteins with a molecular weight above 60 kDa cannot pass the pore by diffusion, nanoparticles are probably actively imported.

While the observed inhibition to 50 % of the initial activity is consistent with the values observed in cell lysates for Amsil8 and Amsil20, the inhibitory effect of the larger Amsil125 was significantly lower in cells (figure 3.33a). This outcome is in agreement with the finding that the wrapping process needed for cellular uptake is optimal for nanoparticles with 15-30 nm diameter [92,162]. Hence, the large Amsil125 nanoparticles are taken up at a lower rate and excluded from nuclear import due to their size, which results in a lower inhibitory potential.

Altogether, the inhibition of Taspase by silica nanoparticles at nanomolar concentrations highlights for the first time that nanoparticles are able to qualitatively inhibit enzymes *in vivo*, and thereby contributes to the comprehension of nanoparticle interactions in cells. Although the nature of silica nanoparticles does not suggest a selective inhibition, this effect does not affect proteases in general. However, possible inhibitory effects of nanoparticles on enzymes need to be considered in future studies and for possible medical applications.

4.3 Succinimide peptides inhibit Taspase competitively

The specific consensus sequence of Taspase (Q-[F,I,L,V]-D | G-X-X-D or Q-[F,I,L,V]-D | G-X-D-X) facilitates targeting the active site by substrate-derived inhibitors and has already been attempted by the Bogyo group in 2009 [69]. However, these vinyl ketone and vinyl sulfone derivatives only targeted the S-site, but not the S'-site and displayed only moderate inhibition (IC_{50} = 30 µM). Consequently, a new class of substrate analog inhibitors targeting both the S- and S'-site was designed and tested in cooperation with the Kaiser group for chemical biology.

4.3.1 Implications for substrate cleavage and binding mode

For the design of novel inhibitors, the cleavage mechanism proposed for Taspase was analyzed (figure 1.9; [69]). Concerning the high structural similarity of Taspase with other type II asparaginases [66,139], the catalytic mechanism is likely to show some similarities. Nevertheless, asparaginases hydrolyze the asparagine side chain, while Taspase is an endopeptidase. However, if the substrate undergoes a rearrangement via a succinimide-hydrate intermediate, Taspase could cleave the isopeptide bond at the asparagine side chain (figure 1.9), which is again very similar to the asparaginase cleavage mechanism [66]. The fact that the compound with isoaspartate (Comp8) displayed only a low inhibitory potential, indicates that Taspase can indeed cleave isopeptide bonds. In contrast, compounds with a succinimide moiety, (Comp2,5,9,10) could effectively inhibit Taspase.

For the first time, conclusions can be drawn about the cleavage mechanism of Taspase based on these experimental data. Indeed, these data strongly support the previously hypothesized substrate rearrangement via a succinimide-hydrate to form an isopeptide bond between aspartate and glycine. In other words, the protein backbone is transferred to the aspartate side chain before the final cleavage step takes place. Hence, Taspase does not directly hydrolyze the peptide bond, but the newly formed isopeptide bond (figure 1.9). Furthermore, the formation of a succinimide-hydrate intermediate is in line with the mandatory presence of the small residue glycine after the aspartate to allow the nucleophilic attack on the aspartate side chain.

Moreover, a photoreactive derivative of the succinimide inhibitor was used to shed light on the binding mode of the substrate, which is still completely enigmatic due to missing experimental data and a lack of homologous proteases. For this critical experiment, the photoreactive cross-linker was located at the P4 position of the substrate. After cross-linking, the inhibitor was found attached to the α-subunit, but not the β-subunit (figure 3.38). As both subunits contribute to the active site located between them, the cross-linking experiment allows a mapping of the putative substrate orientation on the Taspase structure (figure 4.8).

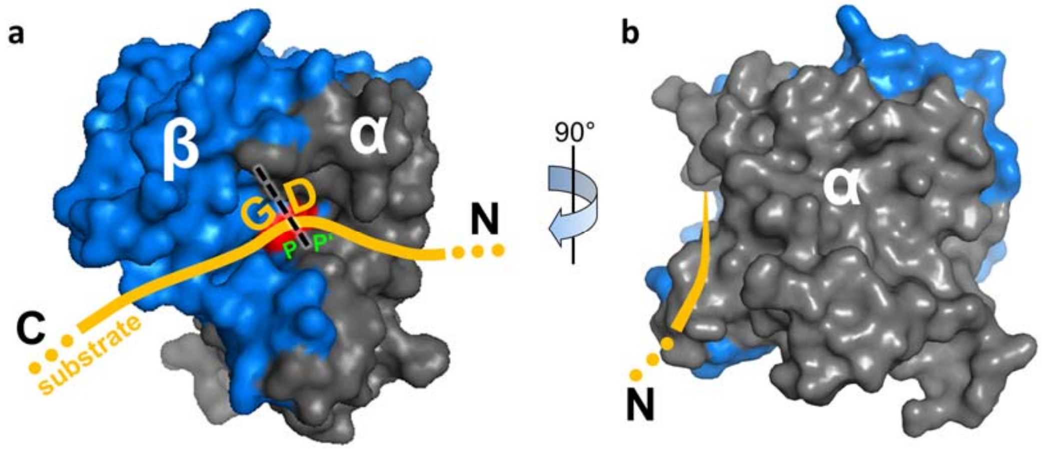

Figure 4.8 Proposed substrate orientation.

The suggested binding mode derived by the photolabeling experiment (see main text) was modeled on the dimer of Taspase (PDB 2a8j). **a** The substrate (yellow) is proposed to bind to the active site (red) with its P-site (green) oriented to the α-subunit (gray) and the P'-site (green) to the β-subunit (blue). N- and C-termini of the substrate are labeled, as well as the substrate cleavage site and the Taspase subunits. **b** The side view shows the catalytic cleft formed by both subunits, in which the substrate can bind.

Thus, the P-site of the substrate is likely to be oriented towards the α-subunit, which in turn means that the P'-site is probably pointing towards the β-subunit. Assuming that this binding mode is correct, the groove formed by both α- and β-subunit could serve as binding cleft for the substrate as shown in figure 4.8b. Although these experiments provide valuable first data about the substrate binding, detailed information about the substrate binding mode cannot be derived from these preliminary experiments. Nevertheless, the developed compounds present a powerful tool for further studies. Possible experiments are discussed in the outlook section.

4.3.2 Scope and limits of the succinimide inhibitors

In vitro applications

The inhibition type of the newly designed peptidyl-succinimide inhibitors is expected to be competitive, as this is usually seen for substrate analog compounds. Indeed, the substrate could replace the inhibitor (figure 3.36b). Furthermore, binding of the inhibitor to Taspase in absence of the substrate was verified by microscale thermophoresis (figure 3.36a) and excludes uncompetitive inhibition (i.e. binding of the enzyme-substrate complex). Moreover, prolonged incubation times of enzyme and inhibitor did not result in increased inhibition, hinting at a reversible nature of the inhibition. However, unlike allosteric inhibitors, substrate analog protease inhibitors are prone to cleavage due to their high structural similarity to the natural substrate. In the case of Taspase, a degradation of the succinimide motif could be ruled out and the inhibitory potential remained constant over time (figure 3.37). Moreover, an artificial influence of the N-terminal Fmoc protection group, which was used for photometric determination of the concentration, was excluded, since Fmoc-valine did not influence Taspase cleavage.

Since Taspase inhibitors addressing only the S-site of Taspase displayed only weak inhibition [69], the role of the S'-site was explored. To this end, the P'-position was changed from glycine to a structurally related isoaspartate. This small structural change indeed caused a twofold weaker inhibition (K_i = 6.8 ± 1.1 µM), which pinpoints the importance of the S'-site for tight inhibitor binding.

Moreover, derivatization of the inhibitory succinimide motif showed that an extension of the 5-membered succinimide motif (K_i = 4.3 ± 1.3 µM) to a 6-membered glutarimide ring yielded a compound with similar inhibitory potential (K_i = 1.6 ± 0.3 µM). However, it should be noted, that although glutarimide is the most probable conformation of the compound, a nucleophile reaction of the glutamate with the preceding NH backbone group cannot be excluded by the LC-MS spectra.

Surprisingly, the most potent inhibitor was a succinimide derivative with a photoreactive benzophenone (Comp9; K_i = 0.4 ± 0.09 µM). This compound represents the most potent Taspase inhibitor described so far. Compared with the next best published inhibitor, the noncompetitive bisarsonic acid NSC48300 [63], its K_i value is tenfold better and it does not rely on the toxic arsenic acid moiety.

Despite its promising inhibitory effect *in vitro*, the inhibitory effect in cell lysates with overexpressed GFP-Taspase was 30-fold lower (IC_{50} = 111 µM). Regarding this, the chloride concentration of 150 mM NaCl in the lysis buffer is to be considered, which was not present in the *in vitro* assay. Chloride is known to bind to the active site and therefore inhibit Taspase competitively [56]. For this reason, the presence of a chloride ion in the active site is also expected to compete with substrate analog inhibitors. This hypothesis is supported by the lower affinity of Comp9 in the presence of 450 mM NaCl (22.1 µM), compared to the salt free binding affinity (0.4 ± 0.09 µM). Consequently, sophisticated equations are needed to describe this system with three ligands (substrate, inhibitor, chloride) binding competitively to one binding site. However, if the substrate concentration is kept constant, the Cheng-Prusoff equation [124] can be applied in a modified form to estimate the salt influence on inhibitor binding using the known chloride affinity (68 ± 7 mM; supplemental figure 7.12).

$$\frac{IC_{50_{no\_salt}}}{IC_{50_{salt}}} = \frac{K_d(Cl^-)}{K_d(Cl^-) + [Cl^-]}$$

This shows that 30 % of the 30-fold lower inhibitory effect in lysates can be attributed to higher salt concentrations. However, to explain the remaining 70 %, corresponding to a 10-fold reduction of the inhibitory effect, other factors need to be taken into account. In particular, the six peptide bonds of the inhibitor might be cleaved by other proteases, since the protease inhibitors present in the lysis buffer cannot guarantee complete inhibition. Moreover, unspecific binding to other proteins can lower the efficiency of the inhibitor. Nevertheless, these studies confirmed that the succinimide inhibitors inhibit eukaryotic Taspase in cell lysates, although the inhibitory potential is rather weak.

Another application of the photoreactive inhibitor derivative (Comp9) is activity based protein profiling (ABPP). For this, the compound was added to Hela cell lysate spiked with 5 µM recombinant Taspase. Subsequent cross-linking of the inhibitor and attachment of a fluorescent dye allowed detection of all proteins interacting with the inhibitor by fluorescence imaging (figure 3.38). The SDS-PAGE gel reveals only two bands corresponding to the sizes of full-length Taspase and the α-subunit. Here, the band for the full-length enzyme can either represent an interaction with the proenzyme, or more likely an interaction with the SDS-resistant αβ-dimer (see section 4.1.3). Furthermore, the absence of other bands in the lysate could indicate that the inhibitor binds selectively to Taspase. However, the comparatively high concentration of 5 µM recombinant Taspase added to the lysate precludes an unequivocal exclusion of binding to less abundant off-target proteins below the detection background.

In vivo applications

For cellular applications, an inhibitor needs to cross the hydrophobic cell membrane. For this, a molecule must generally possess lipophilic groups. For small molecules, the octanol/water partition coefficient (logP) is often used to predict the likeliness of membrane passage. For the developed succinimide inhibitors, a logP value of 0.21 ± 0.91 was calculated, which indicates a good passage of the cell membrane [171]. However, other properties, such as size, the number of hydrogen bond donors and acceptors, and molar refractivity, are also important factors for cell penetration. Table 4.2 shows that the succinimide compounds fail to fulfil these criteria, also known as rule-of-five [172], mainly because of their high molecular weight.

Table 4.2 Parameters for druglikeliness of the peptidyl-succinimide inhibitors.

Parameter	Qualifying range[a]	Comp9
logP	-0.4 to 5.6[a]	2.83 ± 0.97[c]
Mw	160 to 480 Da[a]	1296 Da
Molar refractivity	40 to 130[a]	333[c]
Number of atoms	20 to 70[a]	168
H-bond donors	≤ 5[b]	9
H-bond acceptors	≤ 10[b]	15

[a] according to [171]; [b] according to [173]; [c] predicted with ChemSketch

Nevertheless, eukaryotic cells were assayed for the ability to take up a fluorescent derivative of the succinimide compounds. Unexpectedly, the compound was indeed able to cross the cell membrane and was found evenly distributed in the cells after 5 hours (figure 3.39c). Importantly, the uptake was more than twofold higher if the cells were incubated in serum-free medium. Hence, a fraction of the inhibitor is obviously either degraded or bound to serum proteins like albumin. However, the assay is only qualitative, so that the intracellular inhibitor concentration could not be determined.

Using a cellular Taspase activity assay, the inhibitory potential of the succinimide compounds was tested *in vivo*. However, these inhibitors failed to inhibit Taspase in cells after 18 hours challenge with 50 µM Comp9 (figure 3.39e). The most likely explanation for the inhibitors to be inactive *in* *vivo* despite their promising *in vitro* activity is that their size prevents sufficient internalization. Consequently, the intracellular concentrations are probably too low to cause an inhibitory effect. Furthermore, the cellular chloride concentrations of roughly 50 mM [174–176] further reduce the affinity of the inhibitor, as explicated above. Moreover, degradation or modification of the inhibitor by cellular proteases and transferases, respectively, as well as binding to off-target proteins can limit its effectiveness.

Altogether, the peptidyl-succinimide inhibitors display a novel class of Taspase inhibitors with promising *in vitro* inhibition potential. In particular, the newly discovered succinimide scaffold is expected to be useful for rational drug design in subsequent studies. Suggestions to improve the currently limited *in vivo* bioactivity of the compounds are discussed in the outlook section below.

5 Outlook

In this project, three different strategies were applied to find novel Taspase inhibitors. While the bioinformatics approach did not yield active compounds, silica nanoparticles were found to inhibit Taspase noncompetitively. However, the most promising compounds were substrate analog peptides containing a succinimide moiety, because it is not expected that selectivity is achievable for uncoated nanoparticles by rational design with the current knowledge. These compounds exhibited good inhibitory potential *in vitro*, while the *in vivo* potential was rather low. Hence, these compounds might be improved to achieve higher stability and better bioavailability. Primarily, better bioavailability requires a reduction of the molecular weight and increased hydrophobicity [172,177]. To this end, the molecular weight can be reduced by roughly 15 % by removing the N-terminal Fmoc group, which was shown to be irrelevant for binding. Cellular experiments to elucidate the Taspase consensus sequence revealed that the presence of only one of the two aspartates at P3' and P4' is sufficient for cleavage [70]. Consequently, the peptide part of the inhibitor could be shortened by the C-terminal aspartate at P4', if the P3' asparagine is replaced by aspartate. Furthermore, a substitution of the aspartic acid by benzoic acid would contribute to higher hydrophobicity and therefore increase cellular uptake. However, increased hydrophobicity also increases the risk of unspecific binding to other proteins and should therefore be tested thoroughly.

Moreover, stability and resistance against degradation by cellular proteases can be tested in cell lysates with the fluorescent derivative. If fragmentation is observed after HPLC analysis, either the side chains or the peptide backbone can be altered. With regard to the latter, a substitution of the peptide bond by N-methyl, ether, ketomethylene or retro-inverso groups is a common approach (figure 5.1; [178]).

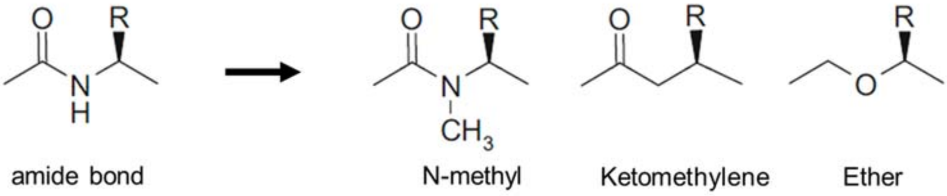

Figure 5.1 Substitutions for amide bonds.

Possible substitutions for amide bonds in peptidomimetics include N-methyl, ketomethylene and ether groups. These modifications yield higher stability and resistance against cellular proteases. According to [178].

Furthermore, side chain modifications can both stabilize the compound and improve the affinity. Especially modifications of the Cβ atom are known to reduce the susceptibility to chymotryptic cleavage [178], but also other side chain modifications are a proven tool to enhance the potential of peptidic ligands. For example, methylation, methoxy or benzyl ether modifications greatly enhanced the affinity of analogs for the neuropeptide substance P [179]. Altogether, critical evaluation of these modifications might help to enhance the *in vivo* potency of the succinimide inhibitors.

Finally, co-crystallization of Taspase and the inhibitor could reveal the active conformation of Taspase. This facilitates bioinformatics approaches and could ultimately yield potent inhibitors by virtual docking.

6 Abstract

The threonine protease Taspase1 is of high interest as new target for cancer therapeutics, due to its implication in leukemias and solid tumors. Although Taspase is not an oncogene itself, it is crucially required for the proteolytic activation of the MLL oncogene as well as MLL fusion proteins generated by chromosomal translocations. Hence, MLL-dependent cells can successfully be targeted by inhibition of Taspase activity. However, Taspase is insensitive to inhibition by general serine, cysteine or metalloprotease inhibitors. Furthermore, the limited number of available Taspase inhibitors display either low inhibitory potential or broad bioactivity. Thus, novel Taspase inhibitors are still urgently required.

In a first step, detailed characterization revealed for the first time that recombinant Taspase and protein overexpressed in eukaryotic cells are comparable with respect to their catalytic parameters.

Moreover, the specific catalytic activity (0.03 U/mg) was determined, as well as a 20-fold higher efficiency regarding cleavage of the CS2 cleavage site of MLL over CS1. Regarding stability, Taspase rapidly loses its catalytic activity (half-life < 3 h), unless it is stabilized by high concentrations of NaCl (≥ 450 mM). Additionally, the autocatalytic processing event required for catalytic competence was found to occur on a time scale of 2-3 days. The flexible loop region between glycine 178 and aspartate 233 generated by this activation event is not resolved in the crystal structure. Hence, NMR and CD spectroscopy were applied and the results suggest a helix-turn-helix structure. Furthermore, analytical gel filtration pinpointed that Taspase is active as a hetero-tetramer in solution. With these data, a fluorogenic *in vitro* assay was optimized for initial inhibitor tests.

While the controversially discussed bisarsonic inhibitor NSC48300 and compounds derived from virtual docking exhibited no inhibitory effect, both silica nanoparticles and succinimide peptides were discovered as novel Taspase inhibitors. In fact, silica nanoparticles are known to bind proteins, albeit nanoparticle-mediated inhibition of enzyme activity is scarcely described. Surprisingly, IC_{50} values in the nanomolar and picomolar range indicate high affinity binding, which was observed *in vitro* and in cells. In addition, comparison of nanoparticles with different diameters (8-125 nm) suggests a positive correlation of size and affinity. Subsequent analyses characterized the inhibition type as noncompetitive and pinpointed that Taspase does not change its structure upon binding. Importantly, inhibition by nanoparticles is no general feature, as three other enzymes (lactate dehydrogenase, chymotrypsin, and proteinase K) showed no or only weak inhibition by silica nanoparticles.

Another approach for Taspase inhibition exploited the cleavage sequence and the proposed mechanism to design substrate analog peptides with a succinimide moiety at the cleavage site. The most promising compound exhibited a K_i value of 400 ± 88 nM and displays thus a tenfold better inhibitory potential than the best reported Taspase inhibitor. Moreover, the competitive inhibition type and the resistance against Taspase cleavage were verified. However, degradation by other proteases and/or limited cellular uptake as well as competition with chloride ions prevents the *in vivo* inhibition of Taspase.

Altogether, these findings demonstrate the potential of silica nanoparticles as well as succinimide peptides as Taspase inhibitors and tools for subsequent studies.

Zusammenfassung

Die Threonin-Protease Taspase1 stellt aufgrund ihrer Beteiligung an Leukämien und soliden Tumoren einen wichtigen neuen Ansatzpunkt für Krebsmedikamente dar. Obwohl Taspase selbst kein Onkogen ist, ist sie unabdingbar für die proteolytische Aktivierung des Onkogens MLL und der durch Translokationen entstandenen MLL-Fusionsproteine. Deshalb reagieren MLL-abhängige Zellen besonders sensitiv auf Taspase-Inhibition. Allerdings sind sämtliche allgemeinen Serin-, Cystein- und Metalloprotease-Inhibitoren unwirksam gegen Taspase, und auch die wenigen verfügbaren Taspase-Inhibitoren besitzen entweder nur geringes Inhibitorpotential oder ein breites Wirkspektrum. Daher sind neue Taspase-Inhibitoren nach wie vor von hoher Relevanz.

Ein Vergleich rekombinanter Taspase mit in eukaryotischen Zellen überexprimiertem Protein zeigte eine vergleichbare spezifische katalytische Aktivität (0.03 U/mg). Weiterhin konnte eine 20-fach höhere Effizienz hinsichtlich der Spaltung der CS2-Schnittstelle von MLL gegenüber der CS1-Schnittstelle festgestellt werden. Bei Betrachtung der Proteinstabilität fiel auf, dass Taspase sehr schnell an Aktivität verliert (Halbwertszeit < 3 h), sofern das Protein nicht durch hohe Salzkonzentrationen (≥ 450 mM NaCl) stabilisiert wird. Zudem wurde für die autokatalytische Prozessierung des Proenzyms, welche wichtig zur Erlangung katalytischer Kompetenz ist, eine Zeitspanne von 2-3 Tagen ermittelt. Der dabei entstehende flexible Bereich zwischen Glycin 178 und Aspartat 233 ist in der Kristallstruktur ungeordnet, konnte aber dank NMR- und CD-Spektroskopie als potentielles Helix-Turn-Helix-Motiv identifiziert werden. Des Weiteren belegten analytische Gelfiltrationen die Aktivität von Taspase als Hetero-Tetramer. Mithilfe dieser Informationen wurde ein *in vitro* Assay optimiert und für Inhibitortests verwendet.

Während der kontrovers diskutierte Inhibitor NSC48300 und die mittels virtuellen Dockings ermittelten Substanzen keine Inhibition zeigten, konnten Silikatnanopartikel und Succinimid-Peptide als neue Taspase-Inhibitoren identifiziert werden. Obwohl Proteinbindung an Nanopartikel bekannt ist, ist eine durch diese vermittelte Enzyminhibition kaum beschrieben. Umso überraschender sind die IC_{50}-Werte im nano- und picomolaren Bereich, die sowohl *in vitro* als auch in Zellen beobachtet wurden. Weiterhin konnte mit verschiedenen Nanopartikelgrößen eine positive Korrelation von Durchmesser und Affinität belegt werden. Weitere Analysen ergaben eine nichtkompetitive Inhibition und keine Strukturänderung bei Bindung. Bemerkenswerterweise stellt Enzyminhibition keine generelle Eigenschaft von Nanopartikeln dar, da drei Kontrollenzyme (Lactatdehydrogenase, Chymotrypsin und Proteinase K) kaum durch Nanopartikel inhibiert wurden.

In einem anderen Ansatz wurde die Taspase-Schnittsequenz und der vermutete Mechanismus für das Design peptidischer Substratanaloga mit Succinimid-Motiv an der Schnittstelle genutzt. Die beste Verbindung zeigte einen K_i-Wert von 400 ± 88 nM und ist damit ein zehnfach besserer Hemmstoff als der beste zuvor beschriebene Taspase-Inhibitor. Des Weiteren konnte die kompetitive Hemmung und die Stabilität gegenüber Abbau durch Taspase gezeigt werden.

Allerdings verhindern schlechte Zellaufnahme und/oder Abbau durch andere Proteasen sowie Kompetition mit Chlorid-Ionen eine Inhibition *in vivo*.

Insgesamt belegen diese Ergebnisse das Potential von Silikatnanopartikel sowie Succinimid-Peptiden als Taspase-Inhibitoren und Werkzeuge für nachfolgende Studien.

7 Supplement

7.1 Recording and processing of NMR spectra

Table 7.1 Pulses used to record NMR spectra.

Pulse	Power level [W]	Length	Description
p1	7.8239	20.86 µs	^{1}H 90° high power pulse
p3	40.617	18 µs	^{13}C 90° high power pulse
p21	89.492	35.5 µs	^{15}N 90° high power pulse
pcpd1	0.17596	50 µs	^{1}H DIPSI-2 decoupling
pcpd2	3.6535	60 µs	^{13}C decoupling
pcpd3	4.352	180 µs	^{15}N GARP decoupling
sp1	0.00039212		^{1}H 90° shaped pulse for H_2O on resonance
sp2	53.544		^{13}C 90° shaped pulse for C_{ali} on resonance
sp3	47.381		^{13}C 180° shaped pulse for C_{ali} on resonance
sp5	47.381		^{13}C 180° shaped pulse for C=O off resonance
sp8	53.544		^{1}H 90° shaped pulse for time reversed pulse
d1		2 s	relaxation delay
d9		90 µs	TOCSY mixing time

Table 7.2 Recording parameters for NMR spectra.

Spectrum **pulse program**	F1					F2					F3				
	nuc	SWH [ppm]	O1 [ppm]	TD	AQ-mode*	nuc	SWH [ppm]	O1 [ppm]	TD	AQ-mode*	nuc	SWH [ppm]	O1 [ppm]	TD	AQ-mode*
^{1}H-^{15}N HSQC **hsqcetf3gpsi2**	^{15}N	40	115	256	DQD	^{1}H	16.08	4. 695	1024	E-AE	-	-	-	-	-
sofast-HMQC **sfhmqcf3gpph**	^{15}N	34	115	200	DQD	^{1}H	15	4. 695	1024	STPPI	-	-	-	-	-
^{15}N-TOCSY-HSQC **dipsihsqc3gpsi3d**	^{1}H	15.94	4.695	128	STPPI	^{15}N	39	119	48	STPPI	^{1}H	16	4.696	2048	DQD
HNCACB **hncacbgpwg3d**	^{13}C	80	39	128	STPPI	^{15}N	34	119	40	STPPI	^{1}H	15	4.696	2048	DQD
CBCACONH **cbcaconhgpwg3d**	^{13}C	75	39	128	STPPI	^{15}N	34	119	36	STPPI	^{1}H	15	4.696	2048	DQD
HBHANH **hbhanhgpwg3d**	^{1}H	15	4.695	128	STPPI	^{15}N	34	119	40	STPPI	^{1}H	8	4.695	2048	DQD
HBHACONH **hbhaconhgpwg3d**	^{1}H	15	4.695	128	STPPI	^{15}N	34	119	40	STPPI	^{1}H	8	4.695	2048	DQD
HCCH-TOCSY **hcchdigp3d**	^{1}H	8	4.695	128	STPPI	^{13}C	75	39	64	STPPI	^{1}H	16	4.695	2048	DQD
HNCA **hncagpwg3d**	^{13}C	32	54	64	STPPI	^{15}N	30	117	40	STPPI	^{1}H	8.4	4.695	2048	DQD

* E-AE: Echo-Antiecho; STPPI: States-TPPI

Table 7.3 Processing parameters for NMR spectra.

	F1					F2					F3				
Spectrum	nuc	SI [ppm]	MC2*	REV	WDW	nuc	SI [ppm]	MC2*	REV	WDW	nuc	SI [ppm]	MC2*	REV	WDW
^{15}N-HSQC	^{15}N	2048	E-AE	False	Qsine	^{1}H	4096	-	False	Qsine	-	-	-	-	-
sofast-HMQC	^{15}N	1024	STPPI	False	Qsine	^{1}H	2048	-	False	Qsine	-	-	-	-	-
^{15}N-TOCSY-HSQC	^{1}H	256	STPPI	False	Qsine	^{15}N	128	E-AE	False	Qsine	^{1}H	1024	-	False	Qsine
HNCACB	^{13}C	256	STPPI	False	Qsine	^{15}N	128	STPPI	True	Qsine	^{1}H	2048	-	False	Qsine
HBHACONH	^{13}C	256	STPPI	False	Qsine	^{15}N	64	STPPI	True	Qsine	^{1}H	2048	-	False	Qsine
HBHANH	^{1}H	256	STPPI	False	Qsine	^{15}N	128	STPPI	True	Qsine	^{1}H	2048	-	False	Qsine
HBHACONH	^{1}H	128	STPPI	False	Qsine	^{15}N	64	STPPI	True	Qsine	^{1}H	2048	-	False	Qsine
HCCH-TOCSY	^{1}H	512	STPPI	False	Qsine	^{13}C	256	STPPI	False	Qsine	^{1}H	2048	-	False	Qsine
HNCA	^{13}C	128	STPPI	False	Qsine	^{15}N	64	STPPI	True	Qsine	^{1}H	1024	-	False	Qsine

* E-AE: Echo-Antiecho; STPPI: States-TPPI

7.2 Bacterial vector maps

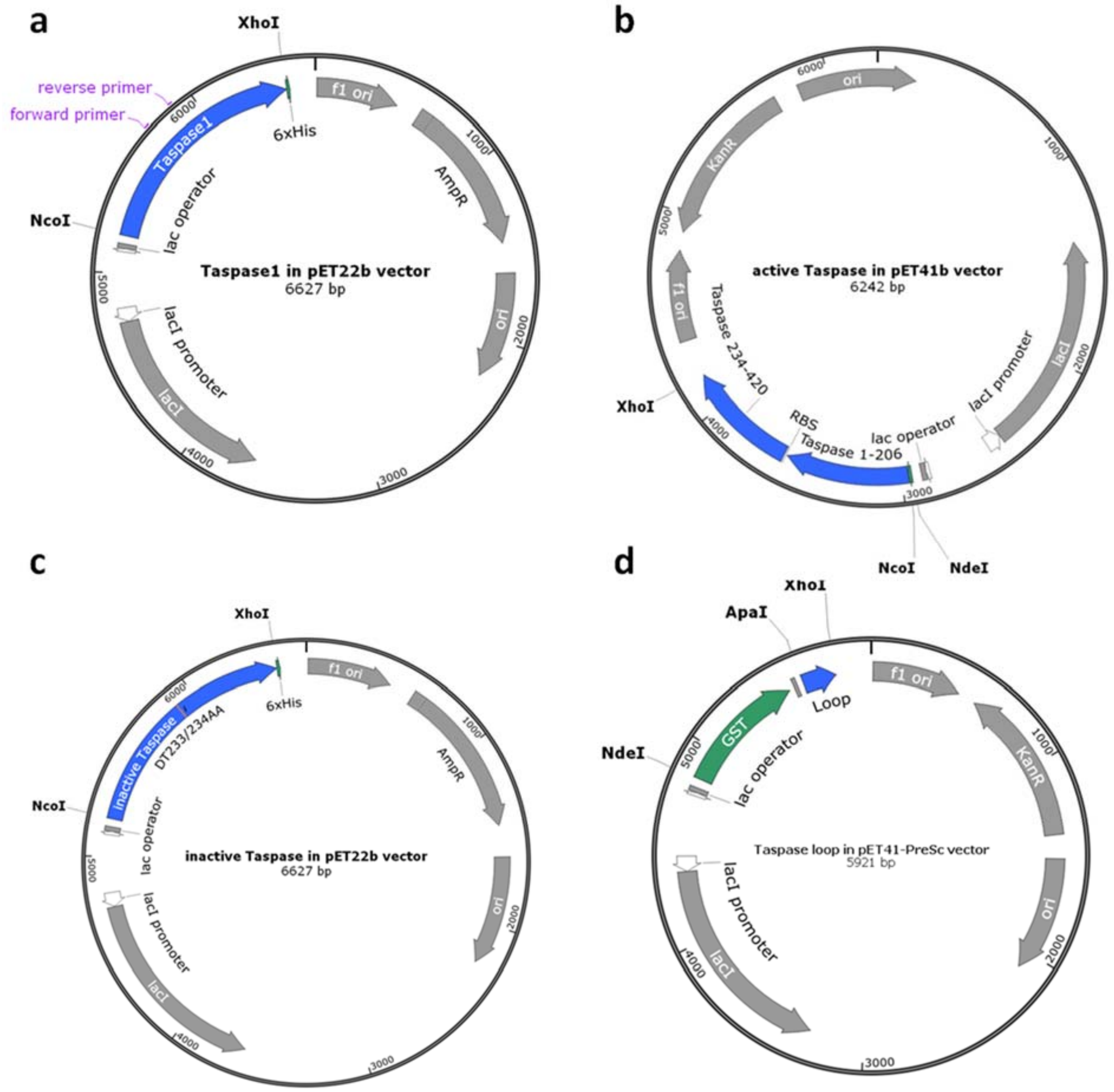

Figure 7.1 Maps of bacterial expression vectors.

a Map of the modified pET-22b vector containing wild type Taspase with C-terminal His-tag. Primer binding sites for the loop cloning are indicated. **b** Map of the modified pET-41b vector containing active Taspase with N-terminal His-tag. The ribosomal binding site (RBS) between the two subunits has the sequence "AGGAGG". **c** Map of the modified pET-22b vector containing inactive Taspase mutant with C-terminal His-tag. D233 and T234 at the active site were mutated to A233 and A234, respectively. **d** Map of the modified pET-41b vector containing the Taspase loop (G178-D233) with N-terminal GST-tag. All vectors are IPTG-inducible and resistance genes as well as restriction sites used for cloning are indicated.

7.3 Eukaryotic vector maps

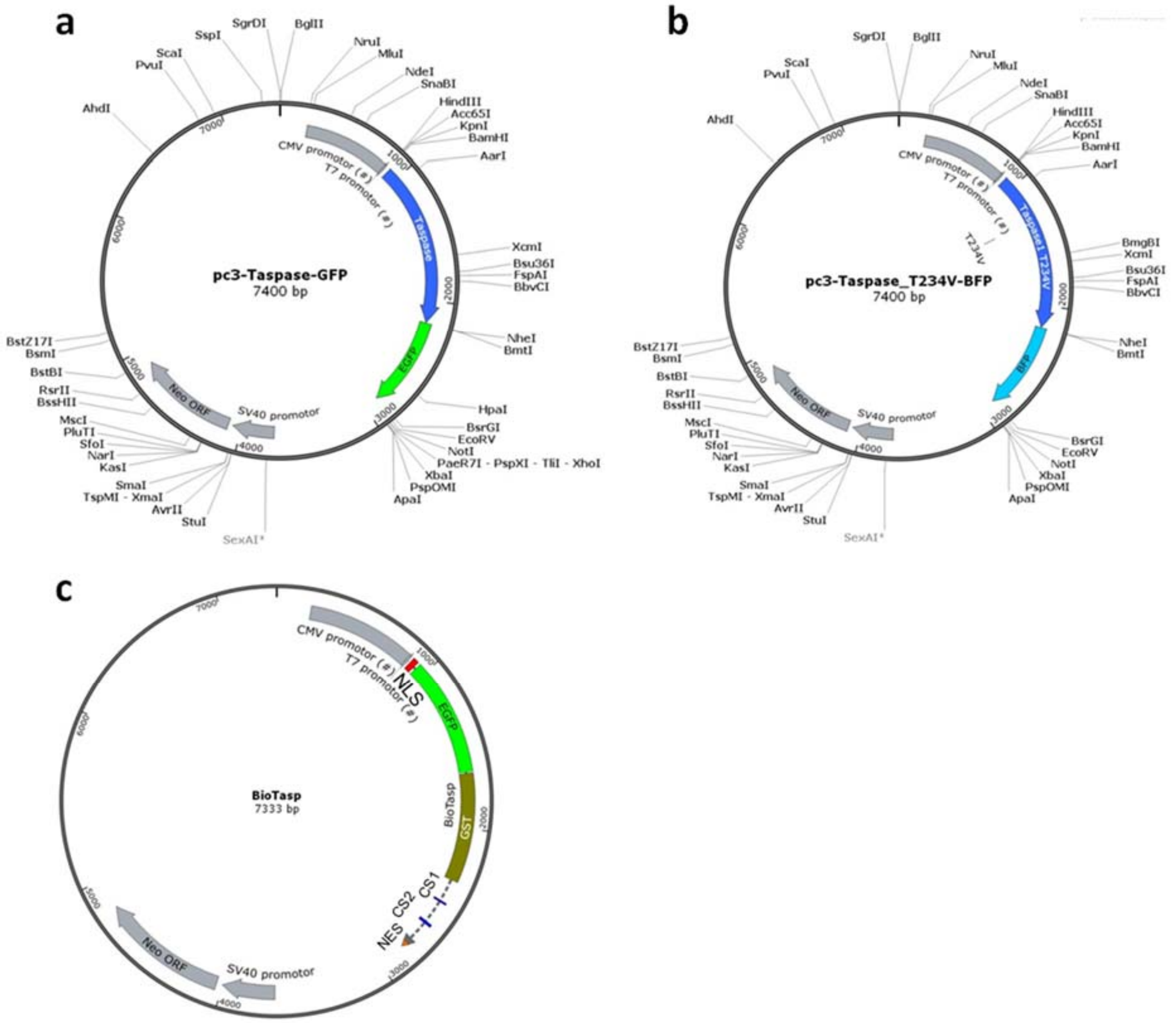

Figure 7.2 Maps of eukaryotic vectors used for transfection.

a Map of the pC3 vector containing wild type Taspase with C-terminal eGFP. **b** Map of the pC3 vector containing inactive Taspase (T234V) with C-terminal BFP. **c** Map of the pC3 vector containing the reporter substrate (BioTasp) used for the cellular Taspase activity assay. The coded protein comprises a nuclear localization signal (NLS), eGFP, glutathione S-transferase (GST), CS1 Taspase cleavage site (CS1), CS2 Taspase cleavage site (CS2) and a reverse nuclear export signal (NES). Resistance genes and restriction sites are indicated.

7.4 Taspase loop cloning scheme

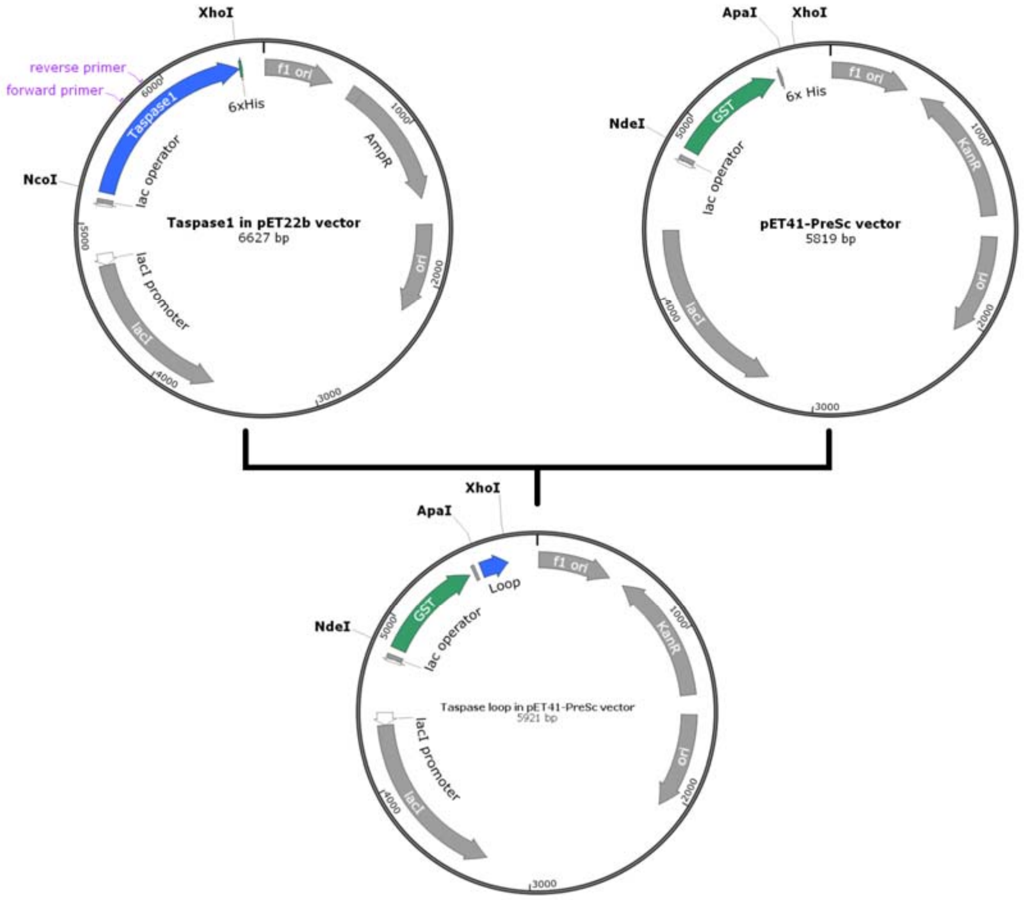

Figure 7.3 Schematic for cloning of the Taspase loop.

The Taspase loop was amplified from the plasmid for wild type Taspase (top left panel) by PCR using primers with binding sites indicated in purple. The target vector (top right panel) was digested with ApaI and XhoI. Respective restriction sites are indicated. Vector and insert were ligated, yielding the Taspase loop with N-terminal GST tag (lower panel).

7.5 Purification of Taspase

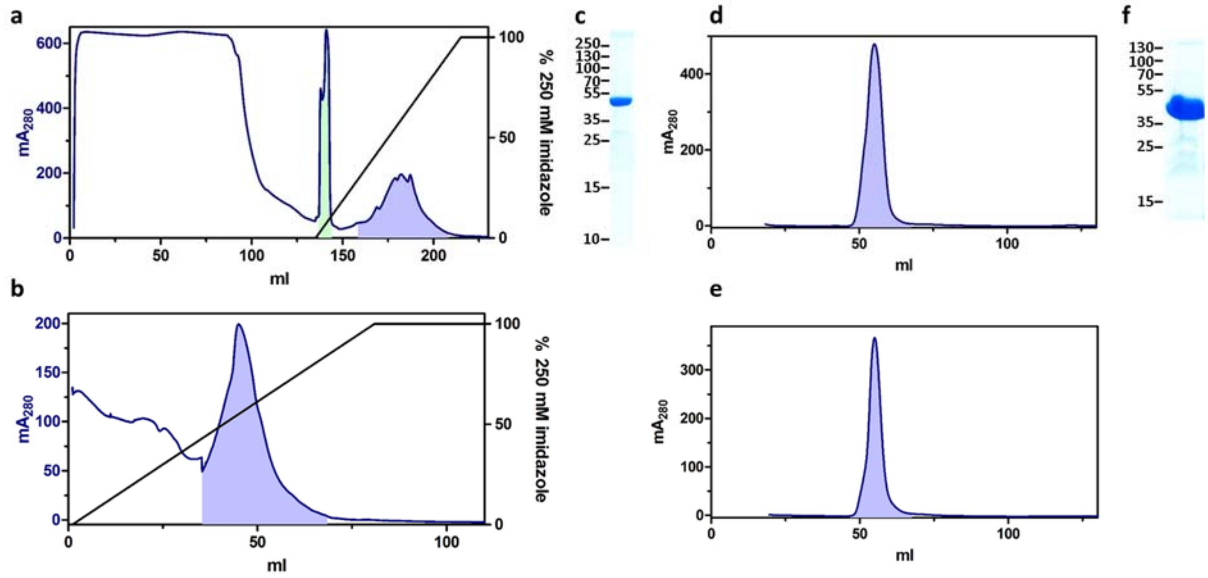

Figure 7.4 Purification of the inactive Taspase mutant.

Purification of inactive Taspase was performed as described for wild type Taspase (section 3.1.3). **a** Chromatogram of the NiNTA column elution. The fractions highlighted in blue were used for gel filtration, while the fractions highlighted in green were purified again by NiNTA affinity chromatography. **b** Chromatogram of the NiNTA affinity chromatography of the peak highlighted green in (a). Fractions highlighted in blue were used for gel filtration. **c** The SDS-PAGE gel shows inactive Taspase with minor impurities after NiNTA affinity chromatography. **d** and **e** show gel filtration chromatograms after NiNTA affinity chromatography runs displayed in (a) and (b), respectively. The fractions highlighted in blue were concentrated, shock frozen and stored at -20 °C. **f** The SDS-PAGE gel confirms pure inactive Taspase after gel filtration.

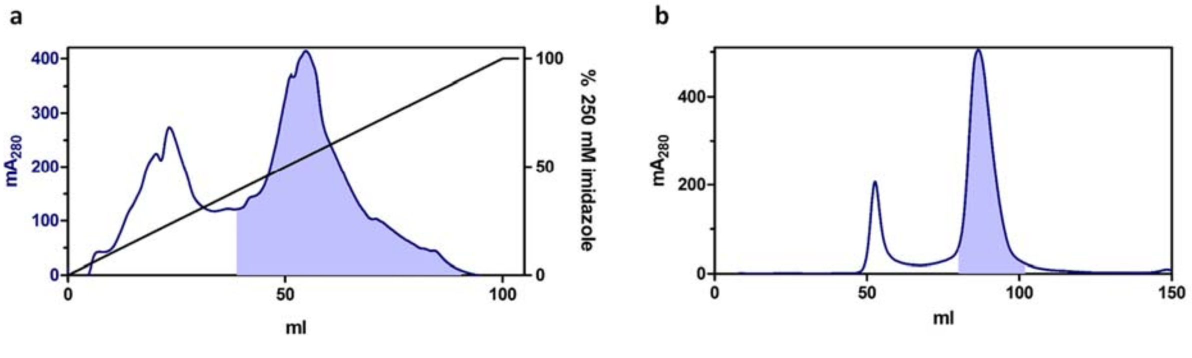

Figure 7.5 Purification of the first elution peak after NiNTA affinity chromatography.

As the first elution peak after NiNTA affinity chromatography contained a significant amount of impure Taspase (section 3.1.3), the peak fractions were diluted to reduce the imidazole concentration to 10 mM and again applied to a NiNTA column. All parameters were taken from the first purification, described in section 3.1.3. **a** Chromatogram of the NiNTA column elution. The fractions highlighted in blue were concentrated and gel filtrated as described in the main text (section 3.1.3). **b** Chromatogram of the subsequent gel filtration. The fractions highlighted in blue were concentrated to 18 mg/ml and stored at -20 °C.

7.6 Expression test of active Taspase

The bicistronic construct for active Taspase comprises the amino acids 1 to 206 (His-tagged α-subunit) and amino acids 234 to 420 (β-subunit; figure 2.3). Initial expression tests showed poor solubility of both subunits, as well as degradation, when expressed longer than 3 hours, plus an increased number of dead cells. This hints at a potential toxicity of the expressed protein. Hence, expression was optimized in the C43(DE3)pLysS strain, which is effective in expressing toxic proteins.

Additionally to the three temperatures (20 °C, 30 °C, 37 °C) and the three expression times (3 h, 6 h, over night), the combination of high cell density (OD_{600}=1.5) and short expression time was tested. The respective SDS gels of pellet and supernatant fractions after ultracentrifugation are shown in figure 7.6.

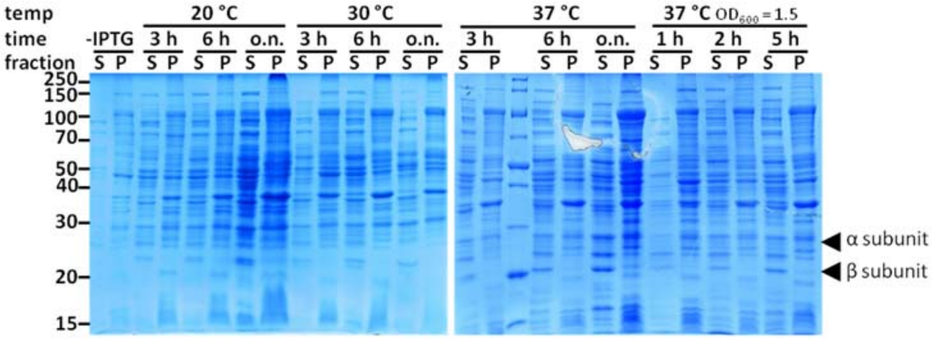

Figure 7.6 SDS-PAGE gels of expression test for active Taspase.

Expression of active Taspase was tested in *E. coli* BL21(DE3)T1r cells at 20 °C, 30 °C and 37 °C after 3 h, 6 h and over night (o.n.). Additionally, expression levels at 37 °C were analyzed 1 h, 2 h and 5 h after induction of cells with an OD_{600} of 1.5 (37 °C OD_{600}=1.5). Supernatant (S) and pellet fractions (P) were compared to a sample before induction by IPTG (-IPTG) and indicated optimum expression conditions at 37 °C after 6 h or over night. The expected sizes of α-subunit (α) and β-subunit (β) are indicated by arrows.

The highest expression levels of soluble protein are achieved at 37 °C after 6 h or over night. Nevertheless, it should be noted that the total amount of active Taspase is significantly lower than for wild type protein.

7.7 Calibration for analytical gel filtration

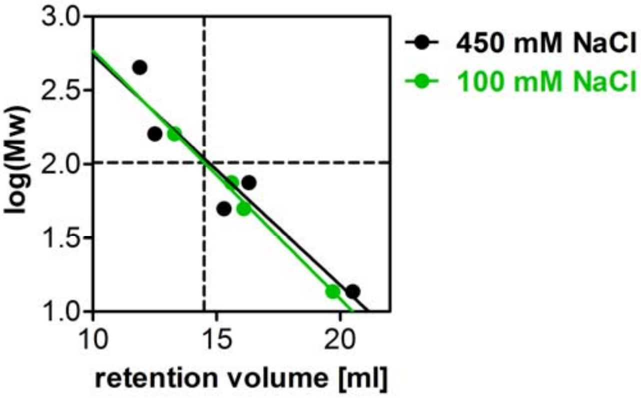

Figure 7.7 Calibration plot for Superdex 200 10/300.

Calibration was performed with gel filtration buffer (section 2.1.3) containing 100 or 450 mM NaCl (green and blue, respectively). Ferritin (450 kDa), aldolase (161 kDa), conalbumin (75 kDa), α-amylase (54 kDa) and ribonuclease A (13.7 kDa) were used as references. Elution volumes were plotted against the logarithmic molecular weight and linear regression was performed. The dashed lines indicate the elution volume (14.5 ml) and corresponding log(Mw) (2.01 = 102 kDa).

7.8 Analytical gel filtration with lower salt conditions

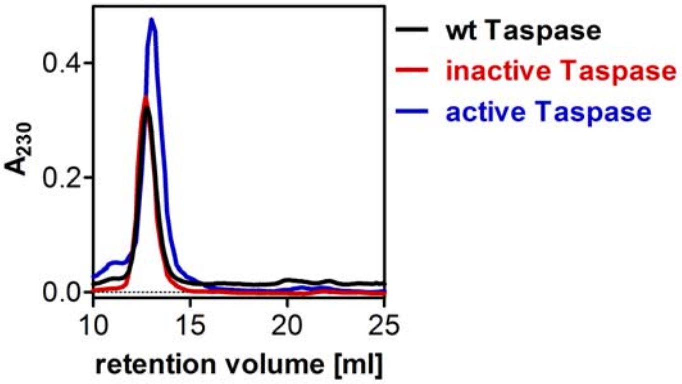

Figure 7.8 Analytical gel filtration of Taspase with 100 mM NaCl.

Analytical gel filtrations with wild type (wt), inactive and active Taspase were performed as described in the main text (section 3.2.4). Wild type and inactive Taspase show an apparent molecular weight of around 100 kDa, while the shorter active Taspase elutes at around 90 kDa.

7.9 NMR shifts of Taspase

Table 7.4 NMR shifts for wild type Taspase.

Shift values are presented in ppm.

aa	Res	HN	N	Cα	Cβ	Hα	Hβ	Hγ	Hδ	Hε
9	Ser	8.379 ± 0.004	117.112 ± 0.142	58.552 ± 0.096	64.041 ± 0.199	4.499 ± 0.005	3.894 ± 0.029	-	-	-
10	Gly	8.382 ± 0.006	110.706 ± 0.097	45.332 ± 0.078	-	3.95 ± 0.017	-	-	-	-
11	Glu	8.223 ± 0.005	120.5 ± 0.049	56.763 ± 0.055	30.194 ± 0.015	4.259 ± 0.007	1.997 ± 0.017	2.197 ± 0.042		
12	Gly	8.386 ± 0.003	109.791 ± 0.086	45.18 ± 0.011	-	3.914 ± 0.02	-	-	-	-
13	Leu	7.994 ± 0.005	122.667 ± 0.032	53.124 ± 0.028	41.668	4.599 ± 0.011	1.594 ± 0.009	1.533	0.896 ± 0.002	-
23	Gly	8.263 ± 0.005	107.765 ± 0.036	45.327 ± 0.005	-	3.912 ± 0.011	-	-	-	-
24	Lys	8.02 ± 0.004	120.824 ± 0.055	56.274 ± 0.054	33.037 ± 0.083	4.305	1.72 ± 0.01	1.382	-	3.006
25	Ile	8.15 ± 0.006	122.453 ± 0.08	61.219 ± 0.057	38.712 ± 0.114	4.206 ± 0.002	1.831 ± 0.027	1.258 / 1.463	-	-
26	Thr	8.2 ± 0.004	118.662 ± 0.061	61.838 ± 0.079	70.13 ± 0.084	4.32 ± 0.012	-	-	1.164	-
27	Ala	8.287 ± 0.005	126.192 ± 0.059	52.94 ± 0.091	19.053 ± 0.094	4.238 ± 0.027	1.36 ± 0.019	-	-	-
28	Lys	8.187 ± 0.003	120.311 ± 0.069	-	-	4.21 ± 0.015	1.716 ± 0.022	-	-	-
32	Thr	8.06 ± 0.003	115.009 ± 0.064	62.212 ± 0.055	69.791 ± 0.074	4.265 ± 0.008		1.091	-	-
33	Lys	8.219 ± 0.004	123.407 ± 0.104	56.576 ± 0.081	32.539	4.259	1.741 ± 0.007		-	-
34	Gln	8.331 ± 0.003	121.675 ± 0.047	56.822 ± 0.08	30.11 ± 0.13	4.214 ± 0.007	1.978 ± 0.019	2.202	-	-
221	Gln	8.281 ± 0.002	122.044 ± 0.021	56.506 ± 0.128	29.762	4.299 ± 0.028	2.02 ± 0.013	-	-	-
222	Ser	8.213 ± 0.006	116.916 ± 0.11	58.492 ± 0.012	63.854	-	3.817	-	-	-
223	Ser	8.322 ± 0.009	117.672 ± 0.154	58.731 ± 0.131	63.948	-	3.899 ± 0.02	-	-	-
224	Glu	8.37 ± 0.007	122.597 ± 0.119	56.784 ± 0.054	30.032 ± 0.025	4.25 ± 0.012	1.79 ± 0.009	-	-	-
225	Lys	8.181 ± 0.003	121.261 ± 0.157	56.585 ± 0.113	32.936	4.262 ± 0.016	1.735 ± 0.011	-	-	-
226	Glu	8.282 ± 0.003	121.292 ± 0.072	57.157 ± 0.007	29.807	4.202 ± 0.004	2.02 ± 0.021	2.223	-	-
227	Asn	8.368 ± 0.004	119.275 ± 0.056	53.357 ± 0.041	39.106 ± 0.031	4.159	2.772 ± 0.011	-	-	-
228	Asp	8.302 ± 0.008	121.214 ± 0.057	54.354 ± 0.096	41.452 ± 0.072	-	2.675 ± 0.013	-	-	-
229	Ser	8.298 ± 0.002	116.311 ± 0.091	58.872 ± 0.131	63.95 ± 0.134	4.433 ± 0.006	3.88 ± 0.013	-	-	-
230	Gly	8.431 ± 0.004	110.723 ± 0.151	45.496 ± 0.068	-	3.965 ± 0.021	-	-	-	-
231	Thr	7.959 ± 0.006	113.633 ± 0.051	61.926 ± 0.078	70.004 ± 0.124	4.323 ± 0.023	4.03 ± 0.005	1.171 ± 0.012	-	-
232	Leu	8.287 ± 0.003	124.764 ± 0.116	55.2 ± 0.062	42.366 ± 0.151	4.388 ± 0.014	1.616 ± 0.014	1.585	0.84 / 0.889	-
233	Asp	7.837 ± 0.004	126.462 ± 0.032	55.802 ± 0.053	42.484 ± 0.072	4.337	2.529 / 2.589	-	-	-
251	Ser	8.284 ± 0.004	119.094 ± 0.067	58.483 ± 0.095	63.81 ± 0.002	4.39 ± 0.022	3.84 ± 0.015	-	-	-
428	His	8.014 ± 0.056	125.365 ± 0.085	-	-	-	3.095 ± 0.026	-	-	-

7.10 ^{1}H-^{15}N HSQC spectra of Taspase

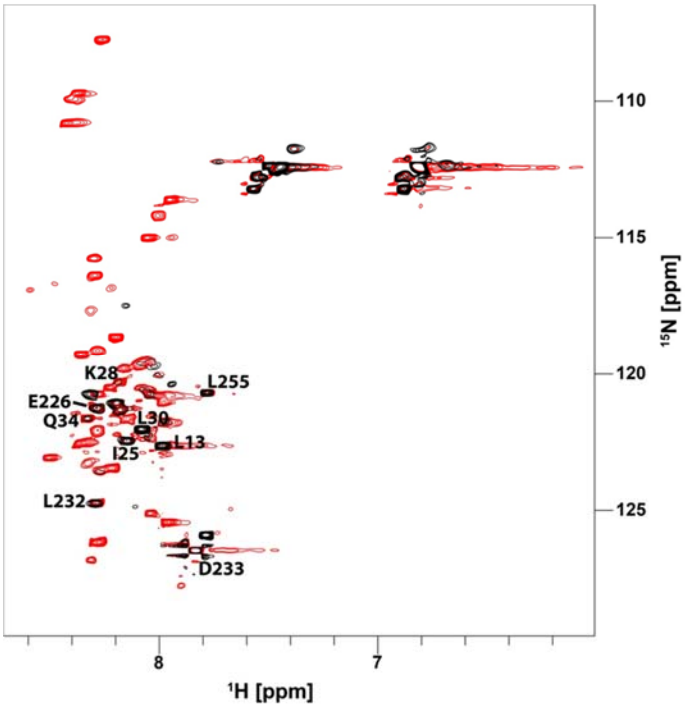

Figure 7.9 Time dependence of the Taspase NMR spectra.

^{1}H-^{15}N HSQC spectra of wild type Taspase were recorded of freshly thawed protein (black) and after one week (red). Peaks of the freshly thawed protein are labeled; a labeling of all assigned peaks can be found in figure 3.12a.

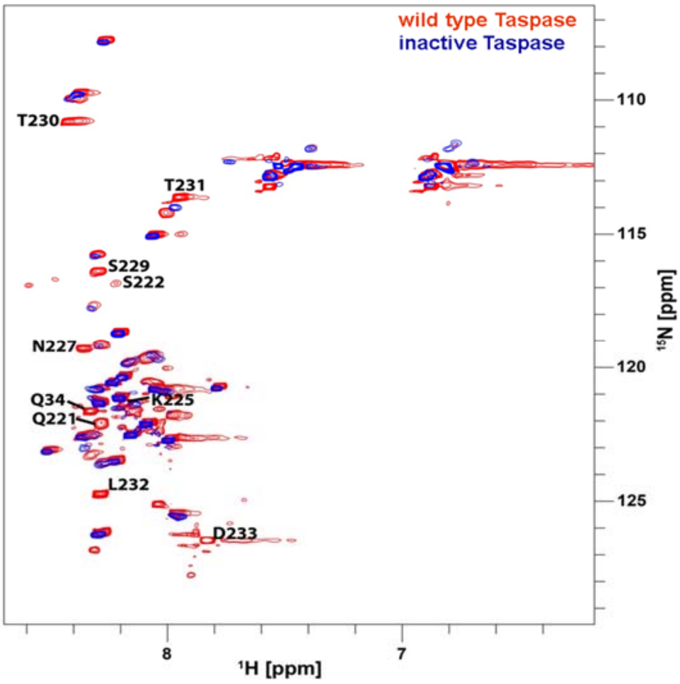

Figure 7.10 Comparison of wild type and mutant Taspase.

^{1}H-^{15}N HSQC spectra of wild type Taspase (red) and inactive Taspase (blue) after 7 days incubation at 30 °C. All backbone peaks of the inactive mutant can be found in the spectrum of the wild type protein. The 10 peaks visible only in the wild type protein are labeled. 9 of these peaks are located in the loop which is released by autocatalytic activation. A labeling of all assigned peaks can be found in figure 3.12a.

7.11 Expression test of the GST-tagged Taspase loop

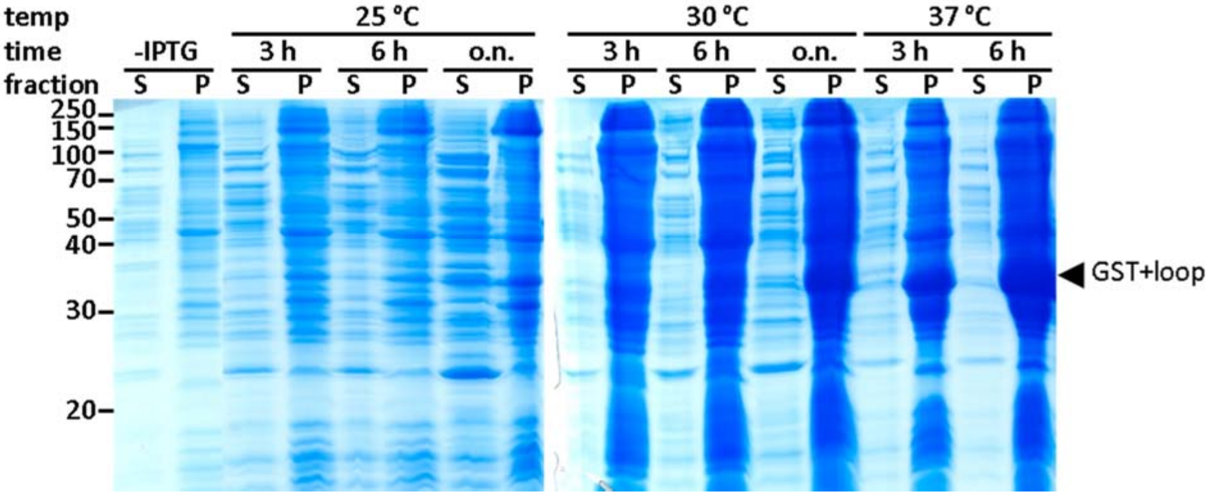

Figure 7.11 Expression test for the Taspase loop.

Expression of the GST-tagged Taspase-loop (GST-loop) was tested in LB medium at 25 °C, 30 °C and 37 °C after 3 h, 6 h and over night (o.n.). After centrifugation, supernatant (S) and pellet (P) fractions were compared to a sample before induction by IPTG (-IPTG). Optimum expression conditions with maximum GST-loop content was found for expression at 25 °C over night.

7.12 NaCl inhibits Taspase activity

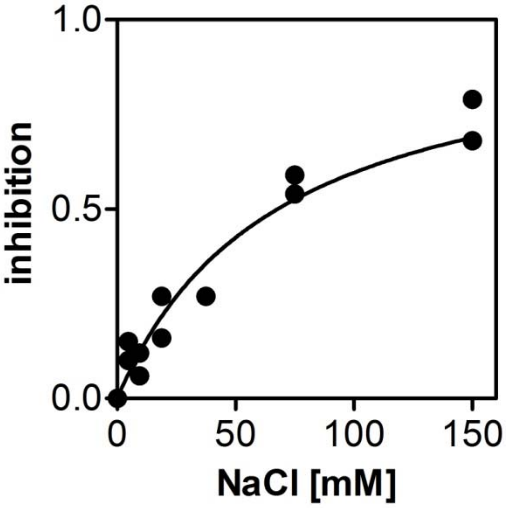

Figure 7.12 Inhibition of Taspase activity by NaCl.

Activity measurements of wild type Taspase in the presence of different NaCl concentrations confirmed an inhibitory effect of NaCl. Nonlinear fitting yielded IC_{50} = 68 ± 7 mM.

7.13 Western blot analysis of Taspase levels in human cell lysates

50 µg cell lysates and 0.5 µg recombinant wild type Taspase were separated in a 12.5 % SDS-PAGE gel. Western blotting on nitrocellulose membrane (Whatman) was performed for 45 minutes at 40 mA per gel (80 mA for 2 gels). Membranes were blocked with 5 % milk powder in TBST for

2 hours at room temperature, before the primary antibodies were added in 5 % BSA over night at 4 °C. The Taspase antibody (Origene; goat anti mouse) was diluted 1:500 and the β-actin antibody (Abgent; sheep anti rabbit) was used in a 1:250 dilution in TBST + 5 % milk powder. Subsequently, the membrane was washed three times with TBST and the respective secondary antibody (anti mouse for Taspase; anti rabbit for β-actin) was applied in a 1:10000 dilution in 5 % milk powder for 2 hours at room temperature. The membrane was washed again three times with TBST and an ECL kit (Thermo Scientific) was applied according to the manufacturer's instructions for visualization. Films (Thermo Scientific) were exposed for 2 minutes and developed using a Cawomat 2000.

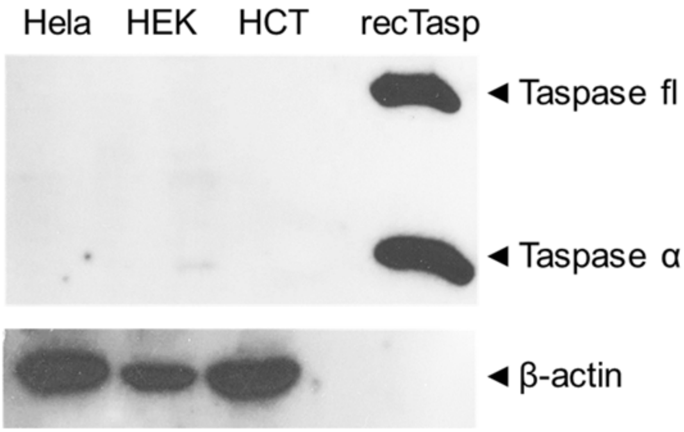

Figure 7.13 Western blot of Taspase in cell lysates.

50 µg eukaryotic cell lysates of Hela, human embryonic kidney 293T (HEK), human colon carcinoma 116 (HCT) and 0.5 µg of recombinant Taspase as positive control were separated by SDS-PAGE, blotted on a nitrocellulose membrane and Taspase was detected with a specific monoclonal antibody (upper panel). Taspase concentrations were below the detection limit in all three cell lines tested. Recombinant Taspase shows two bands, corresponding to the full-length enzyme and the α-subunit. β-actin (lower panel) was used as loading control.

7.14 ESI-LC-MS of NSC48300

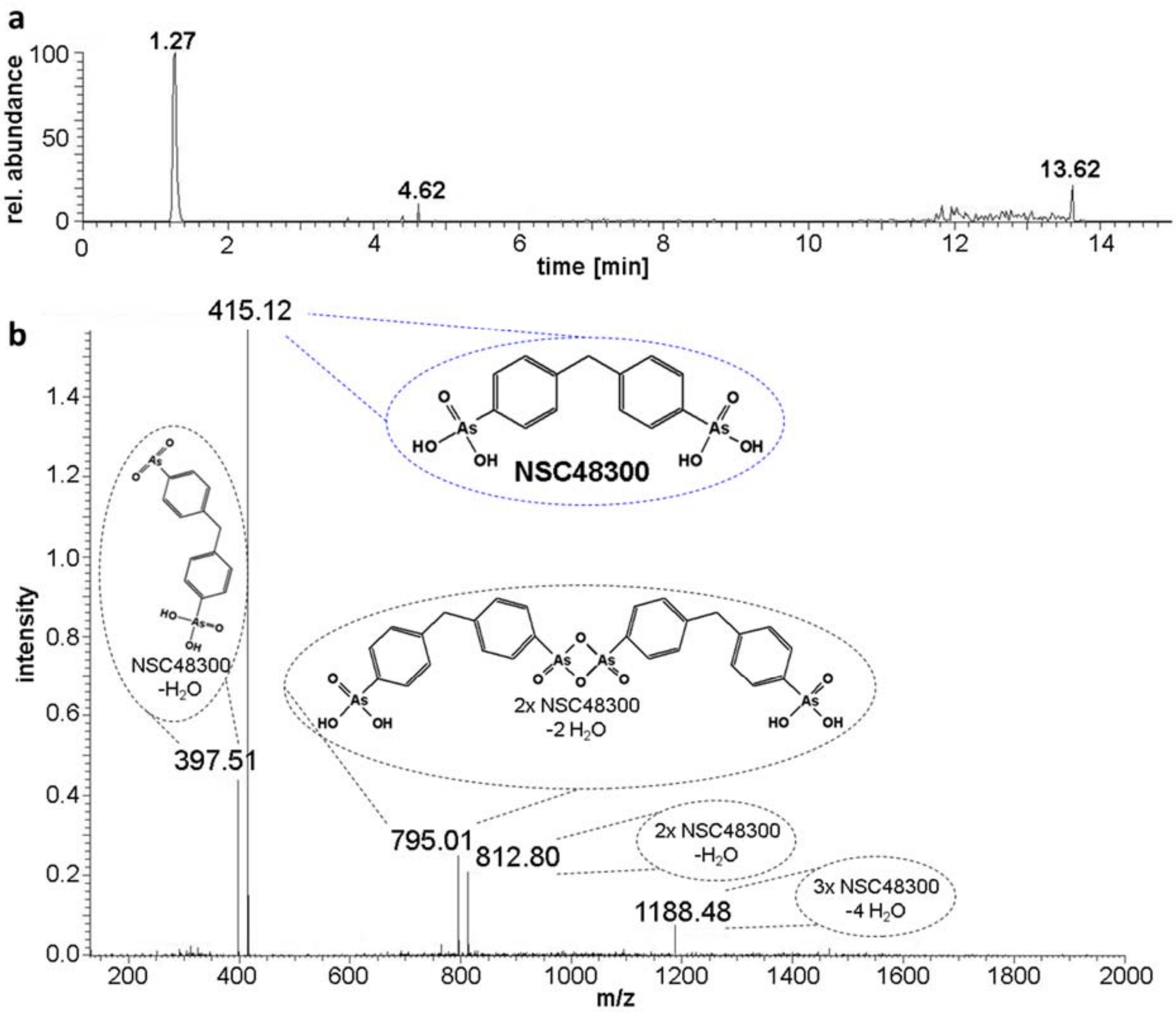

Figure 7.14 ESI-LC-MS of the Taspase inhibitor NSC48300.

a Chromatogram of the LC-MS analysis in negative mode. The peak at 1.27 min contains the NSC48300. **b** Full-range negative mode mass spectrum. Peaks are labeled with the most probable molecules and their structure. The expected mass of NSC48300 is 416 Da.

7.15 Model quality statistics

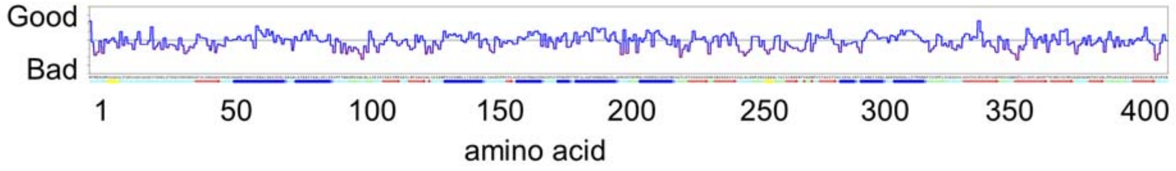

Figure 7.15 Model quality of the full-length Taspase homology model.

A homology model of full-length Taspase was generated based on the crystal structure PDB 2a8i. 75 amino acids were added to the template. Model quality (and Z score) are as follows. Dihedrals: optimal (1.317); packing 1D: satisfactory (-1.450); packing 3D: good (-0.718); overall: good (-0.708).

7.16 Binding controls with nanoparticles

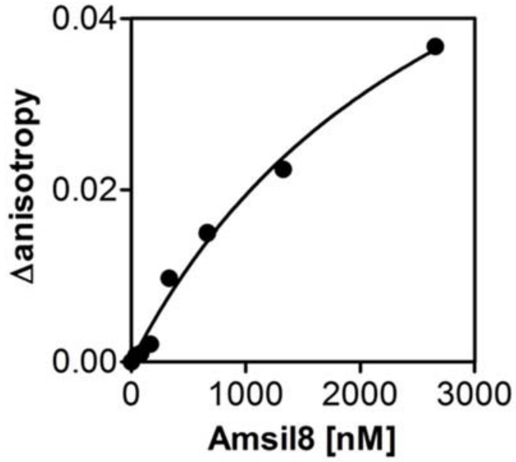

Figure 7.16 Nanoparticles bind parvalbumin with low affinity.

Anisotropy titrations of Atto488-labeled parvalbumin with Amsil8 nanoparticles yield an EC_{50} value of 3 ± 0.8 µM, which is a 300000-fold weaker interaction compared to Taspase.

7.17 Cell morphology in the presence of nanoparticles

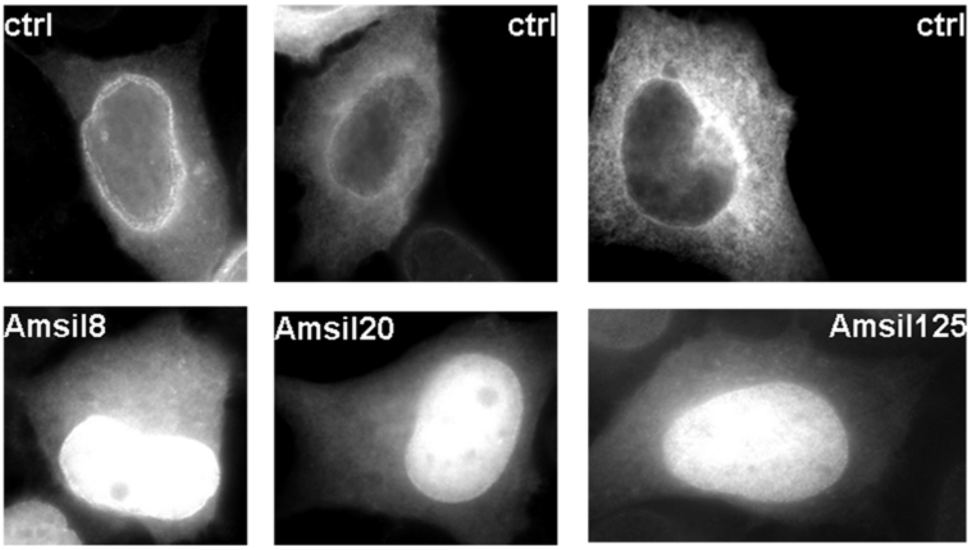

Figure 7.17 Nanoparticles do not alter cell morphology.

Cell morphology of Hela cells incubated with 200 µg/ml silica nanoparticles for 18 hours (lower panel) are similar to untreated cells (top panel; ctrl). GFP fluorescence is displayed for cell shape.

7.18 Titration curves of succinimide peptides

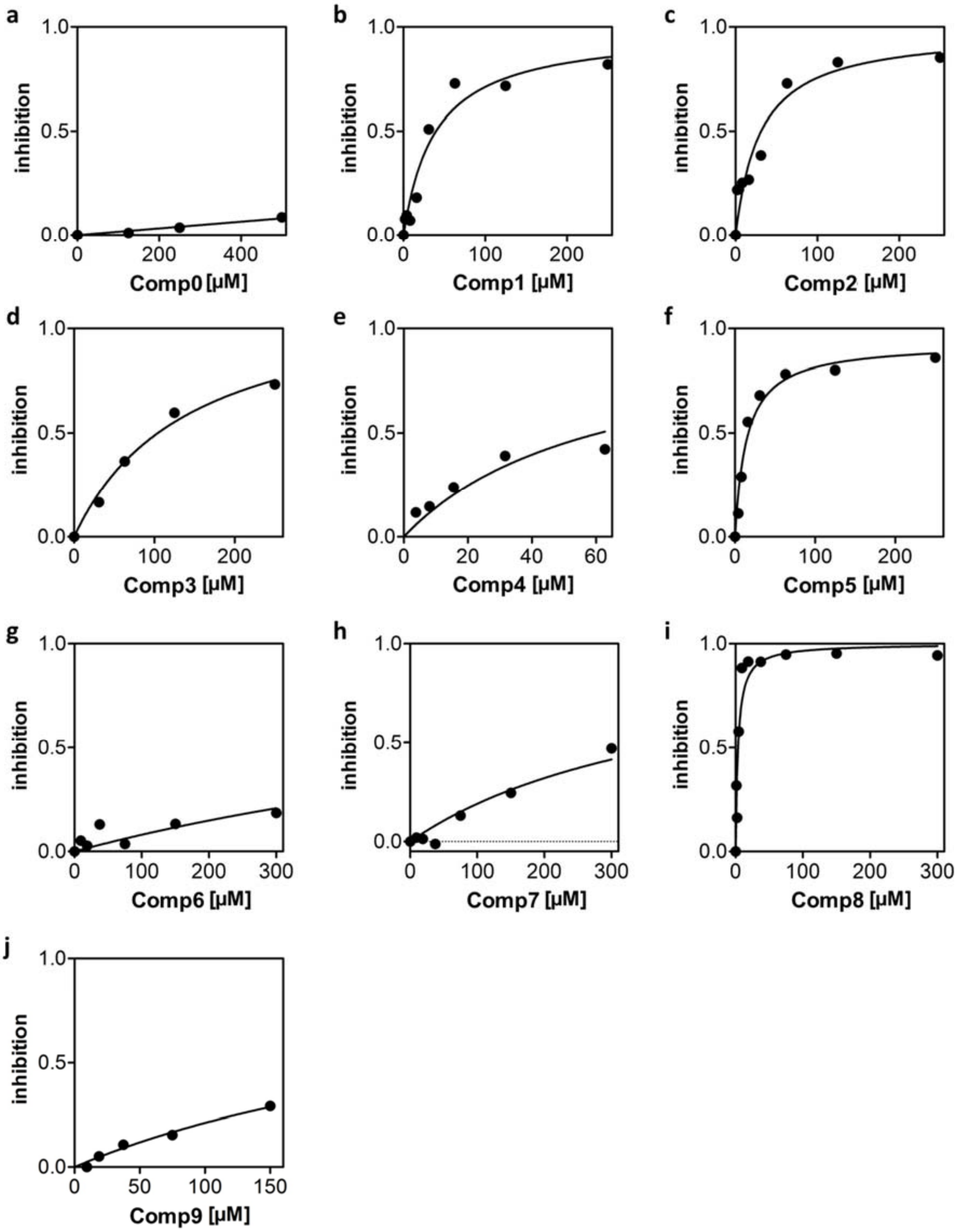

Figure 7.18 Inhibition curves of the peptidyl-succinimide peptides.

Taspase activity was tested in a fluorogenic *in vitro* assay at different inhibitor concentrations. Curves were normalized and nonlinear fitting was applied to obtain IC_{50} values. A list of the IC_{50} values and the structures of the compounds can be found in table 3.2.

7.19 Passage through 50 kDa membrane

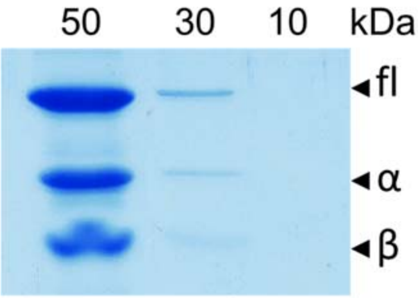

Figure 7.19 Taspase can pass a 50 kDa membrane.

Taspase was diluted in gel filtration buffer and 10-fold concentrated again in a 50 kDa Centricon. This 10-fold dilution followed by 10-fold concentration was repeated two more times. The fraction retained by the 50 kDa membrane was analyzed by SDS-PAGE (first lane). The flow-through was collected and concentrated in a 30 kDa Centricon (second lane). Subsequently, the protein was diluted 10-fold and concentrated again two times. The flow-through was concentrated in a 10 kDa Centricon before analysis (third lane). As a result, Taspase can pass a 50 kDa membrane.

7.20 Structure of the Taspase hetero-tetramer

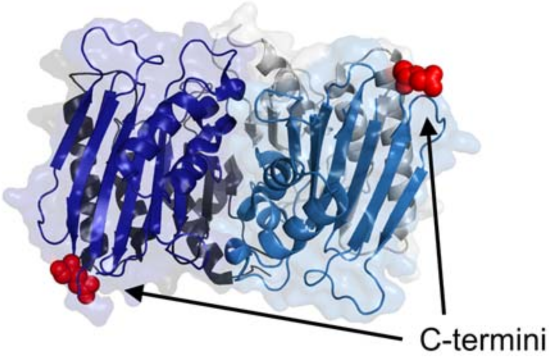

Figure 7.20 Location of the C-termini in the hetero-tetramer of Taspase.

The C-termini (red) of Taspase are located 60 Å apart at the opposite ends of the hetero-tetramer. Enforced dimerization by C-terminal tags, as performed in [68], is therefore likely to result in a dimer with different conformation.

7.21 Molecular plugs tested as Taspase inhibitors

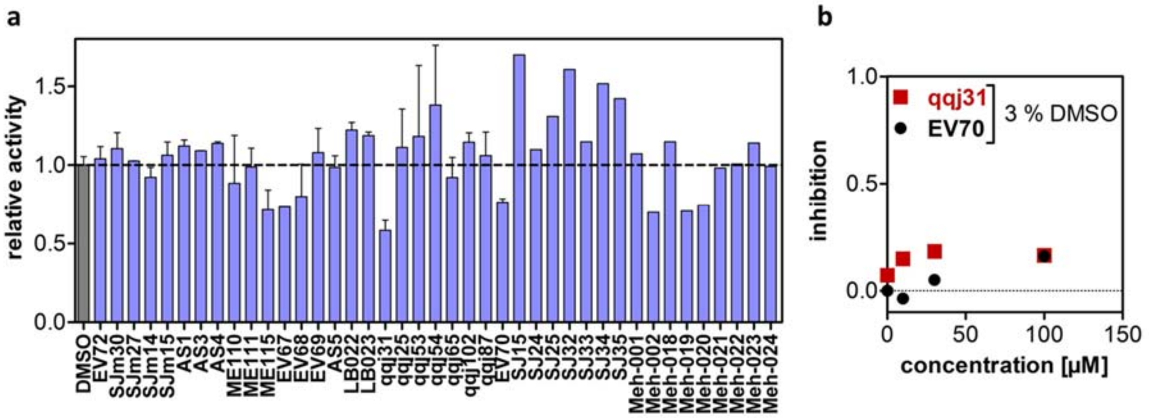

Figure 7.21 Molecular plugs fail to inhibit Taspase.

a Several compounds designed by the Schmuck group as molecular plugs for a variety of other enzymes were prescreened for Taspase inhibition *in vitro*. Measurements were taken in 3 % DMSO to guarantee solubility of the compounds and referenced to a DMSO control. Error bars indicate standard deviations from two independent experiments. The compounds are listed in supplemental figure 7.22 below. **b** Two compounds with promising inhibitory values in the prescreen and sufficient water solubility were deliberately selected for titrations. Both compounds revealed no inhibitory effect.

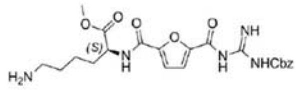

ME020

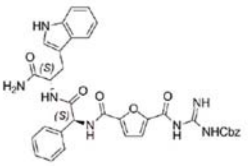

ME019

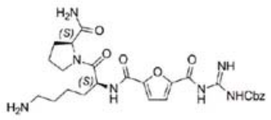

ME022

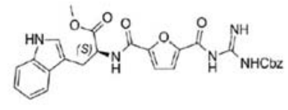

ME001

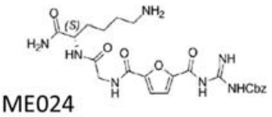

ME024

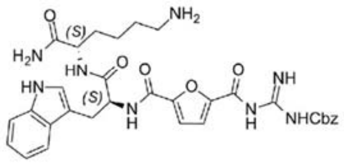

ME002

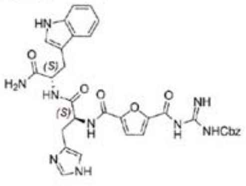

ME021

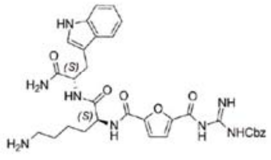

ME018

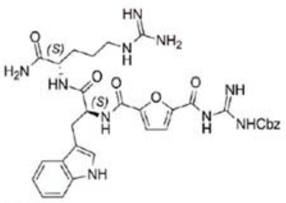

ME023

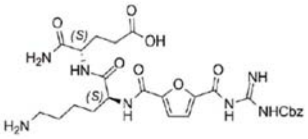

ME025

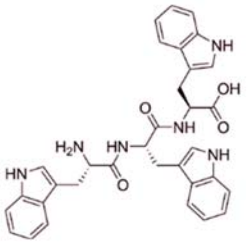

ME078

qqj109

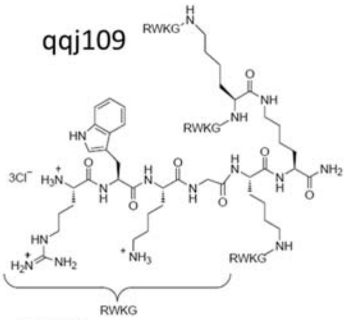

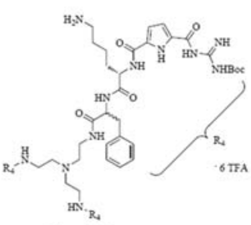

SJm34

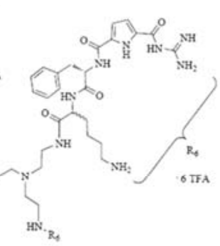

SJm35

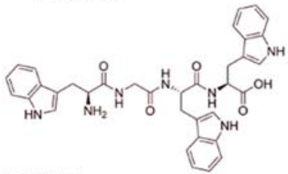

ME080

LB021

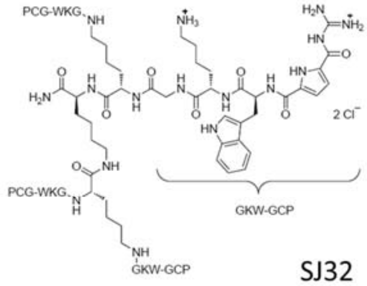

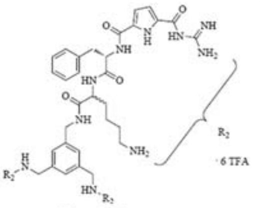

SJm32

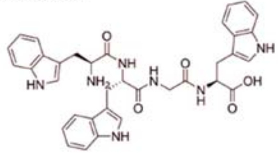

ME079

SJ25

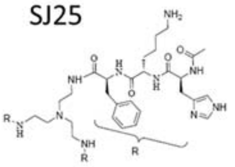

SJ32

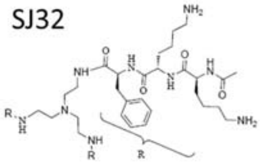

SJ15

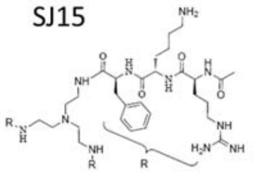

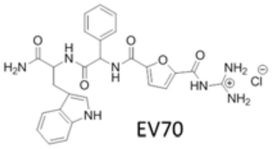

EV70

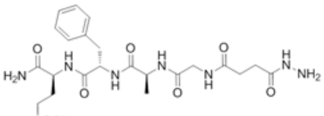

qqj31

ME115

Trp-Trp-Trp-Trp-Gly

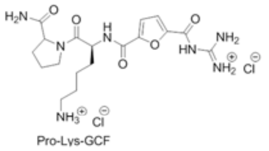

Pro-Lys-GCF

EV72

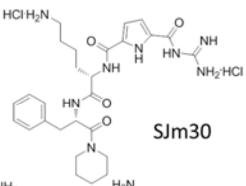

SJm30

SJm27

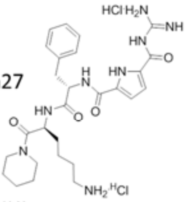

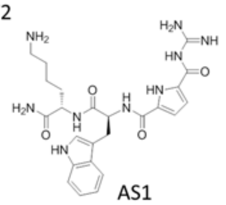

AS1

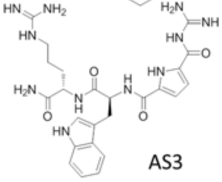

AS3

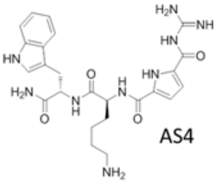

AS4

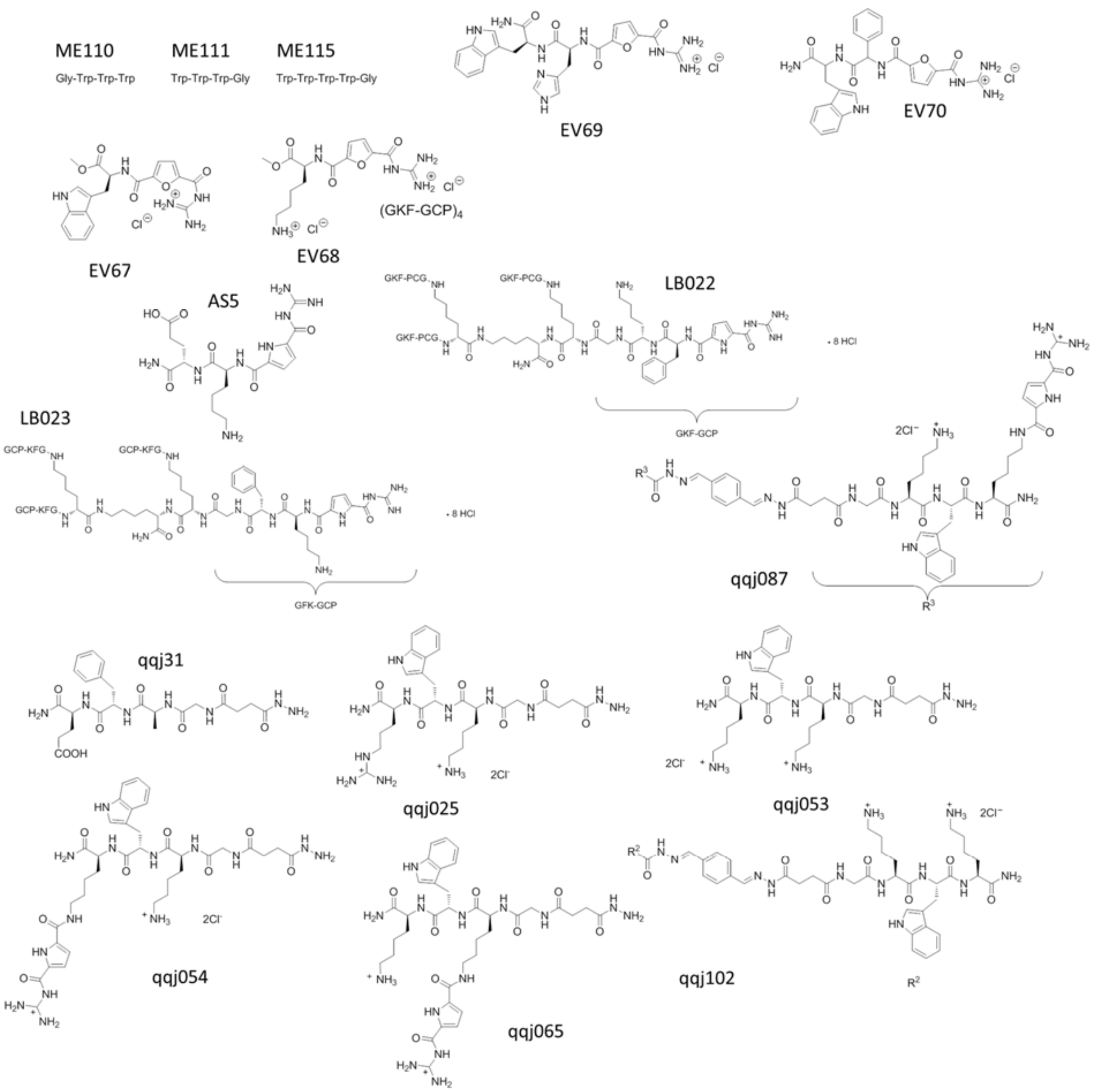

Figure 7.22 Structure of the molecular plug compounds.

Structures of the molecular plug compounds tested for Taspase inhibition. All compounds are courtesy of the Schmuck group.

8 References

1. Howlader N, Noone AM, Krapcho M, Garshell J, Miller D, Altekruse SF, Kosary CL, Yu M, Ruhl J, Tatalovich Z, Mariotto A, Lewis DR, Chen HS, Feuer EJ, Cronin KA (2014) SEER Cancer Statistics Review, 1975-2011.
2. Boyle P, Ferlay J (2005) Cancer incidence and mortality in Europe, 2004. Ann Oncol 16: 481-488. mdi098 [pii];10.1093/annonc/mdi098 [doi].
3. Perez-Diez A, Morgun A, Shulzhenko N (2007) Microarrays for cancer diagnosis and classification. Adv Exp Med Biol 593: 74-85. 10.1007/978-0-387-39978-2_8 [doi].
4. Hanahan D, Weinberg RA (2000) The hallmarks of cancer. Cell 100: 57-70. S0092-8674(00)81683-9 [pii].
5. Pokharel M (2012) Leukemia : A Review Article. IJARPB 2: 397-407.
6. Buffler PA, Kwan ML, Reynolds P, Urayama KY (2005) Environmental and genetic risk factors for childhood leukemia: appraising the evidence. Cancer Invest 23: 60-75.
7. Brown CM, Larsen SR, Iland HJ, Joshua DE, Gibson J (2012) Leukaemias into the 21st century: part 1: the acute leukaemias. Intern Med J 42: 1179-1186. 10.1111/j.1445-5994.2012.02938.x [doi].
8. Gibson J, Iland HJ, Larsen SR, Brown CM, Joshua DE (2013) Leukaemias into the 21st century. Part 2: the chronic leukaemias. Intern Med J 43: 484-494. 10.1111/imj.12135 [doi].
9. Slany RK (2009) The molecular biology of mixed lineage leukemia. Haematologica 94: 984-993. haematol.2008.002436 [pii];10.3324/haematol.2008.002436 [doi].
10. Belson M, Kingsley B, Holmes A (2007) Risk factors for acute leukemia in children: a review. Environ Health Perspect 115: 138-145.
11. Freedman DM, Stewart P, Kleinerman RA, Wacholder S, Hatch EE, Tarone RE, Robison LL, Linet MS (2001) Household solvent exposures and childhood acute lymphoblastic leukemia. Am J Public Health 91: 564-567.
12. Rinsky RA, Young RJ, Smith AB (1981) Leukemia in benzene workers. Am J Ind Med 2: 217-245.
13. Ilhan G, Karakus S, Andic N (2006) Risk factors and primary prevention of acute leukemia. Asian Pac J Cancer Prev 7: 515-517.
14. Mitelman F, Johansson B, Mertens F (2007) The impact of translocations and gene fusions on cancer causation. Nat Rev Cancer 7: 233-245. nrc2091 [pii];10.1038/nrc2091 [doi].
15. Rabbitts TH, Stocks MR (2003) Chromosomal translocation products engender new intracellular therapeutic technologies. Nat Med 9: 383-386. 10.1038/nm0403-383 [doi];nm0403-383 [pii].
16. Aplan PD (2006) Chromosomal translocations involving the MLL gene: molecular mechanisms. DNA Repair (Amst) 5: 1265-1272. S1568-7864(06)00174-1 [pii];10.1016/j.dnarep.2006.05.034 [doi].
17. Melo JV (1996) The molecular biology of chronic myeloid leukaemia. Leukemia 10: 751-756.
18. Lovett BD, Lo NL, Rappaport EF, Blair IA, Osheroff N, Zheng N, Megonigal MD, Williams WR, Nowell PC, Felix CA (2001) Near-precise interchromosomal recombination and functional DNA topoisomerase II cleavage sites at MLL and AF-4 genomic breakpoints in treatment-related acute lymphoblastic leukemia with t(4;11) translocation. Proc Natl Acad Sci U S A 98: 9802-9807. 10.1073/pnas.171309898 [doi];171309898 [pii].
19. Krivtsov AV, Armstrong SA (2007) MLL translocations, histone modifications and leukaemia stem-cell development. Nat Rev Cancer 7: 823-833. nrc2253 [pii];10.1038/nrc2253 [doi].
20. Reichel M, Gillert E, Angermuller S, Hensel JP, Heidel F, Lode M, Leis T, Biondi A, Haas OA, Strehl S, Panzer-Grumayer ER, Griesinger F, Beck JD, Greil J, Fey GH, Uckun FM, Marschalek R (2001) Biased distribution of chromosomal breakpoints involving the MLL gene in infants versus children and adults with t(4;11) ALL. Oncogene 20: 2900-2907. 10.1038/sj.onc.1204401 [doi].
21. Daser A, Rabbitts TH (2005) The versatile mixed lineage leukaemia gene MLL and its many associations in leukaemogenesis. Semin Cancer Biol 15: 175-188. S1044-579X(05)00008-8 [pii];10.1016/j.semcancer.2005.01.007 [doi].
22. So CW, Karsunky H, Passegue E, Cozzio A, Weissman IL, Cleary ML (2003) MLL-GAS7 transforms multipotent hematopoietic progenitors and induces mixed lineage leukemias in mice. Cancer Cell 3: 161-171. S1535610803000199 [pii].
23. Ono R, Ihara M, Nakajima H, Ozaki K, Kataoka-Fujiwara Y, Taki T, Nagata K, Inagaki M, Yoshida N, Kitamura T, Hayashi Y, Kinoshita M, Nosaka T (2005) Disruption of Sept6, a fusion partner

gene of MLL, does not affect ontogeny, leukemogenesis induced by MLL-SEPT6, or phenotype induced by the loss of Sept4. Mol Cell Biol 25: 10965-10978. 25/24/10965 [pii];10.1128/MCB.25.24.10965-10978.2005 [doi].

24. Gu Y, Nakamura T, Alder H, Prasad R, Canaani O, Cimino G, Croce CM, Canaani E (1992) The t(4;11) chromosome translocation of human acute leukemias fuses the ALL-1 gene, related to Drosophila trithorax, to the AF-4 gene. Cell 71: 701-708. 0092-8674(92)90603-A [pii].
25. Huret JL, Dessen P, Bernheim A (2001) An atlas of chromosomes in hematological malignancies. Example: 11q23 and MLL partners. Leukemia 15: 987-989.
26. Hilden JM, Dinndorf PA, Meerbaum SO, Sather H, Villaluna D, Heerema NA, McGlennen R, Smith FO, Woods WG, Salzer WL, Johnstone HS, Dreyer Z, Reaman GH (2006) Analysis of prognostic factors of acute lymphoblastic leukemia in infants: report on CCG 1953 from the Children's Oncology Group. Blood 108: 441-451. 2005-07-3011 [pii];10.1182/blood-2005-07-3011 [doi].
27. Pui CH, Sandlund JT, Pei D, Campana D, Rivera GK, Ribeiro RC, Rubnitz JE, Razzouk BI, Howard SC, Hudson MM, Cheng C, Kun LE, Raimondi SC, Behm FG, Downing JR, Relling MV, Evans WE (2004) Improved outcome for children with acute lymphoblastic leukemia: results of Total Therapy Study XIIIB at St Jude Children's Research Hospital. Blood 104: 2690-2696. 10.1182/blood-2004-04-1616 [doi];2004-04-1616 [pii].
28. Corral J, Lavenir I, Impey H, Warren AJ, Forster A, Larson TA, Bell S, McKenzie AN, King G, Rabbitts TH (1996) An Mll-AF9 fusion gene made by homologous recombination causes acute leukemia in chimeric mice: a method to create fusion oncogenes. Cell 85: 853-861. S0092-8674(00)81269-6 [pii].
29. Bursen A, Schwabe K, Ruster B, Henschler R, Ruthardt M, Dingermann T, Marschalek R (2010) The AF4.MLL fusion protein is capable of inducing ALL in mice without requirement of MLL.AF4. Blood 115: 3570-3579. blood-2009-06-229542 [pii];10.1182/blood-2009-06-229542 [doi].
30. Gaussmann A, Wenger T, Eberle I, Bursen A, Bracharz S, Herr I, Dingermann T, Marschalek R (2007) Combined effects of the two reciprocal t(4;11) fusion proteins MLL.AF4 and AF4.MLL confer resistance to apoptosis, cell cycling capacity and growth transformation. Oncogene 26: 3352-3363. 1210125 [pii];10.1038/sj.onc.1210125 [doi].
31. Zeleznik-Le NJ, Harden AM, Rowley JD (1994) 11q23 translocations split the "AT-hook" cruciform DNA-binding region and the transcriptional repression domain from the activation domain of the mixed-lineage leukemia (MLL) gene. Proc Natl Acad Sci U S A 91: 10610-10614.
32. Xia ZB, Anderson M, Diaz MO, Zeleznik-Le NJ (2003) MLL repression domain interacts with histone deacetylases, the polycomb group proteins HPC2 and BMI-1, and the corepressor C-terminal-binding protein. Proc Natl Acad Sci U S A 100: 8342-8347. 10.1073/pnas.1436338100 [doi];1436338100 [pii].
33. Fair K, Anderson M, Bulanova E, Mi H, Tropschug M, Diaz MO (2001) Protein interactions of the MLL PHD fingers modulate MLL target gene regulation in human cells. Mol Cell Biol 21: 3589-3597. 10.1128/MCB.21.10.3589-3597.2001 [doi].
34. Yu BD, Hess JL, Horning SE, Brown GA, Korsmeyer SJ (1995) Altered Hox expression and segmental identity in Mll-mutant mice. Nature 378: 505-508. 10.1038/378505a0 [doi].
35. Hess JL (2004) MLL: a histone methyltransferase disrupted in leukemia. Trends Mol Med 10: 500-507. S1471-4914(04)00213-8 [pii];10.1016/j.molmed.2004.08.005 [doi].
36. Hess JL (2004) Mechanisms of transformation by MLL. Crit Rev Eukaryot Gene Expr 14: 235-254. 22d69e8b2d47b5ea,0c09f91b76652c8a [pii].
37. Terranova R, Agherbi H, Boned A, Meresse S, Djabali M (2006) Histone and DNA methylation defects at Hox genes in mice expressing a SET domain-truncated form of Mll. Proc Natl Acad Sci U S A 103: 6629-6634. 0507425103 [pii];10.1073/pnas.0507425103 [doi].
38. Kramer OH, Stauber RH, Bug G, Hartkamp J, Knauer SK (2013) SIAH proteins: critical roles in leukemogenesis. Leukemia 27: 792-802. leu2012284 [pii];10.1038/leu.2012.284 [doi].
39. Nakamura T, Mori T, Tada S, Krajewski W, Rozovskaia T, Wassell R, Dubois G, Mazo A, Croce CM, Canaani E (2002) ALL-1 is a histone methyltransferase that assembles a supercomplex of proteins involved in transcriptional regulation. Mol Cell 10: 1119-1128. S1097276502007402 [pii].
40. Hsieh JJ, Ernst P, Erdjument-Bromage H, Tempst P, Korsmeyer SJ (2003) Proteolytic cleavage of MLL generates a complex of N- and C-terminal fragments that confers protein stability and subnuclear localization. Mol Cell Biol 23: 186-194.

41. Turk B (2006) Targeting proteases: successes, failures and future prospects. Nat Rev Drug Discov 5: 785-799. nrd2092 [pii];10.1038/nrd2092 [doi].
42. Villamil MA, Liang Q, Chen J, Choi YS, Hou S, Lee KH, Zhuang Z (2012) Serine phosphorylation is critical for the activation of ubiquitin-specific protease 1 and its interaction with WD40-repeat protein UAF1. Biochemistry 51: 9112-9123. 10.1021/bi300845s [doi].
43. Cardone MH, Roy N, Stennicke HR, Salvesen GS, Franke TF, Stanbridge E, Frisch S, Reed JC (1998) Regulation of cell death protease caspase-9 by phosphorylation. Science 282: 1318-1321.
44. Nicholson DW (1999) Caspase structure, proteolytic substrates, and function during apoptotic cell death. Cell Death Differ 6: 1028-1042. 10.1038/sj.cdd.4400598 [doi].
45. Neurath H, Walsh KA (1976) Role of proteolytic enzymes in biological regulation (a review). Proc Natl Acad Sci U S A 73: 3825-3832.
46. Vergnolle N (2000) Review article: proteinase-activated receptors - novel signals for gastrointestinal pathophysiology. Aliment Pharmacol Ther 14: 257-266. apt690 [pii].
47. Stauber RH, Knauer SK (2013) Taspase1 — Lizenz zum Schneiden. BIOspektrum 19: 134-136.
48. Deu E, Verdoes M, Bogyo M (2012) New approaches for dissecting protease functions to improve probe development and drug discovery. Nat Struct Mol Biol 19: 9-16. nsmb.2203 [pii];10.1038/nsmb.2203 [doi].
49. Rakashanda S, Rana F, Rafiq S, Masood A, Amin S (2012) Role of proteases in cancer: A review. Biotechnology and Molecular Biology Review 7: 90-101.
50. Lopez-Otin C, Hunter T (2010) The regulatory crosstalk between kinases and proteases in cancer. Nat Rev Cancer 10: 278-292. nrc2823 [pii];10.1038/nrc2823 [doi].
51. Soreide K, Janssen EA, Korner H, Baak JP (2006) Trypsin in colorectal cancer: molecular biological mechanisms of proliferation, invasion, and metastasis. J Pathol 209: 147-156. 10.1002/path.1999 [doi].
52. Kawasaki G, Kato Y, Mizuno A (2002) Cathepsin expression in oral squamous cell carcinoma: relationship with clinicopathologic factors. Oral Surg Oral Med Oral Pathol Oral Radiol Endod 93: 446-454. S1079210402889028 [pii].
53. Teitz T, Wei T, Valentine MB, Vanin EF, Grenet J, Valentine VA, Behm FG, Look AT, Lahti JM, Kidd VJ (2000) Caspase 8 is deleted or silenced preferentially in childhood neuroblastomas with amplification of MYCN. Nat Med 6: 529-535. 10.1038/75007 [doi].
54. Duffy MJ (1996) Proteases as prognostic markers in cancer. Clin Cancer Res 2: 613-618.
55. Hoeller D, Hecker CM, Dikic I (2006) Ubiquitin and ubiquitin-like proteins in cancer pathogenesis. Nat Rev Cancer 6: 776-788. nrc1994 [pii];10.1038/nrc1994 [doi].
56. Khan JA, Dunn BM, Tong L (2005) Crystal structure of human Taspase1, a crucial protease regulating the function of MLL. Structure 13: 1443-1452. S0969-2126(05)00265-0 [pii];10.1016/j.str.2005.07.006 [doi].
57. Hsieh JJ, Cheng EH, Korsmeyer SJ (2003) Taspase1: a threonine aspartase required for cleavage of MLL and proper HOX gene expression. Cell 115: 293-303. S009286740300816X [pii].
58. Hsueh WA, Baxter JD (1991) Human prorenin. Hypertension 17: 469-477.
59. Nagel W, Robel KP, Willig F (1965) Über die Aktivierung proteolytischer Proenzyme des Pankreas. Klinische Wochenschrift 43: 173-174.
60. Arendt CS, Hochstrasser M (1999) Eukaryotic 20S proteasome catalytic subunit propeptides prevent active site inactivation by N-terminal acetylation and promote particle assembly. EMBO J 18: 3575-3585. 10.1093/emboj/18.13.3575 [doi].
61. Saarela J, Laine M, Tikkanen R, Oinonen C, Jalanko A, Rouvinen J, Peltonen L (1998) Activation and oligomerization of aspartylglucosaminidase. J Biol Chem 273: 25320-25328.
62. Michalska K, Hernandez-Santoyo A, Jaskolski M (2008) The mechanism of autocatalytic activation of plant-type L-asparaginases. J Biol Chem 283: 13388-13397. M800746200 [pii];10.1074/jbc.M800746200 [doi].
63. Chen DY, Lee Y, Van Tine BA, Searleman AC, Westergard TD, Liu H, Tu HC, Takeda S, Dong Y, Piwnica-Worms DR, Oh KJ, Korsmeyer SJ, Hermone A, Gussio R, Shoemaker RH, Cheng EH, Hsieh JJ (2012) A pharmacologic inhibitor of the protease Taspase1 effectively inhibits breast and brain tumor growth. Cancer Res 72: 736-746. 0008-5472.CAN-11-2584 [pii];10.1158/0008-5472.CAN-11-2584 [doi].
64. Oinonen C, Rouvinen J (2000) Structural comparison of Ntn-hydrolases. Protein Sci 9: 2329-2337. 10.1110/ps.9.12.2329 [doi].
65. Oinonen C, Tikkanen R, Rouvinen J, Peltonen L (1995) Three-dimensional structure of human lysosomal aspartylglucosaminidase. Nat Struct Biol 2: 1102-1108.

66. Nomme J, Su Y, Konrad M, Lavie A (2012) Structures of apo and product-bound human L-asparaginase: insights into the mechanism of autoproteolysis and substrate hydrolysis. Biochemistry 51: 6816-6826. 10.1021/bi300870g [doi].
67. Groll M, Ditzel L, Lowe J, Stock D, Bochtler M, Bartunik HD, Huber R (1997) Structure of 20S proteasome from yeast at 2.4 A resolution. Nature 386: 463-471. 10.1038/386463a0 [doi].
68. Bier C, Knauer SK, Wunsch D, Kunst L, Scheiding S, Kaiser M, Ottmann C, Kramer OH, Stauber RH (2012) Allosteric inhibition of Taspase1's pathobiological activity by enforced dimerization in vivo. FASEB J 26: 3421-3429. fj.11-202432 [pii];10.1096/fj.11-202432 [doi].
69. Lee JT, Chen DY, Yang Z, Ramos AD, Hsieh JJ, Bogyo M (2009) Design, syntheses, and evaluation of Taspase1 inhibitors. Bioorg Med Chem Lett 19: 5086-5090. S0960-894X(09)00989-5 [pii];10.1016/j.bmcl.2009.07.045 [doi].
70. Bier C, Knauer SK, Klapthor A, Schweitzer A, Rekik A, Kramer OH, Marschalek R, Stauber RH (2011) Cell-based analysis of structure-function activity of threonine aspartase 1. J Biol Chem 286: 3007-3017. M110.161646 [pii];10.1074/jbc.M110.161646 [doi].
71. Knauer SK, Fetz V, Rabenstein J, Friedl S, Hofmann B, Sabiani S, Schroder E, Kunst L, Proschak E, Thines E, Kindler T, Schneider G, Marschalek R, Stauber RH, Bier C (2011) Bioassays to monitor Taspase1 function for the identification of pharmacogenetic inhibitors. PLoS One 6: e18253. 10.1371/journal.pone.0018253 [doi];PONE-D-10-05577 [pii].
72. Takeda S, Chen DY, Westergard TD, Fisher JK, Rubens JA, Sasagawa S, Kan JT, Korsmeyer SJ, Cheng EH, Hsieh JJ (2006) Proteolysis of MLL family proteins is essential for taspase1-orchestrated cell cycle progression. Genes Dev 20: 2397-2409. 20/17/2397 [pii];10.1101/gad.1449406 [doi].
73. Zhou H, Spicuglia S, Hsieh JJ, Mitsiou DJ, Hoiby T, Veenstra GJ, Korsmeyer SJ, Stunnenberg HG (2006) Uncleaved TFIIA is a substrate for taspase 1 and active in transcription. Mol Cell Biol 26: 2728-2735. 26/7/2728 [pii];10.1128/MCB.26.7.2728-2735.2006 [doi].
74. Bier C, Knauer SK, Docter D, Schneider G, Kramer OH, Stauber RH (2011) The importin-alpha/nucleophosmin switch controls taspase1 protease function. Traffic 12: 703-714. 10.1111/j.1600-0854.2011.01191.x [doi].
75. Luo J, Solimini NL, Elledge SJ (2009) Principles of cancer therapy: oncogene and non-oncogene addiction. Cell 136: 823-837. S0092-8674(09)00200-1 [pii];10.1016/j.cell.2009.02.024 [doi].
76. Chen DY, Liu H, Takeda S, Tu HC, Sasagawa S, Van Tine BA, Lu D, Cheng EH, Hsieh JJ (2010) Taspase1 functions as a non-oncogene addiction protease that coordinates cancer cell proliferation and apoptosis. Cancer Res 70: 5358-5367. 0008-5472.CAN-10-0027 [pii];10.1158/0008-5472.CAN-10-0027 [doi].
77. Schulte TW, Akinaga S, Soga S, Sullivan W, Stensgard B, Toft D, Neckers LM (1998) Antibiotic radicicol binds to the N-terminal domain of Hsp90 and shares important biologic activities with geldanamycin. Cell Stress Chaperones 3: 100-108.
78. Luo J, Emanuele MJ, Li D, Creighton CJ, Schlabach MR, Westbrook TF, Wong KK, Elledge SJ (2009) A genome-wide RNAi screen identifies multiple synthetic lethal interactions with the Ras oncogene. Cell 137: 835-848. S0092-8674(09)00529-7 [pii];10.1016/j.cell.2009.05.006 [doi].
79. Adams J, Kauffman M (2004) Development of the proteasome inhibitor Velcade (Bortezomib). Cancer Invest 22: 304-311.
80. Sarubbi E, Nolli ML, Andronico F, Stella S, Saddler G, Selva E, Siccardi A, Denaro M (1991) A high throughput assay for inhibitors of HIV-1 protease. Screening of microbial metabolites. FEBS Lett 279: 265-269. 0014-5793(91)80164-X [pii].
81. Yang W, Wang L, Paschen W (2013) Development of a high-throughput screening assay for inhibitors of small ubiquitin-like modifier proteases. J Biomol Screen 18: 621-628. 1087057113479971 [pii];10.1177/1087057113479971 [doi].
82. Rabenstein, Jens (2008) Inhibierung des pathomolekularen Mechanismuseiner t(4;11)-assoziierten Leukämie [dissertation]. Goethe-Universität Frankfurt am Main.
83. Wunsch D, Fetz V, Heider D, Tenzer S, Bier C, Kunst L, Knauer S, Stauber R (2012) Chemico-genetic strategies to inhibit the leukemic potential of threonine aspartase-1. Blood Cancer J 2: e77. 10.1038/bcj.2012.22 [doi].
84. Thiel P, Kaiser M, Ottmann C (2012) Small-molecule stabilization of protein-protein interactions: an underestimated concept in drug discovery? Angew Chem Int Ed Engl 51: 2012-2018. 10.1002/anie.201107616 [doi].

85. Bier C, Hecht R, Kunst L, Scheiding S, Wunsch D, Goesswein D, Schneider G, Kramer OH, Knauer SK, Stauber RH (2012) Overexpression of the catalytically impaired Taspase1 T234V or Taspase1 D233A variants does not have a dominant negative effect in T(4;11) leukemia cells. PLoS One 7: e34142. 10.1371/journal.pone.0034142 [doi];PONE-D-11-20159 [pii].
86. Davis ME, Chen ZG, Shin DM (2008) Nanoparticle therapeutics: an emerging treatment modality for cancer. Nat Rev Drug Discov 7: 771-782. nrd2614 [pii];10.1038/nrd2614 [doi].
87. Yah CS, Simate GS, Iyuke SE (2012) Nanoparticles toxicity and their routes of exposures. Pak J Pharm Sci 25: 477-491.
88. Mohanraj VJ, Chen Y (2006) Nanoparticles - A review. Tropical Journal of Pharmaceutical Research 5: 561-573.
89. Burleson DJ, Driessen MD, Penn RL (2004) On the characterization of environmental nanoparticles. J Environ Sci Health A Tox Hazard Subst Environ Eng 39: 2707-2753.
90. Elsaesser A, Howard CV (2012) Toxicology of nanoparticles. Adv Drug Deliv Rev 64: 129-137. S0169-409X(11)00232-8 [pii];10.1016/j.addr.2011.09.001 [doi].
91. Oberdorster G, Oberdorster E, Oberdorster J (2005) Nanotoxicology: an emerging discipline evolving from studies of ultrafine particles. Environ Health Perspect 113: 823-839.
92. Nel AE, Madler L, Velegol D, Xia T, Hoek EM, Somasundaran P, Klaessig F, Castranova V, Thompson M (2009) Understanding biophysicochemical interactions at the nano-bio interface. Nat Mater 8: 543-557. nmat2442 [pii];10.1038/nmat2442 [doi].
93. Nel A, Xia T, Madler L, Li N (2006) Toxic potential of materials at the nanolevel. Science 311: 622-627. 311/5761/622 [pii];10.1126/science.1114397 [doi].
94. Leroueil PR, Berry SA, Duthie K, Han G, Rotello VM, McNerny DQ, Baker JR, Jr., Orr BG, Holl MM (2008) Wide varieties of cationic nanoparticles induce defects in supported lipid bilayers. Nano Lett 8: 420-424. 10.1021/nl0722929 [doi].
95. Chen M, von MA (2005) Formation of nucleoplasmic protein aggregates impairs nuclear function in response to SiO2 nanoparticles. Exp Cell Res 305: 51-62. S0014-4827(04)00733-5 [pii];10.1016/j.yexcr.2004.12.021 [doi].
96. Marano F, Hussain S, Rodrigues-Lima F, Baeza-Squiban A, Boland S (2011) Nanoparticles: molecular targets and cell signalling. Arch Toxicol 85: 733-741. 10.1007/s00204-010-0546-4 [doi].
97. Shang W, Nuffer JH, Dordick JS, Siegel RW (2007) Unfolding of ribonuclease A on silica nanoparticle surfaces. Nano Lett 7: 1991-1995. 10.1021/nl070777r [doi].
98. Mehrabi M, Wilson R (2007) Intercalating gold nanoparticles as universal labels for DNA detection. Small 3: 1491-1495. 10.1002/smll.200700230 [doi].
99. Tenzer S, Docter D, Kuharev J, Musyanovych A, Fetz V, Hecht R, Schlenk F, Fischer D, Kiouptsi K, Reinhardt C, Landfester K, Schild H, Maskos M, Knauer SK, Stauber RH (2013) Rapid formation of plasma protein corona critically affects nanoparticle pathophysiology. Nat Nanotechnol 8: 772-781. nnano.2013.181 [pii];10.1038/nnano.2013.181 [doi].
100. Bagre AP, Jain K, Jain NK (2013) Alginate coated chitosan core shell nanoparticles for oral delivery of enoxaparin: in vitro and in vivo assessment. Int J Pharm 456: 31-40. S0378-5173(13)00770-9 [pii];10.1016/j.ijpharm.2013.08.037 [doi].
101. Garcia-Bennett AE, Kozhevnikova M, Konig N, Zhou C, Leao R, Knopfel T, Pankratova S, Trolle C, Berezin V, Bock E, Aldskogius H, Kozlova EN (2013) Delivery of differentiation factors by mesoporous silica particles assists advanced differentiation of transplanted murine embryonic stem cells. Stem Cells Transl Med 2: 906-915. sctm.2013-0072 [pii];10.5966/sctm.2013-0072 [doi].
102. Soni S, Tyagi H, Taylor RA, Kumar A (2013) Role of optical coefficients and healthy tissue-sparing characteristics in gold nanorod-assisted thermal therapy. Int J Hyperthermia 29: 87-97. 10.3109/02656736.2012.753162 [doi].
103. Matsumura Y, Maeda H (1986) A new concept for macromolecular therapeutics in cancer chemotherapy: mechanism of tumoritropic accumulation of proteins and the antitumor agent smancs. Cancer Res 46: 6387-6392.
104. Conde J, de la Fuente JM, Baptista PV (2013) Nanomaterials for reversion of multidrug resistance in cancer: a new hope for an old idea? Front Pharmacol 4: 134. 10.3389/fphar.2013.00134 [doi].
105. Teodor E, Litescu SC, Lazar V, Somoghi R (2009) Hydrogel-magnetic nanoparticles with immobilized L-asparaginase for biomedical applications. J Mater Sci Mater Med 20: 1307-1314. 10.1007/s10856-008-3684-y [doi].

106. Ortac I, Ruff L, Yeh Y, Esener S, Messmer BT (2013) Nanoparticle Encapsulated L-Asparaginase. Blood 122: 2669.

107. Wang C, Liu D, Wang Z (2012) Gold nanoparticle based dot-blot immunoassay for sensitively detecting Alzheimer's disease related beta-amyloid peptide. Chem Commun (Camb) 48: 8392-8394. 10.1039/c2cc33568a [doi].

108. Peng G, Tisch U, Adams O, Hakim M, Shehada N, Broza YY, Billan S, Abdah-Bortnyak R, Kuten A, Haick H (2009) Diagnosing lung cancer in exhaled breath using gold nanoparticles. Nat Nanotechnol 4: 669-673. nnano.2009.235 [pii];10.1038/nnano.2009.235 [doi].

109. Karajanagi SS, Vertegel AA, Kane RS, Dordick JS (2004) Structure and function of enzymes adsorbed onto single-walled carbon nanotubes. Langmuir 20: 11594-11599. 10.1021/la047994h [doi].

110. Linet MS, Ries LA, Smith MA, Tarone RE, Devesa SS (1999) Cancer surveillance series: recent trends in childhood cancer incidence and mortality in the United States. J Natl Cancer Inst 91: 1051-1058.

111. Vranken WF, Boucher W, Stevens TJ, Fogh RH, Pajon A, Llinas M, Ulrich EL, Markley JL, Ionides J, Laue ED (2005) The CCPN data model for NMR spectroscopy: development of a software pipeline. Proteins 59: 687-696. 10.1002/prot.20449 [doi].

112. Pettersen EF, Goddard TD, Huang CC, Couch GS, Greenblatt DM, Meng EC, Ferrin TE (2004) UCSF Chimera--a visualization system for exploratory research and analysis. J Comput Chem 25: 1605-1612. 10.1002/jcc.20084 [doi].

113. Sievers F, Wilm A, Dineen D, Gibson TJ, Karplus K, Li W, Lopez R, McWilliam H, Remmert M, Soding J, Thompson JD, Higgins DG (2011) Fast, scalable generation of high-quality protein multiple sequence alignments using Clustal Omega. Mol Syst Biol 7: 539. msb201175 [pii];10.1038/msb.2011.75 [doi].

114. Ewing TJ, Makino S, Skillman AG, Kuntz ID (2001) DOCK 4.0: search strategies for automated molecular docking of flexible molecule databases. J Comput Aided Mol Des 15: 411-428.

115. GraphPad Software SDCU (2009) GraphPad Prism, version 5.03 [computer program].

116. Schneider CA, Rasband WS, Eliceiri KW (2012) NIH Image to ImageJ: 25 years of image analysis. Nat Methods 9: 671-675.

117. Kibbe WA (2007) OligoCalc: an online oligonucleotide properties calculator. Nucleic Acids Res 35: W43-W46. gkm234 [pii];10.1093/nar/gkm234 [doi].

118. Puigbo P, Guzman E, Romeu A, Garcia-Vallve S (2007) OPTIMIZER: a web server for optimizing the codon usage of DNA sequences. Nucleic Acids Res 35: W126-W131. gkm219 [pii];10.1093/nar/gkm219 [doi].

119. Gasteiger E, Gattiker A, Hoogland C, Ivanyi I, Appel RD, Bairoch A (2003) ExPASy: The proteomics server for in-depth protein knowledge and analysis. Nucleic Acids Res 31: 3784-3788.

120. Schrödinger L (2010) The PyMOL Molecular Graphics System, version 1.5 [computer program].

121. [Anonymous] (2014) SIAS - sequence identity and similarity.

122. Arnold K, Bordoli L, Kopp J, Schwede T (2006) The SWISS-MODEL workspace: a web-based environment for protein structure homology modelling. Bioinformatics 22: 195-201. bti770 [pii];10.1093/bioinformatics/bti770 [doi].

123. Bartasun P, Cieslinski H, Bujacz A, Wierzbicka-Wos A, Kur J (2013) A study on the interaction of rhodamine B with methylthioadenosine phosphorylase protein sourced from an Antarctic soil metagenomic library. PLoS One 8: e55697. 10.1371/journal.pone.0055697 [doi];PONE-D-12-29171 [pii].

124. Cheng Y, Prusoff WH (1973) Relationship between the inhibition constant (K1) and the concentration of inhibitor which causes 50 per cent inhibition (I50) of an enzymatic reaction. Biochem Pharmacol 22: 3099-3108.

125. Sreerama N, Woody RW (2000) Estimation of protein secondary structure from circular dichroism spectra: comparison of CONTIN, SELCON, and CDSSTR methods with an expanded reference set. Anal Biochem 287: 252-260. 10.1006/abio.2000.4880 [doi];S0003-2697(00)94880-2 [pii].

126. Zhang H, Neal S, Wishart DS (2003) RefDB: a database of uniformly referenced protein chemical shifts. J Biomol NMR 25: 173-195. 5118302 [pii].

127. Kuntz ID, Blaney JM, Oatley SJ, Langridge R, Ferrin TE (1982) A geometric approach to macromolecule-ligand interactions. J Mol Biol 161: 269-288. 0022-2836(82)90153-X [pii].

128. Meng EC, Shoichet BK, Kuntz ID (1992) Automated docking with grid-based energy evaluation. J Comp Chem 13: 505-524.

129. Irwin JJ, Sterling T, Mysinger MM, Bolstad ES, Coleman RG (2012) ZINC: a free tool to discover chemistry for biology. J Chem Inf Model 52: 1757-1768. 10.1021/ci3001277 [doi].
130. Voigt JH, Bienfait B, Wang S, Nicklaus MC (2001) Comparison of the NCI open database with seven large chemical structural databases. J Chem Inf Comput Sci 41: 702-712. ci000150t [pii].
131. Case DA, Cheatham TE, III, Darden T, Gohlke H, Luo R, Merz KM, Jr., Onufriev A, Simmerling C, Wang B, Woods RJ (2005) The Amber biomolecular simulation programs. J Comput Chem 26: 1668-1688. 10.1002/jcc.20290 [doi].
132. Neumann, D. (2006) Strukturelle und biochemische Charakterisierungder humanen PAPS-Synthetase 2 [dissertation]. Universität Duisburg-Essen.
133. Stauber RH, Bier C, Knauer SK (2012) Targeting Taspase1 for cancer therapy--letter. Cancer Res 72: 2912. 0008-5472.CAN-12-0150 [pii];10.1158/0008-5472.CAN-12-0150 [doi].
134. van den Boom J, Mamic M, Bacchelliere D, Zweering S, Kaschani F, Knauer S, Bayer P, Kaiser M (2014) Peptidyl succinimidyl peptides as potent Taspase1 inhibitors; manuscript submitted.
135. Krasotkina J, Borisova AA, Gervaziev YV, Sokolov NN (2004) One-step purification and kinetic properties of the recombinant L-asparaginase from Erwinia carotovora. Biotechnol Appl Biochem 39: 215-221. 10.1042/BA20030138 [doi];BA20030138 [pii].
136. Pokrovskaya MV, Aleksandrova SS, Pokrovsky VS, Omeljanjuk NM, Borisova AA, Anisimova NY, Sokolov NN (2012) Cloning, expression and characterization of the recombinant Yersinia pseudotuberculosis L-asparaginase. Protein Expr Purif 82: 150-154. S1046-5928(11)00351-2 [pii];10.1016/j.pep.2011.12.005 [doi].
137. Bansal S, Srivastava A, Mukherjee G, Pandey R, Verma AK, Mishra P, Kundu B (2012) Hyperthermophilic asparaginase mutants with enhanced substrate affinity and antineoplastic activity: structural insights on their mechanism of action. FASEB J 26: 1161-1171. fj.11-191254 [pii];10.1096/fj.11-191254 [doi].
138. Nesterchuk MV, Sergiev PV, Dontsova OA (2011) Posttranslational Modifications of Ribosomal Proteins in Escherichia coli. Acta Naturae 3: 22-33.
139. Borek D, Jaskolski M (2000) Crystallization and preliminary crystallographic studies of a new L-asparaginase encoded by the Escherichia coli genome. Acta Crystallogr D Biol Crystallogr 56: 1505-1507. S0907444900010076 [pii].
140. Xuan J, Tarentino AL, Grimwood BG, Plummer TH, Jr., Cui T, Guan C, Van RP (1998) Crystal structure of glycosylasparaginase from Flavobacterium meningosepticum. Protein Sci 7: 774-781. 10.1002/pro.5560070327 [doi].
141. Yao J, Dyson HJ, Wright PE (1997) Chemical shift dispersion and secondary structure prediction in unfolded and partly folded proteins. FEBS Lett 419: 285-289. S0014-5793(97)01474-9 [pii].
142. Neri D, Wider G, Wuthrich K (1992) Complete 15N and 1H NMR assignments for the amino-terminal domain of the phage 434 repressor in the urea-unfolded form. Proc Natl Acad Sci U S A 89: 4397-4401.
143. Vranken WF, Rieping W (2009) Relationship between chemical shift value and accessible surface area for all amino acid atoms. BMC Struct Biol 9: 20. 1472-6807-9-20 [pii];10.1186/1472-6807-9-20 [doi].
144. Fu CH, Sakamoto KM (2007) PEG-asparaginase. Expert Opin Pharmacother 8: 1977-1984. 10.1517/14656566.8.12.1977 [doi].
145. Muller HJ, Boos J (1998) Use of L-asparaginase in childhood ALL. Crit Rev Oncol Hematol 28: 97-113. S1040-8428(98)00015-8 [pii].
146. Jiang QQ, Bartsch L, Sicking W, Wich PR, Heider D, Hoffmann D, Schmuck C (2013) A new approach to inhibit human beta-tryptase by protein surface binding of four-armed peptide ligands with two different sets of arms. Org Biomol Chem 11: 1631-1639. 10.1039/c3ob27302d [doi].
147. Eastman J, Wilson EJ, Cervenansky C, Rosenberry TL (1995) Fasciculin 2 binds to the peripheral site on acetylcholinesterase and inhibits substrate hydrolysis by slowing a step involving proton transfer during enzyme acylation. J Biol Chem 270: 19694-19701.
148. Xiong S, Qi W, Cheng Y, Huang B, Wang M, Li Y (2011) Modeling size effects on the surface free energy of metallic nanoparticles and nanocavities. Phys Chem Chem Phys 13: 10648-10651. 10.1039/c0cp02102d [doi].
149. Niemeyer CM (2001) Nanoparticles, Proteins, and Nucleic Acids: Biotechnology Meets Materials Science. Angewandte Chemie 40: 4128-4158.

150. Tenzer S, Docter D, Rosfa S, Wlodarski A, Kuharev J, Rekik A, Knauer SK, Bantz C, Nawroth T, Bier C, Sirirattanapan J, Mann W, Treuel L, Zellner R, Maskos M, Schild H, Stauber RH (2011) Nanoparticle size is a critical physicochemical determinant of the human blood plasma corona: a comprehensive quantitative proteomic analysis. ACS Nano 5: 7155-7167. 10.1021/nn201950e [doi].
151. Cedervall T, Lynch I, Lindman S, Berggard T, Thulin E, Nilsson H, Dawson KA, Linse S (2007) Understanding the nanoparticle-protein corona using methods to quantify exchange rates and affinities of proteins for nanoparticles. Proc Natl Acad Sci U S A 104: 2050-2055. 0608582104 [pii];10.1073/pnas.0608582104 [doi].
152. Zheng C, Zhang XL, Liu W, Liu B, Yang HH, Lin ZA, Chen GN (2013) A selective artificial enzyme inhibitor based on nanoparticle-enzyme interactions and molecular imprinting. Adv Mater 25: 5922-5927. 10.1002/adma.201302064 [doi].
153. Guerreiro A, Poma A, Karim K, Moczko E, Takarada J, de Vargas-Sansalvador IP, Turner N, Piletska E, de Magalhaes CS, Glazova N, Serkova A, Omelianova A, Piletsky S (2014) Influence of Surface-Imprinted Nanoparticles on Trypsin Activity. Adv Healthc Mater . 10.1002/adhm.201300634 [doi].
154. Linse S, Cabaleiro-Lago C, Xue WF, Lynch I, Lindman S, Thulin E, Radford SE, Dawson KA (2007) Nucleation of protein fibrillation by nanoparticles. Proc Natl Acad Sci U S A 104: 8691-8696. 0701250104 [pii];10.1073/pnas.0701250104 [doi].
155. Asuri P, Karajanagi SS, Vertegel AA, Dordick JS, Kane RS (2007) Enhanced stability of enzymes adsorbed onto nanoparticles. J Nanosci Nanotechnol 7: 1675-1678.
156. Ashtari K, Khajeh K, Fasihi J, Ashtari P, Ramazani A, Vali H (2012) Silica-encapsulated magnetic nanoparticles: enzyme immobilization and cytotoxic study. Int J Biol Macromol 50: 1063-1069. S0141-8130(11)00486-7 [pii];10.1016/j.ijbiomac.2011.12.025 [doi].
157. Lee WA, Pernodet N, Li B, Lin CH, Hatchwell E, Rafailovich MH (2007) Multicomponent polymer coating to block photocatalytic activity of TiO2 nanoparticles. Chem Commun (Camb) 4815-4817. 10.1039/b709449c [doi].
158. Auffan M, Achouak W, Rose J, Roncato MA, Chaneac C, Waite DT, Masion A, Woicik JC, Wiesner MR, Bottero JY (2008) Relation between the redox state of iron-based nanoparticles and their cytotoxicity toward Escherichia coli. Environ Sci Technol 42: 6730-6735.
159. Trueb RM (2009) Oxidative stress in ageing of hair. Int J Trichology 1: 6-14. 10.4103/0974-7753.51923 [doi].
160. Ellis RJ, Minton AP (2006) Protein aggregation in crowded environments. Biol Chem 387: 485-497. 10.1515/BC.2006.064 [doi].
161. van den Berg B, Ellis RJ, Dobson CM (1999) Effects of macromolecular crowding on protein folding and aggregation. EMBO J 18: 6927-6933. 10.1093/emboj/18.24.6927 [doi].
162. Decuzzi P, Ferrari M (2007) The role of specific and non-specific interactions in receptor-mediated endocytosis of nanoparticles. Biomaterials 28: 2915-2922. S0142-9612(07)00153-6 [pii];10.1016/j.biomaterials.2007.02.013 [doi].
163. Akerman ME, Chan WC, Laakkonen P, Bhatia SN, Ruoslahti E (2002) Nanocrystal targeting in vivo. Proc Natl Acad Sci U S A 99: 12617-12621. 10.1073/pnas.152463399 [doi];152463399 [pii].
164. Hoshino A, Fujioka K, Oku T, Nakamura S, Suga M, Yamaguchi Y, Suzuki K, Yasuhara M, Yamamoto K (2004) Quantum dots targeted to the assigned organelle in living cells. Microbiol Immunol 48: 985-994. JST.JSTAGE/mandi/48.985 [pii].
165. Hanley C, Thurber A, Hanna C, Punnoose A, Zhang J, Wingett DG (2009) The Influences of Cell Type and ZnO Nanoparticle Size on Immune Cell Cytotoxicity and Cytokine Induction. Nanoscale Res Lett 4: 1409-1420. 1556-276X-4-1409 [pii];10.1007/s11671-009-9413-8 [doi].
166. Mossman BT, Churg A (1998) Mechanisms in the pathogenesis of asbestosis and silicosis. Am J Respir Crit Care Med 157: 1666-1680. 10.1164/ajrccm.157.5.9707141 [doi].
167. Ovrevik J, Lag M, Schwarze P, Refsnes M (2004) p38 and Src-ERK1/2 pathways regulate crystalline silica-induced chemokine release in pulmonary epithelial cells. Toxicol Sci 81: 480-490. 10.1093/toxsci/kfh214 [doi];kfh214 [pii].
168. Warheit DB, McHugh TA, Hartsky MA (1995) Differential pulmonary responses in rats inhaling crystalline, colloidal or amorphous silica dusts. Scand J Work Environ Health 21 Suppl 2: 19-21. 76 [pii].
169. Cooper GM (2000) The Nuclear Envelope and Traffic between the Nucleus and Cytoplasm. In: The Cell - A Molecular Approach. Boston University.

170. Pante N, Kann M (2002) Nuclear pore complex is able to transport macromolecules with diameters of about 39 nm. Mol Biol Cell 13: 425-434. 10.1091/mbc.01-06-0308 [doi].
171. Ghose AK, Viswanadhan VN, Wendoloski JJ (1999) A knowledge-based approach in designing combinatorial or medicinal chemistry libraries for drug discovery. 1. A qualitative and quantitative characterization of known drug databases. J Comb Chem 1: 55-68.
172. Lipinski CA (2003) Chris Lipinski discusses life and chemistry after the Rule of Five. Drug Discov Today 8: 12-16. S1359644602025564 [pii].
173. Moriguchi I, Hirono S, Liu Q, Nakagome I, Matsushita Y (1992) Simple method of calculating Octanol/Water Partition Coefficient. Chem Pharm Bull 40: 127-130.
174. Faundez V, Hartzell HC (2004) Intracellular chloride channels: determinants of function in the endosomal pathway. Sci STKE 2004: re8. 10.1126/stke.2332004re8 [doi];stke.2332004re8 [pii].
175. Pilas B, Durack G (1997) A flow cytometric method for measurement of intracellular chloride concentration in lymphocytes using the halide-specific probe 6-methoxy-N-(3-sulfopropyl) quinolinium (SPQ). Cytometry 28: 316-322. 10.1002/(SICI)1097-0320(19970801)28:4<316::AID-CYTO7>3.0.CO;2-9 [pii].
176. Huang ZM, Prasad C, Britton FC, Ye LL, Hatton WJ, Duan D (2009) Functional role of CLC-2 chloride inward rectifier channels in cardiac sinoatrial nodal pacemaker cells. J Mol Cell Cardiol 47: 121-132. S0022-2828(09)00158-8 [pii];10.1016/j.yjmcc.2009.04.008 [doi].
177. Congreve M, Carr R, Murray C, Jhoti H (2003) A 'rule of three' for fragment-based lead discovery? Drug Discov Today 8: 876-877. S1359644603028319 [pii].
178. Klebe G (2009) Peptidomimetika. In: Wirkstoffdesign. Spektrum Verlag. pp. 137-150.
179. MacLeod AM, Merchant KJ, Cascieri MA, Sadowski S, Ber E, Swain CJ, Baker R (1993) N-acyl-L-tryptophan benzyl esters: potent substance P receptor antagonists. J Med Chem 36: 2044-2045.

9 Acknowledgement

An erster Stelle möchte ich mich bei meinem Doktorvater Prof. Peter Bayer für seine vorbildliche Betreuung bedanken. Vor allem die Freiheiten, die du mir bei Experimenten gelassen hast und die Offenheit, mit der du neuen Ideen gegenübertrittst, weiß ich sehr zu schätzen. Ebenso war es sehr angenehm, dass du auch abseits der Arbeit immer bemüht bist, eine unkomplizierte Lösung für unsere Probleme zu finden.

Bei Prof. Shirley Knauer möchte ich mich für die Hilfe bei der Projektsuche bedanken und für die vielen hilfreichen Gespräche während meiner Doktorarbeit. Die Kooperation hat mir nicht zuletzt wegen deines Einsatzes für mich und deiner Hilfe so viel Freude gemacht.

Weiterhin geht mein Dank an Prof. Markus Kaiser für die Inhibitoren, ohne die diese Arbeit nur die Hälfte wert wäre. Deine unverblümte Direktheit hat die Gespräche sehr unkompliziert gemacht.

Besonderer Dank geht an Franzi, danke fürs gemeinsame Laufen, die Gassi-Runden mit Sam und viele Grillabende. Du hast mir mit deiner ehrlichen Art nicht nur wissenschaftlich weitergeholfen.

Muchas gracias a Anja por ser una buena oyente, por resistir mis ataques y por reírse siempre de mis chistes.

Hvala an Edisa für die Versorgung mit Süßigkeiten, danke an Lukas, der auch meine flachsten Witze noch unterbieten kann, und danke an André für die spannenden DSA-Runden.

Außerdem möchte ich allen Mitgliedern und Ehemaligen der AG Bayer – Tina, Daniel, Cristina, Peter, Jenny, Irina, Julia, Dana, Mina, Gila, Alma und Christoph – für die vielen lustigen Momente während der Arbeit danken. Vielen Dank an Daniele und Marija für die Versorgung mit Inhibitoren und an Lena für DNA-Nachschub. Danke an Julia und Manu für die kreativen „Accessoires“ für meinen Arbeitsplatz.

Meinen Eltern danke ich für die Unterstützung während des gesamten Studiums. Und meinem Bruder danke ich, dass er mir regelmäßig meine Pizzen wegisst – zum Glück nur die vegetarischen.

Ein ganz großes Dankeschön geht an Claudia, die immer zu mir gehalten hat, auch wenn es nicht immer leicht war. Dafür liebe ich dich und ohne dich hätte ich im Leben höchstens halb so viel Freude.

10 Curriculum Vitae

For reasons of data protection, the curriculum vitae is not included in the online version.

11 Declarations

Erklärung:
Hiermit erkläre ich, gem. § 6 Abs. (2) f) der Promotionsordnung der Fakultäten für Biologie, Chemie und Mathematik zur Erlangung der Dr. rer. nat., dass ich das Arbeitsgebiet, dem das Thema „Novel inhibitors for the protease Taspase1“ zuzuordnen ist, in Forschung und Lehre vertrete und den Antrag von Johannes van den Boom befürworte und die Betreuung auch im Falle eines Weggangs, wenn nicht wichtige Gründe dem entgegenstehen, weiterführen werde.

Essen, den ________________ ______________________________________
Unterschrift eines Mitglieds der Universität Duisburg-Essen

Erklärung:
Hiermit erkläre ich, gem. § 7 Abs. (2) c) + e) der Promotionsordnung Fakultäten für Biologie, Chemie und Mathematik zur Erlangung des Dr. rer. nat., dass ich die vorliegende Dissertation selbständig verfasst und mich keiner anderen als der angegebenen Hilfsmittel bedient habe.

Essen, den ________________ ______________________________________
Unterschrift des/r Doktoranden/in

Erklärung:
Hiermit erkläre ich, gem. § 7 Abs. (2) d) + f) der Promotionsordnung der Fakultäten für Biologie, Chemie und Mathematik zur Erlangung des Dr. rer. nat., dass ich keine anderen Promotionen bzw. Promotionsversuche in der Vergangenheit durchgeführt habe und dass diese Arbeit von keiner anderen Fakultät/Fachbereich abgelehnt worden ist.

Essen, den ________________ ______________________________________
Unterschrift des Doktoranden